DEVELOPMENT OF ANODE MATERIALS USING ELECTROCHEMICAL ATOMIC LAYER DEPOSITION (E-ALD) FOR ENERGY APPLICATIONS

By

Nqobile Xaba

A thesis submitted in fulfilment of the requirements for the degree of Doctor of Philosophy in the Department of Chemistry, Faculty of Natural Science, University of the Western Cape.

Supervisor: Dr L. Khotseng

Co-Supervisor: Dr R.M. Modibedi

April 2018

Declaration

I declare that the development of Anode Materials using electrochemical atomic layer deposition (E-ALD) for energy applications **is my own work**, **that it has not been submitted for any degree or examination in any other university, and that all sources I have used or quoted have been indicated and acknowledged by means of complete references.**

Nqobile Xaba **April 2018**

Signed…….

Keywords

Nanomaterials

Electrodeposition

Underpotential

Thin films

Electrocatalyst

Anode

Fuel cells

Sodium ion battery

Carbon dioxide reduction

Abstract

Nanomaterials have been found to undeniably possess superior properties than bulk structures across many fields of study including natural science, medicine, materials science, electronics etc. The study of nano-sized structures has the ability to address the current world crisis in energy demand and climate change. The development of materials that have various applications will allow for quick and cost effective solutions. Nanomaterials of Sn and Bi are the core of the electronic industry for their use in micro packaging components. These nanomaterials are also used as electrocatalysts in fuel cells and carbon dioxide conversion, and as electrodes for rechargeable sodium ion batteries. There are various methods used to make these nanostructures including solid state methods, hydrothermal methods, sputtering, and vacuum deposition techniques. These methods lack the ability to control the structure of material at an atomic level to fine tune the properties of the final product.

This study aims to use E-ALD technique to synthesis thin films of Sn and Bi for various energy applications, and reports the use of E-ALD in battery applications for the first time. Thin films were synthesised by developing a deposition sequence and optimising this deposition sequence by varying deposition parameters. These parameters include deposition potential, and concentration of precursor solution. The thin films were characterised using cyclic voltammetry, linear sweep voltammetry, chronoamperometry for electrochemical activity. These were also characterised using scanning electron microscope for morphology, x-ray diffraction for crystal phases, energy dispersive spectroscopy for elemental mapping, and focused ion beam scanning electron microscope for thickness. The elemental content was analysed using electron probe micro analysis and inductively coupled plasma mass spectrometry. The electrochemical impedance charge and discharge profile were used for electrochemical battery tests.

Thin films of tin (Sn) and bismuth (Bi) on gold substrate were deposited using the indirect underpotential deposition method from sulphate based electrolytes. Cyclic voltammetry was used to study the deposition of Sn and Bi on Au and a deposition cycle was developed. The deposition parameters were also optimized. CV studies showed that Bi and Sn have an underpotential deposition (UPD) onset of -100 mV and -350 mV respectively. As a result, an indirect UPD method was used to overcome the large potential gap between Bi and Sn UPD. The SnBi films contained SnBi in a ratio of 1:3 with well-defined crystallites of Sn and Bi evenly distributed on the surface. The Bi on Au thin film contained only bismuth with well-

defined particles. The elemental map confirmed the presence of the elements. The SnBi thin film was found to contain phases of Bi, SnBi, and AuSn. The film thickness varied along the deposit from 100 nm to 112 nm.

Bimetallic films of SnBi and Bi were deposited on Cu foil substrate. Cu foil is the electrode component of the anode part of a rechargeable battery. The fabrication of self-supported electrodes not only eliminates the use of toxic binders, it also reduces the production costs of batteries. Sn and Bi thin films were electrodeposited from chloride based electrolytes and parameters including the deposition potential of Bi and the concentration ratio of Sn and Bi were evaluated. The results showed that Bi deposits at different potentials were structurally different while varying the concentration of the elements did not have an effect on the morphology. All the deposits were crystalline. The binary SnBi materials contained Sn, Bi and other phases of Cu and Sn. The elements were distributed all over the film, however, Bi was found concentrated on the surface while Sn was distributed evenly across the film. The film thickness varied slightly across the film and was found to be 2 µm thick for a 300 cycle deposit. The SnBi material exhibited a high initial discharge capacity of 1900 mA h/g and suffered a 65% capacity loss within the first five cycles. However, it was able to maintain some capacity until 100 cycles.

Thin films of Pd, PdSn, PdBi, and PdBiSn on Au substrate were prepared for the electro-oxidation of ethanol and glycerol in alkaline media. The catalysts were found to be made of well-rounded particles evenly distributed on the surface and the elemental map confirmed the presence of all elements on all the prepared materials. The activity of the catalysts towards alcohol electro-oxidation reaction (AOR) revealed that the addition of Sn and Bi on Pd improved the activity for both ethanol and glycerol. Catalysts with Sn showed better activity than Bi catalysts, however, the ternary materials showed the most improved activity and stability. When comparing the oxidation of two alcohols, all the catalysts were more active towards the oxidation of ethanol than glycerol.

The electrodeposited Bi on Au substrate was finally evaluated as a catalyst for CO_2 reduction and the possible products were also tested using cyclic voltammetry. The results showed that two peaks that were due to the by-products emerged at lower potentials than the Au reduction peak and higher potentials than oxygen reduction peaks. These peaks were found to match that found in the CV scan of urea.

This study has demonstrated that thin films of Sn and Bi can be tailor made on different substrates via E-ALD to meet the application requirements. A method was successfully developed to make SnBi and Bi thin films on Au substrate. This method was further used to manufacture these thin films on Cu foil substrate and then used for the first time in battery applications. The SnBi battery electrodes are promising anodes but further work to improve capacity retention needs to be done. E-ALD technique is a versatile tool that can be used across different applications to make materials with improved properties.

Outputs

Oral Presentation:

- The 1st Africa Energy Materials Conference 28-31 March 2017, CSIR-ICC Pretoria South Africa.
- SA Energy Storage Conference 28-30 November 2017, Emperors Palace Ekurhuleni South Africa.

Poster Presentation:

- 5th CSIR Conference, emerging researcher's symposium, 8-9 October 2015 CSIR-ICC Pretoria South Africa.
- The South African Chemical Institute (SACI) North, Young chemist symposium, 23rd November 2016, University of Limpopo, South Africa.

Submitted manuscripts:

- The effect of potential and concentration on underpotentially deposited SnBi on Cu foil for sodium ion batteries.
- Pd, PdSn, PdBi, and PdBiSn Catalysts for the Electro-Oxidation of Alcohols in Alkaline Media.

Acknowledgements

I made a decision that I was going to be a scientist in grade 4 when I first heard the word. Over the years of school I have changed my mind with careers but I have always gone back to being a scientist. Science fascinated me earlier on, I was always eager to learn how the world works, and how everything came to be. Fast forward to first year at University, I again decided that I was going to study until my doctoral degree in Chemistry. As a black female child of first generation who had access to higher education, I have responsivities that make this decision look hasty. This was going to be hard to do but I was determined. I am glad that the day has come where I am finally making this dream come true. It took strength, dedication, resilience and a lot of faith in me to get here. Along this journey I have met the most amazing people, made lifetime friends, family and acquaintances.

My supervisors: ***Dr Mmalewane Modibedi***-I am eternally grateful to you for all the guidance and lessons you have imparted on me over the years. You gave me courage and room to grow, you afforded me invaluable opportunities. More than anything, you made me feel at home in a place where I knew no one; ***Dr Lindiwe Khotseng***-I met you at the start of this journey, you have had more impact in my life more than you know, thank you for the guidance, and the lessons you have impacted me.

Colleagues and collaborators: Energy Materials staff-I thank you for the assistance with my work, the friendly and welcoming environment; **Prof. John Stickney and his team at** the University of Georgia (UGA).-for welcoming me to their laboratory, accommodating me in a faraway land, and the lessons I leant are invaluable and have been critical part of my work.

Funding: This research is financially supported by the Council for Scientific and Industrial Research and the University of Western Cape (CSIR-UWC) co-operation fund, and the US Air Force Office of Scientific Research (AFOSR).

Dad: I talk to you more often than any other person. You are my source of strength, my guide and my mentor, I know no better man than you. I only try to go through this life knowing that I am making you proud, so that all the sacrifices you made for us do not go in vain. I miss you every day, I love you, forever and always.

Family: ***Mama***-I am eternally grateful for raising me to the women I am today, I have come to realise that I am growing more like you every day, I am indeed my mother's daughter,

Everything I do and ever do is for you to have a better life. ***My siblings (Mtuseni, Bonebusa, Sandile, Ngabanaki, Bongokuhle, Mtophethwe)***-I am my brother's keeper and my sister's best friend, I got you, I love you; ***Nephews and Nieces-*** I am still shocked at how grown up you all are every time I see you; I know I am never around but that how life is sometimes; I love you more than you know; I hope to live my life to inspire you, and for you to know that you can achieve anything you set your mind to.

Friends: Thank you for being there when I needed you, for the laughter, for holding my hand, for the sisterhood, for the love. Surely all of you know how much I love you.

"God is love" 1 John 4:8-21

Dedication

"Khulumani, Feleba, Nonkosi, Shwabada"

"Ngiyabonga"

"Lala ngokuthula"

Table of Contents

List of Figures

List of Tables

Abbreviations

E-ALD	Electrochemical atomic layer deposition
UPD	Underpotential deposition
SLR	Surface limited reaction
AOR	Alcohol oxidation reaction
DMFC	Direct methanol fuel cell
CV	Cyclic Voltammetry
LSV	Linear sweep voltammetry
CA	Chronoamperommetry
SEM	Scanning electron microscopy
FE-SEM	Field emission-SEM
FIB-SEM	Focused ion beam-SEM
XRD	X-ray diffraction
ICPMS	Inductively coupled plasma mass spectrometry

Units

Symbol	unit
M	molar
mM	millimolar
mg	milligram
^{o}C	degrees Celsius
At%	atomic percent
wt%	weight percent
vol%	volume percent
ppm	parts per million
Ppb	Parts per billion
µS/cm	microSiemens per centimetre
nm	Nanometre
µm	micrometre
V	Volts
A	Ampere
I	Current
Ω	Ohm
s	Seconds
min/s	Minute/s
hr/s	Hour/s
Hz	Hertz
Å	Angstroms
mV/s	millivolts per second
cm^2	centimetre squared
eV	electron Volts
mAh/g	milliampere hour per gram
kWh/L	killoWatts hour per litre
K	Kelvin
Atm	atmospheres
amu/s	Atomic mass units per second

CHAPTER 1

1 Introduction

This section introduces the study being carried out. A brief background, the rationale for this study, the problem statement, the aim and detailed objectives will be outlined. The scope of the research study with used references and outline will be the given.

1.1 Background

Renewable energy resources continue to receive a lot of attention in the research community recently. This was brought about by the world wide awareness of the limited fossil fuel reserves and the implications arising from the use of fossil fuels (Palacin 2009; Ellis and Nazar 2012; Pan *et al.* 2013; Mahlia *et al.* 2014). Fossil fuels such as coal, oil and natural gas are being depleted and are contributing to the increase in greenhouse gases in the atmosphere. Greenhouse gases including carbon dioxide, methane, nitrous oxide, chloro- and hydrofluorocarbons, are the main cause of global warming. The use of energy sources that can be replenished and those with zero greenhouse gas emissions has thus received a lot of research interest. Renewable energy sources including solar and wind are popular candidates due to infinite amounts of sunlight and wind in the world. Solar and wind energy resources require the use of energy storage systems to balance energy distribution during peak and off peak periods (Ellis and Nazar 2012; Palomares *et al.* 2012). Energy storage devices include electrochemical (secondary batteries and flow batteries), electrical (supercapacitors, superconducting magnetic), mechanical (pumped hydro, compressed air, flywheel), thermochemical (solar fuels), thermal (latent heat storage), and chemical (hydrogen storage) (Luo *et al.* 2015).

1.2 Rationale and Motivation

Research efforts into finding technological solutions for energy storage and conversion are being prioritized to give the uptake of renewable energy sources a potential viability. Finding materials that are abundant, cheap and can be used for a wide range of applications that can save time and maximise technological outputs is the holy-grail for ESC (Energy Storage and Conversion). Nanostructures of Sn and Bi are a huge part of the electronic industry for their use in electro packaging. These nanostructures have been receiving a lot of attention over the

last decade in materials science for applications in rechargeable batteries, carbon dioxide reduction, as well as catalysts for fuel cells.

Energy conversion

The increase in world population, accompanied by the environmental concerns associated with the use of fossil fuels for electricity generation are the driving force into finding ways to develop powerful and finely distributed power generators. The conversion of chemical energy to electrical energy is more important due to the current increase in energy demand for applications in electricity production and hybrid electric vehicles (EHVs). Fuel cells provide a flexible way of electricity generation.

Fuel cells are electrical devices with zero emission of greenhouse gases. Their mode of operation is by converting chemical energy into electrical energy. A fuel and oxidant react to form electricity, water and heat (Kirubakaran *et al.* 2009; Patil *et al.* 2011). The reaction is promoted by a catalyst. Properties of fuel cells include their high power density and efficiency, low temperature of operation, safety and quietness, clean energy, environmentally friendly (Niakolas *et al.* 2016). Direct methanol fuel cells (DMFC) are popular amongst other types because they use a liquid alcohol which is cheap and have high energy density (Jurzinsky *et al.* 2015). Their development is hindered by the slow electro-oxidation of alcohols, the cost of less abundant Pt catalyst and alcohol crossover through the membrane (Motsoeneng *et al.* 2015; Ong *et al.* 2017). These problems have been solved by using alkaline environment (Jurzinsky *et al.* 2015). The advantages of using Alkaline DMFC are that currently a cheaper catalysts can be used, the use of alkaline anion exchange membrane (AAEMs) electrolyte reduces carbon dioxide rejection problem as opposed to traditional fuel cells (Jurzinsky *et al.* 2015). Research effort in this field is directed towards improving and finding metal catalysts for alcohol oxidation under alkaline conditions that are efficient and cost effective. Pt is the most studied and best catalyst, but it is expensive (Sheikh *et al.* 2013). Pd is one of the promising candidates to replace Pt in alkaline medium. Highly ordered and nanosized Pd catalysts, have increased alcohol oxidation reaction (AOR) activity that are due to high surface area (Yi *et al.* 2015). Research studies have found that binary or ternary Pd catalysts have improved and increased AOR activity compared to pure Pd (Sheikh *et al.* 2013; Yi *et al.* 2015). Sn and Bi modified Pd catalysts have shown better activity including Pd-Sn, Pd-Ru-Sn (Modibedi *et al.* 2011), PdSnNi (Yi *et al.* 2015), Pd_xBi (Zalineeva *et al.* 2014), and BiPd/C (Cai *et al.* 2013). The successful synthesis of functional, lower cost

nanoelectrocatalysts with superior alcohol oxidation activities could provide economic potential for Alkaline DMFC so that the goal of reaching an energy balanced system is fully attainable.

Carbon capture and utilisation

Global warming effects have probed review in the way CO_2 is emitted and used. Most of the known processes that release CO_2 are being reviewed to find alternatives or ways of capturing, using or storing CO_2. The most logical way of reducing CO_2 is trapping it, while the economic way is converting it to fuel hydrocarbons (Jitaru 2007; Whipple and Kenis 2010; Zhang *et al.* 2017). The industrial Fischer-Tropsch process used to convert CO_2 uses high temperature and pressure making it expensive (DiMeglio and Rosenthal 2013). Electrochemical methods using metal catalysts to selectively reduce CO_2 to hydrocarbons require room temperature and ambient pressure (Lim *et al.* 2014). Electrochemical conversion methods are more cost effective (Zhang *et al.* 2017). Amongst metal catalysts, Bi and Sn based catalysts have shown great promise for CO_2 reduction. Bi-carbon monoxide evolving catalyst (CMEC) selectively produces CO (DiMeglio and Rosenthal 2013; Medina-Ramos *et al.* 2014), Sn/Pb/Sb-CMEC selectively produces CO less efficient compared to Bi-CMEC (Medina-Ramos *et al.* 2015), and Sn-Pb alloys is selective towards formate production (Choi *et al.* 2016). The key to reducing CO_2 relies on the discovery of efficient, robust and cheap catalysts that can effectively reduce CO_2 rapidly to fuels.

Energy storage

Secondary batteries provide an easier way to store energy compared to primary batteries because they are easy to maintain, are flexible and have high energy conversion efficiency (Pan *et al.* 2013). Lithium ion batteries are by far the most developed secondary batteries, having been successfully used in portable electronics and are being further developed for hybrid electric vehicle applications (Hong *et al.* 2013). Lithium is low in abundance on earth and therefore its use on these applications would increase the price of lithium resources and hence the cost of lithium ion batteries (Slater *et al.* 2013). Therefore, there is a gap to find lithium alternatives. Sodium based batteries have a huge potential to be used in energy storage systems due to the high abundance of sodium, low price and it has the same chemistry as lithium (both group I elements) (Kim *et al.* 2012; Palomares *et al.* 2013; Slater *et al.* 2013). Sodium based batteries have lower energy density and operating voltage than lithium ion batteries due to the larger size of sodium ion (Slater *et al.* 2013). Therefore they

can be used in applications where energy density is not critical such as electrical grid storage (Kim *et al.* 2012). Sodium ion batteries are not in the market yet and for this to happen, electrode materials for a safe, economically viable and long lasting battery must be developed (Palomares *et al.* 2012; Hong *et al.* 2013).

The sodium ion battery consists of three main parts: a cathode, anode and an electrolyte. Its mode of action is by insertion/removal of sodium ion into the cathode during discharging and charging respectively between the cathode and anode through the electrolyte (Ellis and Nazar 2012; Palomares *et al.* 2012; Pan *et al.* 2013; Slater *et al.* 2013). Sodium ion batteries use sodium analogues of the cathode materials used in lithium ion batteries. The common anode used in lithium ion batteries namely graphite, does not intercalate sodium ions. Most of the research is currently being undertaken to find suitable anode materials. Amongst all the currently investigated anode materials, alloys have the most potential due to their high capacity and safety (Zhang 2011). Alloy materials of Sn and Bi have been used in Na ion batteries and has high capacity of 847 and 380 mA h g^{-1} respectively. The challenge with the use of alloy anodes is the capacity loss during cycling. This is due to large volume changes that cause defects in the electrodes (Zhang 2011; Ellis and Nazar 2012; Kim *et al.* 2012). Therefore, Na ion batteries are suitable for applications where energy density is not important such as electrical power grids. Tailor made anode materials have a potential to make anode materials that are able to sustain their capacity during electrochemical cycling.

1.3 Problem Statement

Deposition techniques have been used to fabricate a range of Sn and Bi materials. These include sputtering, molecular beam epitaxy, thermal evaporation, and electrodeposition (Uosaki *et al.* 1995; Venables 2000; Tsai *et al.* 2007; Hu *et al.* 2008; Bedoya-Hincapié *et al.* 2015). These techniques are limited by the use of high temperature, and the need for a vacuum, due to their high costs and specialised equipment. Electrochemical atomic layer deposition (E-ALD) is the one technique that uses atmospheric temperature and pressure, and is cost effective. E-ALD was first reported by Gregory and Stickney (Gregory and Stickney 1991), for the deposition of II-VI semiconductor thin films and from then on it has been widely applied in the production of semiconductor thin films for electronic devices. E-ALD has been used to make thin films of CdTe (Gregory *et al.* 1991; Flowers *et al.* 2002), ZnSe (Pezzatini *et al.* 1999), CdSe (Mathe *et al.* 2004), Sn-Se (Qiao *et al.* 2005), HgTe (Venkatasamy *et al.* 2006), PbSe (Vaidyanathan *et al.* 2006), PbTe (Banga *et al.* 2008; Banga

et al. 2014), $Pb_{(1-x)}Sn_xSe$ (Lin *et al.* 2011), $CuInSe_2$ (Banga *et al.* 2012), Cu_2ZnSnS_4 (Valdes *et al.* 2014; Czerniawski and Stickney 2016), In_2Se_3 (Czerniawski and Stickney 2016). E-ALD involves the alternating deposition of elements to form the desired compound using surface limited reactions and underpotential deposition (UPD) (Gregory and Stickney 1991). E-ALD is convenient to use because it is a low cost process that works at room temperature. The advantages of using this deposition technique are the ability to control nucleation and growth of the films, and it promotes ordered deposition. The thickness of the films is governed by the number of deposition cycles. Parameters such as potential, pH, concentration, type of electrolyte, deposition time, and number of cycles can be optimised to control the deposition and growth. This makes E-ALD an attractive technique for manufacturing nanostructured materials for different applications. The use of E-ALD to make thin films for sodium ion battery anode materials has not been reported in literature.

1.4 Aim and objectives of the study

The aim is to develop anode materials using electrochemical atomic layer deposition for energy application through the following objectives:

- Develop a suitable method for the preparation of Sn, Bi and Pd thin films using E-ALD on Au and Cu substrates.
- Evaluate the effect of parameters including deposition potential and concentration on the formed deposits.
- Characterise the materials using electro analytical techniques namely; cyclic voltammetry (CV), linear sweep voltammetry (LSV), and chronoamperometry (CA).
- Characterise the prepared materials using suitable techniques including, scanning electron microscope (SEM), energy dispersive spectroscopy (EDS), Field Ion beam SEM (FIB SEM), X-Ray Diffraction (XRD).
- Determine the elemental content of the deposits using electron probe micro analysis (EPMA) and inductively coupled plasma mass spectroscopy (ICPMS).
- Electrochemical characteristics of anode materials for Na ion battery applications using CV, electrochemical impedance spectroscopy (EIS), electrochemical charge and discharge.
- Carbon dioxide reduction studies using CV.
- Determine the electrochemical activity for alcohol oxidation reaction (AOR) reaction in alkaline media.

1.5 Framework

Preparation of the thin films using E-ALD

Preparation of thin films will commence with the selection of background electrolyte, precursor salts and pH. The underpotential deposition (UPD) of elements on various substrates will be determined using cyclic voltammetry. UPD will be used to deposit the elements on the substrate using E-ALD. The sequence and number of cycles of deposition will be optimised, while the potential and concentration effects will be evaluated.

Characterisation

The morphology of the films will be determined using SEM. The film thickness and cross sections will be obtained using FIB SEM. Elemental analysis of the films will be determined by using an energy dispersive spectrometer coupled with SEM. Composition of the films will be determined using EPMA and ICPMS. The crystallinity of the materials will be determined using XRD.

Evaluation

The electrochemical performance of the prepared anode films will be investigated at room temperature using coin cells with the films as working electrode and a sodium metal foil as a reference electrode. Cycling rate will be carried out using cyclic voltammetry, and impedance spectroscopy used to determine the impedance. Charge-discharge tests will be determined galvanostatic method. CO_2 reducing capability will be studied using CV. AOR activity will be evaluated using CV, LSV and CA.

1.6 Research outline

Chapter 1: This is the introduction, will give an overview and a broad introduction to the important terms. It will highlight the importance of this study, how it is going to be done and what we hope to achieve.

Chapter 2: The literature related to the topic will be reviewed. The concept of nanomaterials will be introduced, Sn and Bi nanomaterials will be discussed, fabrication methods will be summarised with an emphasis in E-ALD, applications in batteries, conversion of CO_2, and AOR catalyst will be explained focusing on materials.

Chapter 3: This is the methodology, the chemicals and solution preparation is given. Experimental conditions used are also given, as well as the details for characterisation techniques, and electrochemical tests done in all applications.

Chapter 4 (Bi and SnBi on Au using E-ALD): This chapter will report on the development of a suitable method to electrodeposit Bi, and binary SnBi thin film materials using E-ALD on Au (111) substrates. UPD of Sn and Bi on Au will be studied. The deposition cycle will be optimised, the deposits characterised using selected techniques, and also tested for CO_2 reduction capability.

Chapter 5 (Bi and SnBi on Cu foil): This chapter further elaborates on the studies carried out in chapter 4, deposition of Sn and Bi on Cu foil instead of Au substrate using UPD. The effect of Bi UPD and Sn concentration variation on the morphology, content and crystal structure will be evaluated. Suitable characterisation techniques will be used. These materials will be tested as anode material in sodium ion battery.

Chapter 6 (Pd based electro catalyst for AOR): The deposition of binary and ternary materials of Pd, Sn and Bi will be done using E-ALD. The Cu UPD method will be used for Pd deposition, the UPD of Sn and Bi will be evaluated. The deposition cycle will be optimised, the materials will be characterised as needed. These will be tested for alcohol oxidation reaction activity.

Chapter 7(Bi on Au catalyst for CO_2 reduction): The deposited Bi on Au thin film material will be evaluated for the capability to reduce CO_2 to valuable product. The product/s formed will be identified using a suitable technique.

Chapter 8: This will outline the concluding and recommendations remarks. The summary of the main point from each study will be given, tying together all the studies carried out, including the materials that gave better performance. Future work to and recommended plan of action for the unsuccessful studies will be given.

1.7 References

Banga, D, Jarayaju, N, Sheridan, L, Kim, Y-G, Perdue, B, Zhang, X, Zhang, Q, Stickney, J (2012) Electrodeposition of $CuInSe_2$ (CIS) via electrochemical atomic layer deposition (E-ALD). *Langmuir* **28**, 3024-3031.

Banga, D, Perdue, B, Stickney, J (2014) Electrodeposition of a PbTe/CdTe superlattice by electrochemical atomic layer deposition (E-ALD). *Journal of Electroanalytical Chemistry* **716**, 129-135.

Banga, DO, Vaidyanathan, R, Xuehai, L, Stickney, JL, Cox, S, Happeck, U (2008) Formation of PbTe nanofilms by electrochemical atomic layer deposition (ALD). *Electrochimica Acta* **53**, 6988-6994.

Bedoya-Hincapié, CM, de la Roche, J, Restrepo-Parra, E, Alfonso, JE, Olaya-Florez, JJ (2015) Structural and morphological behavior of bismuth thin films grown through DC-magnetron sputtering/Comportamiento estructural y morfológico de películas delgadas de bismuto obtenidas a través de sputtering con magnetrón DC. *Ingeniare: Revista Chilena de Ingenieria* **23**, 92.

Cai, J, Huang, Y, Guo, Y (2013) Bi-modified Pd/C catalyst via irreversible adsorption and its catalytic activity for ethanol oxidation in alkaline medium. *Electrochimica Acta* **99**, 22-29.

Carrette, L, Friedrich, K, Stimming, U (2001) Fuel cells–fundamentals and applications. *Fuel cells* **1**, 5-39.

Choi, SY, Jeong, SK, Kim, HJ, Baek, I-H, Park, KT (2016) Electrochemical reduction of carbon dioxide to formate on tin–lead alloys. *ACS Sustainable Chemistry & Engineering* **4**, 1311-1318.

Czerniawski, JM, Stickney, JL (2016) Electrodeposition of In2Se3 using potential pulse atomic layer deposition. *Journal of Physical Chemistry* **120**, 16162-16167.

DiMeglio, JL, Rosenthal, J (2013) Selective conversion of CO_2 to CO with high efficiency using an inexpensive bismuth-based electrocatalyst. *Journal of the American Chemical Society* **135**, 8798-8801.

Ellis, BL, Nazar, LF (2012) Sodium and sodium-ion energy storage batteries. *Current Opinion in Solid State and Materials Science* **16**, 168-177.

Flowers, BH, Wade, TL, Garvey, JW, Lay, M, Happek, U, Stickney, JL (2002) Atomic layer epitaxy of CdTe using an automated electrochemical thin-layer flow deposition reactor. *Journal of Electroanalytical Chemistry* **524**, 273-285.

Gregory, BW, Stickney, JL (1991) Electrochemical atomic layer epitaxy (ECALE). *Journal of Electroanalytical Chemistry* **300**, 543-561.

Gregory, BW, Suggs, DW, Stickney, JL (1991) Conditions for the deposition of CdTe by electrochemical atomic layer epitaxy. *Journal of the Electrochemical Society* **138**, 1279-1284.

Hong, SY, Kim, Y, Park, Y, Choi, A, Choi, N-S, Lee, KT (2013) Charge carriers in rechargeable batteries: Na ions vs. Li ions. *Energy & Environmental Science* **6**, 2067-2081.

Hu, R, Zhang, Y, Zhu, M (2008) Microstructure and electrochemical properties of electron-beam deposited Sn–Cu thin film anodes for thin film lithium ion batteries. *Electrochimica Acta* **53**, 3377-3385.

Jitaru, M (2007) Electrochemical carbon dioxide reduction-fundamental and applied topics. *Journal of the University of chemical Technology and Metallurgy* **42**, 333-344.

Jurzinsky, T, Cremers, C, Jung, F, Pinkwart, K, Tübke, J (2015) Development of materials for anion-exchange membrane direct alcohol fuel cells. *International Journal of Hydrogen Energy* **40**, 11569-11576.

Kim, SW, Seo, DH, Ma, X, Ceder, G, Kang, K (2012) Electrode materials for rechargeable sodium-ion batteries: potential alternatives to current lithium-ion batteries. *Advanced Energy Materials* **2**, 710-721.

Kirubakaran, A, Jain, S, Nema, R (2009) A review on fuel cell technologies and power electronic interface. *Renewable and Sustainable Energy Reviews* **13**, 2430-2440.

Lim, RJ, Xie, M, Sk, MA, Lee, J-M, Fisher, A, Wang, X, Lim, KH (2014) A review on the electrochemical reduction of CO2 in fuel cells, metal electrodes and molecular catalysts. *Catalysis Today* **233**, 169-180.

Lin, S, Zhang, X, Shi, X, Wei, J, Lu, D, Zhang, Y, Kou, H, Wang, C (2011) Nanoscale semiconductor $Pb_{1-x}Sn_xSe$ (x= 0.2) thin films synthesized by electrochemical atomic layer deposition. *Applied Surface Science* **257**, 5803-5807.

Luo, X, Wang, J, Dooner, M, Clarke, J (2015) Overview of current development in electrical energy storage technologies and the application potential in power system operation. *Applied Energy* **137**, 511-536.

Mahlia, T, Saktisahdan, T, Jannifar, A, Hasan, M, Matseelar, H (2014) A review of available methods and development on energy storage; technology update. *Renewable and Sustainable Energy Reviews* **33**, 532-545.

Mathe, MK, Cox, SM, Flowers, BH, Vaidyanathan, R, Pham, L, Srisook, N, Happek, U, Stickney, JL (2004) Deposition of CdSe by EC-ALE. *Journal of crystal growth* **271**, 55-64.

Medina-Ramos, J, DiMeglio, JL, Rosenthal, J (2014) Efficient reduction of CO_2 to CO with high current density using in situ or ex situ prepared Bi-based materials. *Journal of the American Chemical Society* **136**, 8361-8367.

Medina-Ramos, J, Pupillo, RC, Keane, TP, DiMeglio, JL, Rosenthal, J (2015) Efficient conversion of CO_2 to CO using tin and other inexpensive and easily prepared post-transition metal catalysts. *Journal of the American Chemical Society* **137**, 5021-5027.

Modibedi, RM, Masombuka, T, Mathe, MK (2011) Carbon supported Pd–Sn and Pd–Ru–Sn nanocatalysts for ethanol electro-oxidation in alkaline medium. *International Journal of Hydrogen Energy* **36**, 4664-4672.

Motsoeneng, RG, Modibedi, RM, Mathe, MK, Khotseng, LE, Ozoemena, KI (2015) The synthesis of PdPt/carbon paper via surface limited redox replacement reactions for oxygen reduction reaction. *International Journal of Hydrogen Energy* **40**, 16734-16744.

Niakolas, DK, Daletou, M, Neophytides, SG, Vayenas, CG (2016) Fuel cells are a commercially viable alternative for the production of "clean" energy. *Ambio* **45**, 32-37.

Ong, B, Kamarudin, S, Basri, S (2017) Direct liquid fuel cells: A review. *International Journal of Hydrogen Energy* **42**, 10142-10157.

Palacin, MR (2009) Recent advances in rechargeable battery materials: a chemist's perspective. *Chemical Society Reviews* **38**, 2565-2575.

Palomares, V, Casas-Cabanas, M, Castillo-Martínez, E, Han, MH, Rojo, T (2013) Update on Na-based battery materials. A growing research path. *Energy & Environmental Science* **6**, 2312-2337.

Palomares, V, Serras, P, Villaluenga, I, Hueso, KB, Carretero-González, J, Rojo, T (2012) Na-ion batteries, recent advances and present challenges to become low cost energy storage systems. *Energy & Environmental Science* **5**, 5884-5901.

Pan, H, Hu, Y-S, Chen, L (2013) Room-temperature stationary sodium-ion batteries for large-scale electric energy storage. *Energy & Environmental Science* **6**, 2338-2360.

Patil, MB, Bhagat, S, Sapkal, R, Sapkal, V (2011) A review on the fuel cells development. *Scientific Reviews & Chemical Communications* **1**, 25-41.

Pezzatini, G, Caporali, S, Innocenti, M, Foresti, M (1999) Formation of ZnSe on Ag (111) by electrochemical atomic layer epitaxy. *Journal of Electroanalytical Chemistry* **475**, 164-170.

Qiao, Z, Shang, W, Wang, C (2005) Fabrication of Sn–Se compounds on a gold electrode by electrochemical atomic layer epitaxy. *Journal of Electroanalytical Chemistry* **576**, 171-175.

Sheikh, A, Correa, P, da Silva, EL, Savaris, I, Amico, S, Malfatti, C (2013) Energy conversion using Pd-based catalysts in direct ethanol fuel cell. *Renewable Energy & Power Quality Journal* **11**, 300.

Slater, MD, Kim, D, Lee, E, Johnson, CS (2013) Sodium-ion batteries. *Advanced Functional Materials* **23**, 947-958.

Tsai, Y-D, Hu, C-C, Lin, C-C (2007) Electrodeposition of Sn–Bi lead-free solders: effects of complex agents on the composition, adhesion, and dendrite formation. *Electrochimica Acta* **53**, 2040-2047.

Uosaki, K, Shen, Y, Kondo, T (1995) Preparation of a highly ordered Au (111) phase on a polycrystalline gold substrate by vacuum deposition and its characterization by XRD, GISXRD, STM/AFM, and electrochemical measurements. *The Journal of Physical Chemistry* **99**, 14117-14122.

Vaidyanathan, R, Cox, SM, Happek, U, Banga, D, Mathe, MK, Stickney, JL (2006) Preliminary studies in the electrodeposition of PbSe/PbTe superlattice thin films via electrochemical atomic layer deposition (ALD). *Langmuir* **22**, 10590-10595.

Valdes, M, Modibedi, M, Mathe, M, Hillie, T, Vazquez, M (2014) Electrodeposited Cu2ZnSnS4 thin films. *Electrochimica Acta* **128**, 393-399.

Venables, J (2000) 'Introduction to surface and thin film processes.' (Cambridge University Press:

Venkatasamy, V, Mathe, MK, Cox, SM, Happek, U, Stickney, JL (2006) Optimization studies of HgSe thin film deposition by electrochemical atomic layer epitaxy (EC-ALE). *Electrochimica Acta* **51**, 4347-4351.

Whipple, DT, Kenis, PJ (2010) Prospects of CO2 utilization via direct heterogeneous electrochemical reduction. *The Journal of Physical Chemistry Letters* **1**, 3451-3458.

Yi, Q, Chu, H, Chen, Q, Yang, Z, Liu, X (2015) High Performance Pd, PdNi, PdSn and PdSnNi Nanocatalysts Supported on Carbon Nanotubes for Electrooxidation of C2□ C4 Alcohols. *Electroanalysis* **27**, 388-397.

Zalineeva, A, Serov, A, Padilla, M, Martinez, U, Artyushkova, K, Baranton, Sv, Coutanceau, C, Atanassov, PB (2014) Self-supported Pd x Bi catalysts for the electrooxidation of glycerol in alkaline media. *Journal of the American Chemical Society* **136**, 3937-3945.

Zhang, W, Hu, Y, Ma, L, Zhu, G, Wang, Y, Xue, X, Chen, R, Yang, S, Jin, Z (2017) Progress and Perspective of Electrocatalytic CO_2 Reduction for Renewable Carbonaceous Fuels and Chemicals. *Advanced Science*

Zhang, W-J (2011) A review of the electrochemical performance of alloy anodes for lithium-ion batteries. *Journal of Power Sources* **196**, 13-24.

CHAPTER 2

2 Literature Review

The focus of this chapter is on SnBi nanostructures prepared by electrodeposition techniques. The concept of nanomaterials will be introduced, followed by highlighting of Sn and Bi as metals of interest for nanomaterials. The possible methods used globally to fabricate the SnBi thin film nanostructures will be briefly described while more details are given for E-ALD. Lastly, the different fields of application will be explored focusing on the SnBi materials.

2.1 Nanomaterials

The development of nanomaterials has received attention in recent years due to their superior properties compared to bulk materials affording them a wide range of applications (Gurrappa and Binder 2008; Mohanty 2011). Nanomaterials are used for energy, electronic, environmental and medical applications. By working in a nanometre scale, materials can be tailor made for various applications by controlling the growth of the nanomaterial. Nanomaterials refer to structures with single unit sized between 1 to 1000 nanometres. Nanomaterials contain small grain size, a larger surface area of atoms, resulting in them exhibiting superior or completely new properties compared to the bulk of the same material (Gurrappa and Binder 2008). The production of nanomaterials can be done using a top down approach or a bottom up approach (Oviedo *et al.* 2015; Dimitrov 2016). The former involves starting with large objects to smaller ones, while the latter involves molecular manufacturing. The bottom up strategy is the most favourable way because it involves linking atoms to make larger components, which can be linked with each other to form larger components. This also allows for the formation of specific structures by controlling the reaction conditions. Nanomaterials are also known as nano-crystals, nano-crystalline materials or nanostructures (Gurrappa and Binder 2008). These materials have grain size ranging from 1-100 nm. These can have three, two, and one dimensional structures. Examples are nanowires, nanotubes, superlatices, and thin films amongst others.

2.2 Bi and Sn nanostructures

The current demand for energy storage solutions has caused a renewed interest in research and production of cost effective materials with variety of applications. Bismuth (Bi) and tin

(Sn) compounds are candidates for a wide variety of applications due to their unique properties. Nanomaterials of Bi and Sn have been used in electronic components, energy conversion, and energy storage amongst others (Katayama *et al.* 1996; Sandnes *et al.* 2008; Su *et al.* 2015; Liu *et al.* 2017; Ni *et al.* 2017). Bi is a semimetal group IV element, its unique electronic properties allows for varied applications (Bedoya-Hincapié *et al.* 2015). These properties include lowest effective mass of all elements, high carrier mobility, low carrier density long mean free path, and high magnetoresistance (Bedoya Hincapie *et al.* 2012). Bi transitions from semimetal to semiconductor when moving from bulk nanostructures to thin film. Bi possess an interesting chemistry for knowledge generation, most importantly, its adjustable chemical, electronic, and magnetic properties has generated research interest for use in magnetic sensors (Bedoya-Hincapié *et al.* 2015), electronic and thermoelectric devices (Zhu *et al.* 2005c), energy storage electrodes for rechargeable batteries (Su *et al.* 2015), energy conversion in fuel cells (DiMeglio and Rosenthal 2013). Bi has low toxicity; as a result it has been used as a lead (Pb) replacement in the popular SnPb alloy material used in microchips and electronic packaging components, for environmentally friendly materials (Katayama *et al.* 1996; Sandnes *et al.* 2008; Hu *et al.* 2009). Pb was initially added to Sn to supress the growth of whiskers; whiskers are dangerous in electronics for causing short circuits.

Sn is a group V semiconductor that is soft and ductile (Walsh and Low 2016a). The electroplating industry revolves around Sn due to the enormous and impact of its applications in this field. Sn coatings protect against corrosion, air oxidation, and improve solderability (Walsh and Low 2016b). Sn nanostructures are used for microelectronics, in printed circuit boards, automotive parts, jewellery and décor, and energy storage (Tamura *et al.* 2002; Walsh and Low 2016a). The formation of Sn compound nanostructures is important across all applications to enhance the properties of Sn materials. Solder materials used in the electronic industry include Cu-Sn, Sn-Ag, Sn-Ag-Cu, Sn-Zn, Sn-Bi, Sn-Zn-Bi, which have unique properties (Tsai and Hu 2011). SnBi nanomaterials are of higher interest due to the low temperature flowing properties of the eutectic 42Sn-58Bi (Chen *et al.* 2009; Vieira *et al.* 2017). In addition, the eutectic phase exhibit good joint strength, low surface tension, excellent creep resistance, and corrosion resistance.

2.3 Fabrication Methods

The properties and characteristics of nanomaterials are related to the fabrication method used. The method used allows the ability to control and manipulate shape, size and crystallinity of nanomaterials (Natter and Hempelmann 2003; Gurrappa and Binder 2008). Sn and Bi based nanostructures are no different. Bottom up strategies are best suited for the fabrication of nanomaterials include molecular beam epitaxy, thermal evaporation, sputtering and electrodeposition (Venables 2000; Stickney 2002) . These methods require a high vacuum, and high temperature, making the equipment complex and expensive. They are quick; therefore thicker deposits can be produced in shorter times. Electrodeposition is the opposite amongst them; nanostructures are made at room temperature and atmospheric pressure. Electrodeposition system is simple, and cost effective. The ability to optimise parameters (electrolyte, time, number of cycles) to make the desired nanomaterial, compensate for the many number of cycles required to grow a thinner film. An overview of these fabrication techniques is given.

2.3.1 Thermal evaporation

The temperature of the source material is increased until the material evaporates onto the substrate (Venables 2000). The source of the material can be in an open boat or suspended using a wire. Materials that are able to withstand high temperatures are used; tungsten and molybdenum are good examples. Precaution needs to be taken on the source material container used to avoid the nanomaterials being deposited all over creating a film that is not uniform. This can be avoided by using a crucible or oven to contain material source, as well as rotating the substrate for uniform deposits. The rate at which deposition occurs is depended on the temperature, the distance between source materials and substrate, and source area. It is important that the materials to be deposited do not react with the sample holder (crucible or boat). However, electron beam evaporation can be used to produce localised heating using a very high energy beam. Bi thin films were electrodeposited into silicon substrates using thermal evaporation at different temperatures (Kumari *et al*. 2007). This study found that the structure of the deposited films is depended on temperature and thickness. A bismuth doped tin oxide thin film for hydrogen sensor application was prepared, the study concluded that 5 At%. Bi had maximum activity (Sberveglieri *et al.* 1991). A multilayer material of Bi-Sn-Au was deposited on silicon substrate to eliminate the use of fluxes, this process is useful in making the eutectic 42Sn-58Bi solder alloy used as lead free

solder (Choe *et al.* 2001). Other materials include $(SnS)x–(Bi_2S_3)_{1–}x$ (Tariq *et al.* 2013), quaternary Se–Sn–(Bi,Te) (Yadav and Sharma 2015), and ternary Ag–Sn–Se (Cheng *et al.* 2016).

2.3.2 Molecular beam epitaxy (MBE)

The principle behind this technique is similar to thermal evaporation. In this case, high purity elements contained in fusion cells are evaporated, and these elements condense into the substrate (Venables 2000). The elements do not react with each other until they reach the substrate. Liquid and solid sources can be used. Deposition can be controlled by opening and closing shutters on the fusion cells, therefore also controlling the deposit. High purity materials are formed because the cells are cooled by liquid nitrogen, condensing all possible pollutants. The substrate is rotated for uniform deposition. A range of different materials can be formed by manipulating the shutters. Materials produced can be multi-layered metallic, quantum wires and wells, and superlattices. MBE systems are hyphenated systems making monitoring and characterising materials *in situ* easy. Techniques that fall under the MBE family includes Gas source MBE (GSMBE), metal organic MBE (MOMBE) or chemical beam epitaxy (CBE), and metal organic chemical vapour deposition (MOCVD). Multilayered materials of $Pb_{1-x}Sn_xTe$ ($0 < x < 0.1$) were grown on Si and BaF substrates using MBE, doping with Bi resulted in the formation of material with a wide range of refractive index, these are useful in making high refractive mirrors for vertical cavity injection lasers (Selivanov *et al.* 2010). Thin films of Bi_2Te_3 were grown on Si substrate, these were of high quality and cleanest films reported, these have potential applications in the microchip industry(Li *et al.* 2010). Other studies have fabricated materials including Sb_2Te_3/Bi_2Te_3 (Lanius *et al.* 2016), and Bi_2Se_3 (Mishra *et al.* 1997).

2.3.3 Sputtering

A versatile technique is used for cleaning samples, doping and deposition by varying the energy of the ions (Thornton and Greene 1994; Venables 2000). Also known as ion beam sputtering deposition (IBSD), charged ions or ion clusters can be deposited on a substrate to form thin film materials. This method is able to control where and how the metal is deposited. Sources used include ion beam accelerator, plasma and magnetron source. This technique is able to form quality deposits at lower substrate temperature, the use of charged ions limits mixing; the ion can be directed to a specific site. This level of structural control and precision is important in designing tailor made nanomaterials. Bismuth vanadate ($BiVO_4$) photo anodes used for photo electrochemical water splitting were made using reactive sputtering (Chen *et*

al. 2013). Other prepared materials include Cd_2SnO_4 (Haacke *et al.* 1978), and SnO (Sberveglieri *et al.* 1992).

2.3.4 Electrodeposition

Electrochemistry plays a huge role in the development of novel nanomaterials for technological advancement. The deposition occurs by controlling the potential or current of the metals being deposited. This method requires an understanding and study of the electrochemical behaviour of the metal to be deposited in the system and conditions. During electrodeposition, a potential is applied between two electrodes in contact with a solution containing the precursor metals (electrolyte). The reduction and oxidation of the metal species occurs, where the reduced metal is deposited while the oxidised metal dissolves. The potential of the half reaction is therefore governed by the Nernst equation (1) at room temperature (Stickney 2011).

$$\mathrm{E} = \mathrm{E}^0 + \frac{\mathrm{RT}}{z_e \mathrm{F}} . \mathrm{lin} \left(\frac{a_{ox}}{a_{red}} \right) \qquad (1)$$

F is the Faraday constant, T is the temperature, z is the charge of the ions, R the universal gas constant and, *a* is the activity of oxidation and reduction reactions.

Electrochemical methods offer surface modification and materials synthesis. The fabrication of nanomaterials using electrodeposition methods allows for the control of structure, composition and properties, resulting in novel materials that cannot be obtained using other techniques (Gurrappa and Binder 2008).

2.4 E-ALD

2.4.1 Defined

Atomic layer deposition uses surface limited reaction to form one atomic layer of a nanofilm, repeated a number of times to grow the film. The electrochemical form of atomic layer deposition (ALD) is referred to as electrochemical atomic layer deposition (E-ALD). EALD refers to the deposition of atomic layers of an element using underpotential deposition (UPD) or surface limited reactions (SLR), resulting in the formation of highly ordered products. This method has been previously known as ECALE (Suggs, 1991), EC-ALD, and ECALE (Gregory and Stickney 1991). Underpotential deposition is a SLR process used to the deposit an atomic layer of an element on another at a potential under that required to deposit the element on itself. The deposition results in monolayer (ML) coverage of the element being

deposited (Stickney 2011). ML is a unit of coverage specific to the element being deposited and occurs as a result of one atom being deposited per surface atom. This is a very attractive process because it uses dilute solutions, low energy, operates at room temperature and pressure (Giaccherini *et al.* 2017). The cycle needs to be optimised by varying the applied potential as well as solution composition (pH, electrolyte, concentration, and additive) (Stickney 2002).

2.4.2 UPD

A compound or alloy is formed using UPD due to the strong interaction between two elements as opposed to the interaction of the element with itself (Gregory and Stickney 1991; Gregory *et al.* 1991). The deposition of a metal onto a substrate produces an atomic layer of the element being deposited as a product. This atomic layer has a different electronic structure to that of the bulk element. The UPD chemistry is unique to each element and, must be investigated before deposition, and the formation of a deposition cycle is necessary. A cycle is made up of steps used to deposit one atomic layer of a pure element or compound. The cycle steps need to be optimised using applied potential and solution composition. The cycles steps are executed in a sequence and these can have different chemical reactions governing the deposition. There are a few known cycle chemistry types (Gregory *et al.* 1991; Stickney 2011). These are the oxidative-reductive UPD cycle (O-R), the reductive –reductive UPD (R-R), reductive-reductive UPD and reductive strip (R-R-R), the reductive –reductive UPD and oxidative strip (R-R-O), bait and switch (B&S), and surface limited redox reaction (SLRR). The rules of thin film formation and cycle chemistry depicts that the formed compound should be conformal or epitaxial, due to the deposition of a second element being limited by the first element availability. Factors that inhibit the formation of a conformal compound include; (i) the lack of lattice matching of the element and substrate, (ii) the increase in strain as number of cycles is increased, (iii) dislocations and defects that compensate for the strain.

2.4.3 Surface limited reactions (SLR) Deposition

SLR deposition is widely used in the plating industry, is also referred to as galvanic replacement. There are two main paths which the process occurs as shown in Figure 1 (Oviedo *et al.* 2015; Papaderakis *et al.* 2017). The first (A) one occurs when by complete replacement of a sacrificial monolayer by a noble metal. This method is ideal because it uses less amounts of the noble metal to form monolayer to sub monolayer coverages, therefore cost effective. The main disadvantage is that the preparation process setup is complicated by

the use of a sacrificial metal to deposit another and the requirement of a noble substrate for UPD, and potential control. Secondly, it involves the partial dissolution of surface layers and replacement by more noble metal. This forms mixed thicker shells of the noble metal while the less noble metal migrates to the core of the catalyst. The advantage of this path is that post treatment such as etching results in the formation of a variety of nanostructures, the thick core metal shells enforces stability, no sacrificial layer needed (one less step) decreasing costs, and uses cheap reactive metals (Cu, Fe, Pb). However, there are reduced geometric and electronic effects on the outermost noble metals due to increased thickness. SLR can be analysed using thermodynamics or kinetics or both approaches. The thermodynamic approach uses reaction conditions including pH, temperature and complex agents to determine the most favourable reaction. The kinetic approach on the other hand uses models to study time evolution of the SLR, and it also correlates the monolayer coverage of the UPD to time.

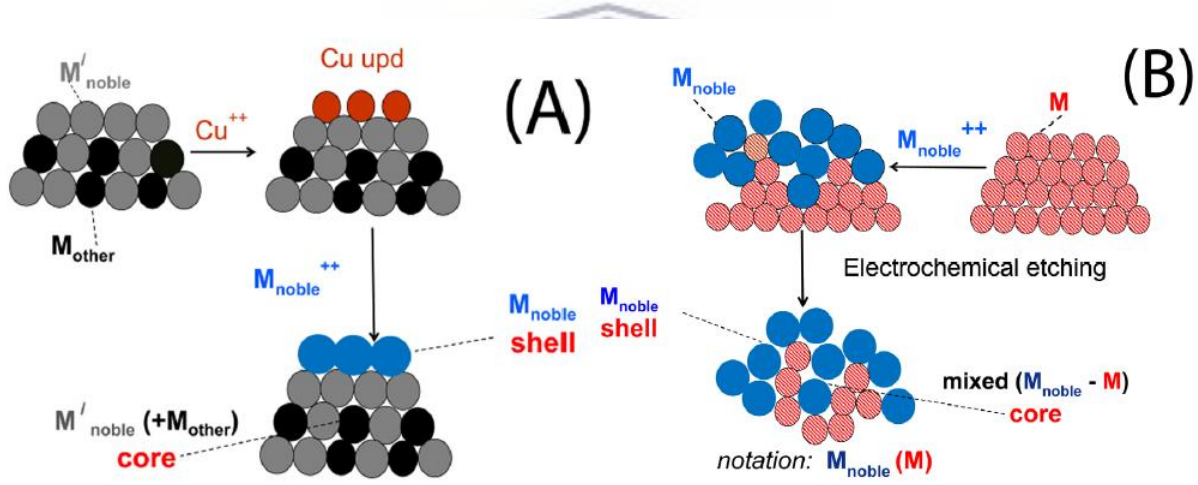

Figure 2.1: Mechanism for the two pathways for SLR (Papaderakis *et al.* 2017).

2.4.3.1 The thermodynamics approach

This process occurs when a metal (reaction 2) is introduced in a solution containing a more noble metal ions (reaction 3), resulting in the noble metal atoms depositing and the less noble metal released into the solution as shown by the overall reaction (reaction 4). A more noble metal between two is the one with a higher standard potential. This is a thermodynamically favoured reaction provided that the metal (M) is stable under the given conditions including pH, temperature, and complexing agents in the system. When the less noble metal dissolves and forms oxides or hydroxides depending on the solution composition, the deposition of the noble metal is accompanied by the growth of oxide or hydroxides of the less noble metal as

shown in equation 5. This is referred to as spontaneous deposition (Oviedo *et al.* 2015; Papaderakis *et al.* 2017).

$$M^{m+} + me^- \rightarrow M\ (E^0) \quad (2)$$

$$M_{noble}{}^{n+} + ne^- \leftrightarrow M_{noble}\ (E^0_{noble}) \quad (3)$$

$$M^{n+}_{noble} + n/m \rightarrow M_{noble} + n/m\, M^{m+}\ (E^0_{noble} - E^0 > 0) \quad (4)$$

$$M^{n+}_{noble} + n/m\ M + n/2\, H_2O \rightarrow M_{noble} + n/2m\, M_2O_M + nH^+\ (E^0_{Mnoble} - E^0_{M2OM} > 0) \quad (5)$$

2.4.3.2 Kinetics approach

The kinetic mechanism views the SLR process as that of corrosion reactions, and therefore analyses it using corrosion kinetics. This is done by relating the corrosion current to the less noble metal dissolution using Faraday's law. This leads to a conclusion that the potential difference of the two metals at equilibrium not only determines thermodynamics but also the kinetics of the SLR. The changes in concentration of the two metals in solution as deposition proceeds, changes the equilibrium potentials, and leads to SLR rate to decrease. When the deposition of the noble metal is controlled by mass transfer, the current rate is determined by mass transfer of noble metal. During the spontaneous deposition, the rate is controlled by the diffusion of the noble element (Oviedo *et al.* 2015; Papaderakis *et al.* 2017)

2.4.4 Deposition set up

2.4.4.1 Compound formation

The formation of a stable compound electrochemically is predicted using Pourbaix diagrams of the elements to be deposited (Stickney 2001). Pourbaix diagrams plot the pH and potential of each element. Finding the pH and potential conditions where both elements occur in their elemental state is ideal. Pourbaix diagrams of each element can be combined to represent the stability zones for compound formation between elements. The construction of compound Pourbaix diagrams also takes into account the free energy of compound formation. This can be illustrated by looking into the electrodeposition of Bi_2Te_3 which has been well studied (Mishra *et al.* 1997; Martın-González *et al.* 2002; Zhu *et al.* 2005c; Zhu *et al.* 2008; Li *et al.* 2010; Lanius *et al.* 2016). The Pourbaix diagram of Bi, Te and Bi_2Te_3 is shown in Figure 2.2 a, b and Figure 2.3 respectively (Parsons 1967; Martın-González *et al.* 2002). The first step is to determine the pH range where Bi and Te dissolves and can then be reduced to form Bi_2Te_3. Figure 2.3 shows that Bi_2Te_3 is stable all over the pH range and at potentials less than 0.5 V.

Therefore the solubility of the precursor salt used will determine the pH to use. Cyclic voltammetry studies are conducted to determine the exact UPD potential to use during the deposition. Bi_2Te_3 is formed by reducing its cations; this is illustrated in equation 6-8 (Martın-González *et al.* 2002). Bi forms from the reduction of Bi^{3+} (equation 6), while Te forms by first generating an intermediate in solution (H_2Te) (equation 7), that is further reduced to Te (equation 8). The question of which element does one deposit first is always complex, can be answered by depositing both elements first, and the deciding factor becomes which sequence of elements forms a stable deposit (Stickney 2001).

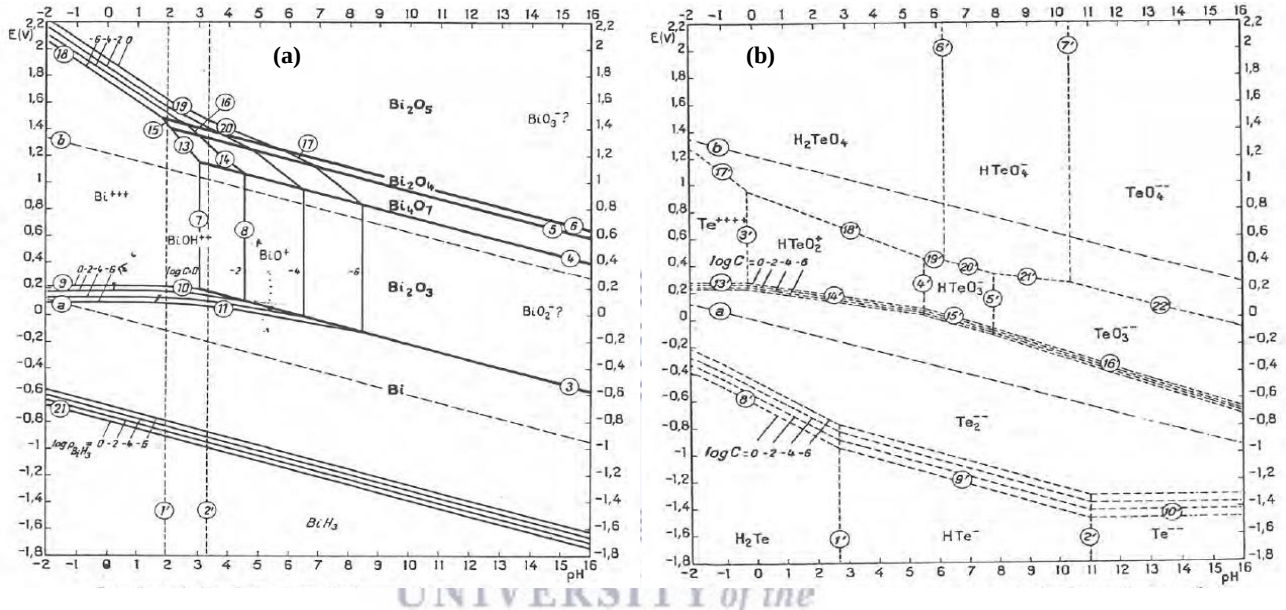

Figure 2.2: (a) Pourbaix diagram of Bi and (b) Te in water at 25 ^{o}C (Parsons 1967).

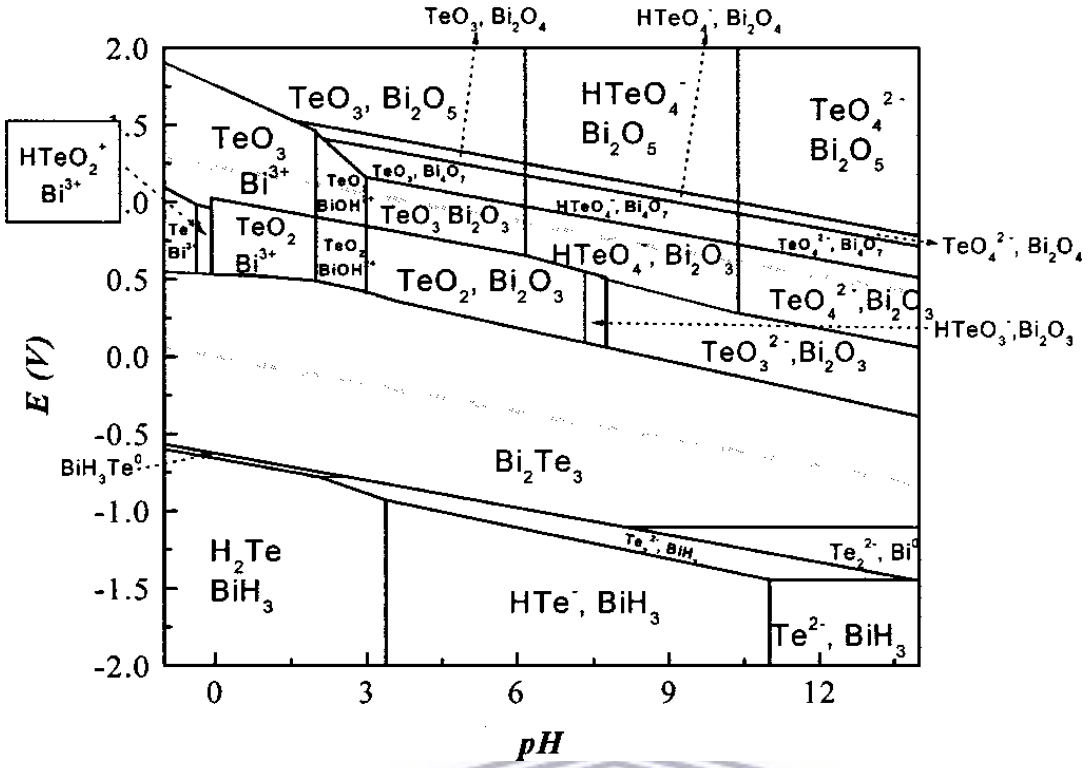

Figure 2.3: Pourbaix diagram of compound formation for the electrodeposition of Bi and Te at 25 ^{o}C and 1 atm (Martın-González *et al.* 2002)

$$Bi^{3+} + 3\,e^{-} \rightarrow Bi \quad E^{0} = 0.286\,V \tag{6}$$

$$HTeO_2^{+} + 5H^{+} + 6\,e^{-} \rightarrow H_2Te_{(aq)} + 2H_2O \quad E^{O} = 0.121\,V \tag{7}$$

$$2H_2Te + HTeO_2^{+} \rightarrow 3\,Te + 2H_2O + H^{+} \tag{8}$$

2.4.4.2 Solutions

The solutions used are prepared using analytical grade chemicals and high purity water. No further purification of reagents is required. Buffer solutions are often used and a combination of NH_4OH (33%) and $HClO_4$ (65%) is common. Precursor solutions used are very low concentrations around 1 mM and below (0.1 mM). Complexing agents and additives are also used depending on the desired materials and reaction conditions. Methane sulfonic acids (MSA) (Suh *et al.* 2006; Sandnes *et al.* 2008; Goh *et al.* 2013b) , ethylenediaminetetraacetic acid (EDTA) (Tsai *et al.* 2007), boric acid, phosphoric acid, hydroquinone and gelatin (Tsai *et al.* 2011; Goh *et al.* 2013a), citric acid (Tsai and Hu 2011), polyethylene glycol (Tsai and Hu 2009b; Tsai *et al.* 2011), are amongst the commonly used. These are often used to combat whisker formation, to bind specific metals, to reduce the potential difference of the metals deposited. Surfactants are also added to reduce the surface tension including perchlorinated

cationic surfactant (Low and Walsh 2008). Organic solvents have also been used during deposition including dichloromethane and supercritical fluids. Other studies have opted for deep eutectic solvents due to their low volatility, high conductivity and larger potential window compared to water (Vieira *et al.* 2017). Deep eutectic solvents choline chloride-ethylene glycol (Gao *et al.* 2014), $AlCl_3$/1-ethyl-3-methylimidazolium chloride and $ZnCl_2$/1-ethyl-3-methylimidazolium chloride (Vieira *et al.* 2017).

2.4.4.3 Substrates

The first layer of the deposit forms directly on the substrate, therefore the substrate used has a huge influence on the morphology of the deposit. Different types of substrate including single crystals, wafers, polycrystalline, film, foil or powders can be used (Stickney 2011). Lattice matching of substrate and deposit results in epitaxial deposits. The crystallographic facets of the substrate will interact differently with the element deposited which in turn affects surface coverage of the deposit on the substrate and structure of the deposit. The use of single crystal well characterised substrates is encouraged but even then, there will be steps and defects that can cause nucleation altering the structure and orientation of the deposit. Nucleation can be minimised by controlling the potential (Gregory *et al.* 1991).

The type of substrate used for deposits usually depend on the application. Most deposits to date of ECALE, ECALD and now E-ALD, have been formed on Au substrates. The electrochemical behaviour of Au has been well studied; Au does not peel off the glass and can be easily cleaned (Stickney 2002). Other methods to form thin films have also used Au as the main substrate including molecular beam epitaxy and sputtering (Sberveglieri *et al.* 1992; Mishra *et al.* 1997). The disadvantage of using Au substrates is that Au can form alloy with the depositing element due to surface mobility of Au atoms. A well-ordered compound will be formed when the lattice parameters matches those of the substrate, Au lacks this characteristic. Single crystal substrates are better able to lattice match with compounds formed using E-ALD. The use of single crystals is not cost effective as it cannot translate into products; the substrates are costly and therefore need an extra step to recycle (Stickney 2001). A number of affordable substrates have been investigated. These include Au on glass (Gregory *et al.* 1991), Cu substrates (foils, Cu on glass) (Tsai and Hu 2009b, 2011), Single crystal Cu (Okamoto *et al.* 2009), silver (Zhu *et al.* 2005b) ,and ITO on glass (Do *et al.* 2015).

2.4.4.4 The E-ALD system

The E-ALD system is described and used in a number of publications (Stickney 2001; Liang *et al.* 2011; Banga *et al.* 2012; Ledina *et al.* 2015; Czerniawski *et al.* 2016; Czerniawski and Stickney 2016; Dimitrov 2016; Giaccherini *et al.* 2017). The system is made up of solution reservoirs, valves, a flow cell, a potentiostat, connected to a computer equipped with software for operation. The electrochemical flow system and flow cell are shown in Figure 2.4 and 2.5 respectively. It is fully automated and can deposit many cycles per hour. The computer program allows for programming of cycles that make up a specific sequence to form the desired compound. Then the sequence for a compound can be executed. The actual deposition takes place onto a substrate in the flow cell. The flow cell contains a gasket and a substrate housed between two pyrex covers. The gasket sets the deposition area on the substrate to around 4 cm^2 and also provides space to contain the solution. The pyrex covers contain an inlet and outlet for solution, the counter electrode is embedded on it, it also has an airtight opening to insert the reference electrode. The reference electrode measures the potential of the working electrode without current passing through. The commonly used is the Ag/AgCl electrode, and others include the standard calomel electrode and standard hydrogen electrode. The counter electrode measures the working electrode potential while current is passing through. Au wire is the commonly used; Pt wire also is an option. The working electrode is where the reaction occurs, in this case, the substrate. The flow cell is a three electrode system. The deposition occurs when a sequence is executed while the potentiostat is connected across all three electrodes on the flow cell.

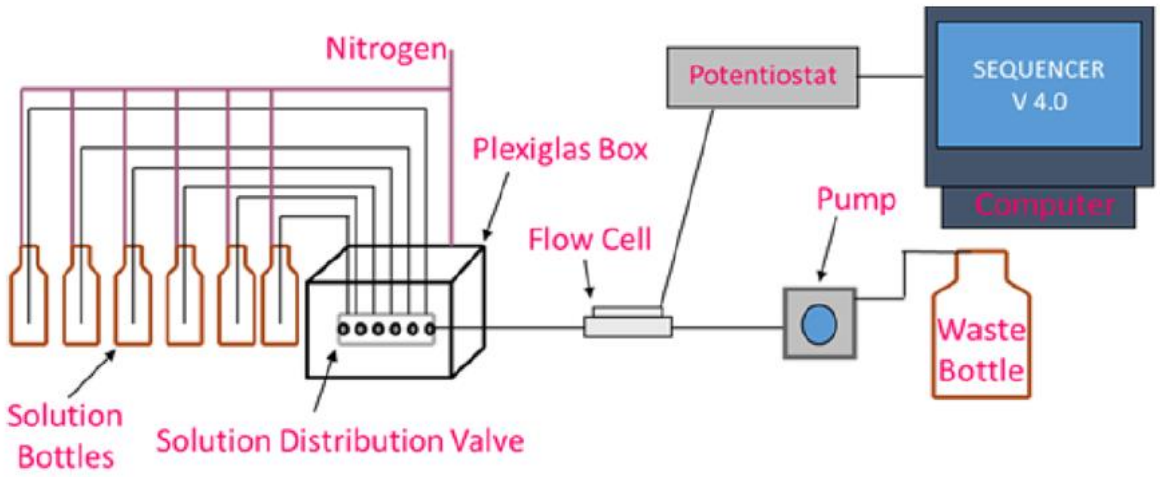

Figure 2.4: The electrochemical flow system (Czerniawski and Stickney 2016).

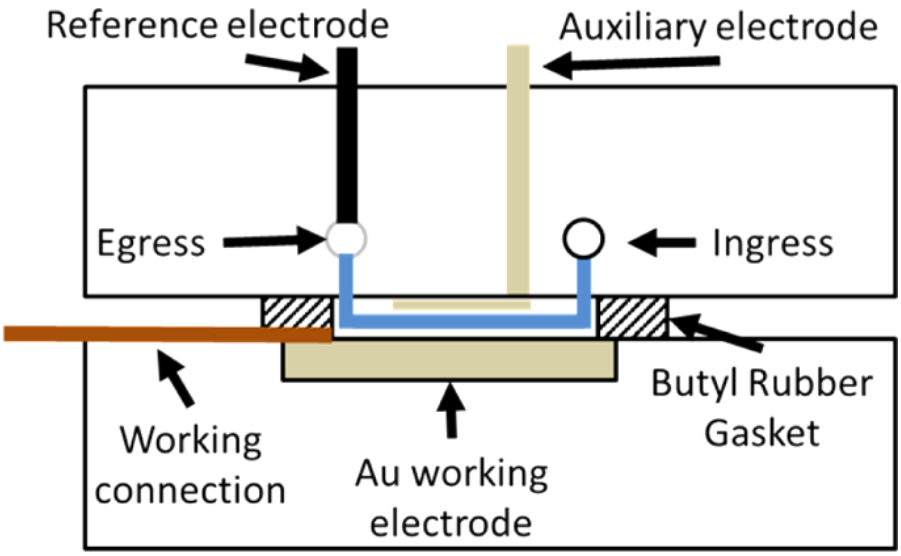

Figure 2.5: The electrochemical flow cell (Czerniawski *et al.* 2016).

2.5 Applications

2.5.1 Energy conversion

Fuel cells are devices that convert chemical reactions of fuels directly to chemical electrical energy, and water and heat as by-product (Berger 1968; Carrette *et al.* 2001; Wang *et al.* 2003; Demirbas 2007; Patil *et al.* 2011). The cell is made up of an anode and cathode separated using an electrolyte. The working principle is as follows; There is a continuous flow of hydrogen or any other fuel to the anode and air is fed to the cathode, hydrogen decompose to positive and negative ions, the positive ions move through the electrolyte, free electron move to the cathode via an external circuit, the electrons recombine with air at the cathode to stabilise the system and form water (Kirubakaran *et al.* 2009; Bard 2010). This is illustrated in equations (9-11) and in Figure 2.6.

Anode: $H_2 \rightarrow 2H^+ + 2e^-$ (9)

Cathode: $\frac{1}{2}O_2 + 2H^+ + 2e^- \rightarrow H_2O$ (10)

Overall: $H_2 + \frac{1}{2}O_2 \rightarrow H_2O$ (11)

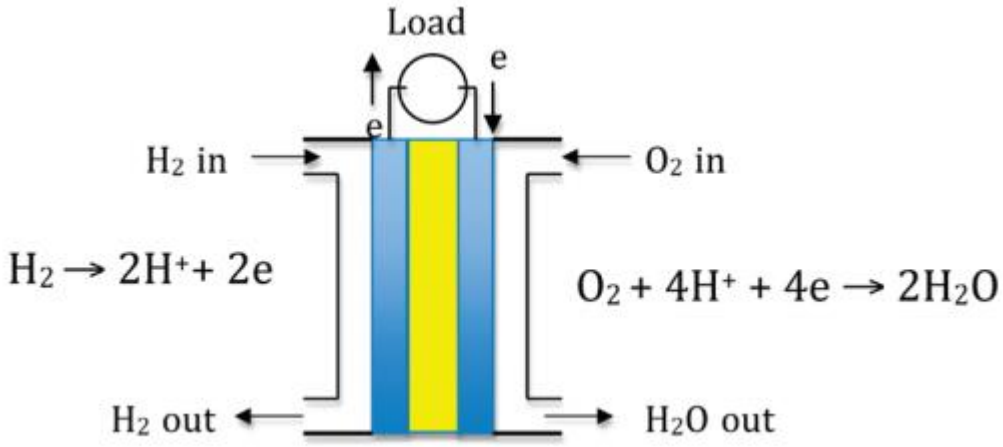

Figure 2.6: Scheme showing a polymer membrane fuel cell (Bard 2010)

There are different known types of fuel cells available in accordance to their fuels, and these are Proton exchange membrane fuel cells (PEMFC), alkaline fuel cells (AFC), phosphoric acid fuel cells, molten carbonate fuel cells (MCFC), solid oxide fuel cells (SOFC), direct methanol fuel cell (DMFC) (Kirubakaran *et al.* 2009; Patil *et al.* 2011; Niakolas *et al.* 2016). Fuel cells are primarily classified based on their properties like operating temperature and electrolyte type as shown in Table 2.1. The fuel cell types have been studied and documented well in a number of literature reviews (Carrette *et al.* 2001; Kirubakaran *et al.* 2009; Patil *et al.* 2011; Friedl and Stimming 2013; Jurzinsky *et al.* 2015; Niakolas *et al.* 2016; Ong *et al.* 2017).

Direct alcohol fuel cells (DAFC) are strong candidates to compete with batteries for applications in portable electronic devices as well as auxiliary power in transportation amongst other fuel cell types (Sheikh *et al.* 2013). This is primarily due to their high energy density, with ethanol and methanol exhibiting 6.3 and 4.8 kWh/L compared to hydrogen fuel cells having 2.6 kWh/L only. Their thermodynamic efficiency of 97% is higher than hydrogen fuel cell with only 87%. DAFC are the closest to commercialisation, but this will not be possible without improving two major factors: (i) the slow kinetics of alcohol oxidation, (ii) the alcohol crossover through the membrane to the cathode (Arico *et al.* 2001; Jurzinsky *et al.* 2015). Thus far, alkaline media is the solution to these challenges; this will also allow the use of cheaper catalysts than Pt. The electrolyte used in alkaline DAFC is an anion exchange membrane, reduces the problem of carbon dioxide rejection that occurs in traditional fuel cells.

Research efforts are being driven towards alkaline media and Pt free catalysts because of ease of transportation of the alkaline media fuels with a potential benefit of using more affordable electrocatalysts. Pd has been investigated as a substitute for Pt, due to similar chemical properties, and fifty times more abundant. Pd catalysts in alkaline media are stable and have high efficiency, are also economically more viable choice. The catalytic activity and selectivity of the Pd catalysts can be improved by increasing surface area and addition of a second metal to enhance the catalyst effect (Zalineeva *et al.* 2014). Self-supported Pd_4Bi catalysts were found to have high activity for glycerol oxidation, due to their unique structure and morphology. The pores of the catalysts acts as small reactors that houses reactants and intermediates, making the catalyst highly selective (Zalineeva *et al.* 2014). Carbon supported PdPt electrocatalysts were prepared using surface limited reaction method as opposed to ink printing, and there showed activity towards ORR and less affected by methanol (Motsoeneng *et al.* 2015). Nanocatalysts of Pd, Pd_8Ni_2, Pd_8Sn_2, $Pd_8Sn_1Ni_1$ supported on multiwalled carbon nanotubes were tested for oxidation of C2-C4 alcohols in alkaline medium (Yi *et al.* 2015). This study found that addition of Sn or Ni enhanced the activity of Pd catalyst, and the ternary $Pd_8Sn_1Ni_1$ catalyst exhibited the highest activity. Sheikh and co-workers also studied Pd/C catalyst for ethanol oxidation reaction in alkaline media, and reported that the addition of Sn enhanced the activity of the catalyst (Sheikh *et al.* 2013). Another study conducted on electro-oxidation of ethanol in alkaline media using Pd-Sn/C, Pd-Ru/C, Pd-Ru-Sn/C reported that Pd-Sn/C catalyst had the highest activity and less susceptibility towards poisoning (Modibedi *et al.* 2011).

Table 2.1: Characteristics of fuel cells (Berger 1968; Carrette *et al.* 2001; Kirubakaran *et al.* 2009)

Fuel cell type	**Operating Temperature (^oC)**	**Efficiency (%)**	**Electrolyte**	**Fuel**	**Advantages**	**Disadvantages**	**Application**
PEMFC	50-100	40-45	Solid polymer membrane	H_2, HCOOH	Higher power density; quick start up for automotive vehicles	Low efficiency; Expensive platinum catalyst.	automotive and electronic industry
AFC	60-120	60-70	KOH	H_2	Quick start; Separate reformer not required	Sensitive to CO_2, corrosive electrolyte has a short life span	Fleet vehicles, boats, space shuttle
PAFC	175-200	40-80	H_3PO_4	H_2	Very tolerant to impurities; cogeneration is possible	Expensive platinum catalyst;	Stationery and heat
MCFC	600-700	50-60	Molten carbonate	Hydro-carbons, CO	No need for metal catalyst and separate reformer	Intolerant to sulphur; slow start up	Medium and large power grid
SOFC	800-1000	50-60	Yttrium stabilised zirconia	Hydro-carbons, CO	Separate reformer not required; cogeneration is possible	Intolerant to sulphur; slow start up; expensive	Medium to large power grids
DMFC	50-100	40-45	Polymer membrane	CH_3OH or Alcohol	No reformer required; low cost	Low efficiency; slow kinetics	Portable electronics

2.5.2 Carbon capture and utilisation

The extensive use of fossil fuels has resulted in an increase in atmospheric carbon dioxide levels in the atmosphere (Hu *et al.* 2013). Higher carbon dioxide levels decreases air quality resulting in global warming. Therefore, there is an urgent need to find solutions to decrease the CO_2 content. One of the ways to reduce CO_2 content is by trapping it. However, the best option is to convert it to fuels providing clean energy solutions. The well-established high Fischer Tropsch reaction reduces CO_2 to hydrocarbons. Carbon monoxide (CO) and hydrogen (H_2) are the reactants, in the presence of iron or cobalt catalyst, producing hydrocarbons and water. This reaction (12) is accompanied by a competing water gas reaction (13) where CO reacts with water to form carbon dioxide and hydrogen (Lim *et al.* 2014).

$$CO + 2.15H_2 \rightarrow Hydrocarbons + H_2O \quad (12)$$

$$CO + H_2O \leftrightarrow CO_2 + H_2 \quad (13)$$

Efforts are being made to reduce CO_2 selectively into CO and H_2 at high temperatures without a need for applied potential. The electrochemical reduction of CO_2 in aqueous electrolyte can be done at atmospheric temperature and pressure using metal catalysts. The products are various hydrocarbons, formic acid, and alcohols as shown in the electrochemical reactions (14-19) (Lim *et al.* 2014).

$$CO_2 + e^- \leftrightarrow CO_2^- \ (-0.19\,V) \quad (14)$$

$$CO_2 + H_2O + 2e^- \leftrightarrow CO + 2OH^- \ (-0.52\,V) \quad (15)$$

$$CO_2 + 6H_2O + 8e^- \leftrightarrow CH_4 + 8OH^- \ (-0.25\,V) \quad (16)$$

$$2CO_2 + 8H_2O + 12e^- \leftrightarrow C_2H_4 + 12OH^- \ (-0.34\,V) \quad (17)$$

$$2CO_2 + 9H_2O + 12e^- \leftrightarrow C_2H_5OH + 12OH^- \ (-0.33\,V) \quad (18)$$

$$3CO_2 + 13H_2O + 18e^- \leftrightarrow C_3H_7OH + 18OH^- \ (-0.32\,V) \quad (19)$$

The electrochemical reduction of CO_2 is well covered in literature (Gattrell and Gupta 2006; Jitaru 2007; Whipple and Kenis 2010; Hu *et al.* 2013; Jones *et al.* 2014; Lim *et al.* 2014; Larrazábal *et al.* 2017; Zhang *et al.* 2017; He *et al.* 2018). Electrocatalytic reduction of CO_2 can be done using metal organic complexes, metals, metal alloys, inorganic metal compounds, and carbon based metal free catalysts (Zhang *et al.* 2017). Sn is a first class metal catalyst, it weakly bonds with carbon dioxide intermediates, resulting in the formation

of formic acid. Bi is a second class metal catalyst, and is selective toward CO formation. Cubic ternary oxides of $Bi_2M_2O_7$ (M = Ti, Zr, Hf) were studied and found to have enhanced CO_2 adsorption (Walker *et al.* 2015). A bismuth carbon dioxide evolving catalysts (Bi-CMEC) used in the presence of ionic liquids was found to selectively produce CO with a 95% efficiency (DiMeglio and Rosenthal 2013; Medina-Ramos *et al.* 2014). Further studies were done on Sn-CMEC, Pb-CMEC, Sb-CMEC, and Sn exhibited high activity and selectivity for CO production as shown by the Bi-CMEC, while Pb catalyst was only 10% efficient, and Sb based catalysts had no activity (Medina-Ramos *et al.* 2015). Nanosized bismuth on Cu foil showed a 91.3% selectivity towards CO_2 conversion to formate (Lv *et al.* 2017), Sn-Pb alloys exhibited an efficiency of 79.8% (Choi *et al.* 2016), and carbon supported BiO_x nanoparticles showed 93.4% efficiency (Lee *et al.* 2017). Cu-Sn was found to have an efficiency of 63% for CO_2 conversion to CO (Sarfraz *et al.* 2016).

2.5.3 Energy storage

Rechargeable batteries have been used as power sources due to their excellent electrochemical properties. Na ion batteries are favourable cost effective storage systems over lithium ion batteries. A number of papers have reviewed literature on Na ion batteries (Stevens and Dahn 2000; Palacin 2009; Ong *et al.* 2011; Ellis and Nazar 2012; Kim *et al.* 2012; Palomares *et al.* 2012; Hong *et al.* 2013; Slater *et al.* 2013; Yabuuchi *et al.* 2014; Kubota and Komaba 2015). The basic rechargeable battery set up is shown in Figure 2.7, where Na ions are shuffled in out of a cathode and anode to charge or discharge the battery. Cathode materials used are similar to those used in Li ion batteries. The anode is where most research is done because the graphite used in Li batteries does not intercalate sodium. Anode materials for sodium ion batteries have been excellently reviewed (Stevens and Dahn 2000; Dahbi *et al.* 2014; Luo *et al.* 2016; Cui *et al.* 2017). These reviews concluded that further research needs to be done to find new materials and to improve capacity retention in alloy anodes.

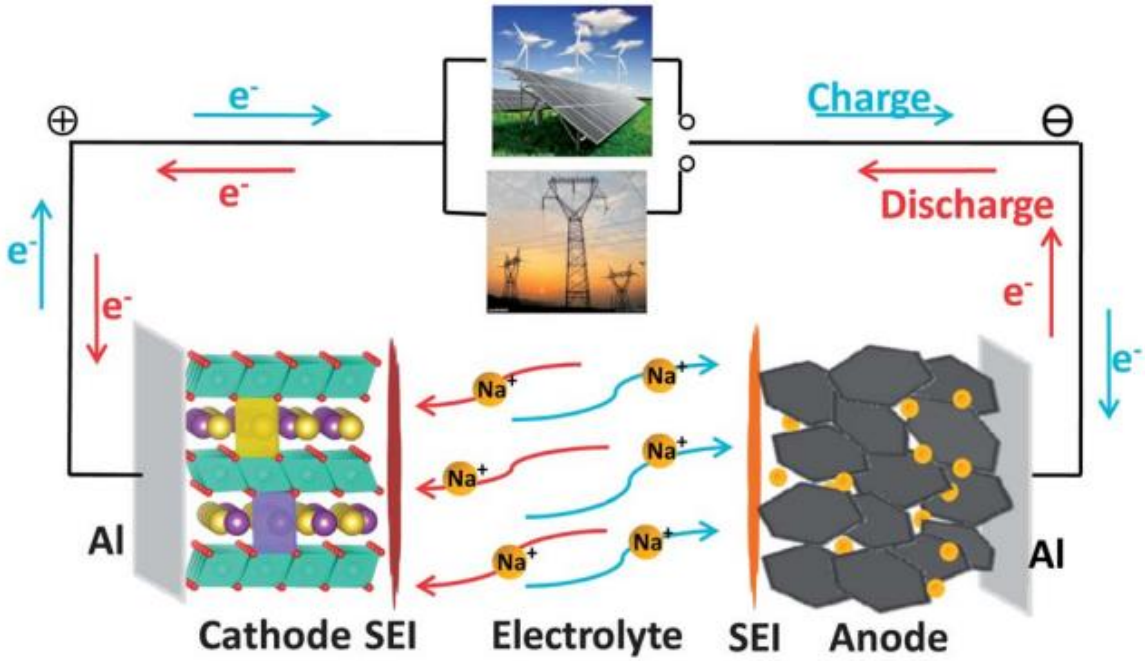

Figure 2.7: Na ion battery working principle (Pan *et al.* 2013).

Alloy materials of Sn and Bi are suitable for Na ion battery anodes due to their high capacity. Pure Sn has a theoretical capacity of 847 mA h g^{-1} while that of Bi is 380 mA h g^{-1}(Cui *et al.* 2017). These materials do suffer from gravimetric expansion during cyclic, causing capacity fade. Therefore, research efforts are being undertaken to find solutions for this problem. Liu and co-workers (Liu *et al.* 2017) made a composite material of bismuth nanosheets on carbon fiber (Bi/CFC), this anode had excellent rate capability and a reversible capacity of 350 mAh g^{-1} at 50 mA g^{-1}. Bismuth oxychloride nanoplates were found to have an initial discharge capacity of 1050 mAh g^{-1} (Zhang *et al.* 2016), while bismuth nanoparticles wrapped in graphene had a reversible capacity of 561 mAh g^{-1} at 2.0-0.01V range (Su *et al.* 2015). Ni and co-workers (Ni *et al.* 2017) provides a detailed review of Bi chalcogenide compounds and their applications in Na ion battery. Tin and tin compounds anodes for sodium ion batteries were reviewed focusing on material performance and phase transformation (Li *et al.* 2015). Tin oxide (SnO_2) was found to have superior rate capability with 440 mAh g^{-1}, while a tin oxide carbon (SnO_2/C) composite delivered 411 mAh g^{-1} at 50 mA g^{-1} (Lu *et al.* 2015). Composite material of tin selenide ($SnSe_x$) had an initial capacity of 877 mAh g^{-1} at 100 mA g^{-1}.

2.5.4 Electronic components and coatings

The worldwide awareness of the detrimental environmental impacts of metal wastes from disposed electronic components has brought about strict regulations that promote the use of less harmful and easily disposable metals in the industry. Sn is the most prominent material for interconnecting and packaging electronics, Sn-Pb alloys being the most widely used (Walsh and Low 2016a). The ban of toxic Pb inspired the search for Pb replacement in Sn alloy materials (Sandnes *et al.* 2008; Chen *et al.* 2009). The similarities in the chemical and physical properties of Pb and Bi, drove research into Bi being the main replacement for Pb in Sn-Pb alloys (Tsai and Hu 2009a). Research efforts focus on optimising the plating parameters to improve materials including bath composition (Suh *et al.* 2006; Tsai *et al.* 2007; Low and Walsh 2008; Wang and Pritzker 2008; Gao *et al.* 2014; Walsh and Low 2016b; Vieira *et al.* 2017), and current density (Mallik *et al.* 2014), and deposition method. Alloy of Sn-Bi deposits was pulse deposited on Cu foil from a commercial MSA electrolyte in-order to combat whisker formation (Sandnes *et al.* 2008). Whiskers are not ideal on Sn-Bi alloys used in electronics because they cause short circuits. The microstructure of substitutional deposited Sn films on Cu foils, and the orientation of the substrate effects on Sn whisker formation, and heat treatment was investigated by Okamoto and co-workers (Okamoto *et al.* 2009). This study found that the structure of the substrate affect Sn whisker formation and no whiskers were found on heat treated material. Studies have been done to control the composition of the alloy by converting the metal stacks into an alloy through reflow (Lee *et al.* 2012; Goh *et al.* 2013b). The eutectic Bi-43Sn alloys is important in electronics due to its properties including low melting temperature, superior wettability, and nearly void free bonding (Chen *et al.* 2009; Shang *et al.* 2013; Gao *et al.* 2014). The eutectic Sn-Bi alloy nanowires were made using a hydraulic pressure injection process. The microstructure and morphological changes occurring at the Cu joint were studied, and intermetallic compound were found to occur at the substrate alloy joint (Shang *et al.* 2013). Other studies have fabricated the eutectic Sn-Bi alloy from deep eutectic solvents (Gao *et al.* 2014; Vieira *et al.* 2017).

Semiconductors used in thermoelectronics and optoelectronic devices are also of great importance. Bismuth telluride films have been widely studied by optimisation of electrochemical deposition conditions(Yang *et al.* 2005), the growth mechanism (Zimmer *et al.* 2015), the underpotential deposition parameters and effect of cold rolled silver substrate (Zhu *et al.* 2005b), formation of highly uniform sheets of Au (Zhu *et al.* 2005c; Zhu *et al.*

2008), and the effect of deposition potential on film growth (Zhu *et al.* 2005a). Other materials that have been studied include Bi_2Se_3 (Xiao *et al.* 2009), $Bi_xSb_{2-x}Te_y$ (Kim *et al.* 2018), $Pb_{1-x}Sn_xSe$ (Lin *et al.* 2011), and SnS (Do *et al.* 2015).

2.6 Summary

The fabrication of versatile materials that can be used in a wide variety of applications is important in the current times. Versatile material development saves time and costs. Sn and Bi materials are amongst these materials. The different applications including electronics, electrocatalysts for energy conversion, carbon capture and utilisation has been discussed. The main aim of this review was to highlight the different uses of Sn and Bi nanomaterials.

2.7 References

Arico, A, Srinivasan, S, Antonucci, V (2001) DMFCs: from fundamental aspects to technology development. *Fuel cells* **1**, 133-161.

Banga, D, Jarayaju, N, Sheridan, L, Kim, Y-G, Perdue, B, Zhang, X, Zhang, Q, Stickney, J (2012) Electrodeposition of $CuInSe_2$ (CIS) via electrochemical atomic layer deposition (E-ALD). *Langmuir* **28**, 3024-3031.

Bard, AJ (2010) Inner-sphere heterogeneous electrode reactions. Electrocatalysis and photocatalysis: the challenge. *Journal of the American Chemical Society* **132**, 7559-7567.

Bedoya Hincapie, CM, Pinzon Cardenas, MJ, Orjuela, A, Edgar, J, Restrepo Parra, E, Olaya Florez, JJ (2012) Physical-chemical properties of bismuth and bismuth oxides: Synthesis, characterization and applications. *Dyna* **79**, 139-148.

Bedoya-Hincapié, CM, de la Roche, J, Restrepo-Parra, E, Alfonso, JE, Olaya-Florez, JJ (2015) Structural and morphological behavior of bismuth thin films grown through DC-magnetron sputtering/Comportamiento estructural y morfológico de películas delgadas de bismuto obtenidas a través de sputtering con magnetrón DC. *Ingeniare: Revista Chilena de Ingenieria* **23**, 92.

Berger, C (1968) Handbook of fuel cell technology. *Prentice hall*: New Jersey,

Carrette, L, Friedrich, K, Stimming, U (2001) Fuel cells–fundamentals and applications. *Fuel Cells* **1**, 5-39.

Chen, L, Alarcón-Lladó, E, Hettick, M, Sharp, ID, Lin, Y, Javey, A, Ager, JW (2013) Reactive sputtering of bismuth vanadate photoanodes for solar water splitting. *The Journal of Physical Chemistry C* **117**, 21635-21642.

Chen, SH, Chen, CC, Luo, ZP, Chao, CG (2009) Fabrication and characterization of eutectic bismuth-tin (Bi-Sn) nanowires. *Materials Letters* **63**, 1165-1168.

Cheng, K-W, Wu, Y-H, Chiu, T-H (2016) Photoelectrochemical salt water splitting using ternary silver–tin–selenide photoelectrodes. *Journal of Power Sources* **307**, 329-339.

Choe, S, Chuang, R, Lee, CC (2001) 'Fluxless Sn-Bi-Au bonding process using multilayer design, *Electronic Components and Technology Conference, 2001. Proceedings.*, 51st.'IEEE

Choi, SY, Jeong, SK, Kim, HJ, Baek, I-H, Park, KT (2016) Electrochemical reduction of carbon dioxide to formate on tin–lead alloys. *ACS Sustainable Chemistry & Engineering* **4**, 1311-1318.

Cui, J, Yao, S, Kim, J-K (2017) Recent progress in rational design of anode materials for high-performance Na-ion batteries. *Energy Storage Materials* **7**, 64-114.

Czerniawski, JM, Perdue, BR, Stickney, JL (2016) Potential pulse atomic layer deposition of Cu2Se. *Chemistry of Materials* **28**, 583-591.

Czerniawski, JM, Stickney, JL (2016) Electrodeposition of In2Se3 using potential pulse atomic layer deposition. *Journal of Physical Chemistry C* **120**, 16162-16167.

Dahbi, M, Yabuuchi, N, Kubota, K, Tokiwa, K, Komaba, S (2014) Negative electrodes for Na-ion batteries. *Physical Chemistry Chemical Physics* **16**, 15007-15028.

Demirbas, A (2007) Fuel cells as clean energy converters. *Energy Sources, Part A* **29**, 185-191.

DiMeglio, JL, Rosenthal, J (2013) Selective conversion of CO_2 to CO with high efficiency using an inexpensive bismuth-based electrocatalyst. *Journal of the American Chemical Society* **135**, 8798-8801.

Dimitrov, N (2016) Recent advances in the growth of metals, alloys, and multilayers by surface limited redox replacement (SLRR) based approaches. *Electrochimica Acta* **209**, 599-622.

Do, HW, Kwon, YH, Cho, HK (2015) Single phase tin sulfide films prepared by one-bath electrodeposition. *Journal of Materials Science: Materials in Electronics* **26**, 8609-8615.

Ellis, BL, Nazar, LF (2012) Sodium and sodium-ion energy storage batteries. *Current Opinion in Solid State and Materials Science* **16**, 168-177.

Friedl, J, Stimming, U (2013) Model catalyst studies on hydrogen and ethanol oxidation for fuel cells. *Electrochimica Acta* **101**, 41-58.

Gao, Y, Hu, W, Gao, X, Duan, B (2014) Electrodeposition of SnBi coatings based on deep eutectic solvent. *Surface Engineering* **30**, 59-63.

Gattrell, M, Gupta, N (2006) A review of the aqueous electrochemical reduction of CO_2 to hydrocarbons at copper. *Journal of Electroanalytical Chemistry* **594**, 1-19.

Giaccherini, A, Felici, R, Innocenti, M (2017) Operando Structural Characterization of the E-ALD Process Ultra-Thin Films Growth. In 'X-ray Characterization of Nanostructured Energy Materials by Synchrotron Radiation.' (Ed. DM Khodaei.)

Goh, Y, Haseeb, A, Sabri, MFM (2013a) Effects of hydroquinone and gelatin on the electrodeposition of Sn–Bi low temperature Pb-free solder. *Electrochimica Acta* **90**, 265-273.

Goh, Y, Lee, SF, Haseeb, A (2013b) Formation of Sn-Bi solder alloys by sequential electrodeposition and reflow. *Journal of Materials Science-Materials in Electronics* **24**, 2052-2057.

Gregory, BW, Stickney, JL (1991) Electrochemical atomic layer epitaxy (ECALE). *Journal of Electroanalytical Chemistry* **300**, 543-561.

Gregory, BW, Suggs, DW, Stickney, JL (1991) Conditions for the deposition of CdTe by electrochemical atomic layer epitaxy. *Journal of the Electrochemical Society* **138**, 1279-1284.

Gurrappa, I, Binder, L (2008) Electrodeposition of nanostructured coatings and their characterization-a review. *Science and Technology of Advanced Materials* **9**, 043001.

Haacke, G, Mealmaker, W, Siegel, L (1978) Sputter deposition and characterization of Cd_2SnO_4 films. *Thin Solid Films* **55**, 67-81.

He, J, Johnson, NJ, Huang, A, Berlinguette, CP (2018) Electrocatalytic Alloys for CO_2 Reduction. *ChemSusChem* **11**, 48-57.

Hong, SY, Kim, Y, Park, Y, Choi, A, Choi, N-S, Lee, KT (2013) Charge carriers in rechargeable batteries: Na ions vs. Li ions. *Energy & Environmental Science* **6**, 2067-2081.

Hu, B, Guild, C, Suib, SL (2013) Thermal, electrochemical, and photochemical conversion of CO2 to fuels and value-added products. *Journal of CO_2 Utilization* **1**, 18-27.

Hu, C-C, Tsai, Y-D, Lin, C-C, Lee, G-L, Chen, S-W, Lee, T-C, Wen, T-C (2009) Anomalous growth of whisker-like bismuth–tin extrusions from tin-enriched tin–Bi deposits. *Journal of Alloys and Compounds* **472**, 121-126.

Jitaru, M (2007) Electrochemical carbon dioxide reduction-fundamental and applied topics. *Journal of the University of Chemical Technology and Metallurgy* **42**, 333-344.

Jones, JP, Prakash, G, Olah, GA (2014) Electrochemical CO_2 reduction: recent advances and current trends. *Israel Journal of Chemistry* **54**, 1451-1466.

Jurzinsky, T, Cremers, C, Jung, F, Pinkwart, K, Tübke, J (2015) Development of materials for anion-exchange membrane direct alcohol fuel cells. *International Journal of Hydrogen Energy* **40**, 11569-11576.

Katayama, J, Okuno, K, Izaki, M (1996) Solderability of bismuth/tin double layer deposits. *Metal Finishing* **1**, 12-19.

Kim, J, Lim, J-H, Myung, NV (2018) Composition and crystallinity dependent thermoelectric properties of ternary $Bi_xSb_{2-x}Te_y$ films. *Applied Surface Science* **429**, 158-163.

Kim, SW, Seo, DH, Ma, X, Ceder, G, Kang, K (2012) Electrode materials for rechargeable sodium-ion batteries: potential alternatives to current lithium-ion batteries. *Advanced Energy Materials* **2**, 710-721.

Kirubakaran, A, Jain, S, Nema, R (2009) A review on fuel cell technologies and power electronic interface. *Renewable and Sustainable Energy Reviews* **13**, 2430-2440.

Kubota, K, Komaba, S (2015) Practical issues and future perspective for Na-ion batteries. *Journal of The Electrochemical Society* **162**, A2538-A2550.

Lanius, M, Kampmeier, Jr, Weyrich, C, Kölling, S, Schall, M, Schüffelgen, P, Neumann, E, Luysberg, M, Mussler, G, Koenraad, PM (2016) P–N junctions in ultrathin topological insulator Sb_2Te_3/Bi_2Te_3 heterostructures grown by molecular beam epitaxy. *Crystal Growth & Design* **16**, 2057-2061.

Larrazábal, GO, Martín, AJ, Pérez-Ramírez, J (2017) Building blocks for high performance in electrocatalytic CO_2 reduction: materials, optimization strategies, and device engineering. *The Journal of Physical Chemistry Letters* **8**, 3933-3944.

Ledina, M, Liang, X, Kim, Y-G, Jung, J, Perdue, B, Tsang, C, Soriaga, M, Stickney, JL (2015) (Invited) Investigations into the formation of germanene using electrochemical atomic layer deposition (E-ALD). *ECS Transactions* **66**, 129-140.

Lee, CW, Hong, JS, Yang, KD, Jin, K, Lee, JH, Ahn, H-Y, Seo, H, Sung, N-E, Nam, KT (2017) Selective electrochemical production of formate from carbon dioxide with bismuth-based catalysts in an aqueous electrolyte. *ACS Catalysis.*

Lee, SF, Goh, YX, Haseeb, A, Ieee (2012) Effects of Stacking Sequence of Electrodeposited Sn and Bi Layers on reflowed Sn-Bi Solder Alloys. *2012 35th IEEE/Cpmt International Electronic Manufacturing Technology Symposium (IEMT)* 6.

Li, YY, Wang, G, Zhu, XG, Liu, MH, Ye, C, Chen, X, Wang, YY, He, K, Wang, LL, Ma, XC (2010) Intrinsic topological insulator Bi_2Te_3 thin films on Si and their thickness limit. *Advanced Materials* **22**, 4002-4007.

Li, Z, Ding, J, Mitlin, D (2015) Tin and tin compounds for sodium ion battery anodes: phase transformations and performance. *Accounts of Chemical Research* **48**, 1657-1665.

Liang, X, Jayaraju, N, Thambidurai, C, Zhang, Q, Stickney, JL (2011) Controlled electrochemical formation of $Ge_xSb_yTe_z$ using atomic layer deposition (ALD). *Chemistry of Materials* **23**, 1742-1752.

Lim, RJ, Xie, M, Sk, MA, Lee, J-M, Fisher, A, Wang, X, Lim, KH (2014) A review on the electrochemical reduction of CO_2 in fuel cells, metal electrodes and molecular catalysts. *Catalysis Today* **233**, 169-180.

Lin, S, Zhang, X, Shi, X, Wei, J, Lu, D, Zhang, Y, Kou, H, Wang, C (2011) Nanoscale semiconductor $Pb_{1-x}Sn_xSe$ (x = 0.2) thin films synthesized by electrochemical atomic layer deposition. *Applied Surface Science* **257**, 5803-5807.

Liu, S, Luo, Z, Guo, J, Pan, A, Cai, Z, Liang, S (2017) Bismuth nanosheets grown on carbon fiber cloth as advanced binder-free anode for sodium-ion batteries. *Electrochemistry Communications* **81**, 10-13.

Low, C, Walsh, F (2008) Electrodeposition of tin, copper and tin–copper alloys from a methanesulfonic acid electrolyte containing a perfluorinated cationic surfactant. *Surface and Coatings Technology* **202**, 1339-1349.

Lu, YC, Ma, C, Alvarado, J, Kidera, T, Dimov, N, Meng, YS, Okada, S (2015) Electrochemical properties of tin oxide anodes for sodium-ion batteries. *Journal of Power Sources* **284**, 287-295.

Luo, W, Shen, F, Bommier, C, Zhu, H, Ji, X, Hu, L (2016) Na-ion battery anodes: materials and electrochemistry. *Accounts of Chemical Research* **49**, 231-240.

Lv, W, Zhou, J, Bei, J, Zhang, R, Wang, L, Xu, Q, Wang, W (2017) Electrodeposition of nano-sized bismuth on copper foil as electrocatalyst for reduction of CO_2 to formate. *Applied Surface Science* **393**, 191-196.

Mallik, M, Mitra, A, Sengupta, S, Das, K, Ghosh, RN, Das, S (2014) Effect of current density on the nucleation and growth of crystal facets during pulse electrodeposition of Sn–Cu lead-free solder. *Crystal Growth & Design* **14**, 6542-6549.

Martın-González, MS, Prieto, AL, Gronsky, R, Sands, T, Stacy, AM (2002) Insights into the electrodeposition of Bi2Te3. *Journal of The Electrochemical Society* **149**, C546-C554.

Medina-Ramos, J, DiMeglio, JL, Rosenthal, J (2014) Efficient reduction of CO_2 to CO with high current density using in situ or ex situ prepared Bi-based materials. *Journal of the American Chemical Society* **136**, 8361-8367.

Medina-Ramos, J, Pupillo, RC, Keane, TP, DiMeglio, JL, Rosenthal, J (2015) Efficient conversion of CO_2 to CO using tin and other inexpensive and easily prepared post-transition metal catalysts. *Journal of the American Chemical Society* **137**, 5021-5027.

Mishra, S, Satpathy, S, Jepsen, O (1997) Electronic structure and thermoelectric properties of bismuth telluride and bismuth selenide. *Journal of Physics: Condensed Matter* **9**, 461.

Modibedi, RM, Masombuka, T, Mathe, MK (2011) Carbon supported Pd–Sn and Pd–Ru–Sn nanocatalysts for ethanol electro-oxidation in alkaline medium. *International Journal of Hydrogen Energy* **36**, 4664-4672.

Mohanty, U (2011) Electrodeposition: a versatile and inexpensive tool for the synthesis of nanoparticles, nanorods, nanowires, and nanoclusters of metals. *Journal of Applied Electrochemistry* **41**, 257-270.

Motsoeneng, RG, Modibedi, RM, Mathe, MK, Khotseng, LE, Ozoemena, KI (2015) The synthesis of PdPt/carbon paper via surface limited redox replacement reactions for oxygen reduction reaction. *International Journal of Hydrogen Energy* **40**, 16734-16744.

Natter, H, Hempelmann, R (2003) Tailor-made nanomaterials designed by electrochemical methods. *Electrochimica Acta* **49**, 51-61.

Ni, J, Bi, X, Jiang, Y, Li, L, Lu, J (2017) Bismuth chalcogenide compounds Bi_2X_3 (X= O, S, Se): Applications in electrochemical energy storage. *Nano Energy* **34**, 356-366.

Niakolas, DK, Daletou, M, Neophytides, SG, Vayenas, CG (2016) Fuel cells are a commercially viable alternative for the production of "clean" energy. *Ambio* **45**, 32-37.

Okamoto, N, Fujii, Y, Kurihara, H, Kondo, K (2009) Effects of microstructure of deposited sn films and orientation index of Cu Foils on Sn whisker formation using substitutionally-deposited Sn Films. *Materials Transactions* **50**, 2570-2577.

Ong, B, Kamarudin, S, Basri, S (2017) Direct liquid fuel cells: A review. *International Journal of Hydrogen Energy* **42**, 10142-10157.

Ong, SP, Chevrier, VL, Hautier, G, Jain, A, Moore, C, Kim, S, Ma, X, Ceder, G (2011) Voltage, stability and diffusion barrier differences between sodium-ion and lithium-ion intercalation materials. *Energy & Environmental Science* **4**, 3680-3688.

Oviedo, O, Vélez, P, Macagno, V, Leiva, E (2015) Underpotential deposition: From planar surfaces to nanoparticles. *Surface Science* **631**, 23-34.

Palacin, MR (2009) Recent advances in rechargeable battery materials: a chemist's perspective. *Chemical Society Reviews* **38**, 2565-2575.

Palomares, V, Serras, P, Villaluenga, I, Hueso, KB, Carretero-González, J, Rojo, T (2012) Na-ion batteries, recent advances and present challenges to become low cost energy storage systems. *Energy & Environmental Science* **5**, 5884-5901.

Pan, H, Hu, Y-S, Chen, L (2013) Room-temperature stationary sodium-ion batteries for large-scale electric energy storage. *Energy & Environmental Science* **6**, 2338-2360.

Papaderakis, A, Mintsouli, I, Georgieva, J, Sotiropoulos, S (2017) Electrocatalysts prepared by galvanic replacement. *Catalysts* **7**, 80.

Parsons, R, 1967. Atlas of electrochemical equilibria in aqueous solutions: by Marcel Pourbaix, Pergamon Press, Oxford etc, Cebelcor, Brussels, 1966, 644 pages,£ 12. Elsevier,

Patil, MB, Bhagat, S, Sapkal, R, Sapkal, V (2011) A review on the fuel cells development. *Scientific Reviews & Chemical Communications* **1**, 25-41.

Sandnes, E, Williams, ME, Vaudin, MD, Stafford, GR (2008) Equi-axed grain formation in electrodeposited Sn-Bi. *Journal of Electronic Materials* **37**, 490-497.

Sarfraz, S, Garcia-Esparza, AT, Jedidi, A, Cavallo, L, Takanabe, K (2016) Cu–Sn bimetallic catalyst for selective aqueous electroreduction of CO_2 to CO. *ACS Catalysis* **6**, 2842-2851.

Sberveglieri, G, Faglia, G, Groppelli, S, Nelli, P (1992) Methods for the preparation of NO, NO_2 and H_2 sensors based on tin oxide thin films, grown by means of the rf magnetron sputtering technique. *Sensors and Actuators B: Chemical* **8**, 79-88.

Sberveglieri, G, Groppelli, S, Nelli, P, Camanzi, A (1991) Bismuth-doped tin oxide thin-film gas sensors. *Sensors and Actuators B: Chemical* **3**, 183-189.

Selivanov, YG, Chizhevskii, E, Martovitskiy, V, Knotko, A, Zasavitskii, I (2010) Molecular beam epitaxy of $Pb_{1-x}Eu_xTe$ and $Pb_{1-x}Sn_xTe$ layers and related periodic structures. *Inorganic Materials* **46**, 1065-1071.

Shang, P, Zhang, L, Liu, Z, Tan, J, Shang, J (2013) Ex situ observations of fast intermetallic growth on the surface of interfacial region between eutectic SnBi solder and Cu substrate during solid-state aging process. *Microelectronics Reliability* **53**, 899-905.

Sheikh, A, Correa, P, da Silva, EL, Savaris, I, Amico, S, Malfatti, C (2013) Energy conversion using Pd-based catalysts in direct ethanol fuel cell. *Renewable Energies & Power Quality Journal* **11**, 300.

Slater, MD, Kim, D, Lee, E, Johnson, CS (2013) Sodium-ion batteries. *Advanced Functional Materials* **23**, 947-958.

Stevens, D, Dahn, J (2000) High Capacity Anode Materials for Rechargeable Sodium-Ion Batteries. *Journal of the Electrochemical Society* **147**, 1271-1273.

Stickney, JL (2001) Electrochemical atomic layer epitaxy (EC-ALE):Nanoscale control in the electrodeposition of compound semiconductors. In 'Advances in electrochemical science and engineering.' (Eds RC Alkire, DM Kolb.) Vol. 7 pp. 1-105. (Wiley-VCH: Germany)

Stickney, JL (2002) Electrochemical atomic layer epitaxy (EC-ALE): nanoscale control in the electrodeposition of compound semiconductors. *Advances in Electrochemical Science and Engineering* **7**, 1-106.

Stickney, JL (2011) Deposition. *Electrochemical Society Interface* 29.

Su, D, Dou, S, Wang, G (2015) Bismuth: A new anode for the Na-ion battery. *Nano Energy* **12**, 88-95.

Suh, M-S, Park, C-J, Kwon, H-S (2006) Effects of plating parameters on alloy composition and microstructure of Sn–Bi electrodeposits from methane sulphonate bath. *Surface and Coatings Technology* **200**, 3527-3532.

Tamura, N, Ohshita, R, Fujimoto, M, Fujitani, S, Kamino, M, Yonezu, I (2002) Study on the anode behavior of Sn and Sn–Cu alloy thin-film electrodes. *Journal of Power Sources* **107**, 48-55.

Tariq, G, Hutchings, K, Lane, D, Rogers, K, Anis-ur-Rehman, M (2013) Annealing effects on the microstructural properties of complex sulfosalt $(SnS)_x$–$(Bi_2S_3)_{1-x}$ gradient thin films. *Journal of Physics D: Applied Physics* **46**, 485302.

Thornton, JA, Greene, JE (1994) Sputter deposition processes. *Handbook of Deposition Technologies for Films and Coatings* 249-319.

Tsai, Y-D, Hu, C-C (2009a) Composition control of lead-free Sn–Bi deposits using experimental strategies. *Journal of the Electrochemical Society* **156**, D58-D63.

Tsai, Y-D, Hu, C-C, Lin, C-C (2007) Electrodeposition of Sn–Bi lead-free solders: effects of complex agents on the composition, adhesion, and dendrite formation. *Electrochimica Acta* **53**, 2040-2047.

Tsai, YD, Hu, CC (2009b) Composition control of Sn-Bi deposits: Interactive fffects of citric acid, ethylenediaminetetraacetic acid, and poly(ethylene glycol). *Journal of the Electrochemical Society* **156**, D490-D496.

Tsai, YD, Hu, CC (2011) Composition and microstructure control of tin-bismuth alloys in the pulse plating process. *Journal of the Electrochemical Society* **158**, D482-D489.

Tsai, YD, Lien, CH, Hu, CC (2011) Effects of polyethylene glycol and gelatin on the crystal size, morphology, and Sn^{2+}-sensing ability of bismuth deposits. *Electrochimica Acta* **56**, 7615-7621.

Venables, J (2000) 'Introduction to surface and thin film processes.' (Cambridge University Press:

Vieira, L, Burt, J, Richardson, PW, Schloffer, D, Fuchs, D, Moser, A, Bartlett, PN, Reid, G, Gollas, B (2017) Tin, bismuth, and tin–bismuth alloy electrodeposition from chlorometalate salts in deep eutectic solvents. *Chemistry Open*

Walker, RJ, Pougin, A, Oropeza, FE, Villar-Garcia, IJ, Ryan, MP, Strunk, J, Payne, DJ (2015) Surface termination and CO_2 adsorption onto bismuth pyrochlore oxides. *Chemistry of Materials* **28**, 90-96.

Walsh, F, Low, C (2016a) A review of developments in the electrodeposition of tin. *Surface and Coatings Technology* **288**, 79-94.

Walsh, F, Low, C (2016b) A review of developments in the electrodeposition of tin-copper alloys. *Surface and Coatings Technology* **304**, 246-262.

Wang, H, Pritzker, M (2008) Effect of low concentrations of Pb^{2+} on Sn electrodeposition in methyl sulphonic acid solutions. *Electrochimica Acta* **53**, 2430-2440.

Wang, Y, Li, L, Hu, L, Zhuang, L, Lu, JT, Xu, BQ (2003) A feasibility analysis for alkaline membrane direct methanol fuel cell: thermodynamic disadvantages versus kinetic advantages. *Electrochemistry Communications* **5**, 662-666.

Whipple, DT, Kenis, PJ (2010) Prospects of CO_2 utilization via direct heterogeneous electrochemical reduction. *The Journal of Physical Chemistry Letters* **1**, 3451-3458.

Xiao, C, Yang, J, Zhu, W, Peng, J, Zhang, J (2009) Electrodeposition and characterization of Bi_2Se_3 thin films by electrochemical atomic layer epitaxy (ECALE). *Electrochimica Acta* **54**, 6821-6826.

Yabuuchi, N, Kubota, K, Dahbi, M, Komaba, S (2014) Research development on sodium-ion batteries. *Chemical Reviews* **114**, 11636-11682.

Yadav, P, Sharma, A (2015) Linear and nonlinear optical properties of new Se-based quaternary Se–Sn–(Bi, Te) chalcogenide thin films. *Phase Transitions* **88**, 109-120.

Yang, J, Zhu, W, Gao, X, Bao, S, Fan, X (2005) Electrochemical aspects of the formation of Bi_2Te_3 thin film via the route of ECALE. *Journal of Electroanalytical Chemistry* **577**, 117-123.

Yi, Q, Chu, H, Chen, Q, Yang, Z, Liu, X (2015) High Performance Pd, PdNi, PdSn and PdSnNi Nanocatalysts Supported on Carbon Nanotubes for Electrooxidation of C2-C4 Alcohols. *Electroanalysis* **27**, 388-397.

Zalineeva, A, Serov, A, Padilla, M, Martinez, U, Artyushkova, K, Baranton, Sv, Coutanceau, C, Atanassov, PB (2014) Self-supported Pd_xBi catalysts for the electrooxidation of glycerol in alkaline media. *Journal of the American Chemical Society* **136**, 3937-3945.

Zhang, W, Hu, Y, Ma, L, Zhu, G, Wang, Y, Xue, X, Chen, R, Yang, S, Jin, Z (2017) Progress and perspective of electrocatalytic CO_2 reduction for renewable carbonaceous fuels and chemicals. *Advanced Science **5**,* 10.1002/advs.201700275

Zhang, Y, Lu, S, Wang, M-Q, Niu, Y, Liu, S, Li, Y, Wu, X, Bao, S-J, Xu, M (2016) Bismuth oxychloride ultrathin nanoplates as an anode material for sodium-ion batteries. *Materials Letters* **178**, 44-47.

Zhu, W, Yang, J, Gao, X, Bao, S, Fan, X, Zhang, T, Cui, K (2005a) Effect of potential on bismuth telluride thin film growth by electrochemical atomic layer epitaxy. *Electrochimica Acta* **50**, 4041-4047.

Zhu, W, Yang, J, Gao, X, Hou, J, Bao, S, Fan, X (2005b) The underpotential deposition of bismuth and tellurium on cold rolled silver substrate by ECALE. *Electrochimica Acta* **50**, 5465-5472.

Zhu, W, Yang, J, Zhou, D, Xiao, C, Duan, X (2008) Electrochemical atom-by-atom growth of highly uniform thin sheets of thermoelectric bismuth telluride via the route of ECALE. *Journal of Electroanalytical Chemistry* **614**, 41-48.

Zhu, W, Yang, JY, Hou, J, Gao, XH, Bao, SQ, Fan, XA (2005c) Optimization of the formation of bismuth telluride thin film by using ECALE. *Journal of Electroanalytical Chemistry* **585**, 83-88.

Zimmer, A, Broch, L, Boulanger, C, Stein, N (2015) Growth mechanism during the early stages of electrodeposition of bismuth telluride films. *Electrochimica Acta* **174**, 376-383.

CHAPTER 3

3 Methodology

The methodology followed will be described in the following sections. Materials and the reagents used to prepare the SnBi and Pd based materials will be given. The procedure to electrodeposit the materials using E-ALD technique will be described. The formed materials were characterised using electrochemical methods and physical methods; these are also described. This is summarised in Figure 3.1, the detailed procedure is given in the following sections and the techniques used are defined in the last section.

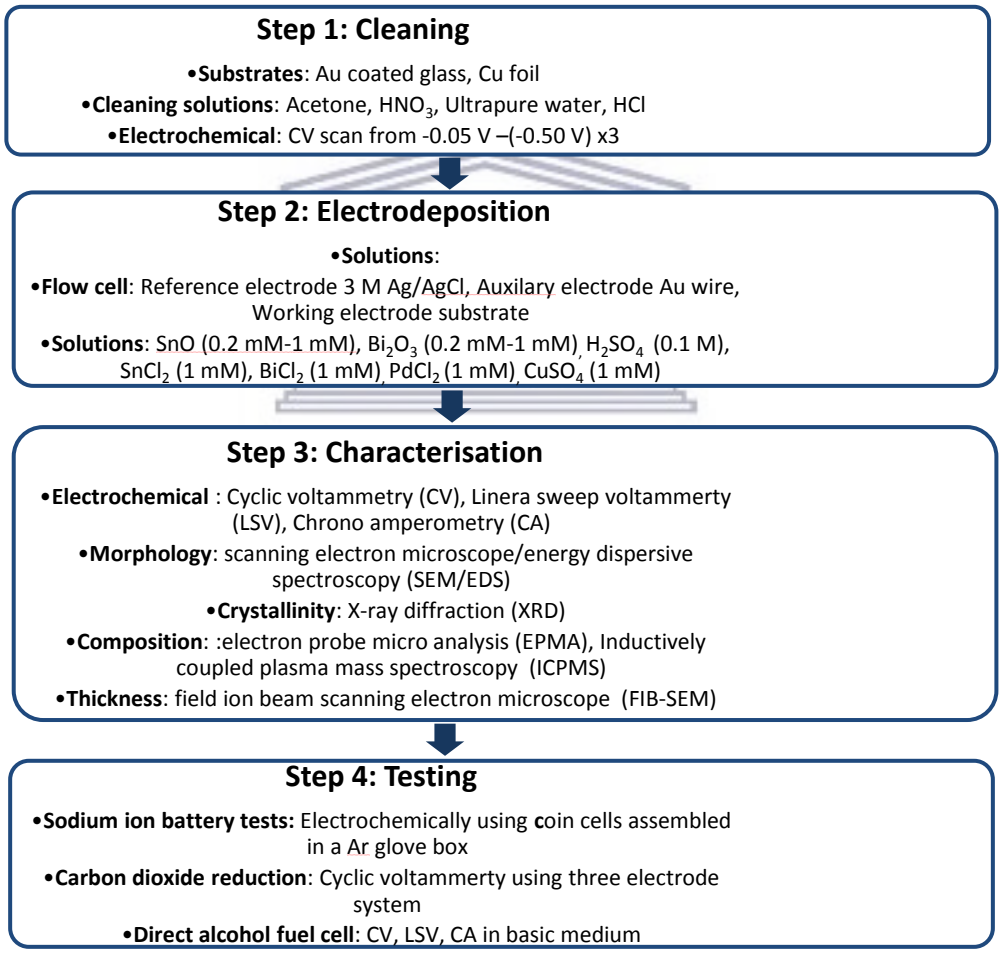

Figure 3.1: Summary of experimental procedure

3.1 Materials and Reagents

The solutions used in this study were prepared from ACS reagent grade chemicals purchased from Sigma Aldrich. High purity (≤ 1 µS/cm) deionised water was used to prepare all solutions.

3.1.1 Preparation of SnBi alloys on Au substrate

The chemical solutions used consisted of the electrolyte was 0.1 M H_2SO_4 (98 %, Associated Chemical Enterprise), 0.2 mM SnO (Sigma Aldrich), and 0.2 mM Bi_2O_3 (Sigma Aldrich). All solutions were prepared in electrolyte solution. The pH of all solutions was 1.8.

3.1.2 Preparation of SnBi alloys on Cu foil substrate

The chemical solutions used were 1 mM $SnCl_2$ (Sigma Aldrich), 1 mM $BiCl_3$ (Sigma Aldrich), and 0.5 M HCl (32%, Associated Chemical Enterprise) as the electrolyte. A range of 0.1 mM, 0.2 mM, 0.4 mM, 0.6 mM, 0.8 mM $SnCl_2$ solution in 0.1 M HCl were used, as well as 0.2 mM $BiCl_3$ solution. All solutions were prepared in electrolyte solution. The pH of the resulting solutions was 2.3.

3.1.3 Preparation of PdSnBi on Au substrate

The chemical solutions prepared were 0.1 mM $PdCl_2$ (Sigma Aldrich) in 0.5M HCl (1 mM $CuSO_4$ (Sigma Aldrich) in 0.1 M H_2SO_4, 0.2 mM SnO in 0.1 M H_2SO_4, and 0.2 mM Bi_2O_3 in 0.1 M H_2SO_4.

3.2 Substrate treatment

3.2.1 Au coated glass

Au-coated glass slides containing 100 nm Au film on 5 nm Ti on glass (Evaporated Metal films, Ithaca, NY). These slides were cleaned in the following manner: sonication in acetone for 5 minutes, deionised water rinse, dipped in concentrated HNO_3 for 2 minutes, deionised water rinse, and finally dried with nitrogen.

3.2.2 Cu foil

The Cu foils (99 %, 9 µm, Gelon) were cleaned in a dilute nitric acid (5 wt %), rinsed with deionised water, dipped in acetone, and air dried.

3.3 E-ALD deposition

Figure 3.2 shows the electrochemical flow system. The deposition system is housed in pyrex glass box with a controlled environment. Prior to any deposition, the solutions are degassed for a period of 1 hr using the nitrogen gas. The degassed solution was pumped using masterflex peristatic pump fitted with masterflex tubes housed in the pyrex glass box. The degassed solution passes into the electrochemical flow cell (Figure 3.3) where deposition occurs. To ensure that the substrate is well prepared and clean for the synthesis, a cleaning and condition step using sulfuric acid is used. The substrate was placed into the electrochemical flow cell and immediately further cleaned with 0.1 M H_2SO_4 while the potential of the cell was alternated three times between 1400 mV and -200 mV for Au substrate. A solution of 0.1M HCl was used for Cu foil substrate at a potential of 50 mV and -500 mV. A three-electrode electrochemical flow cell was used. Au wire and Ag/AgCl (3 M KCl) (MF-2021, BASI) served as auxiliary and reference electrodes, respectively. Copper tape was used as mode of contact for the working electrode (Au coated glass). The solutions were degassed with nitrogen gas for at least 60 minutes and then pumped through master flex tubes from their reservoirs using a peristaltic pump. A rubber gasket was used to limit the surface area of the Au electrode to 4.06 cm^2. A scan rate of 10 mV/s and a flow rate of 2.8 mL/min were used in all experiments. The deposition conditions were studied and optimised using cyclic voltammetry and analysis of current-potential time traces. The system was automatically controlled using software called sequencer 4.

3.3.1 Equipment

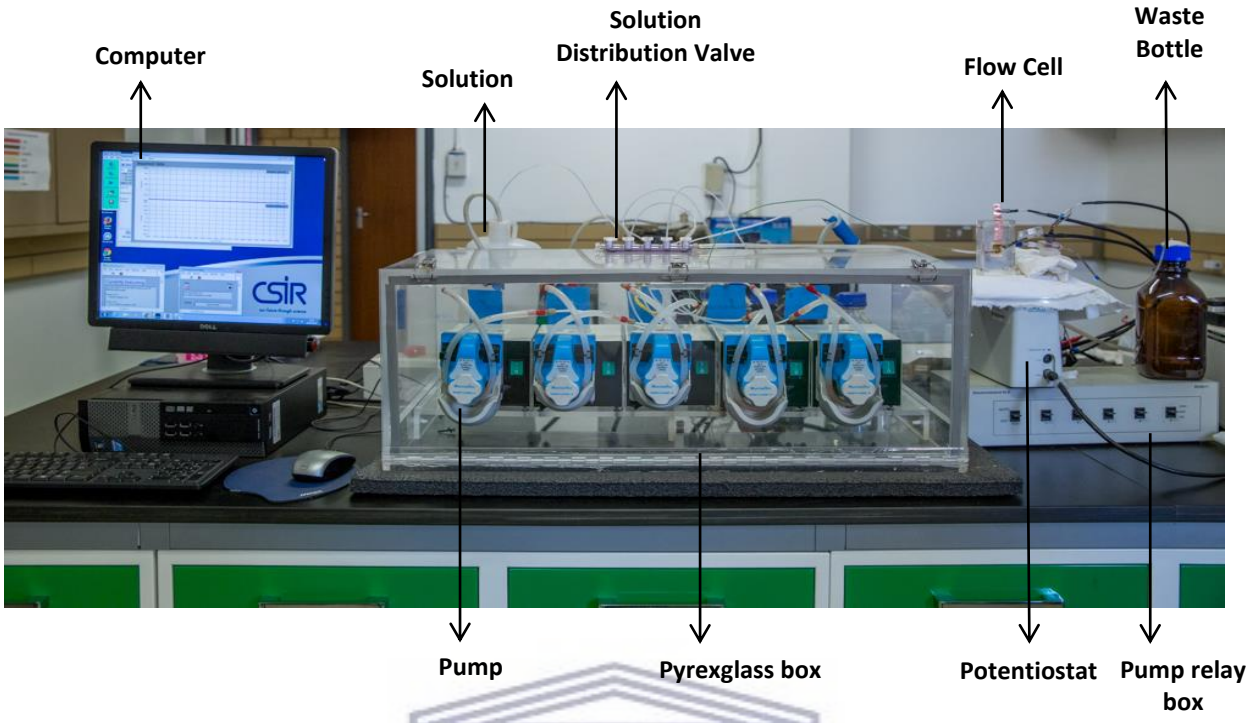

Figure 3.2: Scheme of the electrochemical flow system

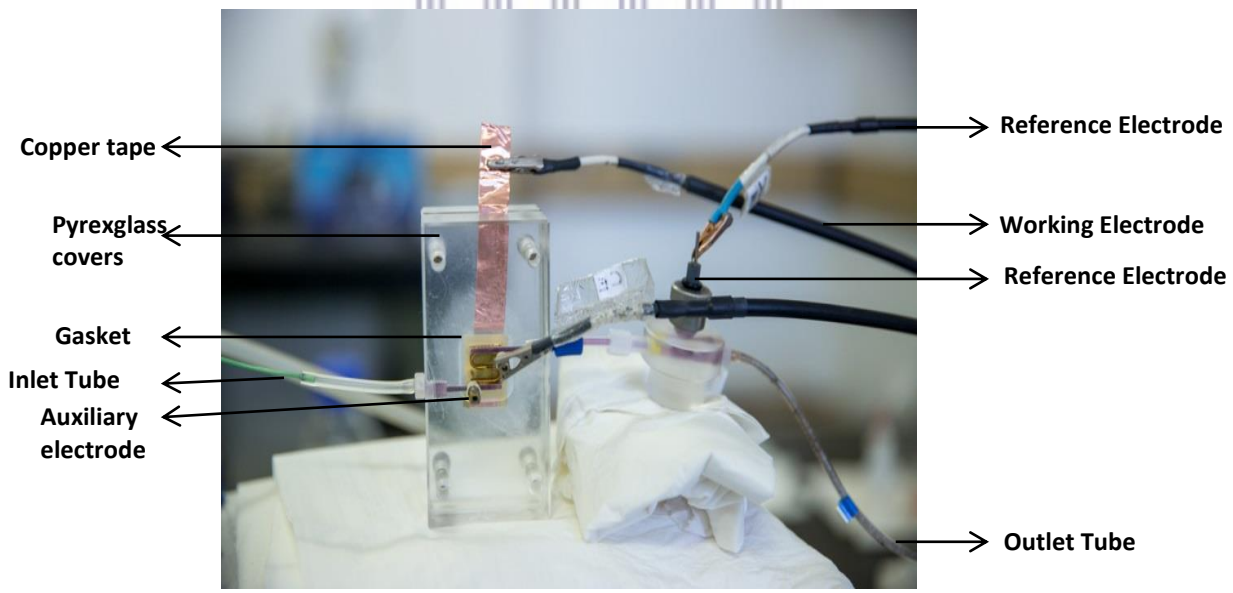

Figure 3.3: The electrochemical flow cell

Electrodeposition of Pd based materials on Au substrate

The electrodeposition of Pd nanostructures using Cu UPD on Au substrate is shown in Figure 3.4. The basic deposition cycle with a number of steps is as follows. (i) Pump the Cu solution

into the cell at an applied potential, (ii) Keep the Cu solution in the flow cell to deposit Cu, (iii) Pump Pd solution into the cell, (iv) Keep Pd solution in the cell for deposit Pd (SLRR), (v) Rinse with electrolyte. This cycle was repeated as many times as required to form the deposit. This procedure was adapted from the work done by Mkwizu and co-workers (Mkwizu *et al.* 2010), and Modibedi and co-workers (Modibedi *et al.* 2013), as well as other sources (Sheridan *et al.* 2012; Sheridan *et al.* 2013) . The formation of Pd material with Sn and Bi was formed by introducing a second element in the following steps and depositing it at UPD as described in results section, forming PdSn, and PSnBi materials.

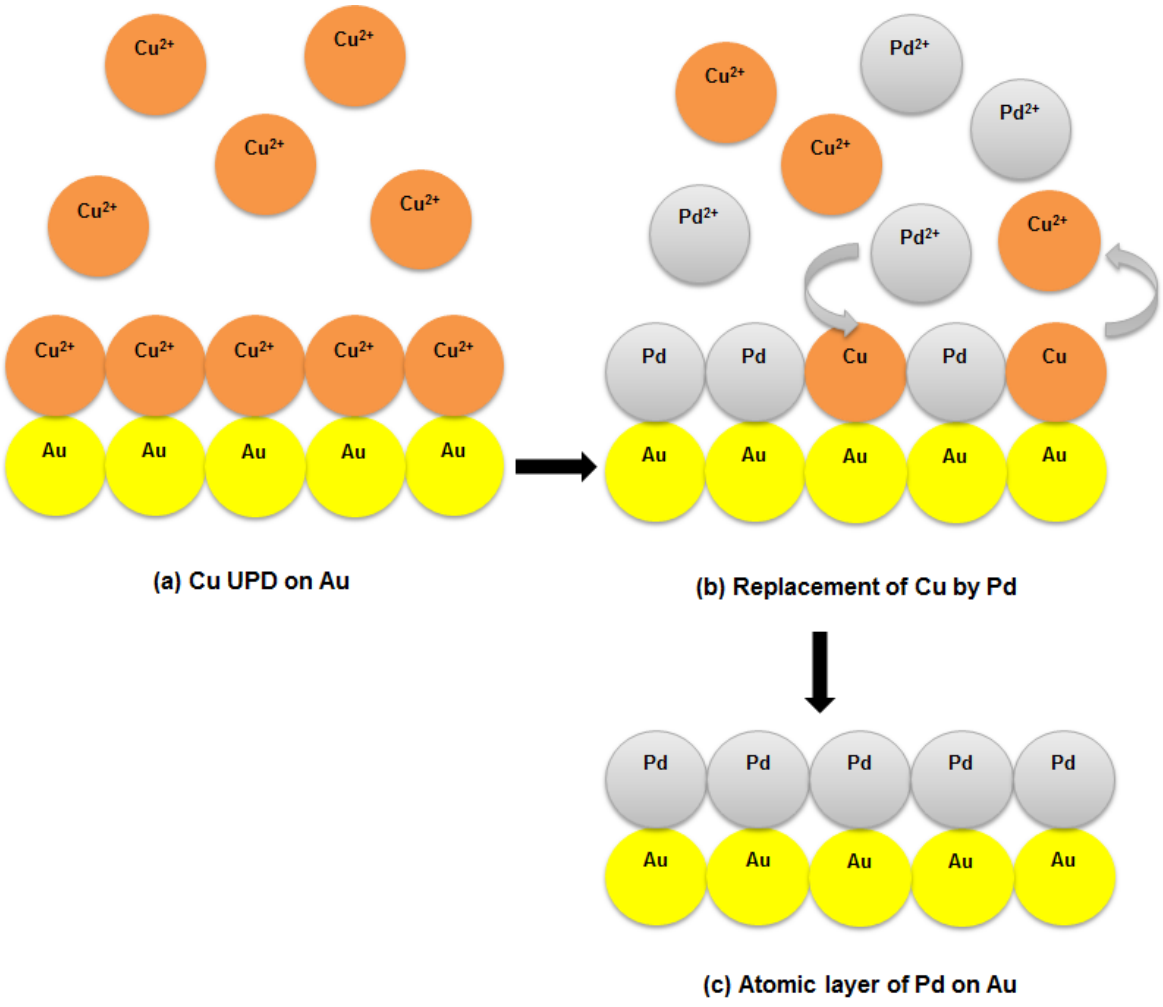

Figure 3.4: Electrodeposition of Pd using Cu UPD (Sheridan *et al.* 2012)

3.4 Electrodeposition of SnBi based materials on Au substrate

The formation of SnBi materials was adapted and motivated by previous work done on Sn UPD deposition on Au (Meier *et al.* 2012) and that of Bi UPD deposition on Au (Zhu *et al.* 2005). While bimetallic alloy has been deposited in various work (Sandnes *et al.* 2008; Hu *et*

al. 2009; Tsai and Hu 2009a; Tsai and Hu 2009b, 2011; Tsai *et al.* 2011; Gao *et al.* 2014), other parameters including the type of precursor solutions and E-ALD technique still needed to be further explored. The development and optimisation of SnBi deposition cycles is first reported in the results and discussion section.

3.5 Electrochemical Characterisation

3.5.1 Electrochemical activity of PdSnBi

The electrochemical flow cell (figure 3.3) with three electrode system described above was used to study the electrochemical activity of the materials using cyclic and linear sweep voltammetry in N_2 saturated 0.1 M KOH, 0.1M EtOH, and 0.1 M glycerol. A potentiostat Metrohm PGSTAT101 controlled by NOVA 1.8 software was used with the electrochemical flow cell.

3.5.2 CO_2 reduction studies using Bi on Au substrate

Electrochemical activity studies were conducted using the standard three electrode system by means of cyclic voltammetry. A potentiostat, Metrohm PGSTAT302, equipped with NOVA 2.0 software was used, the counter electrode was Pt (Metrohm) rod, the reference electrode was Ag/AgCl/ 3 M KCl, and the working electrode was Bi on Au connected using Cu tape. CV scans were done in 0.5M $NaHCO_3$ solution (pH 8.62) between 1.3 V and -1.3 V. The scan rate used for all CV scans was 50 mV/s. Three scans were obtained for each sample in air, N_2, and CO_2 saturated $NaHCO_3$ solution. CV scan were also done in methanol, ethanol, formic acid and ethylene glycol N_2 saturated solutions.

3.5.3 Electrochemical Battery tests using SnBi on Cu foil

The SnBi materials were evaluated as anode materials using 2032-type coin cells. The material was first tested for Na ion battery application using Na disc as counter electrode, and 1 M $NaClO_4$ in ethylene carbonate-diethylene carbonate (EC:DEC, 50:50 vol%) solution as electrolytes, and a glass microfiber Whatman GF/F used as a separator. The coin cells were assembled in an Ar filled glove box (MBraun MB 150B-G, Germany, maintaining the concentrations of O_2 and H_2O< 1 ppm). The fabricated cells were electrochemically characterized by galvanostatic cycling (GC) using MACCOR series 4000 tester. Cyclic voltammetry (CV) and electrochemical impedance spectroscopy (EIS) was evaluated by using a Bio-Logic VMP3 potentiostat / galvanostat controlled by EC-Lab v10.40 software at the scan rate of 0.1 mV s^{-1} with the potential range of 0.005–3.0 V. The EIS plots were

recorded by applying 10 mV amplitude over the frequency range from 100 kHz to 10mHz at room temperature and the data was analysed by using Z-view software (version 2.2, Scribner Assoc., Inc., USA).

3.6 Physical Characterisation and quantitative analysis

3.6.1 Scanning electron microscope/energy dispersive spectroscopy (SEM/EDS)

The morphology of the films was studied using a scanning electron microscope and energy dispersive detector was used for elemental mapping.

3.6.1.1 Cu substrate

The samples are stuck onto the SEM stage with conductive double stick carbon tape and coated with Cr. The coater is quorum Q150T ES. The cross section of the samples is viewed with a ZEISS Auruga field ion beam scanning electron microscope (FIB-SEM) using martSEN software version V05.04.00. The EDS was done using Oxford X-Men detector and Aztec software.

3.6.1.2 Au substrate

The cross section images were obtained by fracturing the sample in LN2 and placed the fractured edge facing up on the stub. The samples are viewed with a ZEISS Auriga FIB-SEM using martSEN software version V05.04.00. The EDS was done using Oxford X-Men detector and Aztec software.

3.6.2 X-Ray diffraction

The crystal features and phases were determined using a Rigaku Ultima IV X-Ray diffractometer with a mono-chromatized Cu Kα radiation of λ=1.5406 Å at the 2θ range of 10^{o}-90^{o}. The spectra were matched and refined using High Score Plus software and PDF 4 FILE 2017.

3.6.3 Electron probe micro analysis (EPMA)

The elemental analysis was done using a JEOL 8600 Superprobe electron probe microscope (EPMA) instrument with a 10 KeV accelerating voltage, a 15 nA beam current and 10 µm beam diameter.

3.6.4 Inductively coupled plasma mass spectroscopy (ICPMS)

The elemental content was analysed using Thermo Scientific iCAP Q ICP-MS equipped with Qtegra Intelligent Scientific Data Solution (ISDS) software. SnBi on Cu foil material were

prepared by digestion in 10 mL HNO_3 and the residue diluted to the desired concentration. Standard solutions used were in the range of 20 ppb -100 ppb prepared using multi-element standard solution 1 for ICP (10% HNO_3, Sigma Aldrich). All measurements were done in standard mode.

3.7 Characterisation Techniques

3.7.1 Voltammetry

This is a technique used to measure the electrochemical reaction mechanisms of a reaction. This is done by applying a voltage to the electrode and the measuring current flow (Bard *et al.* 1980; Mabbott 1983; Skoog *et al.* 2007; Elgrishi *et al.* 2018). The basic requirements needed are: (i) the electrode usually an inert metal; (ii) A solvent to aid dissolution of the electrolyte and current passage; (iii) A background electrolyte made of inert salt in high concentration to allow current passage; (iv) A reactant made up of low concentration of the species being investigated. Voltammetry measurements are carried out using a potentiostat by controling the potential applied to the working electrode (WE) relative to the reference electrode (RE), while the current flowing between the auxiliary electrode (CE) and working electrode is measured (Elgrishi *et al.* 2018). There are various types of voltammetry techniques and two are discussed below.

3.7.2 Linear Sweep Voltammetry (LSV)

The voltage is scanned from a lower limit to a higher limit at a fixed range and plots the current is as a function of potential as shown in Figure 3.5 (Bard *et al.* 1980; Skoog *et al.* 2007). The resulting linear sweep voltammograms characteristics depend on the scan rate, the rate of electron transfer and the chemical reactivity of the species of interest (Garreau and Savéant 1972). When the voltage is initially scanned from V_1, the current start to flow disturbing the equilibrium at the surface. As the potential is scanned further towards V_2, the equilibrium is shifted to the right, the current increases, and more reactant is converted (oxidation). The peak observed is due to rapid current increase when the growth of diffusion layer above the electrode making the flux of the reactants to electrode not fast enough. Changing the scan rate will also change the current response.

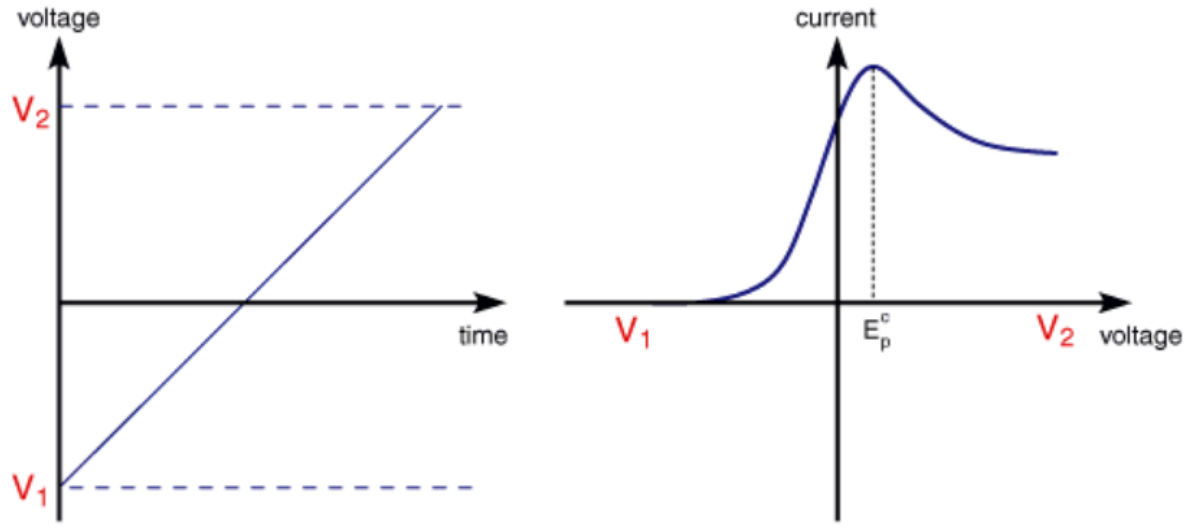

Figure 3.5: LSV scan of voltage vs time, and current vs voltage.

3.7.3 Cyclic Voltammetry

This technique is similar to LSV, but the potential scanned between two limits V_1 and V_2, it is then scanned in reverse back to V_2 (Mabbott 1983; Skoog *et al.* 2007). The current response is plotted against the potential and there is also a time response directly proportional to the potential as shown in Figure 2. During a CV scan the potential is scanned forward and reverse past the formal potential (E^o) of the analyte, the current flowing through electrode either oxidises or reduce the analyte (Kissinger and Heineman 1983; Elgrishi *et al.* 2018). The current response peak is proportional to the concentration of the analyte in solution. CV allows for the investigation of the kinetics of the electrochemical reaction. The amplitude, width and potential of the observed peaks can be used to investigate adsorption or diffusion mechanisms.

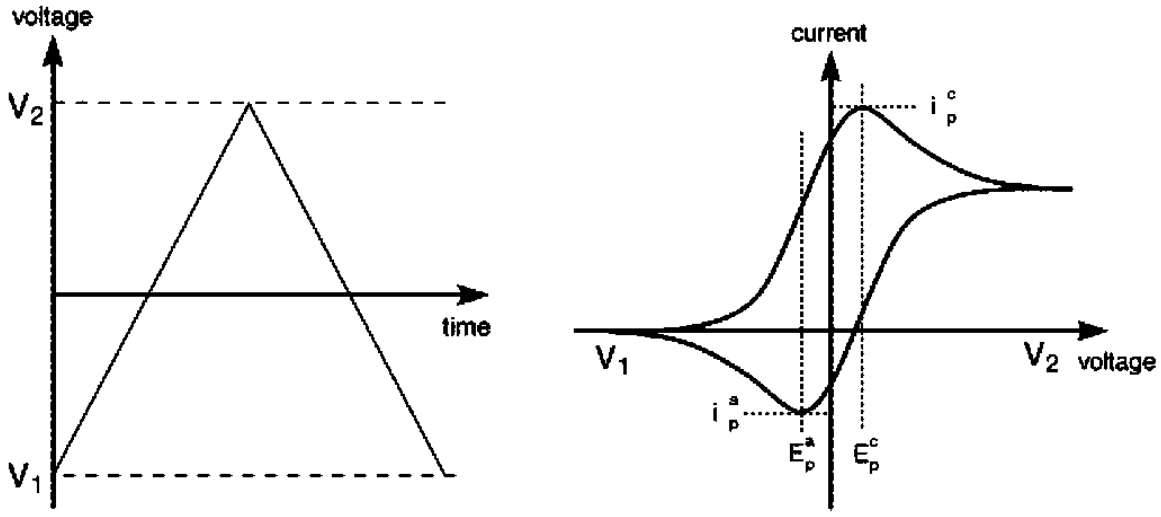

Figure 3.6: CV showing voltage vs time and current vs potential.

3.7.4 Chronoamperommetry (CA)

This technique involves applying a constant potential to an electrode, and monitoring the current response over time (Bard *et al.* 1980; Skoog *et al.* 2007). The voltage is stepped from V_1 where no reaction occurs to V_2 where a current response begins as shown in Figure 3. The current response drops over time due to diffusion barrier on the electrode surface.

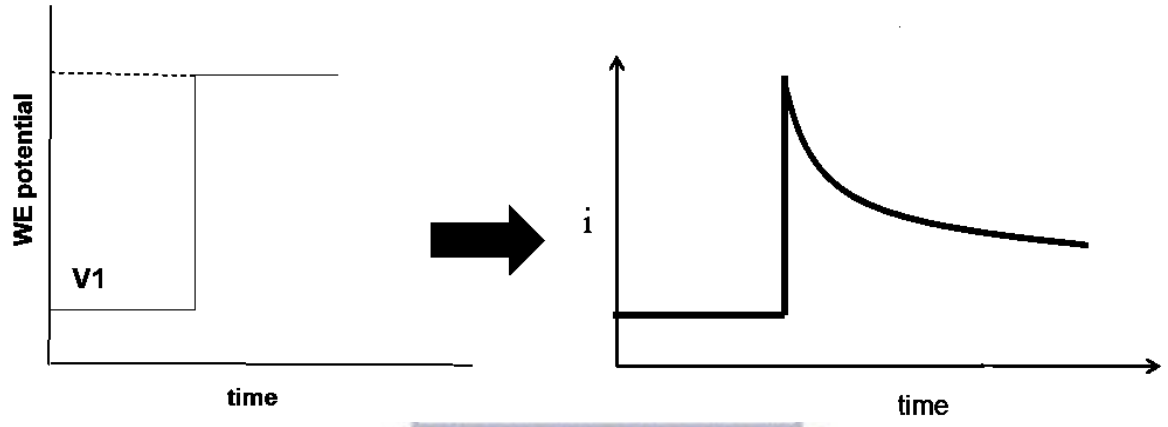

Figure 3.7: Scan for potential vs time, and current vs time.

CA can be used to measure surface area, diffusion co-efficient, rate constant and diffusion layer thickness using the Cottrell equation (equation 20) (Swartzfager 1976)

$$i_t = \frac{n\,F\,A\,C_0\,D_0^{1/2}}{\pi^{1/2} t^{1/2}} \qquad (20)$$

3.7.5 Electrochemical impedance spectroscopy (EIS)

Impedance is a useful tool to characterise surface of the electrodes in electrochemical cells. It is the measure of the ability of the circuit to resist the flow of current (Macdonald 1992). Unlike resistance; impedance is not governed by Ohms law. The impedance is measured by applying a potential to an electrochemical cell and measuring the current (Macdonald 1992; Zia and Mukhopadhyay 2016). A small excitation signal is used to measure electrochemical impedance. The obtained data in impedance spectroscopy is represented using Nyquist plots as shown in Figure 3.8.

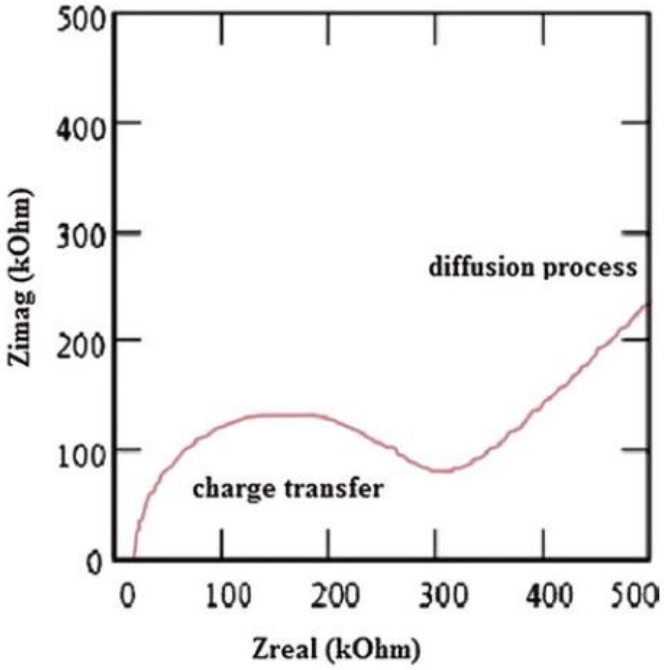

Figure 3.8: Nyquist plot for Randle's electrochemical cell (Zia and Mukhopadhyay 2016)

Nyquist plots evaluate the electrochemical parameters including electrolytic solution resistance (R_s), electrode polarization resistance (R_p) and double layer capacitance (C_{dl}). The plot represents the impedance Z where the imaginary part Z' is plotted against the real Z" part as show in Figure 3.8. The Randle's electrochemical cell equivalent model takes into account the double-layer capacitance, solution resistance, and charge electron transfer resistance R_{ct}. The absolute impedance Z_w is expressed as the sum of the imaginary part and the real part (equation 21-22), where w is the angular frequency and j is the response current signal (Zia and Mukhopadhyay 2016).

$$Z(w) = R_s + Z'(w) - Z''(w) \quad (21)$$

$$Z(w) = R_s + \frac{R_{ct}}{1+w^2R_{ct}^2C_{dl}^2} - \frac{jwR_{ct}^2C_{dl}}{1+w^2R_{ct}^2C_{dl}^2} \quad (22)$$

3.7.6 Electrochemical charge/discharge

Charge and discharge profile are useful tools in battery chemistry that are used to evaluate how much energy the battery can deliver (Park *et al.* 2001). This energy is the capacity of the battery in Ah. An Ah is the discharged current delivered over time. The amount of energy a battery can store is measured by discharging it at a specific current rate (c-rate) (Park *et al.* 2001; Simon and Gogotsi 2008). The c-rate governs the discharge and charge rates. 1C the

standard used for fully charged batteries, this battery should be able to supply 1 A for 1 hour. C rates can be varied (0.5C, 0.2C) to test the ability of the battery to deliver full capacity regardless of how fast is discharging (stability tests) (Fleischauer *et al.* 2004).

3.7.7 X-Ray diffraction

X-Rays are electromagnetic radiation with a wavelength between 0.01-10 nm and photon energy in the range of 100 eV-1000 keV (Thibault and Elser 2010; Li and Sun 2017). X-ray diffraction is used to identify the phases of crystalline materials. X-ray diffraction patterns are generated by a constructive interference of monochromatic x-rays and a crystalline sample (Thibault and Elser 2010; Hansford 2016; Li and Sun 2017; Tobbens and Schorr 2017). The source of these x-rays is a cathode ray tube that produces monochromatic light. A diffracted ray is produced when the sample and incidence ray collide producing constructive interference and the provided Braggs law is satisfied (Hansford 2016). Braggs law (equation 23) depicts the relationship between the wavelength (λ) of the electromagnetic radiation to the sample diffraction angle (θ) and lattice spacing (*d*) (Hansford 2016).

$$n\lambda = 2d \sin\theta \tag{23}$$

The diffracted x-rays are detected. A voltage is applied to accelerate the x-rays towards the sample, the electrons in the incident x-ray have sufficient energy to remove inner core electron on the sample, resulting in a characteristic spectra for the sample. Different materials have characteristic wavelengths that are used for identification of specific elements.

3.7.8 Scanning electron microscopy

This technique uses a beam of high energy electrons that interact with a sample (Smith and Oatley 1955). The electron decelerate when they collide with the sample, releasing energy in different types of signal including the secondary electrons, backscattered electrons, diffracted backscattered electrons, photons, visible light and heat (Smith and Oatley 1955; Bogner *et al.* 2007; Klang *et al.* 2012; Reimer 2013; Suga *et al.* 2014). Each of these signals provides specific information about the sample being analysed. Sample imaging is done using secondary and backscatter electrons. Topography and morphology is obtained using secondary electrons while backscattered electrons provide the contrast for composition and phase analysis. Characteristic x-rays are used to identify sample composition (Suga *et al.* 2014). The schematic diagram is shown in Figure 3.9. The source of electrons is a gun, the sample is placed in a stage (mobile), and a detector for varied signals, the system is under vacuum and electric fields, needs a cooling system and steady power supply.

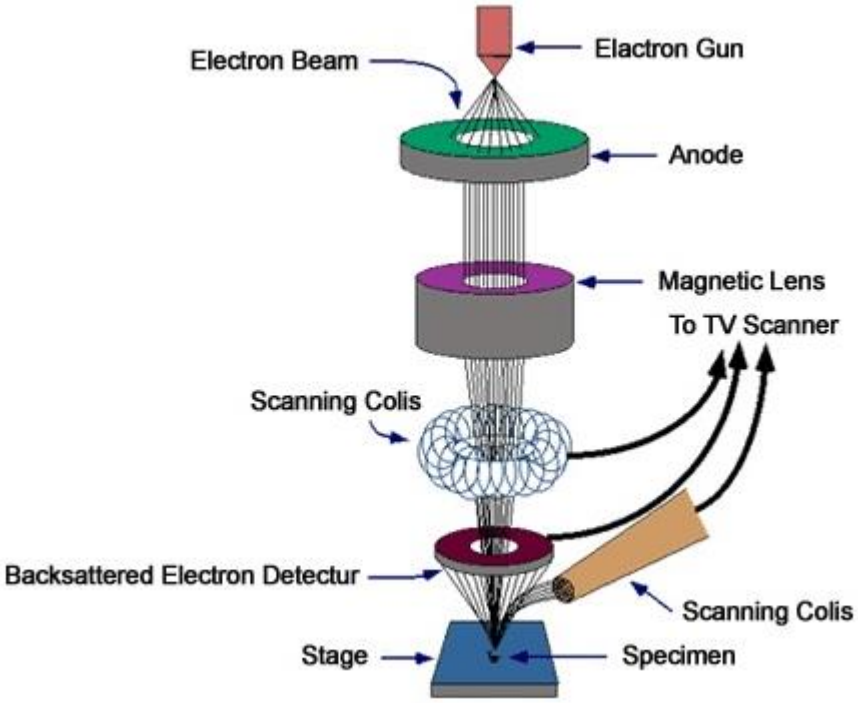

Figure 3.9: Schematic of the scanning electron microscope (Bogner *et al.* 2007).

3.7.9 Focused ion beam scanning electron microscope

This instrument principle is similar to SEM except that is uses a focused ion beam to scan over the sample, generating a very high resolution image (Volkert and Minor 2007). Like SEM, Secondary and backscattered electrons are detected in the EDS detector. This technique uses a beam of gallium ion that is much heavier than electrons (Giannuzzi and Stevie 1999; Reyntjens and Puers 2001; Tseng 2004). This ensures that the sample interaction is stronger with lower penetration, therefore chemical bonds and ionisation of substrate is possible. This technique is thus allows for milling, etching and deposition on the surface of the sample. The high resolution and probes gives it the ability to measure depth (sample thickness)

3.7.10 Electron probe micro analysis

This technique is fundamentally the same as SEM, with the same operating principle. It uses an electron probe as the source of electrons instead of an electron gun, also uses the EDS detector (Freestone 1982). The added abilities provided by EPMA is the precision and quantitative analysis using very small spot sizes (1-2 microns) (Chu *et al.* 1989). The technique is non-destructive, can analyse very small samples, and can also be used for *in situ* analysis (Raudsepp 1995).

3.7.11 Inductively coupled plasma mass spectroscopy (ICPMS)

The high temperature of the inductively coupled plasma **(**ICP) is coupled with a mass spectrometer detector (Houk and Thompson 1988; Ye *et al.* 2003; Beauchemin 2010; Kashani and Mostaghimi 2010). Argon flows through the ICP torch. The plasma is a cloud of gaseous argon ions generated by applying voltage to the ICP torch (Houk and Thompson 1988). The sample being analysed is introduced by spraying it using a nebuliser. The sample is immediately ionised by high temperature (6000-10000 K) and then transferred into the mass spectrometer region through interference cones. These cones separate the plasma region and the low pressure mass spectrometer region using a vacuum (Ye *et al.* 2003). The sample ions are focussed into the mass spectrometer slit by electrostatic lenses. The mass spectrometer then filters the ions based on the mass to charge ratio. The most commonly used are quadrupole mass filters that can separate up to 2400 amu/s (Beauchemin 2010). They operate by switching the potential applied to the rods, thereby electrostatically filtering specific mass to charge ratio ions to pass. The ICP components are shown in Figure 3.10. These are very high resolution quantitative instruments that are almost interference free. They use very low amount and dilute samples, their detection limit is at a ppb level.

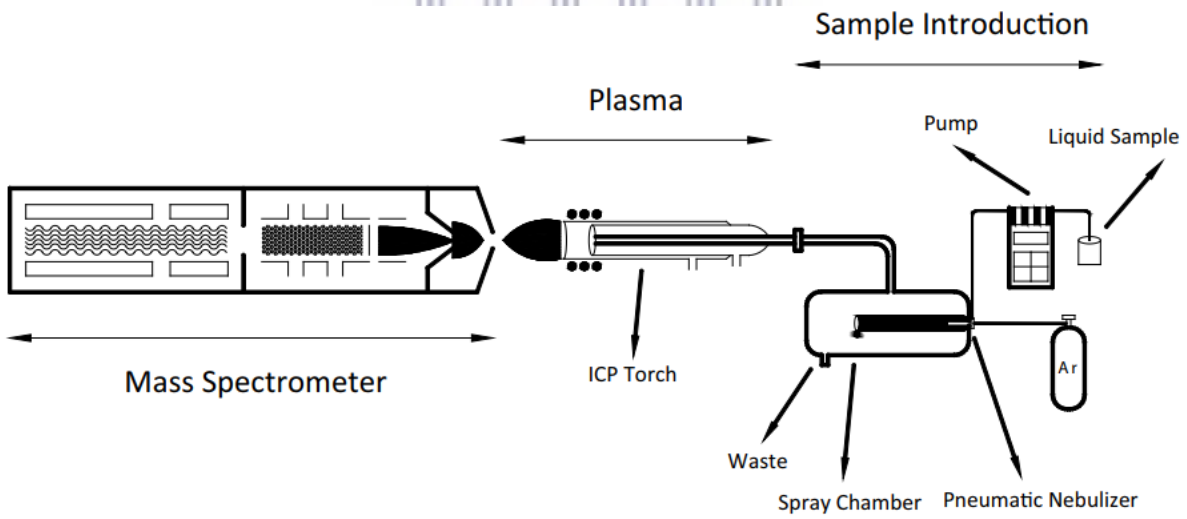

Figure 3.10: Schematic diagram of the ICPMS components (Kashani and Mostaghimi 2010)

3.8 References

Bard, AJ, Faulkner, LR, Leddy, J, Zoski, CG (1980) 'Electrochemical methods: fundamentals and applications **2**, New York: Wiley

Beauchemin, D (2010) Inductively coupled plasma mass spectrometry. *Analytical Chemistry* **82**, 4786-4810.

Bogner, A, Jouneau, P-H, Thollet, G, Basset, D, Gauthier, C (2007) A history of scanning electron microscopy developments: towards “wet-STEM” imaging. *Micron* **38**, 390-401.

Chu, J, Fox, J, Higuchi, W, Nash, W (1989) Electron probe micro-analysis for subsurface demineralization and remineralization of dental enamel. *Journal of Dental Research* **68**, 26-31.

Elgrishi, N, Rountree, KJ, McCarthy, BD, Rountree, ES, Eisenhart, TT, Dempsey, JL (2018) A practical beginner's guide to cyclic voltammetry. *Journal of Chemical Education* **95**, 197-206.

Fleischauer, M, Hatchard, T, Bonakdarpour, A, Dahn, JR (2004) Combinatorial investigations of advanced Li-ion rechargeable battery electrode materials. *Measurement Science and Technology* **16**, 212.

Freestone, IC (1982) Applications and potential of electron probe micro-analysis in technological and provenance investigations of ancient ceramics. *Archaeometry* **24**, 99-116.

Gao, Y, Hu, W, Gao, X, Duan, B (2014) Electrodeposition of SnBi coatings based on deep eutectic solvent. *Surface Engineering* **30**, 59-63.

Garreau, D, Savéant, J (1972) Linear sweep voltammetry-compensation of cell resistance and stability: Determination of the residual uncompensated resitance. *Journal of Electroanalytical Chemistry and Interfacial Electrochemistry* **35**, 309-331.

Giannuzzi, LA, Stevie, FA (1999) A review of focused ion beam milling techniques for TEM specimen preparation. *Micron* **30**, 197-204.

Hansford, GM (2016) Phase-targeted X-ray diffraction. *Journal of Applied Crystallography* **49**, 1561-1571.

Houk, RS, Thompson, JJ (1988) inductively coupled plasma mass spectrometry. *Mass Spectrometry Reviews* **7**, 425-461.

Hu, C-C, Tsai, Y-D, Lin, C-C, Lee, G-L, Chen, S-W, Lee, T-C, Wen, T-C (2009) Anomalous growth of whisker-like bismuth–tin extrusions from tin-enriched tin–Bi deposits. *Journal of Alloys and Compounds* **472**, 121-126.

Kashani, A, Mostaghimi, J (2010) Aerosol characterization of concentric pneumatic nebulizer used in inductively coupled plasma-mass spectrometry (ICP-MS). *Atomization and Sprays* **20**, 415-433.

Kissinger, PT, Heineman, WR (1983) Cyclic voltammetry. *Journal of Chemical Education* **60**, 702.

Klang, V, Matsko, NB, Valenta, C, Hofer, F (2012) Electron microscopy of nanoemulsions: an essential tool for characterisation and stability assessment. *Micron* **43**, 85-103.

Li, J, Sun, JL (2017) Application of x-ray diffraction and electron crystallography for solving complex structure problems. *Accounts of Chemical Research* **50**, 2737-2745.

Mabbott, GA (1983) An introduction to cyclic voltammetry. *Journal of Chemical Education* **60**, 697.

Macdonald, JR (1992) Impedance spectroscopy. *Annals of Biomedical Engineering* **20**, 289-305.

Meier, LA, Garcia, SG, Salinas, DR (2012) New insights into the Sn underpotential deposition on Au(100). *Surface and Interface Analysis* **44**, 37-40.

Mkwizu, TS, Mathe, MK, Cukrowski, I (2010) Electrodeposition of multilayered bimetallic nanoclusters of ruthenium and platinum via surface-limited redox-replacement reactions for electrocatalytic applications. *Langmuir* **26**, 570-580.

Modibedi, RM, Louw, EK, Ozoemena, KI, Mathe, MK, 2013. The electrochemical atomic layer deposition of pt and pd nanoparticles on ni foam for the electro-oxidation of alcohols. *Electrochemical Society Transactions*. **50**: 9-18.

Park, S, Savvides, A, Srivastava, M (2001) 'Battery capacity measurement and analysis using lithium coin cell battery, Proceedings of the 2001 international symposium on Low power electronics and design. ACM.

Raudsepp, M (1995) Recent advances in the electron-probe micro-analysis of minerals for the light elements. *Canadian Mineralogist* **33**, 203-203.

Reimer, L (2013) Scanning electron microscopy: physics of image formation and microanalysis **45**, *Springer*.

Reyntjens, S, Puers, R (2001) A review of focused ion beam applications in microsystem technology. *Journal of Micromechanics and Microengineering* **11**, 287.

Sandnes, E, Williams, ME, Vaudin, MD, Stafford, GR (2008) Equi-axed grain formation in electrodeposited Sn-Bi. *Journal of Electronic Materials* **37**, 490-497.

Sheridan, LB, Czerwiniski, J, Jayaraju, N, Gebregziabiher, DK, Stickney, JL, Robinson, DB, Soriaga, MP (2012) Electrochemical atomic layer deposition (E-ALD) of palladium nanofilms by surface limited redox replacement (SLRR), with EDTA complexation. *Electrocatalysis* **3**, 96-107.

Sheridan, LB, Gebregziabiher, DK, Stickney, JL, Robinson, DB (2013) Formation of palladium nanofilms using electrochemical atomic layer deposition (E-ALD) with chloride complexation. *Langmuir* **29**, 1592-1600.

Simon, P, Gogotsi, Y (2008) Materials for electrochemical capacitors. *Nature Materials* **7**, 845.

Skoog, DA, Holler, FJ, Crouch, SR, 2007. Principles of instrumental analysis. Thomson Brooks/Cole.

Smith, K, Oatley, C (1955) The scanning electron microscope and its fields of application. *British Journal of Applied Physics* **6**, 391.

Suga, M, Asahina, S, Sakuda, Y, Kazumori, H, Nishiyama, H, Nokuo, T, Alfredsson, V, Kjellman, T, Stevens, SM, Cho, HS (2014) Recent progress in scanning electron microscopy for the characterization of fine structural details of nano materials. *Progress in Solid State Chemistry* **42**, 1-21.

Swartzfager, DG (1976) Amperometric and differential pulse voltammetric detection in high performance liquid chromatography. *Analytical Chemistry* **48**, 2189-2191.

Thibault, P, Elser, V (2010) X-ray diffraction microscopy.

Tobbens, DM, Schorr, S (2017) The use of anomalous x-ray diffraction as a tool for the analysis of compound semiconductors. *Semiconductor Science and Technology* **32**,

Tsai, Y-D, Hu, C-C (2009a) Composition control of lead-free Sn–Bi deposits using experimental strategies. *Journal of the Electrochemical Society* **156**, D58-D63.

Tsai, YD, Hu, CC (2009b) Composition control of Sn-Bi deposits: interactive effects of citric acid, ethylenediaminetetraacetic acid, and poly(ethylene glycol). *Journal of the Electrochemical Society* **156**, D490-D496.

Tsai, YD, Hu, CC (2011) Composition and microstructure control of tin-bismuth alloys in the pulse plating process. *Journal of the Electrochemical Society* **158**, D482-D489.

Tsai, YD, Lien, CH, Hu, CC (2011) Effects of polyethylene glycol and gelatin on the crystal size, morphology, and Sn2+-sensing ability of bismuth deposits. *Electrochimica Acta* **56**, 7615-7621.

Tseng, AA (2004) Recent developments in micromilling using focused ion beam technology. *Journal of Micromechanics and Microengineering* **14**, R15.

Volkert, CA, Minor, AM (2007) Focused ion beam microscopy and micromachining. *MRS Bulletin* **32**, 389-399.

Ye, M, Yin, X, Fang, Z (2003) Progress in techniques of interfacing capillary electrophoresis with inductively coupled plasma mass spectrometry. *Guang pu xue yu guang pu fen xi= Guang pu* **23**, 89-93.

Zhu, W, Yang, JY, Hou, J, Gao, XH, Bao, SQ, Fan, XA (2005) Optimization of the formation of bismuth telluride thin film by using ECALE. *Journal of Electroanalytical Chemistry* **585**, 83-88.

Zia, AI, Mukhopadhyay, SC (2016) Impedance spectroscopy and experimental setup. in 'electrochemical sensing: carcinogens in beverages.' pp. 21-37, Springer.

CHAPTER 4

4 SnBi Thin Films Using Electrochemical Atomic Layer Deposition (E-ALD) Technique

Electrodeposition of thin films of tin (Sn) and bismuth (Bi) on gold using indirect underpotential deposition method from sulphate based electrolyte is reported. The deposition parameters were optimized using cyclic voltammetry. The morphology, thickness, elemental mapping and composition were determined using SEM/EDS, FESEM, EPMA and XRD. A UPD onset of -100 mV and -350 mV for Bi and Sn respectively was observed from cyclic voltammetry studies. Indirect UPD was used to overcome the large potential gap between Bi and Sn UPD. The results found that the SnBi film contains SnBi in a ratio of 1:3 with well-defined crystallites of Sn and Bi evenly distributed on the surface.

4.1 Introduction

Sn is a common coating material used in electronic devices due to its electrical conductivity and corrosion resistance (Sandnes *et al*. 2008). Sn electrodeposited in electrical components suffers from spontaneous growth of Sn whiskers which causes short circuits (Okamoto *et al*. 2009; Sandnes *et al*. 2008). Bi and its oxides are important components in the microchip packaging process and have been found to have very large magnetic resistance and are good semiconductors, and are thermo efficient (Jeffrey *et al*. 2002; Stafford & Bertocci, 2006). Alloy Materials of SnBi compositions have found renewed interest as lead free solder materials used in the interconnecting and packaging electronic components. These materials exhibit excellent joint strength, creep resistance, low surface tension and high shear strength and corrosion resistance (Tsai and Hu, 2009) . Bismuth is an attractive alternative to lead (Pb) because the deposition of Bi and Sn is similar to that of Pb and Sn, the addition of Bi prevents the formation of the undesirable whiskers. Various compositions of alloy materials of SnBi can be formed due to amongst others, their potentials being close enough to codeposit and yet also far enough for pulse depositions. Therefore it is important to select a method that ensures control of the microstructure of the material, due to the dependence of material properties on the composition of the alloy material.

SnBi thin films have been prepared by electroplating methods including bath deposition (Lee *et al*. 2012b; Tsai and Hu, 2009), pulse plating process (Sandnes et al., 2008; Tsai & Hu,

2011), and sequential electroplating (Goh *et al*. 2013; Lee *et al*. 2012b). These fabrication methods make use of complexing agents, wetting agents and other additives. Lee et al. (2012b) electrodeposited Sn and Bi layers on Cu from Sn solution containing citric acid and Bi solution with methane sulfonic acid to promote better surface coverage. They concluded that the deposition cycle of Bi/Sn sequence was the best to achieve a eutectic composition and uniform film. A recent study on the electrodeposition of Bi, Sn, and their alloys on Au sputtered glass from tetrabutylammonium cholorometalate salts in choline chloride/ethylene glycol solutions was reported (Vieira *et al*. 2017). They reported the formation of an alloy composed Sn/Bi ratio of 35:65 wt% deposited at -0.4 V that can be reversed at slightly more negative potential of -0.6 V. A study on the effect of post annealing electroplated Sn rich SnBi alloys using citrate based bath, found that thermal expansion of Sn post annealing causes Bi-Sn extrusions in Sn rich alloys (Hu *et al*. 2009). Studies of Bi deposition have investigated the structures of active Bi UPD layers on Au (111) and the kinetic process involved for catalytic oxygen reduction (Tamura *et al*. 2002; Tamura *et al*. 2004). They found that the low coverage Bi phase promoted oxygen reduction to a four electron reaction with slow kinetics. While that of the close packed Bi phase formed at negative potentials had limited sites for four electron reduction with faster reaction kinetics.

The challenge in the formation of SnBi alloy materials is overcoming the large deposition potential difference of +0.45 V (Katayama *et al*. 1996). The formation of materials by deposition of monolayers into well-defined surfaces gives rise to materials with superior properties than those of pure components (Meier *et al*. 2012). This can be done using underpotential deposition (UPD) where an element is deposited onto another at a potential under that required to deposit the element on itself, or by using surface limited redox replacement reaction (SLRR) where a sacrificial element is deposited and then replaced by the element of interest at open circuit. This process is referred to as electrochemical atomic layer deposition (E-ALD) (Gregory and Stickney, 1991). The process has previously been referred to as ECALE or E-ALD. E-ALD uses aqueous solutions to deposit atomic layers, and it does not require a vacuum, making the process cost effective. Compounds of group II-VI and III-V including HgSe (Venkatasamy *et al*. 2006), CdS (Gichuhi *et al*. 2002), CdSe (Mathe *et al*. 2004), CdTe, (Zhang *et al*. 2014), SbTe (Zhu *et al*. 2008), ZnSe, PbSe/PbTe (Bang *et al*. 2011), $CuInSe_2$ (Banga *et al*. 2012) have been successfully prepared using E-ALD. This process has also been used to form metals such as Pt (Jayaraju *et al*. 2012), Ge (Ledina *et al*. 2015), Pd (Sheridan *et al*. 2012) and Cu. (Thambidurai *et al*. 2010)

This study is aimed to develop a suitable method to electrodeposit Sn, Bi, and binary SnBi thin film materials using electrochemical atomic layer deposition. SnBi thin films were deposited on Au (111) substrates from aqueous solutions of SnO and Bi_2O_3 in H_2SO_4 electrolyte, using electrochemical atomic layer deposition (E-ALD). Cyclic voltammetry was used to study the oxidation and reduction of the each precursor and in the development of the deposition process. The prepared films were characterised using focused ion beam scanning electron microscope (FIB SEM) for morphology and thickness, energy dispersive spectroscopy (EDS) for surface elemental mapping, crystal features using x-ray diffraction, and electron probe microscope for composition.

4.2 Experimental

4.2.1 Chemicals and Solutions

The solutions used in this study were prepared from ACS reagent grade chemicals purchased from Sigma Aldrich. High purity (≤ 1 µS/cm) deionised water was also used to prepare all solutions. The tin solution was made by dissolving 0.0151 g of SnO in 0.1 M H_2SO_4 and made up to 500 mL in a volumetric flask. The bismuth solution was made by dissolving 0.0932 g of Bi_2O_3 in 0.1 M H_2SO_4 and made up to 1 L. The electrolyte was prepared by accurately transferring 5.6 mL of H_2SO_4 98 % stock solution to 200 mL deionised water and made up to 1 L. The pH of the solutions was 1.8.

4.2.2 Substrate treatment

The substrates used were Au coated glass slides containing 100 nm Au film on 5 nm Ti on glass (Evaporated Metal films, Ithaca, NY). These slides were cleaned by first sonicating in acetone for 5 min, rinsed with deionised water, and then dipped in concentrated HNO_3 for 2 min, rinsed with deionised water and finally dried with nitrogen.

4.2.3 E-ALD deposition

The substrate was placed into the electrochemical flow cell and immediately further cleaned by flushing with 0.1 M H_2SO_4 while the potential of the cell was alternated three times between 1400 mV – (-200 mV). A three electrode electrochemical flow cell was used during the deposition. Au wire and Ag/AgCl (3 M KCl) (MF-2021, BASI) served as auxiliary and reference electrodes respectively. Copper tape was used as mode of contact for the working electrode (Au coated glass). The solutions were degassed for 60 minutes and then pumped through master flex tubes from their reservoirs using a peristaltic pump. A rubber gasket was

used to limit the surface of the Au electrode to 4 cm^2. The scan rate of 10 mV/s and a flow rate of 2.8 mL/min were used in all experiments. The deposition conditions were studied and optimised using cyclic voltammetry and sequencer.

4.2.4 Characterisation

The morphology of the films was studied using a LEO 1525 field emission scanning microscope (FE-SEM) with the acceleration voltage of 2.00 kV and energy dispersive detector (EDS) was used for elemental mapping. The crystal features and phases of the film were determined using PANalytical X'PERT Pro X-Ray diffraction (XRD) with an open Eulerian cradle utilizing a 1.54 Å Cu K_α source and a parallel plate collimator. The elemental analysis was done using a JEOL 8600 Superprobe electron probe microscope (EPMA) with a 10 KeV accelerating voltage, a 15 nA beam current and 10 µm beam diameter. The thickness of the film was determined using focused ion beam scanning electron microscope (FIBSEM)

4.3 Results and Discussion

4.3.1 Electrochemical studies

A characteristic cyclic voltammogram of the Au electrode in 0.1 M H_2SO_4 is shown in Figure 4.1. The negative scan shows reduction peak corresponding to Au_2O_3 being reduced to Au (Chen *et al.* 2015).

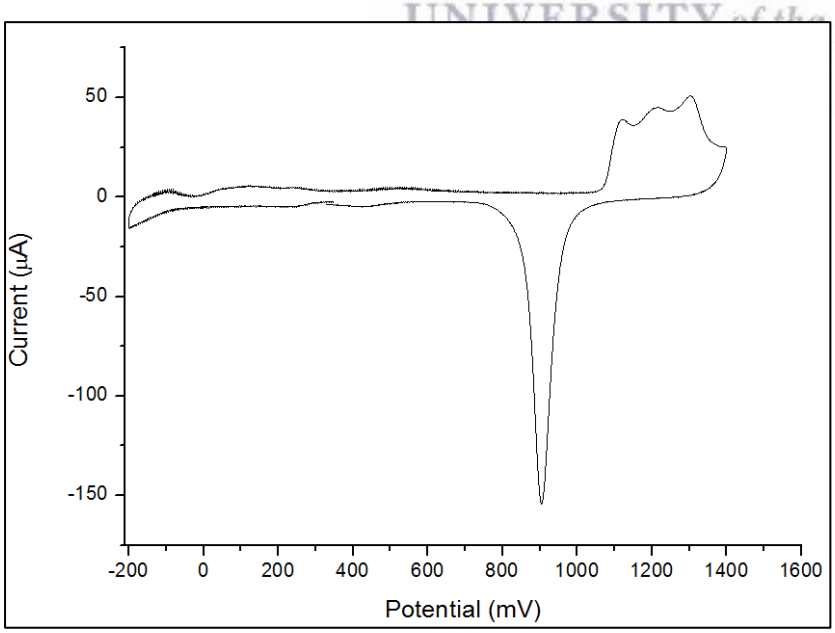

Figure 4.1: Cyclic voltammograms for Au electrode in 0.1 M H_2SO_4 vs Ag/AgCl, at a scan rate of 10 mV/s

The scan was stopped at -200 mV before hydrogen evolution peak could appear. The reverse scans negatively until -1600 mV, this results in the appearance of the oxidation peaks, indicating the oxidation of surface Au atoms from different crystallographic planes.

The window opening cyclic voltammetry (CV) study of Bi deposition on Au in 0.2 mM Bi^{3+} solution is shown in Figure 4.2.

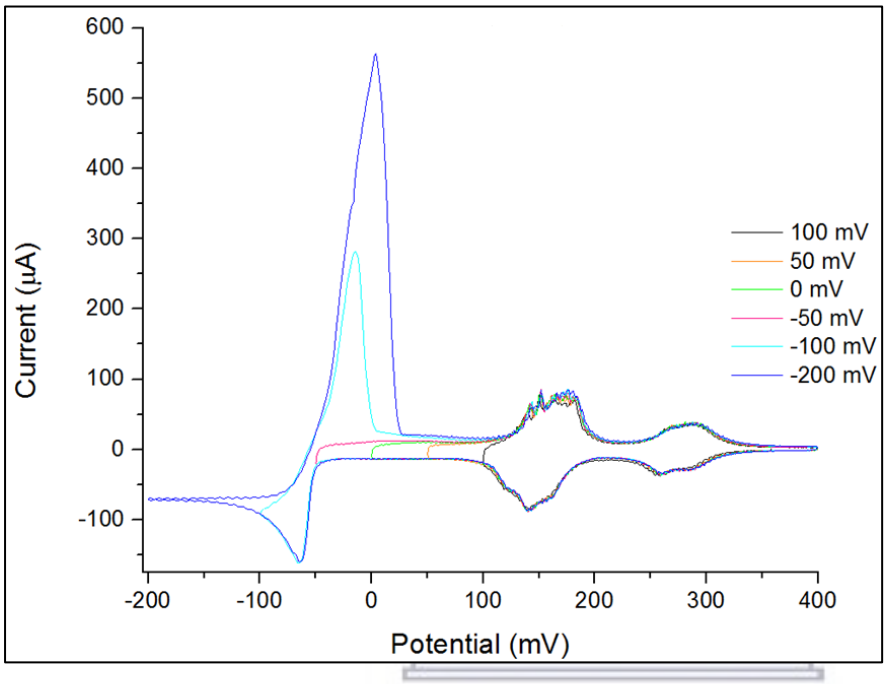

Figure 4.2: Cyclic voltammograms for Au electrode in 0.2 mM Bi_2O_3 vs Ag/AgCl, at a scan rate of 10 mV/s

All the CVs were scanned negatively and then reversed. There are three clear oxidation peaks observed at 0 mV, 150 mV and 275 mV. The peak at 0 mV was found to have a height that increased when scanned more negatively, and therefore assigned to bulk Bi deposition. The latter two peaks had the same peak height in all forward and reverse scans. These peaks are representative of the UPD stripping peaks. The UPD began at 100 mV and slowly grew to bulk deposition at -50 mV and beyond. The bulk strip was found at 0 mV, followed by two UPD stripping peaks near 150 mV.

The study of Sn deposition on Au in 0.2 mM Sn^{2+} solution is shown in the cyclic voltammogram in Figure 4.3. The potential was scanned from open circuit potential of 550 mV negatively and held at different negative limits for 30 seconds to force the stripping peak of Sn to appear. As a result, no reductive regions were observed on the scan, only three

oxidative features were visible. The onset UPD potential was found to be at -350 mV which slowly grew to bulk deposition at -425 mV and beyond.

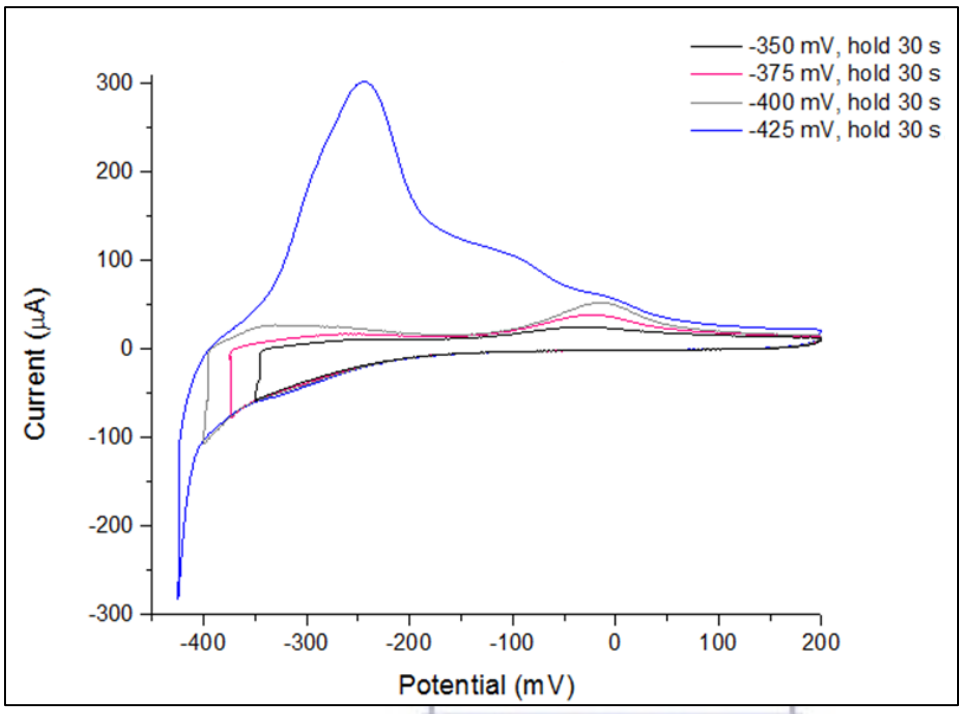

Figure 4.3: Cyclic voltammogram for Au electrode in 0.2 mM SnO vs Ag/AgCl, at a scan rate of 10 mV/s

4.3.2 Electrodeposition cycle development

The study of the cyclic voltammograms of Sn and Bi deposition provided the ballpark deposition potentials for the two elements. In order to also determine coverage, Bi and Sn were deposited at set potentials for 5 minutes followed by oxidation stripping. Bi was found to have a maximum coverage of 0.540 ML at 0 mV assuming a 3 electron process while Sn had 0.274 ML at -375 mV assuming a 2 electron process, and using 1.35×10^{15} atoms/cm^2 of Au (111) (Liang *et al*. 2009; Czerniawski *et al*. 2016). The CVs showed that Bi is stripped from the surface beyond -50 mV whereas Sn UPD starts at -350 mV. On the other hand Bi UPD deposits at 100 mV while that area is beyond the stripping Sn region. This poses a challenge when directly depositing both elements at UPD because they strip during the deposition of the other and this prohibits film growth. As a result, a deposition cycle where both elements are indirectly deposited, meaning that the deposition occurs at bulk region followed by the stripping of the bulk element leaving the underpotential deposited layer on the surface. A number of experiments were performed to find the optimum deposition cycle where most challenges were addressed. The three important ones are explained as follows;

Firstly, going to open circuit at 550 mV resulted in no film growth due to this being the stripping region of both Sn and Bi. So the potential needed to be controlled at all times. Secondly, rinsing with 0.1 M H_2SO_4 at a controlled potential after deposition of first Bi layer followed by Sn first layer deposition at -425 mV also prohibited film growth (Figure 4.4 b). This was due to oxidation and reduction occurring, and observed as current changes during deposition. However, depositing Bi at slightly more negative potential of -150 mV did not affect the film growth as shown by the similarities between image (a) and (c) in Figure 4.4. Thirdly, the deposition of Sn first layer followed by Bi second layer resulted in the formation of Bi only thin films. Bi is a nobler element that Sn, noble elements always prudentially deposits over the less noble element. The process involves the displacement of Sn by Bi at open circuit potential (OCP), a common phenomenon known as surface limited replacement reaction (SLRR).

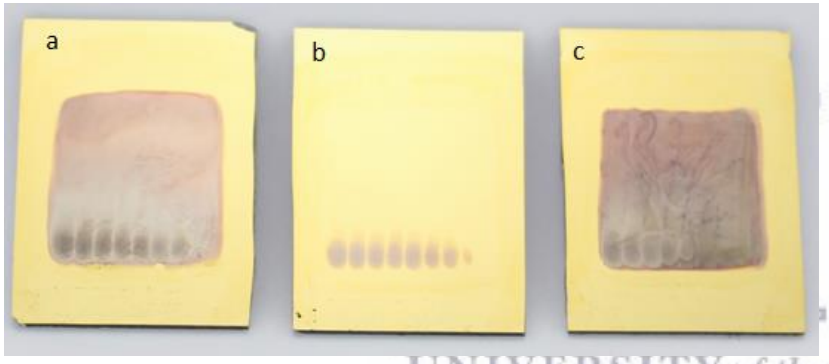

Figure 4.4: Image of a 50 cycle SnBi deposit on Au coated glass substrate at (a) Bi deposited at -100 mV and no rinsing, (b) Bi deposited at -100 mV and rinsed with bank, (c) Bi deposited at -150 mV and no rinsing

4.3.2.1 Bi thin films

Surface limited replacement reaction method was used to form thin films containing only Bi by the following cycle steps: (i) pump Sn solution at OCP for 10 s, (ii) deposit Sn at -425 mV for 5 s, (iii) pump Bi solution at OCP. This process is illustrated on the current potential versus time plot in figure 4.5 showing three cycles. The morphology of the film on the SEM images in figure 4.6a-c shows well defined structures, distributed evenly on the surface as shown on the elemental map in figure 4.6d. The EDS spectrum in figure 4.7 clearly shows only the presence on Bi.

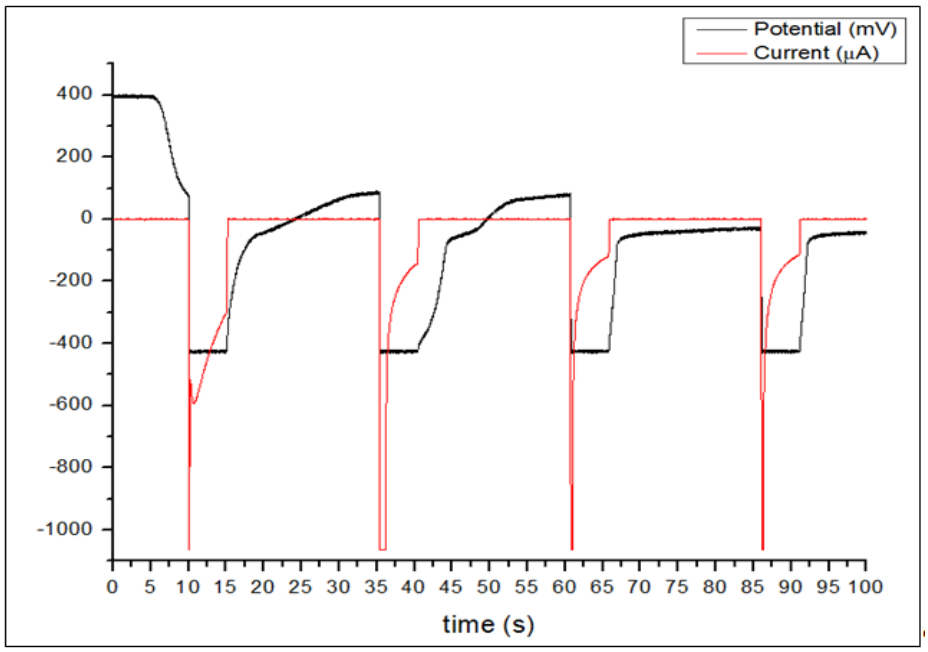

Figure 4.5: Current and potential profile for 3 E-ALD cycles for Bi deposit.

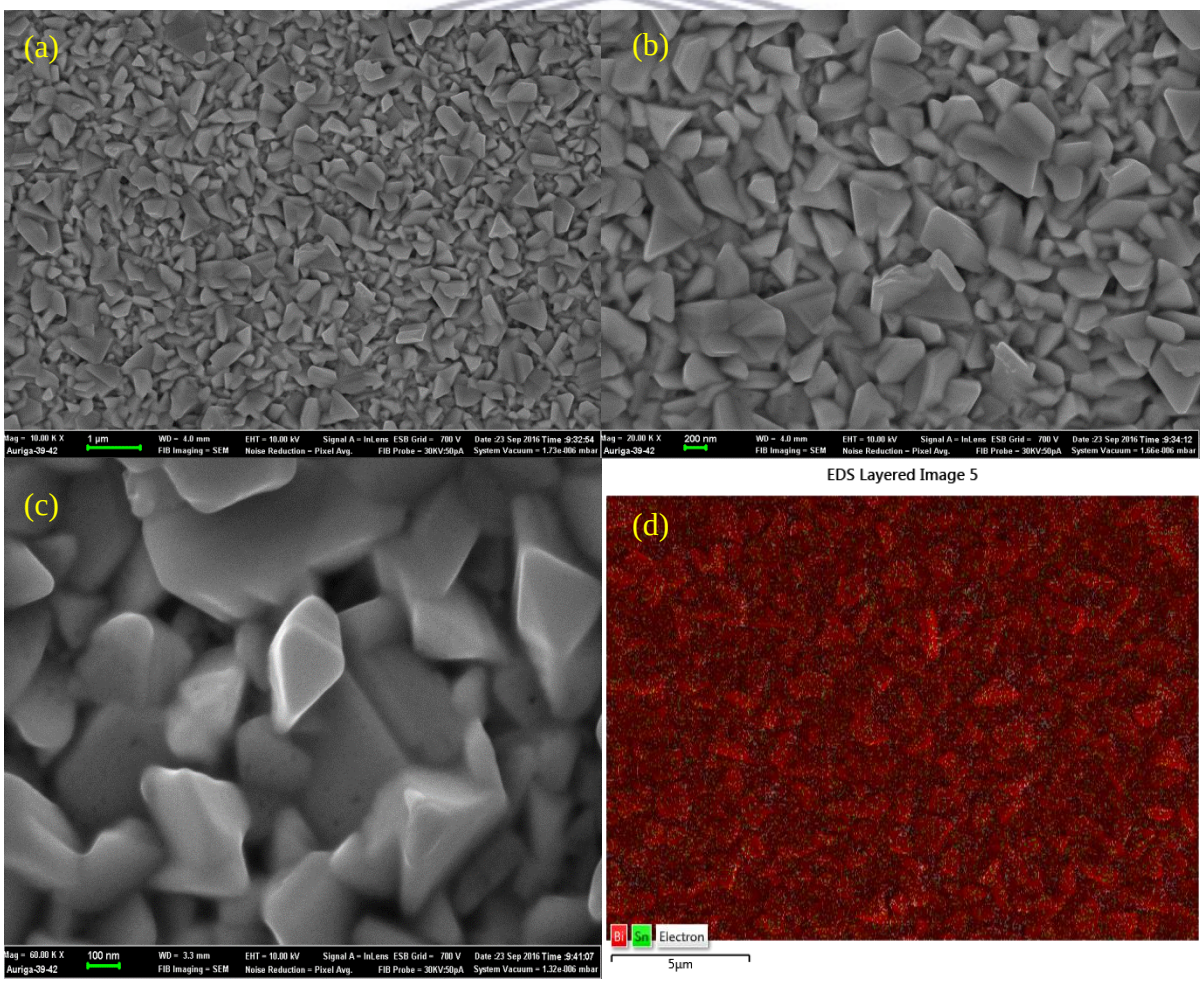

Figure 4.6: SEM images of Bi 300 cycle deposit (a, b, and c) and an EDS map (d).

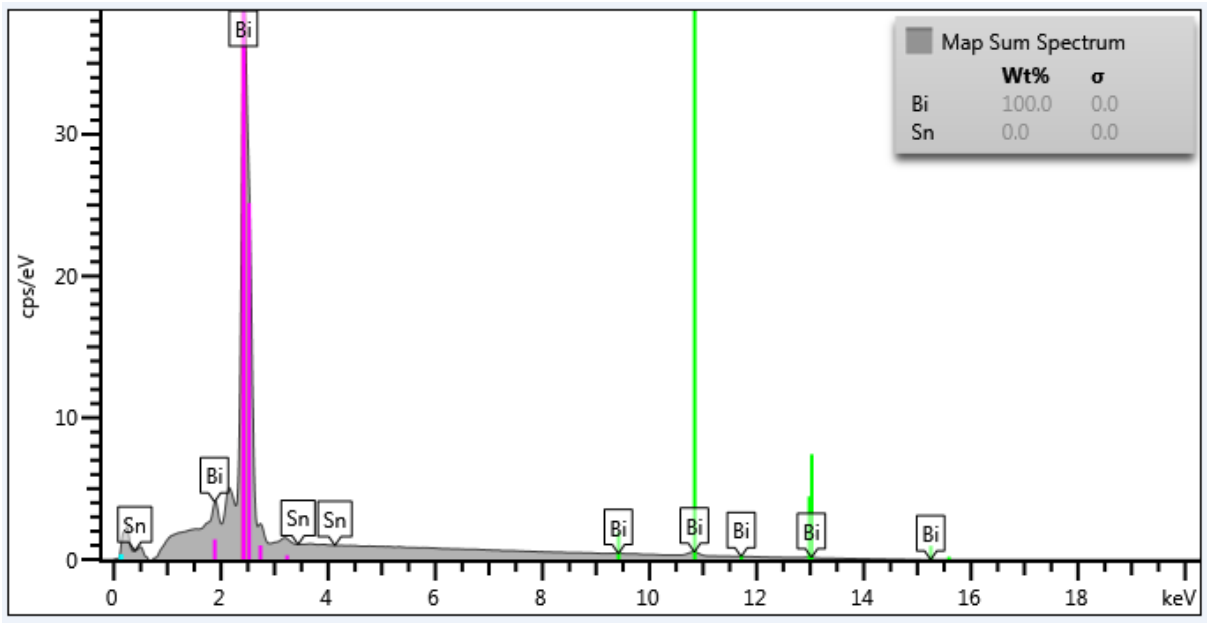

Figure 4.7: EDS spectrum of Bi deposit

4.3.2.2 SnBi thin films

The deposition cycle that was used to form a visible deposit of SnBi involved 5 steps: (i) flow Bi^{3+} solution at -50 mV for 10 s, (ii) Deposit Bi at -150 mV for 5 s, (iii) flow Sn^{2+} solution at -50 mV for 15 s, (iv) Deposit Sn at -425 mV for 5 s, (v) flow 0.1 M H_2SO_4 at -425 mV for 15 s. The current potential versus time plot for the first 3 deposition cycles is shown in Figure 4.8 below. The deposition and stripping of both Sn and Bi during the process is clearly visible from the changes in current observed. The Bi was found to deposit immediately as the potential was changed to -150 mV, a reductive peaks is observed at time 10 -15 s, when the potential is changed back to -50 mV between 15-30 s an oxidative current is observed which indicates the stripping of bulk Bi, this is a relatively small oxidation peak indicating that some of the Bi is left on the surface. At this point the Sn^{2+} solution is pumped slowly into the cell. The potential is then changed to -425 mV to deposit the Sn for 5 s; this is shown on the plot by the reducing current peak onset at 30 s. The 0.1 M H_2SO_4 blank solution is then pumped into the cell, where a small oxidation current was observed corresponding to the stripping of some of the Sn.

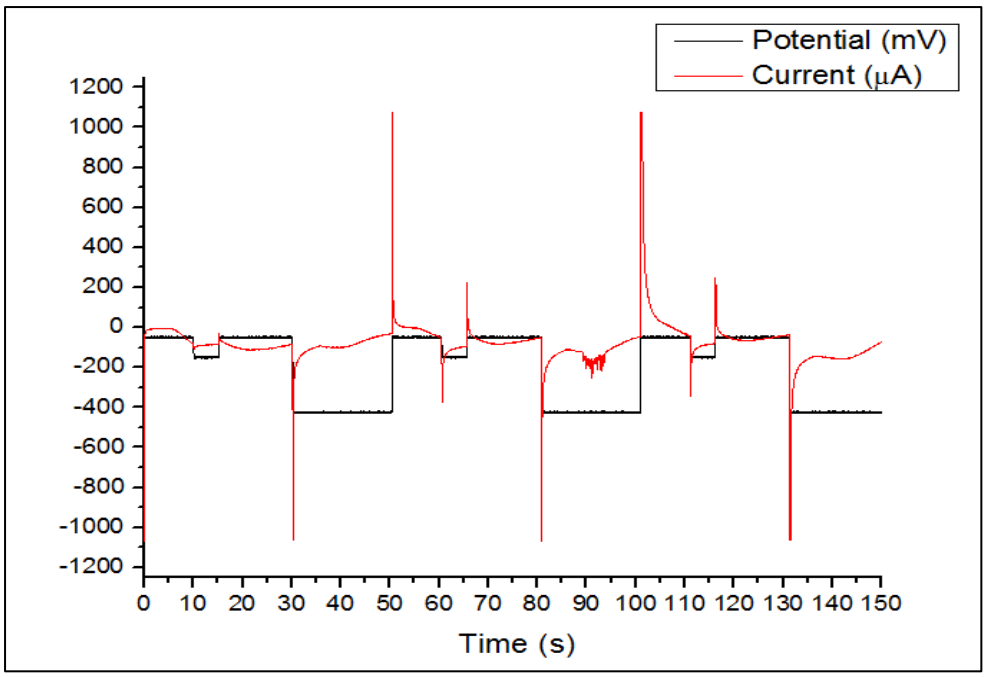

Figure 4.8: Current and potential profile for 3 E-ALD cycles for SnBi deposit.

The deposition cycle was repeated 300 times to form a thicker deposit as shown in Figure 4.9. The image shows nine vertical stripes that are darker at the ingress showing excess growth and more grey towards the egress. Stickney and co-workers explains that this occurs as a result of the fresh solution entering the ingress at a right angle causing excess growth of micrometre sized particles that scatter light and giving rise to the observed smudges (Czerniawski *et al*. 2016). It has also been previously reported that the roughness of the film varies depending on how close it is towards the inlet or outlet of the electrolyte *(Jayaraju et al*. 2012; Sheridan *et al*. 2012). This observation was confirmed and supported by the results obtained from elemental analysis done using electron probe microscope shown in Table 4.1. The Bi content was found to increase from ingress to egress, the highest being 40.9 At% at the inlet and lowest value of 16 At% at the egress. The Sn content was found to be relatively the same throughout the deposit with a highest value of 5.2 At% and the lowest of 4.2 At%. The relative ratio of SnBi is about 1:4 in this deposit. The difference in the deposition of Bi and Sn across the surface suggests that they could have different deposition mechanisms. The deposition of Bi appears to be diffusions controlled while that of Sn in more of a kinetic process. The deposition of Bi is favourable over that of Sn due to its lower deposition potential compared to that of Sn. As a result, formation of the film containing both elements is difficult because Sn will be most likely displaced by Bi due to its more negative deposition potential. A study on the effect of Sn concentration and current density on the

electrodeposition of SnBi from sulphuric acid based electroplating bath also reported the formation of deposits with very high Bi content than Sn (97 wt% of Bi and 2.23 wt% of Sn). (Heong *et al*. 2012) This is because of the Bi deposition potential is more noble than that of Sn. They were able to get over 90 wt% Sn by increasing the current density.

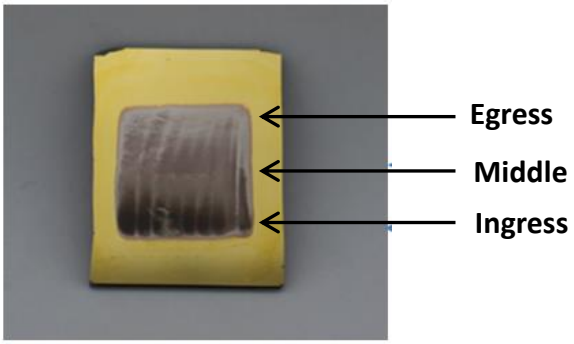

Figure 4.9: Image of a 300 cycle SnBi deposit on Au coated glass substrate

Table 4.1: EPMA data of a 300 cycle SnBi deposit on Au coated glass substrate

Bi (At%)		**Sn (At%)**		**SnBi Ratio**	
Left	**Right**	**Left**	**Right**	**Left**	**Right**
17.983	16.402	4.682	5.227	1:3.84	1:3.14
18.894	17.831	4.203	4.537	1:4.50	1:3.93
40.949	31.241	4.838	5.120	1:8.46	1:6.10

Figure 4.10 shows the scanning electron microscope images of the deposited SnBi film at different magnifications (Figure 4.10 a-c), the overlaid elemental map (Figure 4.10 d), and the elemental map of Sn and Bi (Figure 4.10 e-f). The surface of the film was found to be homogenous with well-defined structures. The surface particles have a rock like structure, and up close exhibited sheet like structures indicating stalked growth pattern. The elemental map showed that both elements are distributed evenly across the surface and that the particles are made up of both Sn and Bi, the map also showed that the lower lying structures are still Sn and Bi materials. The EDS spectrum shown in figure 4.11 further confirms that the film is made up of Sn and Bi, and that higher amounts of Bi are deposited than Sn. The thickness of the film was determined using FIB SEM imaging; figure 4.12 shows the cross section image

of the deposited film. Three distinct layers can be seen consisting of the glass and Au coating which makes up the substrate. The top layer is that of the film and it was found to be 111.5 nm at the highest point and 99.99 nm at the lowest point. The thickness slightly differs as expected due to the differences between ingress and egress deposition as explained above.

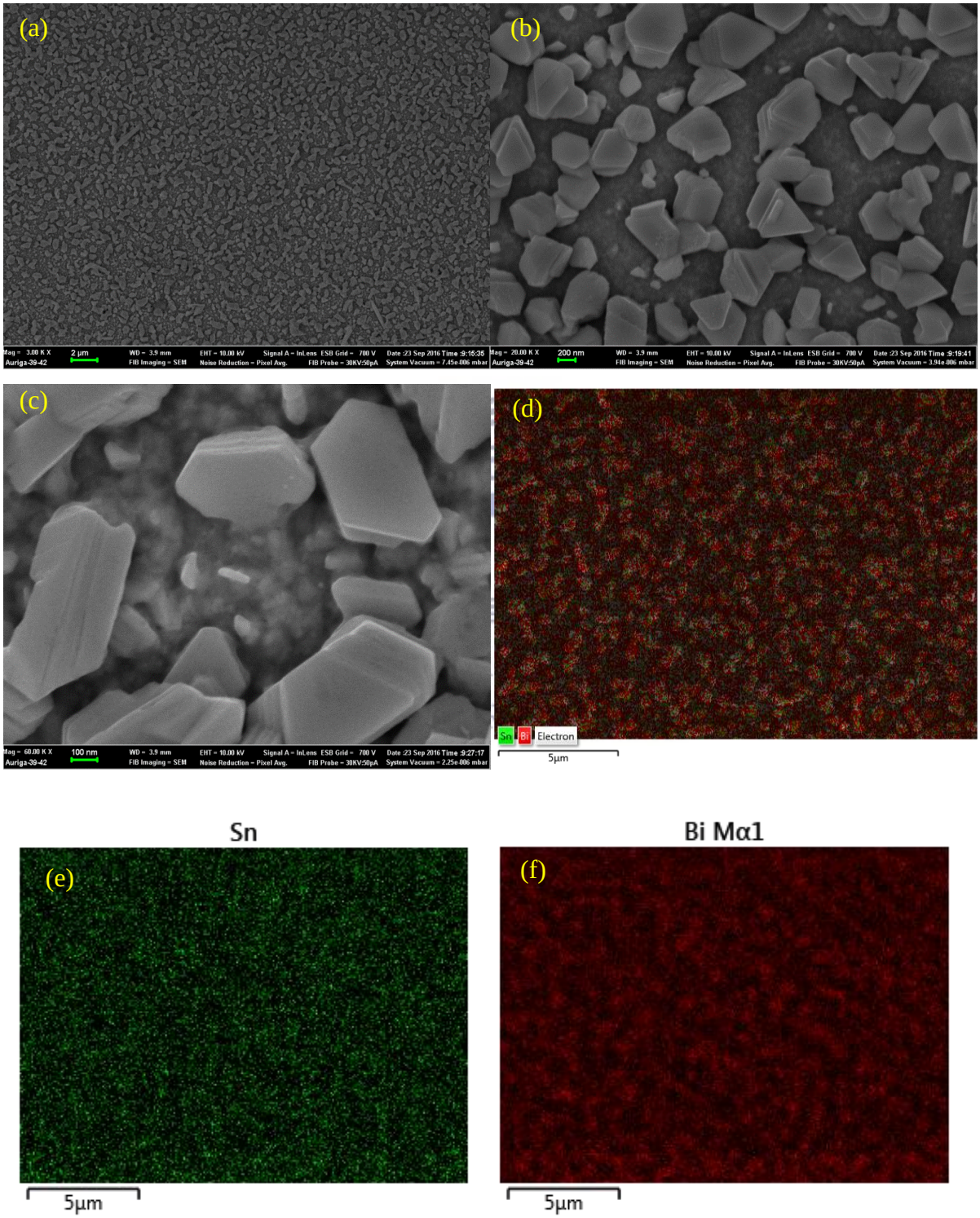

Figure 4.10: SEM images of SnBi 300 cycle deposit (a, b and c) and an EDS map (d, e and f)

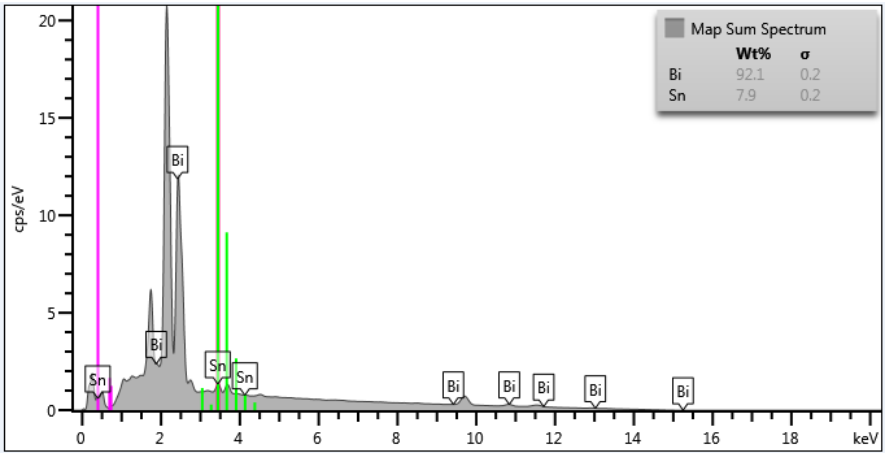

Figure 4.11: EDS spectrum of SnBi deposit

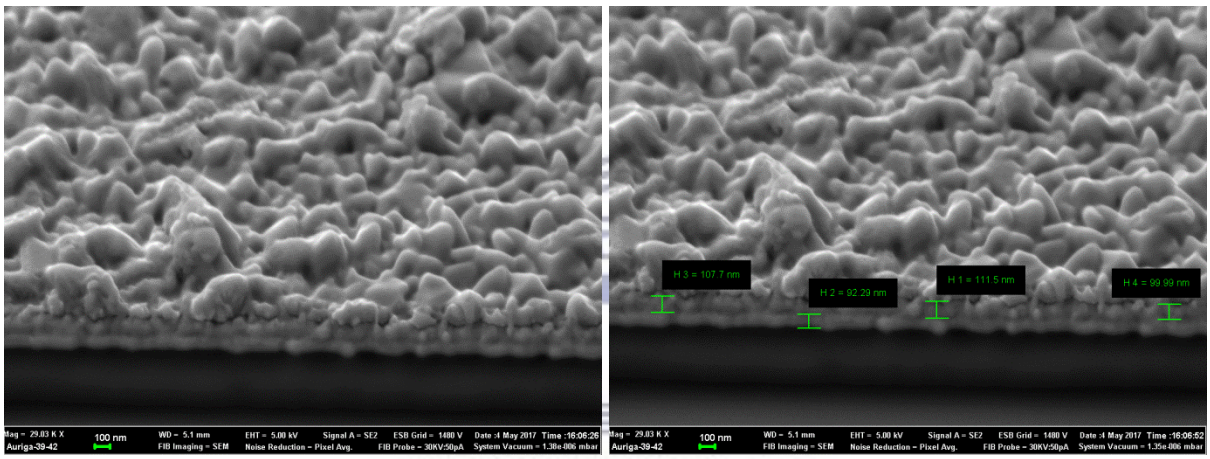

Figure 4.12: FIBSEM images of SnBi 300 cycle deposit

The XRD spectra in figure 4.13 a-c shows the pattern for Au coated glass substrate, Bi on Au coated glass deposit and the SnBi deposit. The XRD pattern for Au can be indexed to the cubic structure of Au (ICDD 00 004 0784), diffraction peaks at angles 38.4º, 44.5º, 81.3º corresponds to 111, 002, 311 and 222 reflections of Au. These diffraction peaks were also found to occur at the same diffraction angles on the SnBi deposit (Figure 4.13c). The diffraction peaks were assigned by matching the pattern with reference database using High score plus and PDF4 file 2015 as shown in figure 4.13c. The diffraction peaks were further identified from the reference patterns of rhombohedral (ICDD 00 027 0054) and monoclinic bismuth oxide (ICDD 00 014 0699), the orthorhombic (00 028 0440) and cubic (01 082 5413) gold tin intermetallic phases between the substrate and tin, orthorhombic (01 076 7575) bismuth tin, and the (00 016 0737) triclinic tin oxide.

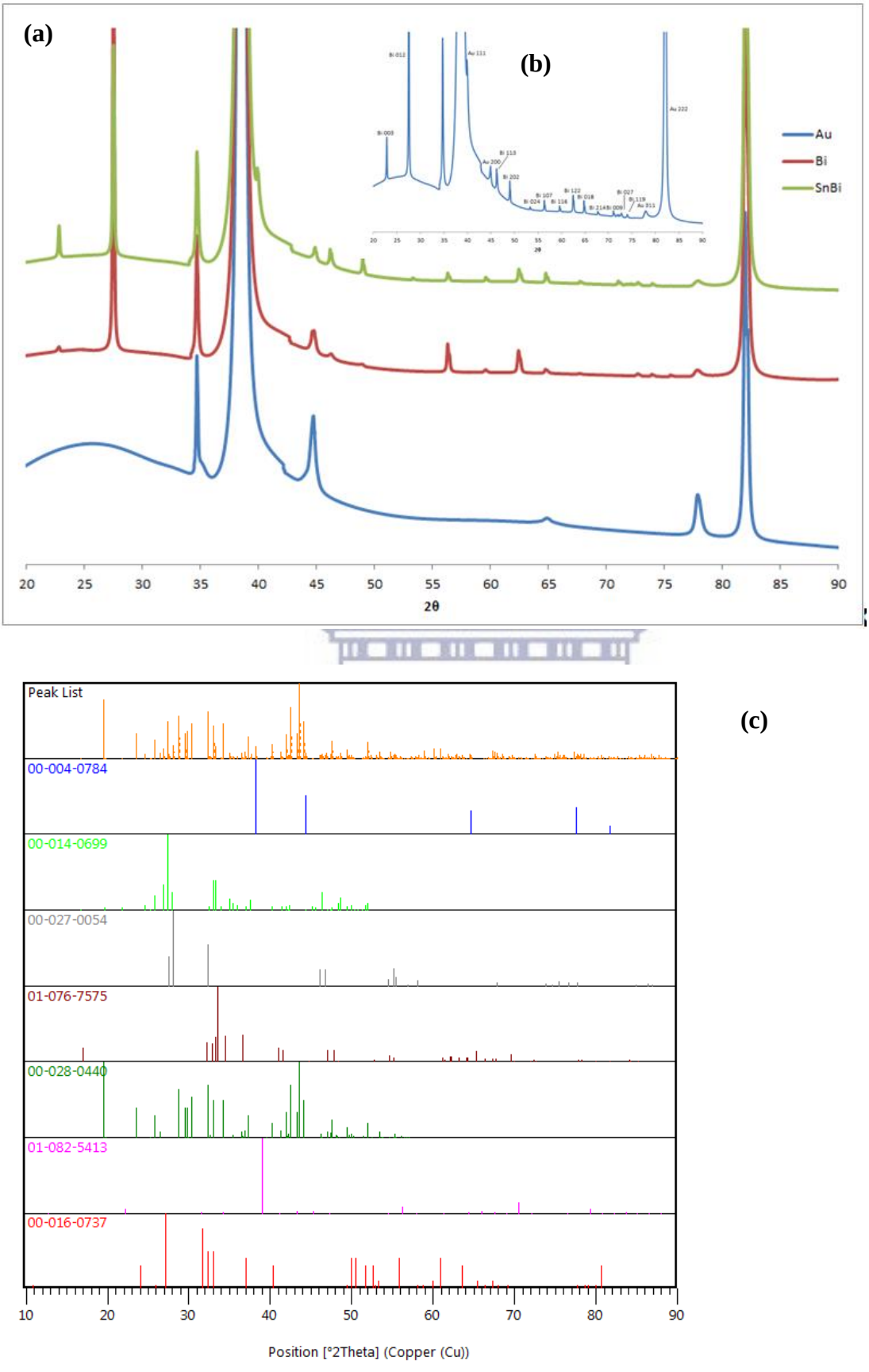

Figure 4.13: XRD pattern SnBi deposit (a), an insert of the assigned XRD spectra (b), and the matched XRD spectra.

These intermetallic gold tin phases were also observed when depositing SnBi from chlorometalate salts in deep eutectic solvents, Sn has been reported to form several (AuSn, $AuSn_2$, Au_3Sn) binary phases with gold (Vieira *et al*. 2017). The d-spacing of possible reflections of the prepared SnBi and Bi films based on Bi 012 were found to be 3.253 Å and 3.246 Å obtained using Rietveld refinement respectively. The corresponding crystallite size for SnBi and Bi films were found to be 1333.386 Å and 28806.440 Å. Bi particles alone have well defined particles as confirmed by SEM preferring rhombohedral and monoclinic bismuth oxide phases, where else the addition of Sn introduces other phases such intermetallic gold tin and tin bismuth that affected the crystallite size. The preferred orientation of Bi metal is (012) on the deposit. There was no shift in the Bi 012 peak or any other peaks observed on the overlaid spectra (Figure 12a). The SnBi and Bi only spectra were found to be exactly the same. This might be due to the low amount of Sn which is difficult to detect with XRD as discussed by Tsai and Hu[30]. Sn was only found to occur as the intermetallic phase with Au as well as SnBi phase. A study conducted by Tsai and Hu (2009) on the composition of SnBi deposited on copper plates reported that the diffraction peaks of β-Sn are not visible when the concentration of Sn is equal to or less than 10 wt% on SnBi deposit. They further suggested that Sn forms tiny particulates that are homogeneously dispersed within Bi matrix; these Sn particulates are hard to detect using XRD. β-Sn was also found to be visible on the XRD spectra when Sn content was 70 wt% or greater by depositing Sn and Bi from methane sulfonic acid bath with hydroquinone and gelatin as additives (Goh *et al*. 2013).

4.4 Conclusion

Thin films of SnBi on Au coated glass, and Bi Au coated glass were prepared using electrochemical atomic layer deposition. These thin films were formed by an indirect underpotential deposition method and surface limited replacement reaction respectively. SnBi thin films were found to contain SnBi ratio of 1:3 while the Bi thin films contained 100% Bi. Sn and Bi were found to be evenly distributed on the surface with well-defined structures. SnBi film contained Bi, AuSn, SnBi intermetallic phases. The XRD was unable to detect the presence of Sn due to low Sn content.

4.5 References

Banga, D, Jarayaju, N, Sheridan, L, Kim, Y-G, Perdue, B, Zhang, X, Zhang, Q, Stickney, J (2012) Electrodeposition of $CuInSe_2$ (CIS) via electrochemical atomic layer deposition (E-ALD). *Langmuir* **28**, 3024-3031.

Banga, D, Kim, Y-G, Stickney, J (2011) PbSe⁄ PbTe superlattice formation via E-ALD. *Journal of the Electrochemical Society* **158**, D99-D106.

Chen, Y, Wang, L, Pradel, A, Merlen, A, Ribes, M, Record, M-C (2015) Underpotential deposition of selenium and antimony on gold. *Journal of Solid State Electrochemistry* **19**, 2399-2411.

Czerniawski, JM, Perdue, BR, Stickney, JL (2016) Potential pulse atomic layer deposition of Cu2Se. *Chemistry of Materials* **28**, 583-591.

Gichuhi, A, Boone, BE, Shannon, C (2002) Resonance Raman scattering and scanning tunneling spectroscopy of CdS thin films grown by electrochemical atomic layer epitaxy - thickness dependent phonon and electronic properties. *Journal of Electroanalytical Chemistry* **522**, 21-25.

Goh, Y, Haseeb, A, Sabri, MFM (2013a) Effects of hydroquinone and gelatin on the electrodeposition of Sn–Bi low temperature Pb-free solder. *Electrochimica Acta* **90**, 265-273.

Goh, Y, Lee, SF, Haseeb, A (2013b) Formation of Sn-Bi solder alloys by sequential electrodeposition and reflow. *Journal of Materials Science-Materials in Electronics* **24**, 2052-2057.

Gregory, BW, Stickney, JL (1991) Electrochemical atomic layer epitaxy (ECALE). *Journal of Electroanalytical Chemistry* **300**, 543-561.

Heong, CY, Haseeb, A, Goh, YX, Fang, LS, Ieee (2012) Effects of Sn concentration and current density on Sn-Bi electrodeposition in additive free plating bath. *2012 4th Asia Symposium on Quality Electronic Design (Asqed)* 286-290.

Hu, C-C, Tsai, Y-D, Lin, C-C, Lee, G-L, Chen, S-W, Lee, T-C, Wen, T-C (2009) Anomalous growth of whisker-like bismuth–tin extrusions from tin-enriched tin–Bi deposits. *Journal of Alloys and Compounds* **472**, 121-126.

Jayaraju, N, Vairavapandian, D, Kim, YG, Banga, D, Stickney, JL (2012) Electrochemical atomic layer deposition (E-ALD) of Pt nanofilms using SLRR cycles. *Journal of the Electrochemical Society* **159**, D616-D622.

Jeffrey, CA, Harrington, DA, Morin, S (2002) In situ scanning tunneling microscopy of bismuth electrodeposition on Au (111) surfaces. *Surface Science* **512**, L367-L372.

Katayama, J, Okuno, K, Izaki, M (1996) solderability of bismuth/tin double layer deposits. *Metal Finishing* **1**, 12-19.

Ledina, M, Liang, X, Kim, Y-G, Jung, J, Perdue, B, Tsang, C, Soriaga, M, Stickney, JL (2015) (Invited) Investigations into the formation of germanene using electrochemical atomic layer deposition (E-ALD). *ECS Transactions* **66**, 129-140.

Lee, SF, Goh, YX, Haseeb, A, Ieee (2012) Effects of stacking sequence of electrodeposited sn and bi layers on reflowed Sn-Bi solder alloys. *2012 35th IEEE/Cpmt International Electronic Manufacturing Technology Symposium (Iemt)* 6.

Liang, XH, Zhang, QH, Lay, MD, Stickney, JL (2011) Growth of Ge nanofilms using electrochemical atomic layer deposition, with a "bait and switch" surface-limited reaction. *Journal of the American Chemical Society* **133**, 8199-8204.

Mathe, MK, Cox, SM, Flowers, BH, Vaidyanathan, R, Pham, L, Srisook, N, Happek, U, Stickney, JL (2004) Deposition of CdSe by EC-ALE. *Journal of Crystal Growth* **271**, 55-64.

Meier, LA, Garcia, SG, Salinas, DR (2012) New insights into the Sn underpotential deposition on Au(100). *Surface and Interface Analysis* **44**, 37-40.

Okamoto, N, Fujii, Y, Kurihara, H, Kondo, K (2009) Effects of microstructure of deposited sn films and orientation index of cu foils on sn whisker formation using substitutionally-deposited sn films. *Materials Transactions* **50**, 2570-2577.

Sandnes, E, Williams, ME, Vaudin, MD, Stafford, GR (2008) Equi-axed grain formation in electrodeposited Sn-Bi. *Journal of Electronic Materials* **37**, 490-497.

Sheridan, LB, Czerwiniski, J, Jayaraju, N, Gebregziabiher, DK, Stickney, JL, Robinson, DB, Soriaga, MP (2012) Electrochemical atomic layer deposition (E-ALD) of palladium nanofilms by surface limited redox replacement (SLRR), with EDTA complexation. *Electrocatalysis* **3**, 96-107.

Stafford, GR, Bertocci, U (2006) In situ stress and nanogravimetric measurements during underpotential deposition of bismuth on (111)-textured Au. *Journal of Physical Chemistry B* **110**, 15493-15498.

Tamura, K, Ocko, B, Wang, J, Adžić, R (2002) Structure of active adlayers on bimetallic surfaces: oxygen reduction on Au (111) with Bi adlayers. *The Journal of Physical Chemistry B* **106**, 3896-3901.

Tamura, K, Wang, J, Adžic, R, Ocko, B (2004) Kinetics of monolayer Bi electrodeposition on Au (111): Surface X-ray scattering and current transients. *The Journal of Physical Chemistry B* **108**, 1992-1998.

Thambidurai, C, Gebregziabiher, DK, Liang, X, Zhang, Q, Ivanova, V, Haumesser, P-H, Stickney, JL (2010) E-ALD of Cu nanofilms on Ru/Ta wafers using surface limited redox replacement. *Journal of the Electrochemical Society* **157**, D466-D471.

Tsai, Y-D, Hu, C-C (2009a) Composition control of lead-free Sn–Bi deposits using experimental strategies. *Journal of the Electrochemical Society* **156**, D58-D63.

Tsai, YD, Hu, CC (2009b) Composition Control of Sn-Bi Deposits: Interactive effects of citric acid, ethylenediaminetetraacetic acid, and poly(ethylene glycol). *Journal of the Electrochemical Society* **156**, D490-D496.

Tsai, YD, Hu, CC (2011) Composition and microstructure control of tin-bismuth alloys in the pulse plating process. *Journal of the Electrochemical Society* **158**, D482-D489.

Venkatasamy, V, Mathe, MK, Cox, SM, Happek, U, Stickney, JL (2006) Optimization studies of HgSe thin film deposition by electrochemical atomic layer epitaxy (EC-ALE). *Electrochimica Acta* **51**, 4347-4351.

Vieira, L, Burt, J, Richardson, PW, Schloffer, D, Fuchs, D, Moser, A, Bartlett, PN, Reid, G, Gollas, B (2017) Tin, Bismuth, and Tin–Bismuth Alloy Electrodeposition from Chlorometalate Salts in Deep Eutectic Solvents. *Chemistry Open.*

Zhang, JQ, Yang, JY, Liu, M, Li, G, Li, WX, Gao, S, Luo, YB (2014) Fabrication of CdTe Quantum Dots Sensitized TiO2 Nanorod-Array-Film Photoanodes via the Route of Electrochemical Atomic Layer Deposition. *Journal of the Electrochemical Society* **161**, D55-D58.

Zhu, W, Yang, JY, Zhou, D, Xiao, CJ, Duan, XK (2008) Development of growth cycle for antimony telluride film on Au(111) disk by electrochemical atomic layer epitaxy. *Electrochimica Acta* **53**, 3579-3586.

CHAPTER 5

5 The Effect of Potential and Concentration on Underpotentially Deposited SnBi on Cu Foil and Applications in Na-ion Batteries.

Bimetallic material of SnBi and Bi were deposited on Cu foil substrate using electrochemical atomic layer deposition (E-ALD). The deposition of Sn and Bi were studied using cyclic voltammetry (CV) and linear sweep voltammetry (LSV). The deposition potential of Bi was varied along the UPD region, and the concentration of Sn was varied on the bimetallic material. The materials were characterised using SEM/EDS for morphology and elemental distribution, FIBSEM for thickness, XRD for crystallinity, and ICPMS for composition analysis. It was found that the Bi deposited at different potentials were structurally different. The deposits were crystalline, SnBi materials contained Sn, Bi and other phases of Cu and Sn. Bi was found concentrated on the surface while Sn was distributed evenly across the film. The SnBi electrodes were tested for anode materials for Na-ion batteries using galvanostatic cycling, CV, and EIS.

5.1 Introduction

The development of thin film materials in today's booming technology is of critical importance. Thin films have important applications in electronic components, photonics, sensors as well as in energy conversion and storage (Sheridan *et al.* 2013). Alloy materials of Sn and Bi are important components in interconnecting and packaging electronic components (Hu *et al.* 2009). The importance of using Bi as Pb replacement in Sn-Pb alloys came about as a need for environmentally friendly materials and to reduce to use of toxic lead based materials. Alloys of Sn and Bi have recently found renewed interest in the use as anode materials for rechargeable sodium ion batteries (Pan *et al.* 2013). This is due to their high theoretical capacity where Bi has a capacity of 386 mAh/g and Sn has 847 mAh/g (Dahbi *et al.* 2014; Li *et al.* 2015). Their use is limited by the large volumetric expansion of the electrode during cycling causing capacity loss and material development research is focusing on this area (Stevens and Dahn 2000; Kubota and Komaba 2015; Cui *et al.* 2017).

Methods to prepare alloys materials for electronic components include vacuum evaporation, screen printing, electroplating, sonochemistry, hydrothermal synthesis, and solid state method (Tsai and Hu 2009a; Gao *et al.* 2014; Su *et al.* 2015; Zhang *et al.* 2016). Electrodeposition is

the most attractive method to prepare alloy materials because it is versatile, simple and cheap (Gao *et al.* 2014). SnBi materials on various copper substrates have been previously prepared using electrodeposition methods. SnBi alloys were electrodeposited from a bath using pulse deposition into planar Cu sheets (Sandnes *et al.* 2008), bath electrodeposition with complex agents into Cu/Ni plates (Tsai and Hu 2011), electroless deposition into Cu foil (Okamoto *et al.* 2009), and electrodeposition from a deep eutectic solvent into Cu foil (Gao *et al.* 2014). The above mentioned methods use complex agents and additives including methane sulfonic acid (MSA), ethylenediaminetetraacetic acid (EDTA), polyethylene glycol (PEG), gelatin, choline chloride ethylene glycol, and H_3BO_3 respectively. Complex agents and additives supress the formation of dendrite structure, and they reduce the difference in potentials of the elements deposited.

The process of SnBi deposition is an interesting chemistry. Bi standard reduction potential (equation 24) is about 0.45V more positive than that of Sn (equation 25). This potential difference allow for the codeposition of SnBi forming a wide range of alloys, and also the deposition can be selectively turned on and off the deposition of Sn (Sandnes *et al.* 2008).

$$Bi^{3+} + 3e^{-} \rightarrow Bi \quad (+0.317V) \qquad (24)$$

$$Sn^{2+} + 2e^{-} \rightarrow Sn \quad (-0.137V) \qquad (25)$$

Electrochemical atomic layer deposition (E-ALD) is an attractive process to prepare thin film materials. This process was derived from atomic layer deposition and electrochemical epitaxy developed by Gregory and Stickney (Gregory and Stickney 1991). It involves layer by layer growth of atomic layers of elements in a cycle to form a compound using surface limited redox reactions (SLRR) and underpotential deposition (UPD). UPD refers to the deposition of atomic layer of an element on another element as a potential under that required to deposit the element on itself. E-ALD has been used to make compounds of II-IV elements including HgSe (Venkatasamy *et al.* 2006), CdTe (Zhang *et al.* 2014), CdS (Gichuhi *et al.* 2002), PdSe, PbTe (Banga *et al.* 2011), $CuInSe_2$ (Banga *et al.* 2012), $Ge_xSb_yTe_z$ (Liang *et al.* 2011), In_2Se_3 (Czerniawski and Stickney 2016), Cu_2Se (Czerniawski *et al.* 2016), Bi_2Te_3 (Zhu *et al.* 2005), Pt, Pd based electro catalysts including Pd nanofilms (Sheridan *et al.* 2012), Pt nanofilms (Jayaraju *et al.* 2012), Pt-Ru (Mkwizu *et al.* 2010; Jayaraju *et al.* 2014).

This study demonstrates the preparation of SnBi thin films using E-ALD technique without the use of any additives. Also, we report their use as binder free electrode anode materials for

Na ion batteries. Sn-Bi alloys were deposited on Cu foil substrates from aqueous solutions of $SnCl_2$ and $BiCl_3$ in HCl electrolyte. Cyclic voltammetry (CV) and linear sweep voltammetry (LSV) were used to study the oxidation and reduction of each precursor solution for the development of the deposition process. The morphological features, thickness and crystal phases of the prepared SnBi films were investigated using field emission scanning electron microscope (FE-SEM) for morphology, focused ion beam scanning electron microscope (FIB-SEM), and X-Ray diffraction (XRD). Energy dispersive X-Ray spectroscopy (EDS) was used for surface elemental mapping. Further compositional analysis was done using inductively coupled plasma mass spectroscopy (ICPMS). The electrochemical performance for Na-ion batteries was evaluated using galvanostatic cycling, CV, and electrochemical impedance spectroscopy (EIS).

5.2 Experimental

5.2.1 Chemicals and Solutions

The chemical solutions used were 1 mM $SnCl_2$ (Sigma Aldrich), 1 mM $BiCl_3$ (Sigma Aldrich), and 0.5 M HCl (32%, Associated Chemical Enterprise) as the electrolyte. A range of 0.1 mM, 0.2 mM, 0.4 mM, 0.6 mM, 0.8 mM $SnCl_2$ solution in 0.1 M HCl were used, as well as 0.2 mM $BiCl_3$ solution. All solutions were prepared in electrolyte solution. ACS reagent grade chemicals and high purity ($\leq$ 1 µS/cm) deionised water were used. The pH of the solutions was 2.3.

5.2.2 Substrate treatment

Cu foil (99%, 9 µm, Gelon) was used as a substrate. The foils were cleaned with dilute nitric acid (5 wt %), rinsed with deionised water, dipped in acetone, and air dried.

5.2.3 E-ALD deposition

Electrodeposition of SnBi on Cu foil was done as reported in section 4.2.3.

5.2.4 Characterisation

The following characterisation methods were carried out in addition to the reported procedure in section 4.2.4. Cross section scanning electron microscope was done fracturing the sample in LN2 and placed the fractured edge facing up on the stub. The samples are viewed with a ZEISS Auriga FIB-SEM using martSEN software version V05.04.00. The EDS was done using Oxford X-Men detector and Aztec software. Quantitative analysis was done using

Thermo Scientific iCAP Q ICP-MS equipped with Qtegra Intelligent Scientific Data Solution (ISDS) software.

5.2.5 Electrochemical battery tests

The SnBi on Cu foil materials were tested as anode for Na ion battery application using in 2032-type coin cells. The cell components included Na disc as counter electrode, and 1 M $NaClO_4$ in ethylene carbonate-diethylene carbonate (EC: DEC, 50:50 vol%) solution as electrolytes, and a glass microfiber Whatman GF/F used as a separator. The coin cells were assembled in an Ar filled glove box (MBraun MB 150B-G, Germany, maintaining the concentrations of O_2 and H_2O< 1 ppm). The cells were characterized by galvanostatic cycling (GC), cyclic voltammetry (CV) and electrochemical impedance spectroscopy (EIS). The GC were done using MACCOR series 4000 tester. CV and EIS were done using a Bio-Logic VMP3 potentiostat / galvanostat controlled by EC-Lab v10.40 software at the scan rate of 0.1 mV s^{-1} with the potential range of 0.005–3.0 V. The EIS plots were recorded by applying 10 mV amplitude over the frequency range from 100 kHz to 10 mHz at room temperature and the data was analysed by using Z-view software (version 2.2, Scribner Assoc., Inc., USA).

5.3 Results and Discussion

5.3.1 Electrochemical studies: cyclic voltammetry

Figure 5.1 (insert) shows a cyclic voltammogram (CV) for a Cu foil substrate in 0.1 M HCl solution. All the scans were started positively and scanned towards the negative limit and then reversed. The CV shows that the initial open circuit potential of -0.05 V, a reduction peak of Cu oxides at -0.1 V was found, and hydrogen evolution occurred beyond -0.5 V. Stickney and Ehlers (Stickney and Ehlers 1989) found a similar outcome from a study of Cu (111) electrodes in aqueous HCl solution. They concluded that the copper oxide layer dissolves when the substrate is immersed in solution, and then replaced by a copper chloride monolayer, resulting in a change in the initial potential from -0.05 V to about -0.12 V. The CV of 0.1 M $BiCl_3$ in 0.5 M HCl is also shown in Figure 1; the CV has two reduction peaks at -0.1 V and -0.2 V. The peak at -0.1 V is a characteristic of Cu substrate, the same peak if found in the Cu substrate CV. The peak at -0.2 V is that of Bi underpotential deposition (UPD), with an onset UPD potential of -0.15 V, and beyond -0.5 V hydrogen evolution starts. The UPD stripping peak is not visible indicating that the oxidation of Bi does not occur, this is caused by the dissolution of Cu occurring first and depolarizing the electrode.

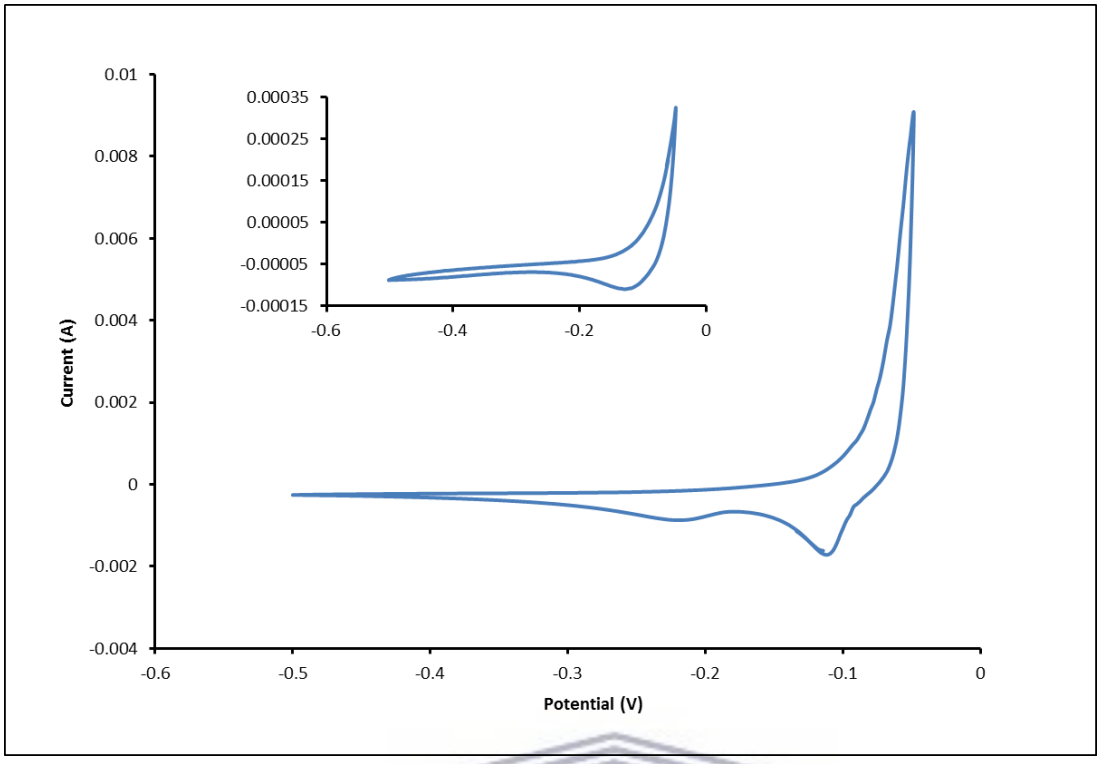

Figure 5.1: Cyclic voltammogram for Cu foil electrode in 1 mM $BiCl_3$ in 0.5 M HCl vs Ag/AgCl. Insert: of Cu foil electrode in 0.1 M HCl, at a scan rate of 10 mV/s.

The same phenomenon was reported using the deposition of Sb on Cu in chloride solutions (Ward and Stickney 2001). Figure 5.2 shows the CV of 0.1 M $SnCl_2$ in 0.1M HCl, four reduction peaks at -0.1 V, -0.3 V, -0.43 V, -0.51 V were found, and these were due to Cu substrate, and the preceding three from Sn species. The peak at -0.43 V was assigned as the Sn UPD, the other two peaks indicate bulk alloy formation. Two oxidation peaks of Sn species were found at -0.48 V and -0.35 V corresponding to bulk Sn stripping and UPD Sn stripping, and hydrogen evolution occurred beyond -0.85 V. A study of Sn deposition on Au (100) reported similar observation that the deposition of Sn occurs in three stages involving the UPD deposition, surface alloy deposition and bulk alloy deposition (Fonticelli *et al.* 2004).

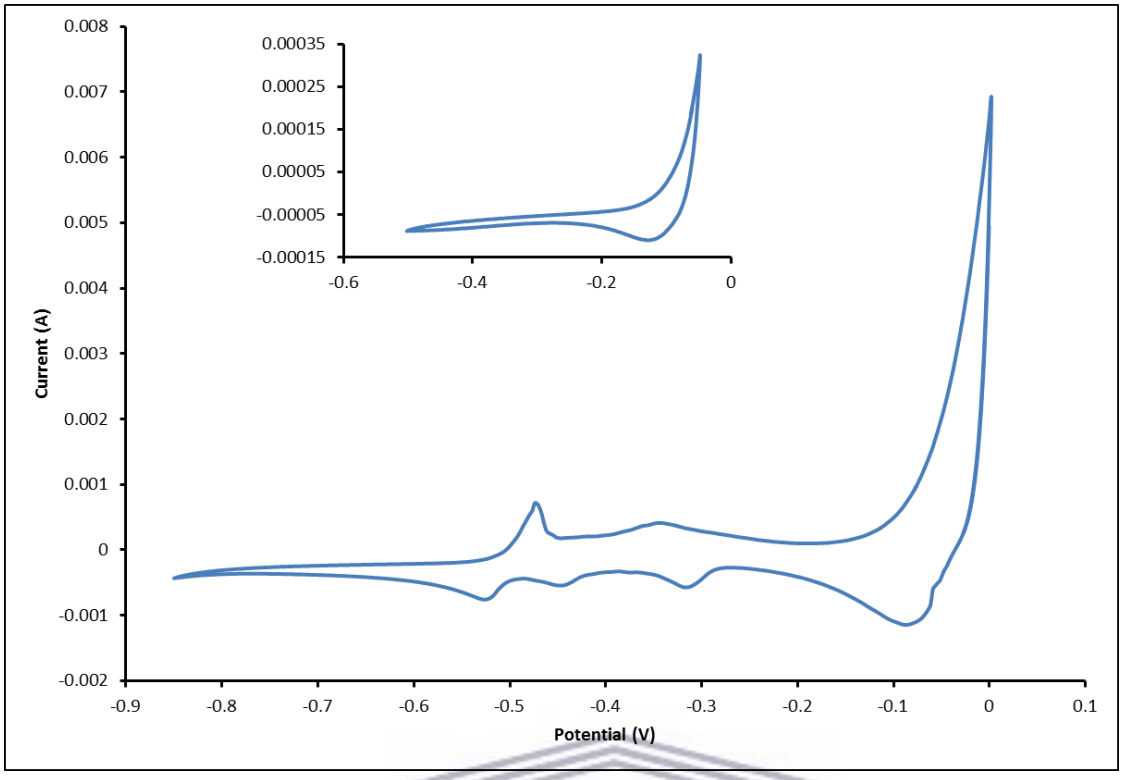

Figure 5.2: Cyclic voltammogram of Cu foil electrode in 1 mM $SnCl_2$ in 0.1 M HCl vs Ag/AgCl. Insert: Cu foil electrode in 0.1 M HCl, at a scan rate of 10 mV/s

5.3.2 Electrodeposition studies

5.3.2.1 Bi thin films

Bi thin films were made by the deposition of $BiCl_3$ at UPD potential using a cycle; the cycle was repeated up to 300 times to grow the film. The potential and point number plot for the first ten cycles is shown in Figure 5.3. The cycle used was made up of the following steps: (i) Pump $BiCl_3$ for 15 s, (ii) Deposit $BiCl_3$ at -200 mV for 10 s (no solution pump), (iii) Rinse with 0.1 M HCl at -200 mV for 5 s, (iv) Rinse with 0.1 M HCl at OCP for 5 s. Figure 5.4 shows the morphology of the formed material where very thin hexagonal structures were obtained, no ordered packing was observed. The formed films was found to contain bismuth as shown on the spectra in Figure 5.5, and were evenly distributed on the surface as shown on the EDS map.

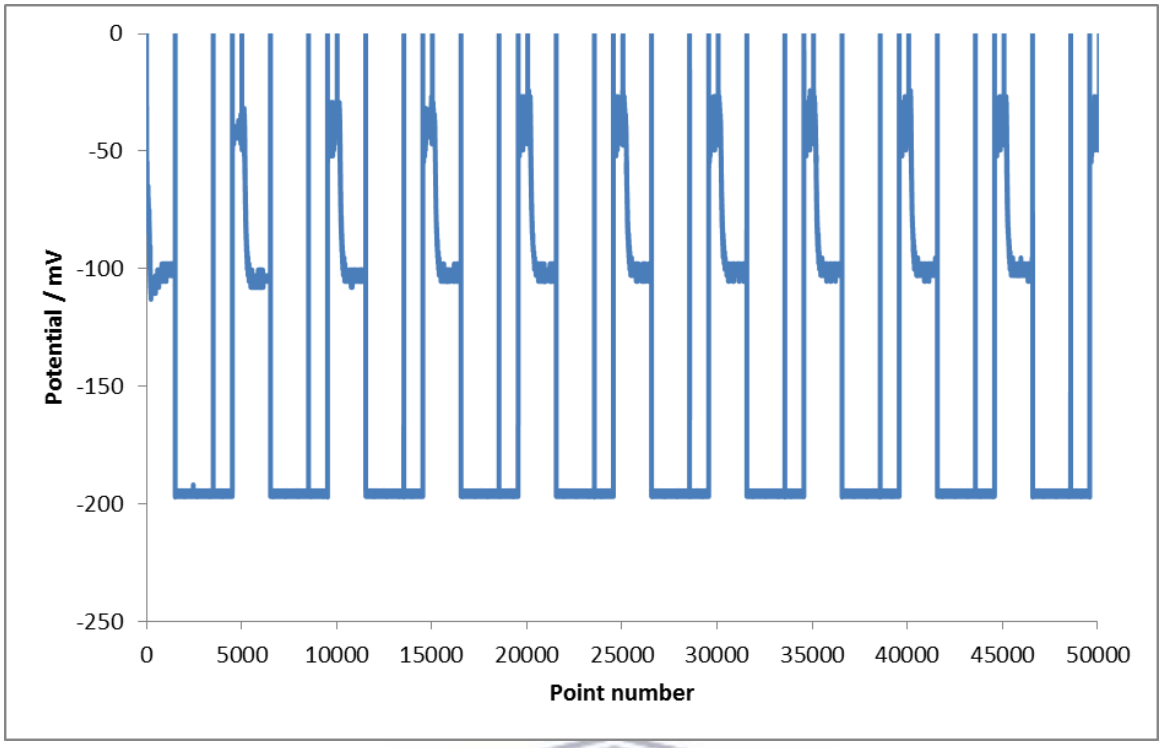

Figure 5.3: E-ALD cycle of Bi deposition on Cu foil.

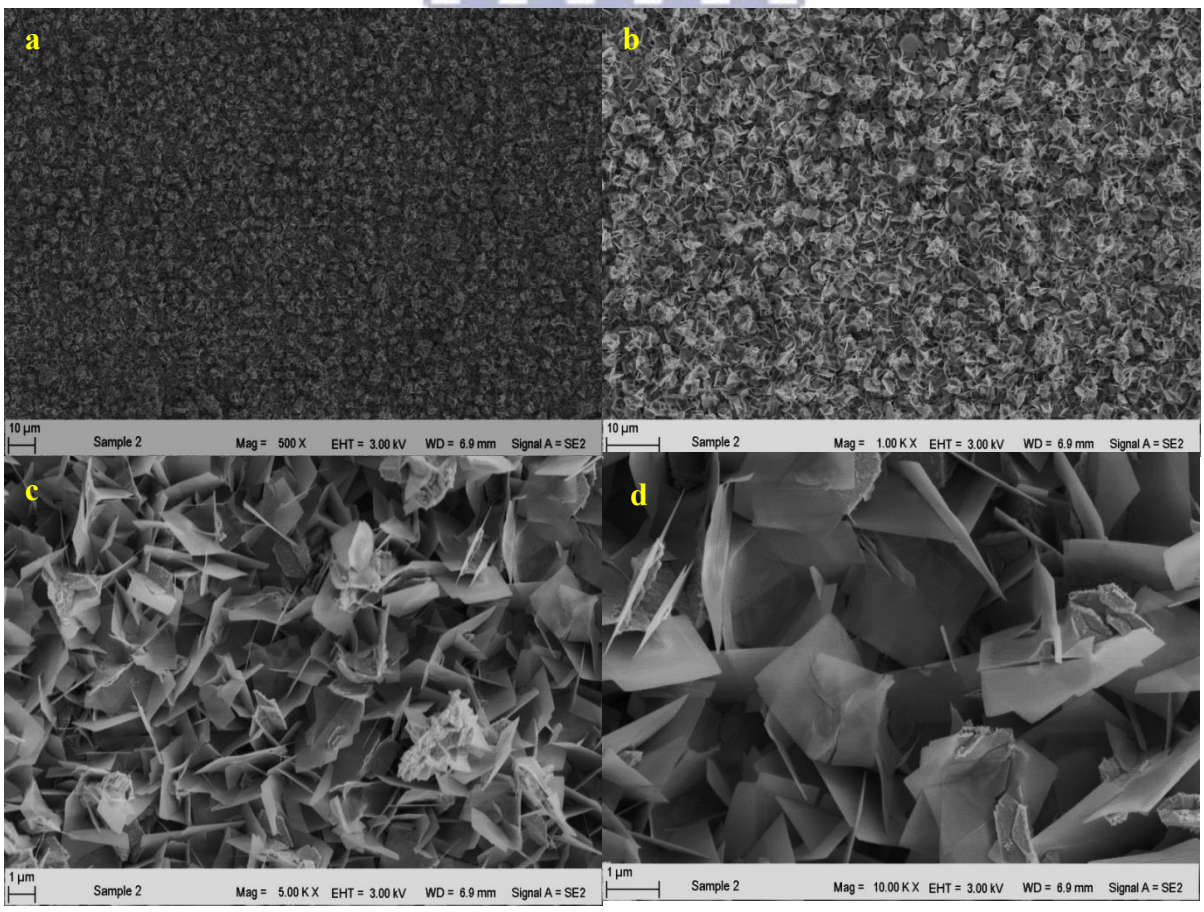

Figure 5.4: Electrodeposited $BiCl_3$ for 300 cycles

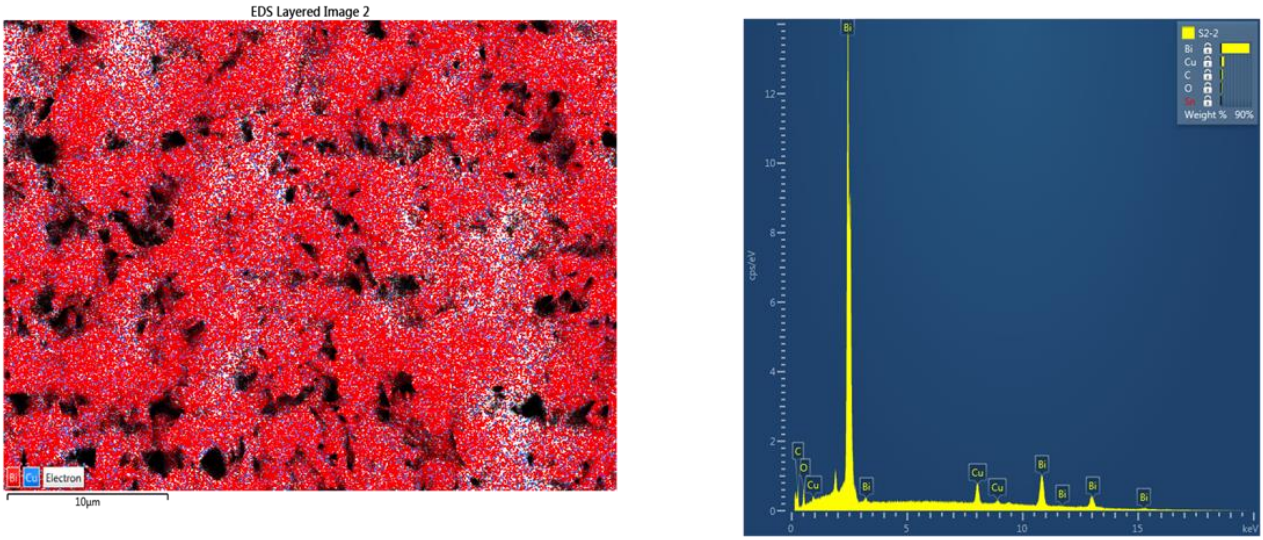

Figure 5.5: EDS map and spectra of $BiCl_2$ on Cu foil deposit.

The crystal features of the prepared Bi material were investigated using X-ray diffraction. The XRD spectrum in figure 5.6 shows the pattern for Cu foil substrate, Bi on Cu foil deposit with the assigned peaks and the matched spectra is shown in Figure 5.6. The XRD pattern for Cu can be indexed to the cubic structure of Cu (ICDD 00-004-0836), diffraction peaks at angles 38.9, 43.6, 50.2, 66.0, 74.5 corresponds to 111, 200, and 220 reflections of Cu. These diffraction peaks were also found to occur at the same diffraction angles on the Bi deposit (Figure 4.6 a and b). The diffraction peaks were assigned by matching the pattern with reference database using High score plus and PDF4 file 2015 as shown in figure 8. The diffraction peaks were further identified from the reference patterns of monoclinic copper oxide (ICDD 01-089-5899), hexagonal bismuth (ICDD 01-070-5673) and monoclinic bismuth oxide (ICDD 01-079-6670, ICDD 01-079-6671, ICDD 01-079-6672, ICDD 01-079-6673, ICDD 00-014-0699).

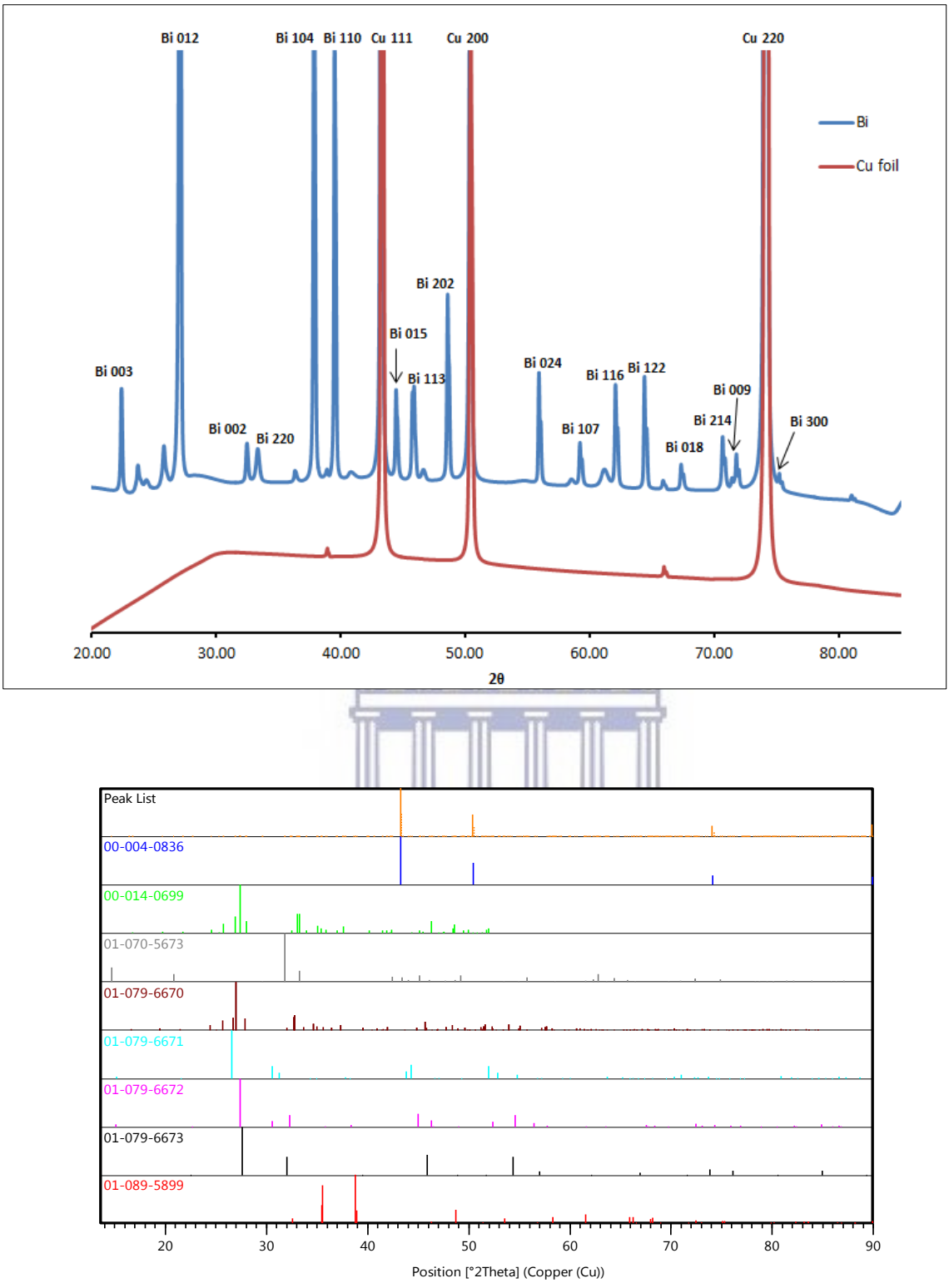

Figure 5.6: (a): XRD spectra of Bi thin films, and (b) XRD spectra of Bi thin films.

The thickness of the Bi material was determined using FIB SEM shown on the images in Figure 5.7 (a-b) at two different sites. A Bi material made of 300 cycles was used. The images show that the surface of the Cu foil is not uniform or flat, and that the material grows into the grooves found on the surface. As a result of this, the thickness of the deposited Bi was found to vary along the film between 3-5 µm. The elemental map in Figure 5.7 (c-d) shows the cross section of the material, and the presence of Cu substrate and Bi on the surface was observed.

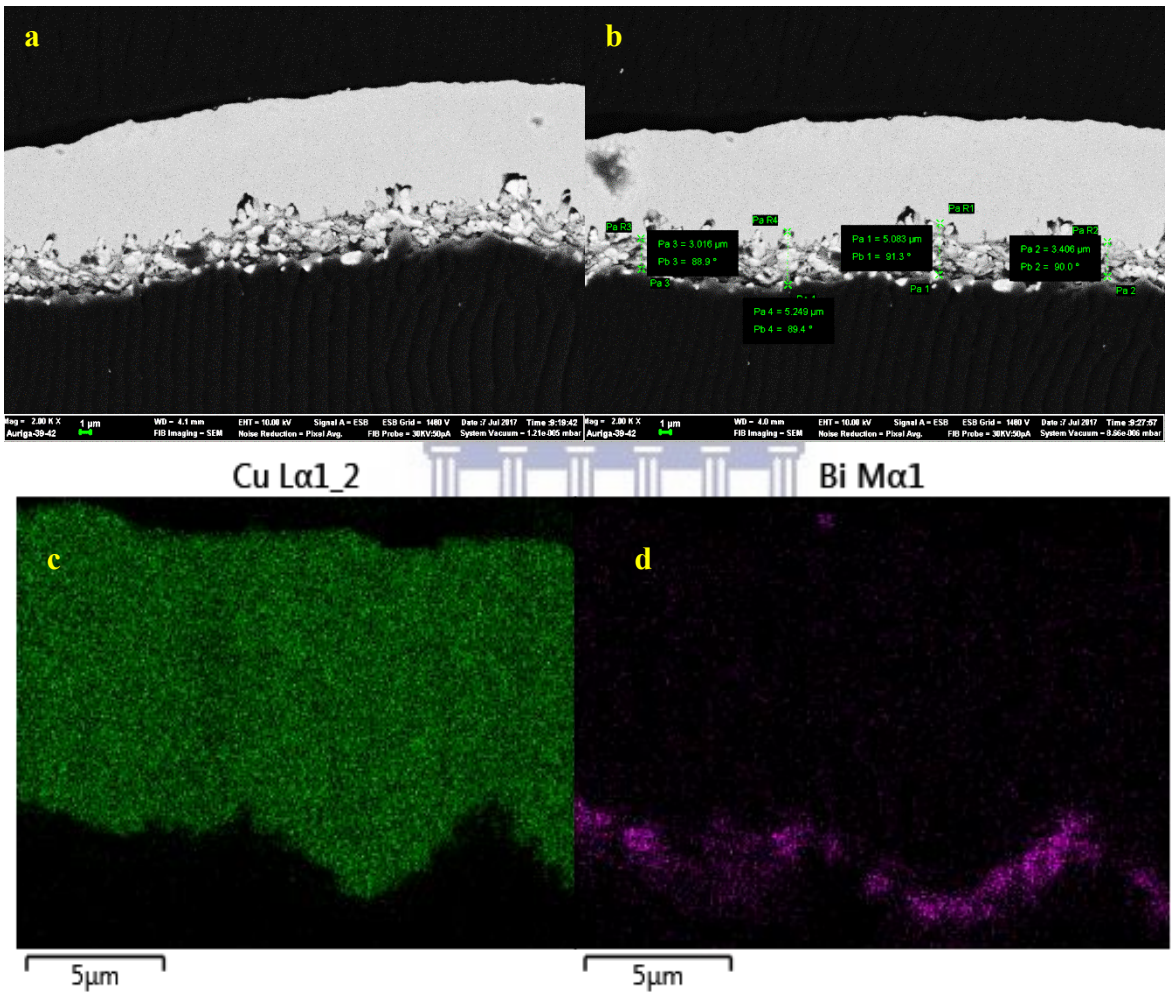

Figure 5.7: FIB SEM image (a & b) and cross sectional elemental map (c & d) of Bi on Cu foil

5.3.2.1.1 Effect of deposition potential on of Bi thin films (content and morphology)

The deposition potential was varied to investigate the effect it has on the deposition of the films. $BiCl_3$ was deposited at -0.15 V, -0.2 V, -0.25 V, -0.3 V potentials using a single deposition cycle, followed by linear sweep voltammetry measurements from a 0.5 M HCl solution shown in Figure 5.8. All the peaks shifted to lower potential value than the UPD

used, with the materials deposited at -0.2 V and -0.25 V showing the largest potential shift as well as higher current. This indicates that the Bi layer formed is strongly bound to Cu and therefore will reduce at more negative potential. The films deposited at potential of -0.15 V and 0.3 V were found to have the lowest potential shift and low current. The largest peak was found when the deposition was done at -0.2 V and this shifted to -0.33 V during LSV measurements. The charge associated with each potential deposition was obtained from integrating the area under the peaks in Figure 5.8, the relationship between the charge and potential is shown in Figure 5.9. It was found that the charge increased with the increase in the deposition potential of Bi, the charge decreased when moving toward more negative potential values. The morphology of the films in Figure 5.10 showed that the Bi thin films formed are structurally different. Well defined structural features are found at -0.15 V (a-b), when the potential is increased to -0.2 V (c-d) very thin hexagonal structures are formed while the large particles are also present. Increasing the potential to -0.25 V (e-f) and -300 mV (g-h) results in the formation of larger more defined and well-structured particles with the small thin structures observed at -0.2 V disappearing. Smaller particles are present at less negative potentials (-0.15 V- (-0.2 V)), low nucleation rate occurs at positive potentials generating coarse particles. The opposite occurs when the potential is more negative (-0.25-(-0.3 V)), where larger particles form due to high rate of nucleation. This was also found to occur when Gao et al.(2014) electrodeposited SnBi from deep eutectic solvent. This study also reported that Bi deposition potential influences the Bi content of the formed SnBi deposit. Bi electrodeposited films usually contain dendrites, which are very easy to form when deposition is done without additives (Tsai and Hu 2011). Dendrite presence is favoured by grain nucleation. The lack of dendrites on the formed Bi films indicates that the deposition occurs by growth of already deposited crystals which explains the stacking of crystallites observed on the SEM micrograms.

The EDS map (Figure 5.11) and spectra (Figure 5.12) further confirmed the distribution of the deposit across the surface as well the presence of Bi. The XRD pattern in Figure 5.13 further confirms that the deposit at -0.2 V is slightly different to the other deposits. The spectra for -0.2 V deposit has additional peaks at angles of 25.98, 36.40, 41.10 corresponding to Bi. The peaks at -0.2 V deposition of Bi are well resolved than at the other deposition potentials as indicated on the graph by Bi 002 and Bi 220 peaks.

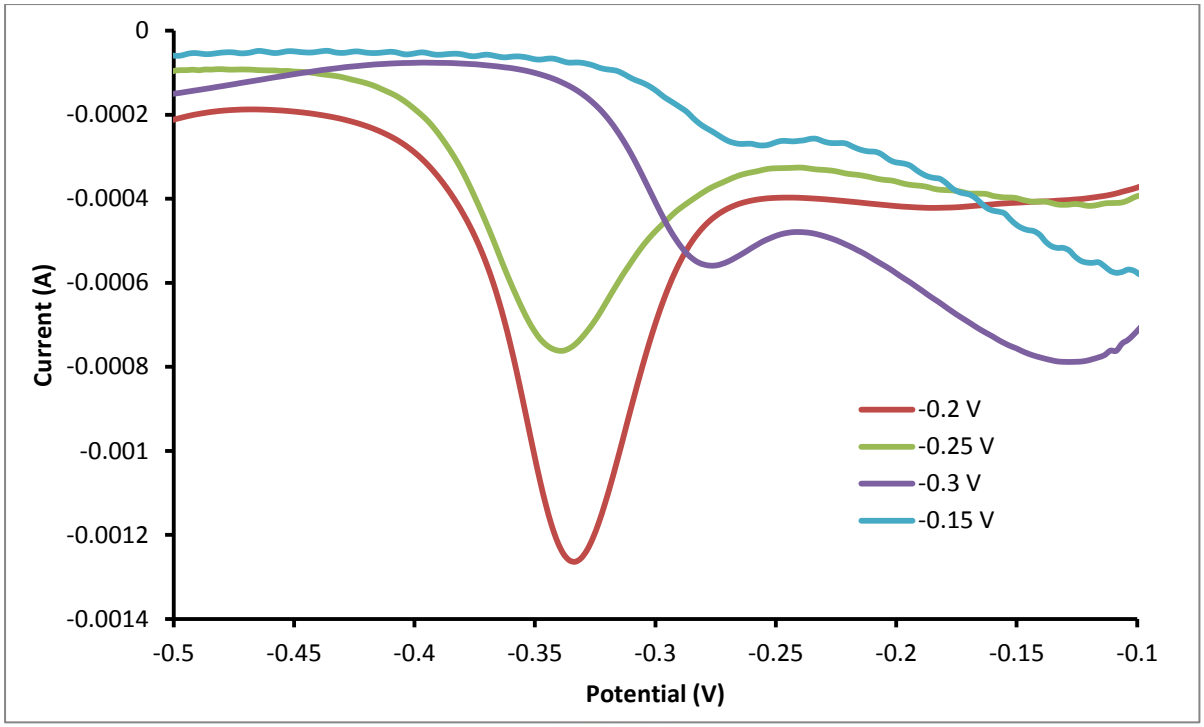

Figure 5.8: LSV curve of Bi in Cu foil deposited at various potentials within UPD region.

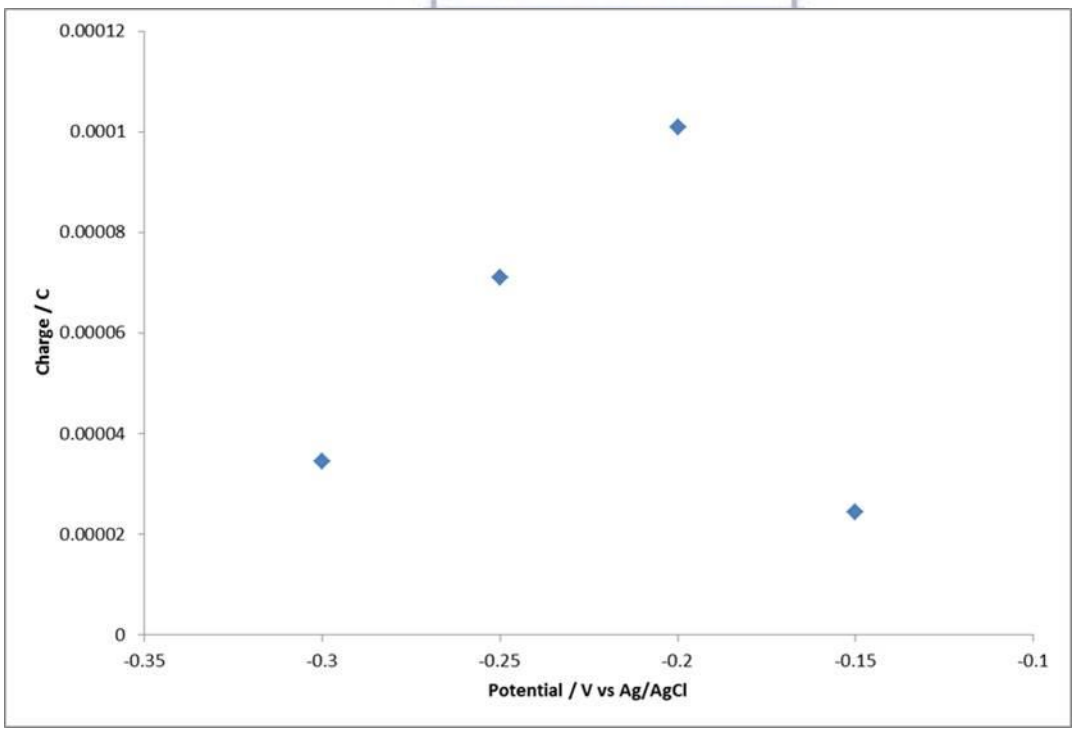

Figure 5.9: Charge and potential plot of Bi deposition at various potentials within UPD region.

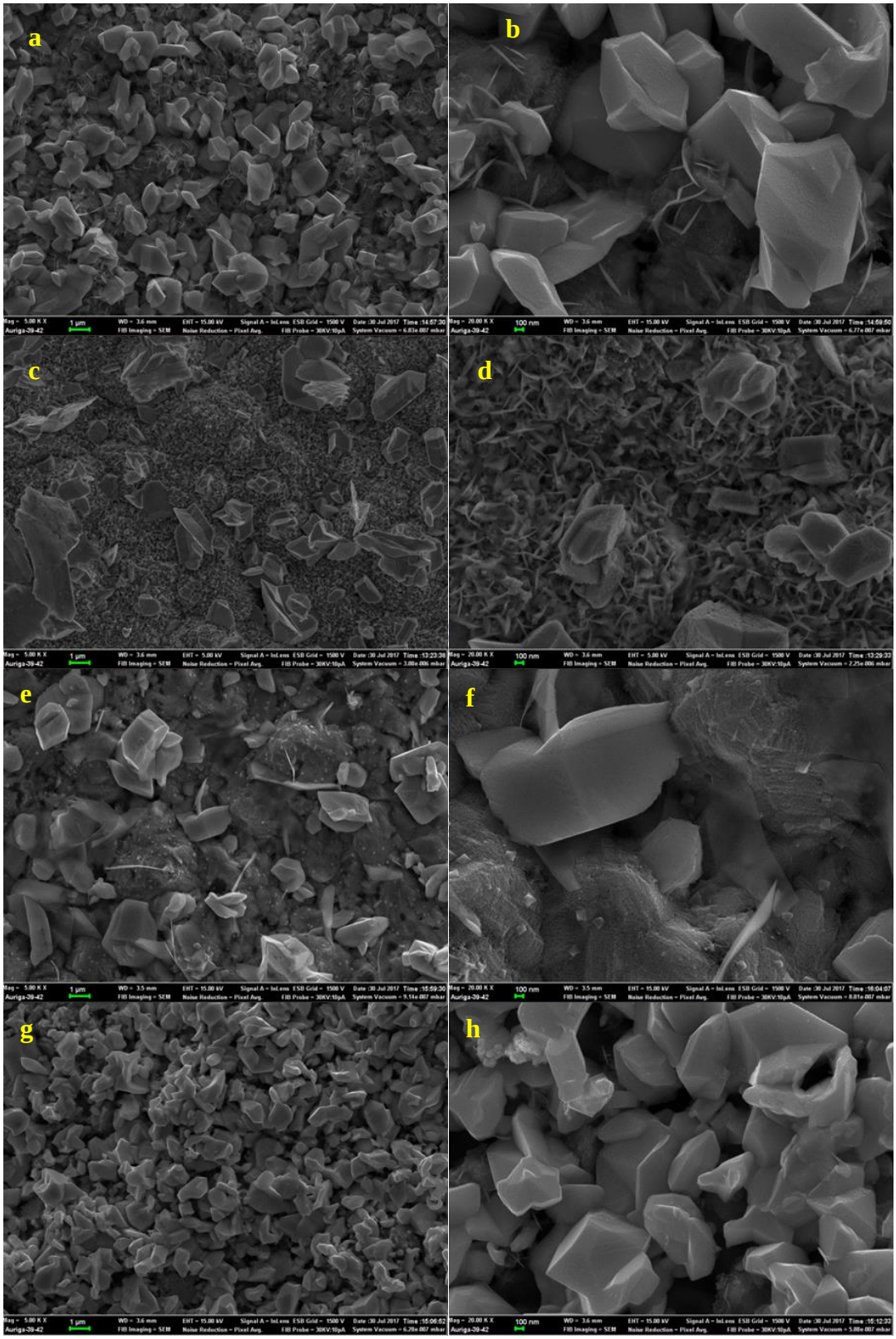

Figure 5.10: Electrodeposited Bi at -0.15 V (a-b), -0.20 V (c-d), -0.25 V (e-f), and -0.30 mV (g-h) for 100 cycles.

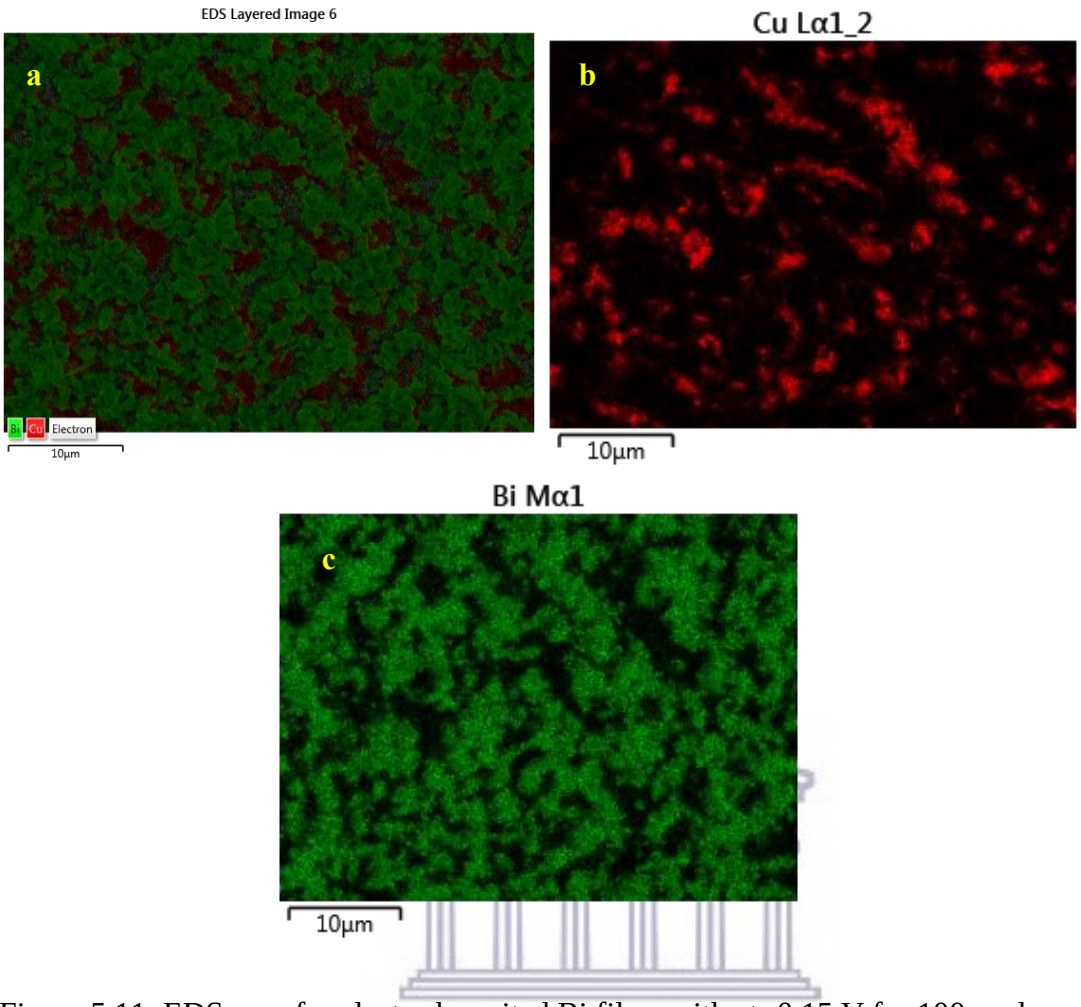

Figure 5.11: EDS map for electrodeposited Bi films with at -0.15 V for 100 cycles

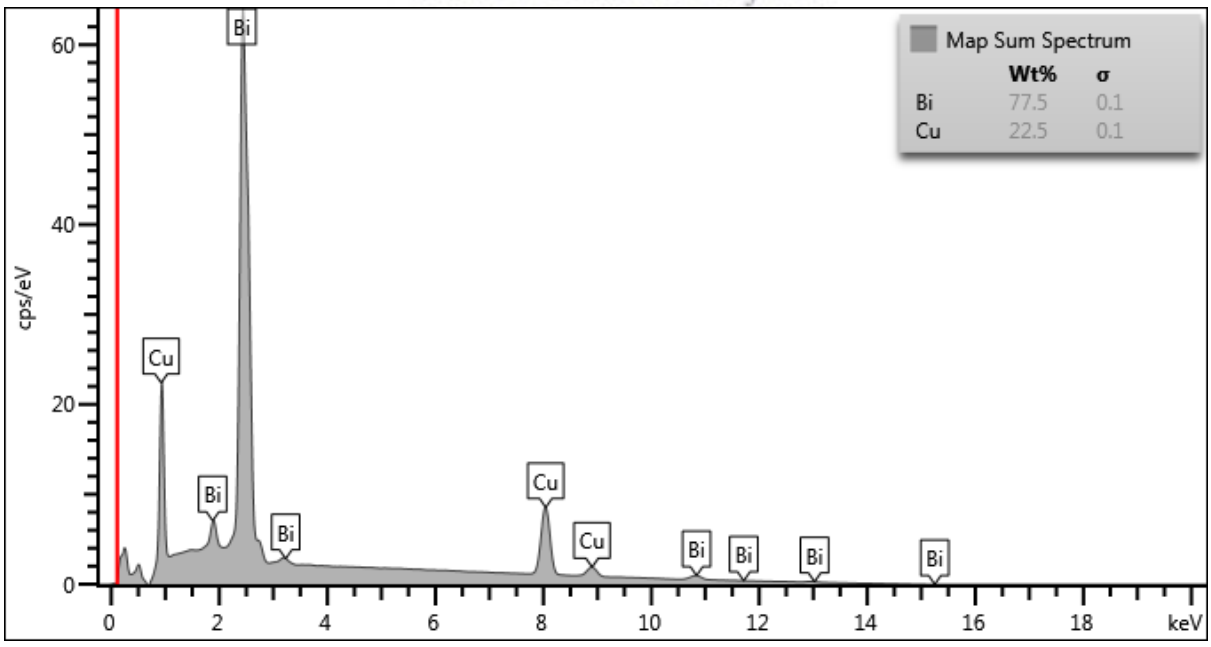

Figure 5.12: EDS spectra for electrodeposited Bi at -0.15 V for 100 cycles

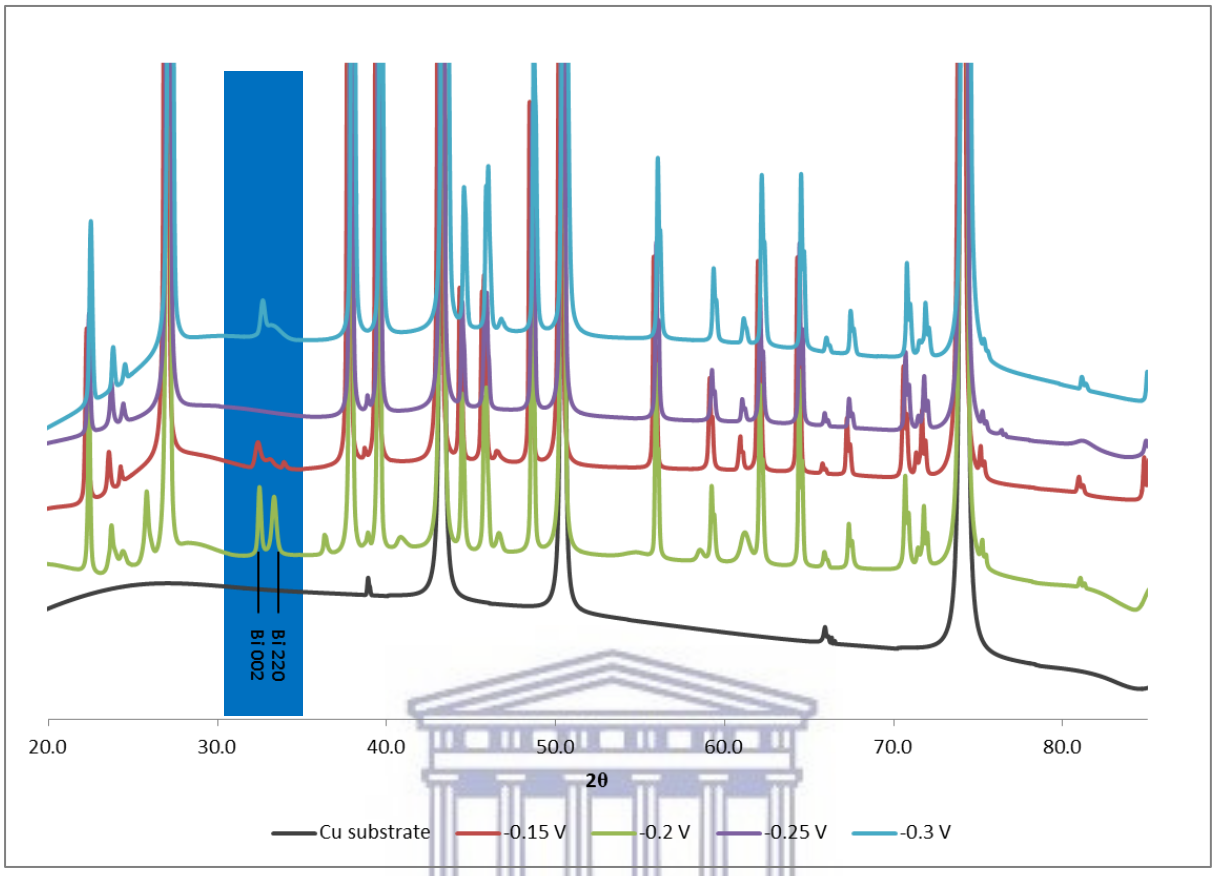

Figure 5.13: XRD pattern for Bi on Cu foil at varied potentials.

5.3.2.2 SnBi thin films

SnBi thin films were deposited at UPD potentials of Sn and Bi deduced from the CV curves in Figure 5.1 and 5.2. The Bi deposition is thoroughly discussed in the previous section. Sn deposition was further investigated by the deposition of Sn at -480 mV into Cu foil and conducting a linear sweep voltammetry scan (Figure 5.14) to reduce the deposited Bi in the electrolyte solution. The presence of Sn was shown by the appearance of the reduction peak at -0.32 V. Further experiments were done to determine the deposition of Sn at potentials of -0.35 V, -0.4 V, -0.45 V and -0.55 V. The relationship between the charge and each potential is shown in Figure 5.15. It was found that the maximum deposition of Sn occurs at -0.45 V and decreases with decrease in potential.

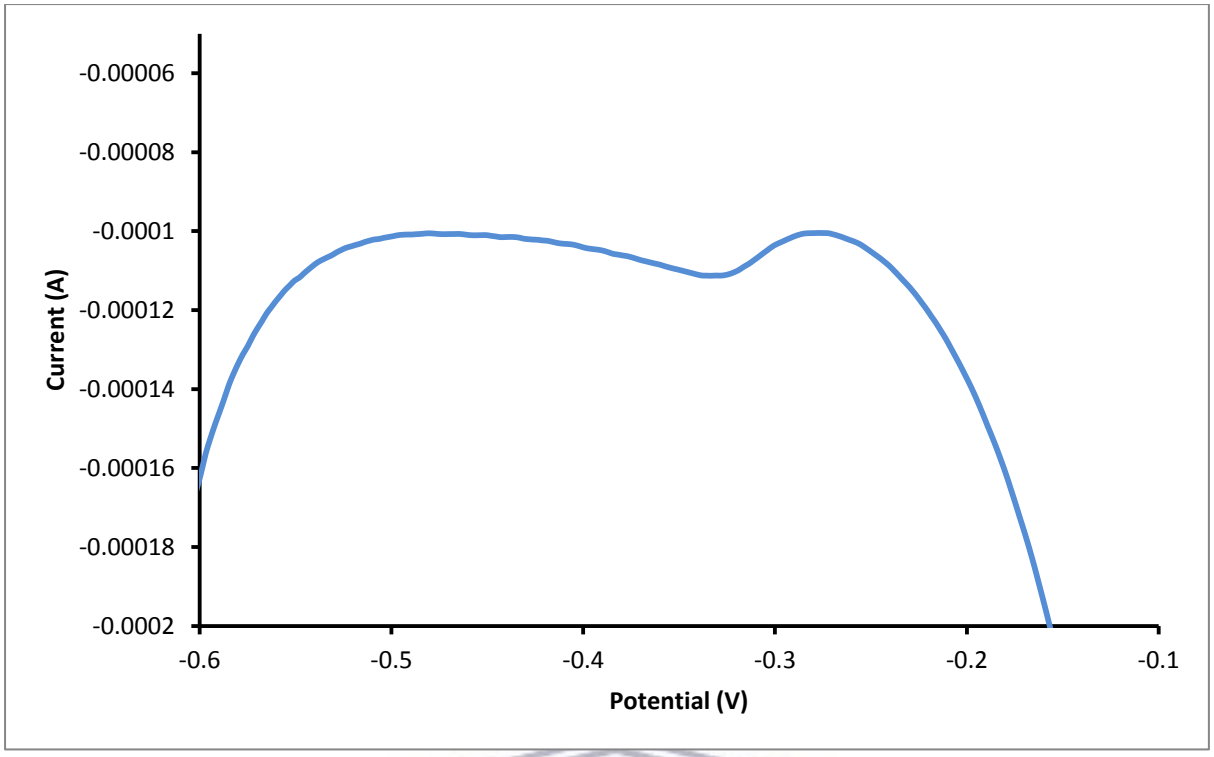

Figure 5.14: LSV curve of Sn deposited at -0.48 V for 10 s in 0.1 M HCl solution

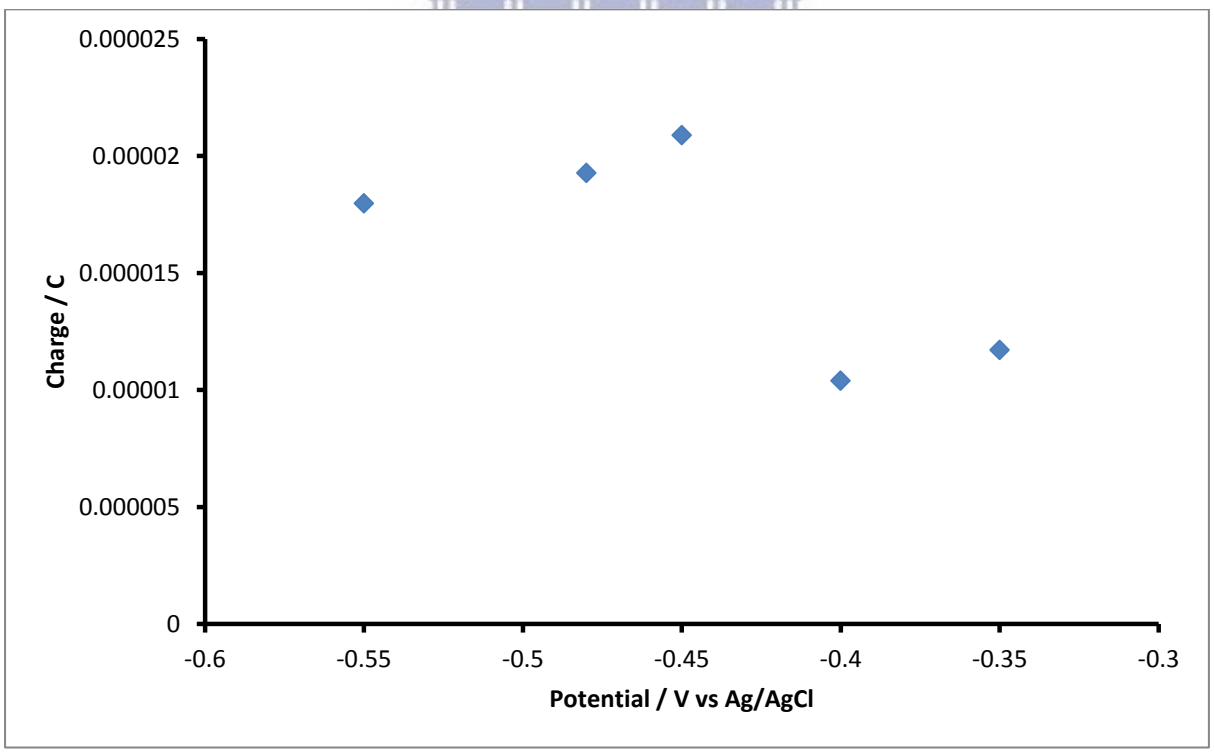

Figure 5.15: Charge and potential plot of Sn deposition at various UPD potentials

The combination of the above information about Sn deposition and the investigation of Bi deposition in Cu foil were used to formulate a deposition cycle for both elements. A few

problems were encountered that were hindering the formation of the films. Bi has been successfully deposited at UPD on Cu foil; the next step was the introduction of Sn deposition step. Deposition of Sn layer step first followed by Bi will not work because of surface replacement reaction of Sn by Bi. Therefore, first layer of Bi needed to be deposited. Using open circuit potential of -0.05 V to rinse in between the deposition of each element resulted in no film growth. This is due to the dissolution of Cu oxide in the electrolyte that causes a change in open circuit potential gradually over time as explained in the electrochemical studies section for Figure 5.1. Therefore the potential needed to be controlled until both layers have been deposited, and also rinsing with electrolyte after depositing the first layer of Bi at OCP was altogether eliminated to allow enough time for the Sn solution to be within the deposition chamber and to promote Sn deposition. The deposition cycle used was made of the following steps: (i) Flow Bi for 15 s, (ii) Deposit Bi at -200 mV for 10 s, (iii) Pump Sn at -480 mV for 15 s, (iv) Deposit Sn at -480 mV for 10 s, (v) Rinse with 0.1 M HCl at OCP for 15 s. The first ten cycles used are shown in Figure 5.16. Bi was deposited at -200 mV regardless of that -150 mV indicated a higher Bi content, even though both potentials are still within the UPD region. Bi preferentially deposits over Sn, slight lowering of the potential was done to give Sn deposition a competitive edge or to favour the deposition of Sn. Parameters including the deposition potential of Bi, and the concentration of Sn were investigated for their effect on the structure and morphology of the films.

The morphology of the SnBi material was investigated using SEM microscopy and the obtained images shown in figure 5.17 at different magnifications. The material was found to be made of thin sheet like material, agglomerating together. The material was found to contain both Sn and Bi distributed across the surface, showing that the material is made up of both elements as shown by the EDS map in figure 5.18. The crystal structure was determined using XRD as shown the spectra in Figure 5.19 (a). The XRD pattern of SnBi material was overlaid with that of Bi material and Cu foil substrate. The diffraction peaks were assigned by matching the pattern with reference database using High score plus and PDF4 file 2017 as shown in figure 19 (b). The diffraction peaks were identified from the reference patterns of Cu (ICDD 00-004-0836), Bi (ICDD 01-070-5673), BiSn (ICDD 00-076-7574) (ICDD 00-076-7575), $Bi_{1.2}Sn_{0.2}$ (ICDD 01-082-9505), $Bi_2Sn_2O_7$ (ICDD 00-056-0646), CuSn (IDCC 00-006-0621), Cu_6Sn_5 (ICDD 00-045-1498) (ICDD 01-081-8261), and SnO (ICDD 00-007-0195).

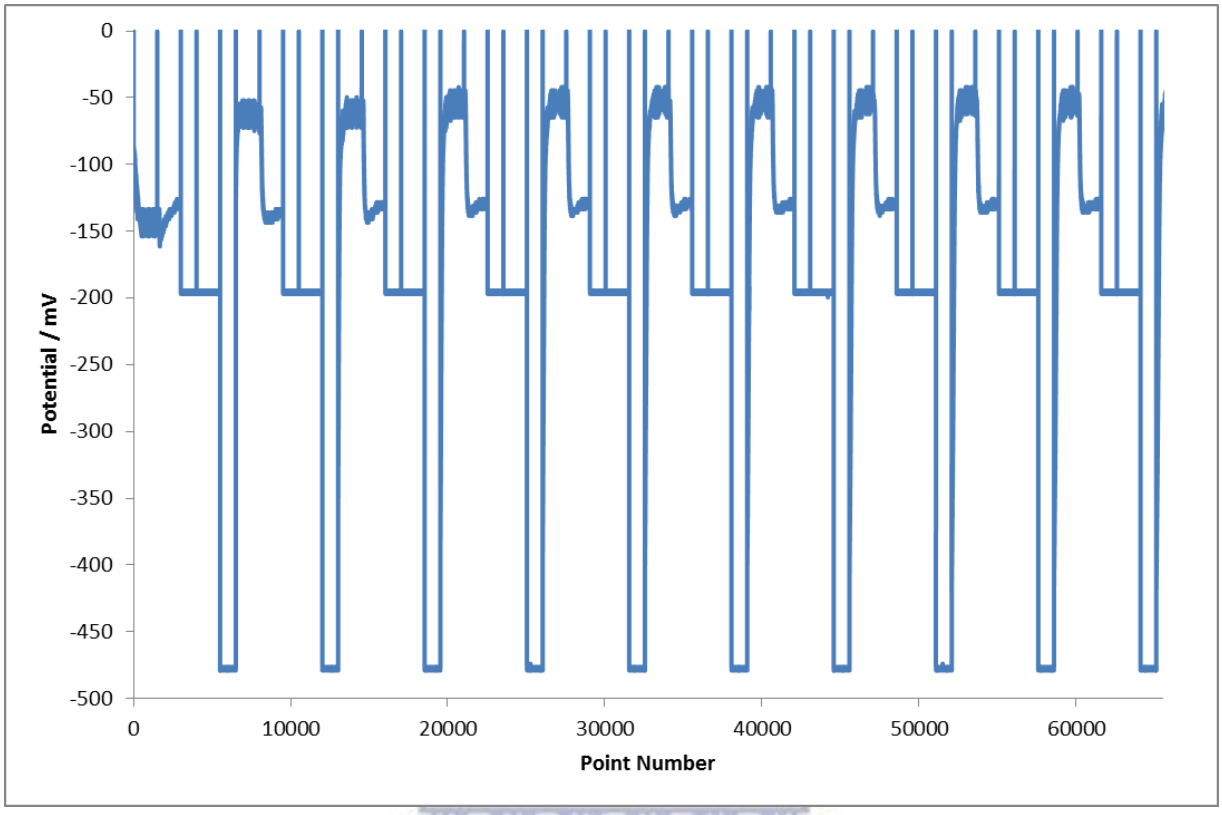

Figure 5.16: E-ALD cycle of SnBi on Cu foil.

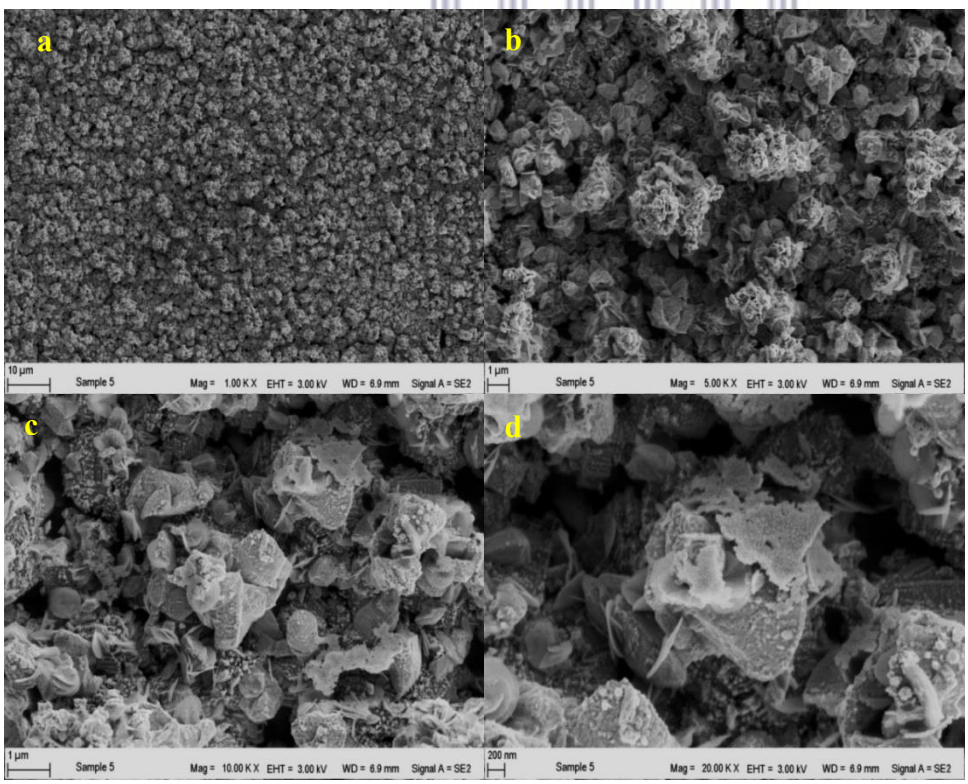

Figure 5.17: Electrodeposited SnBi material for 300 cycles

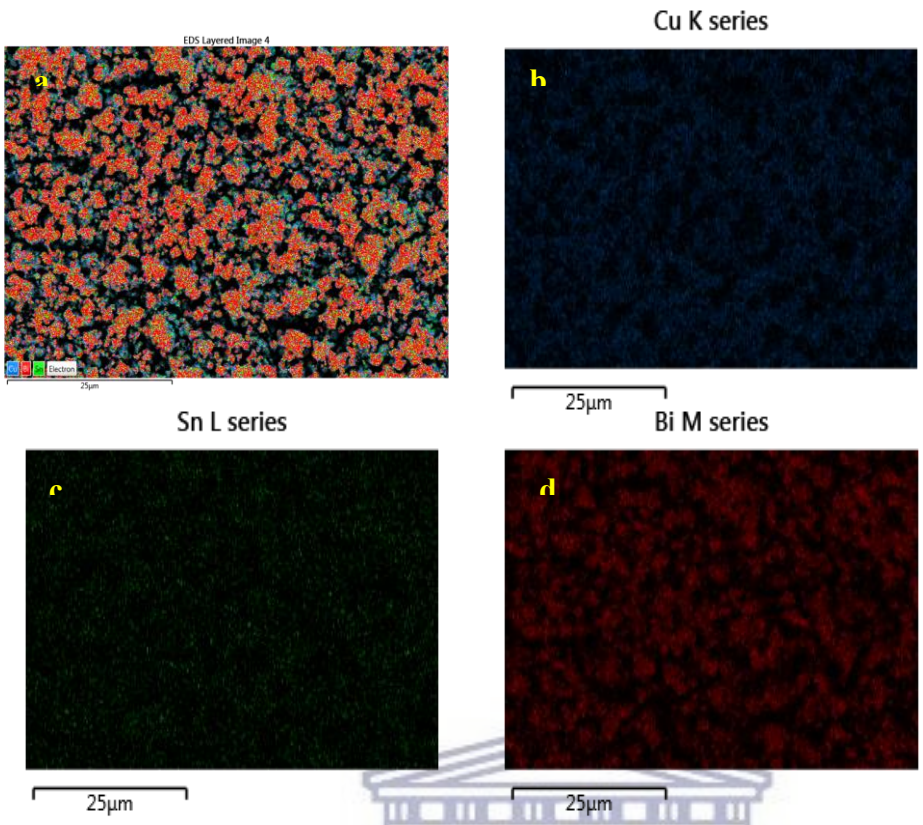

Figure 5.18: EDS map for the SnBi material.

The peaks at angles 26.9, 28.7, 32.8, 33.5, 53.3, and 54.3 were assigned to Sn 200, 101, 220, 211, 301, and 400 respectively. There was a slight shift and broadness of Cu foil peaks observed on the SnBi on Cu foil material. The Bi peaks were also found to have shifted; while new peaks were identified The Bi peaks were found to have shifted to the lower diffraction angles while those of Cu were broader. The d-spacing of possible reflections of the prepared SnBi and Bi films based on Bi 012 were found to be 3.008 Å and 3.263 Å obtained using Rietveld refinement respectively. The shifting of the 012 Bi peaks and the presence of other phases of the SnBi including $Bi_{1.2}Sn_{0.2}$ indicates that an alloy was formed.

The formation of intermetallic Cu-Sn phases (CuSn, Cu_6Sn_5) during electrochemical alloy deposition is better explained through the findings of a study by contact immersion deposition of Sn onto Cu (Fujiwara and Enomoto 2004).

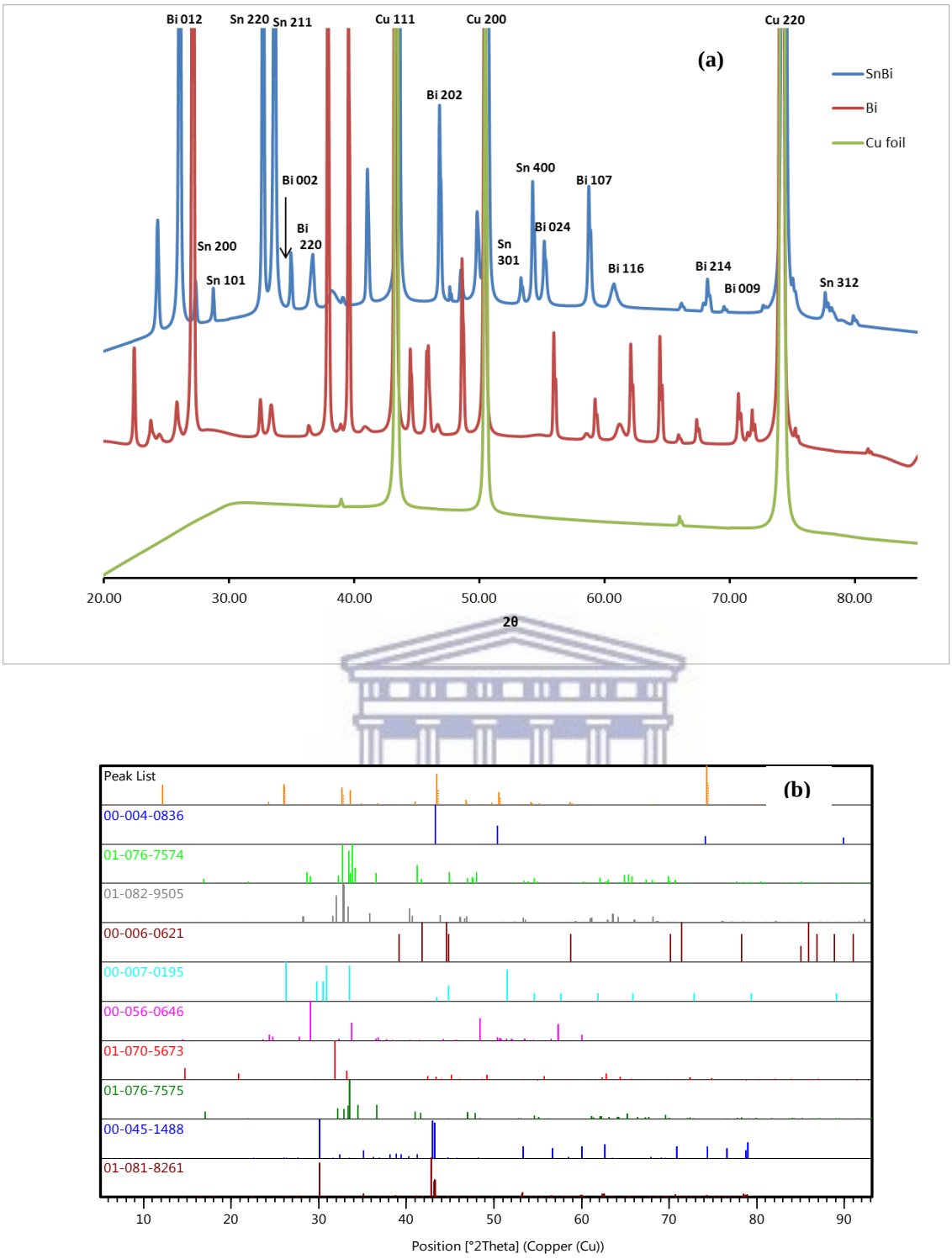

Figure 5.19: (a) XRD spectra of SnBi thin films (b) Matched XRD spectra of SnBi thin films

The mechanism of Cu-Sn alloy growth was also investigated. They reported that the growth mechanism involves; (i) the formation of Sn monoatomic layer on Cu surface at UPD, (ii) exchange of site between Cu and UPD deposited Sn resulting in Cu atoms moving into the surface, this becomes the nuclei of Cu-Sn intermetallic phases, (iii) the following UPD layer of Sn on Cu will then form on the Cu-Sn intermetallic layer. The diffusion of Sn and Cu atoms through the alloy layer limits the growth rate of Cu-Sn intermetallic phases. Intermetallic phases were also found when Sn and Bi layers were electrodeposited on reflowed Sn-Bi solder alloys using Cu substrate (Lee *et al.* 2012). They found that a layer of Cu_6Sn_5 forms at room temperature. They reported that the growth mechanism explained above for Cu-Sn formation does not occur when Bi is deposited as the first layer contrary to our findings. It is important to note that the method used was bath deposition in methane sulphonic and citric acid based, and not a potential control or UPD method. The presence of intermetallic Cu-Sn phases reported in this study indicates that the first layer of Bi does not cover the entire surface or leaves space within the monoatomic layer for the diffusion of Cu atoms. Electrodeposition of SnBi coatings on Cu foil from deep eutectic solvent was able to produce films that contains phases of Sn, Bi, and Cu substrate and not trace of other intermetallic phases (Gao *et al.* 2014).

5.3.2.2.1 Effect of Sn concentration on morphology of SnBi thin film

The concentration of Sn was varied while the Bi was kept constant to investigate the effect it has on the formed film. The Sn concentration ratio in SnBi of 10:1, 5:1, 4:1, 3:1, 2:1, 1:1 were used to form deposits using 100 cycles. The morphology of the SnBi materials formed at different concentration of Sn is shown in Figure 5.20. It was found that well defined structures with larger particles were formed when Bi and Sn were the same, increasing the concentration of Sn resulted in smaller thin sheet like particle formation.

The deposition behaviour of Sn and Bi affects the structural features of the formed deposit. There are two ways in which SnBi deposits can form, this is by growth of already deposited crystallites or nuclei formation (Tsai and Hu 2011). The morphology of the SnBi films indicated that deposition occurs by both, where the stacked particles are a result of particle growth on already existing deposits. They grow up to a certain point, until the conditions are favourable for new nuclei formation. These two growth mechanisms results in the observed grove like or excavated shape on the surface. Changing the composition of the deposition solution or the total concentration of the precursor metal ions as observed during a study on the control and microstructure Sn-Bi alloys (Tsai and Hu 2011) affects the structure of

material. This study found that when Bi:Sn ratio is solution is 1:1, the formed deposits were uniform polyhedral crystallites. The formation of less structurally defined particles when Sn is increased is due to the simultaneous occurrence of hydrogen evolution and SnBi deposition. The differences in grain sizes indicate that the formation of SnBi is dependent on the composition (amount of Sn and Bi on the precursor solutions).

The presence of Sn and Bi was further confirmed using EDS map shown in Figure 5.21 and the spectra in Figure 22. The elemental map showed that Sn and Bi are found distributed evenly over the surface. Further structural differences were investigated using XRD, the pattern for all the different concentrations is shown in Figure 5.23. The results showed that all diffraction peaks are at the same angles for the different ratio materials, therefore these materials are crystalline and that their crystal structure is the same.

The content of each element on the deposits was confirmed using ICPMS (Table 5.1). The highest amount of 0.3589 mg Bi was obtained when using a ratio of 1:1 for Sn:Bi, while the highest Sn content of 0.005481 mg was obtained for a 1:10 SnBi ratio. Bi content decreased with increase in Sn content, and vice versa, even though the Bi content remained much higher than that of Sn. Half the amount of Bi was obtained when the concentration of Sn was doubled based on the ratio of 1:80 for BiSn (1:1) and 1:40 for BiSn (1:2). Further increase in Sn content decreased Bi content to as low as 1:21 for BiSn (1:10). Increasing the concentration of Sn was able to effectively decrease the content of Bi on the deposit formed due to the competitive nature of Sn and Bi deposition (Gao *et al.* 2014). Even though, overall, Bi content on the deposit will be higher than Sn due to Bi being much nobler than Sn, as well as that Bi has a higher atomic mass than Sn (208 vs 118 g/mol) (Tsai and Hu 2011). Efforts to increase Sn content in SnBi deposit uses additives such as polyethylene glycol to inhibit Bi deposition therefore increasing Sn deposition and content (Tsai and Hu 2009b, 2011; Tsai *et al.* 2011). Suh and co-workers (2006) investigated the effects of plating conditions on composition and microstructure of Sn-Bi electrodeposit using methane sulphonate bath. They also reported similar observations where increasing the Sn content in the bath (solution) increased the content of Sn on the deposits. Similar observations were found for the electrodeposit of SnBi coatings from deep eutectic solvent on Cu foil substrate (Gao *et al.* 2014). Tsai also found a higher Sn content when the bath Sn concentration was increased ten time higher compared to that of Bi in the same solution (Tsai and Hu 2011).

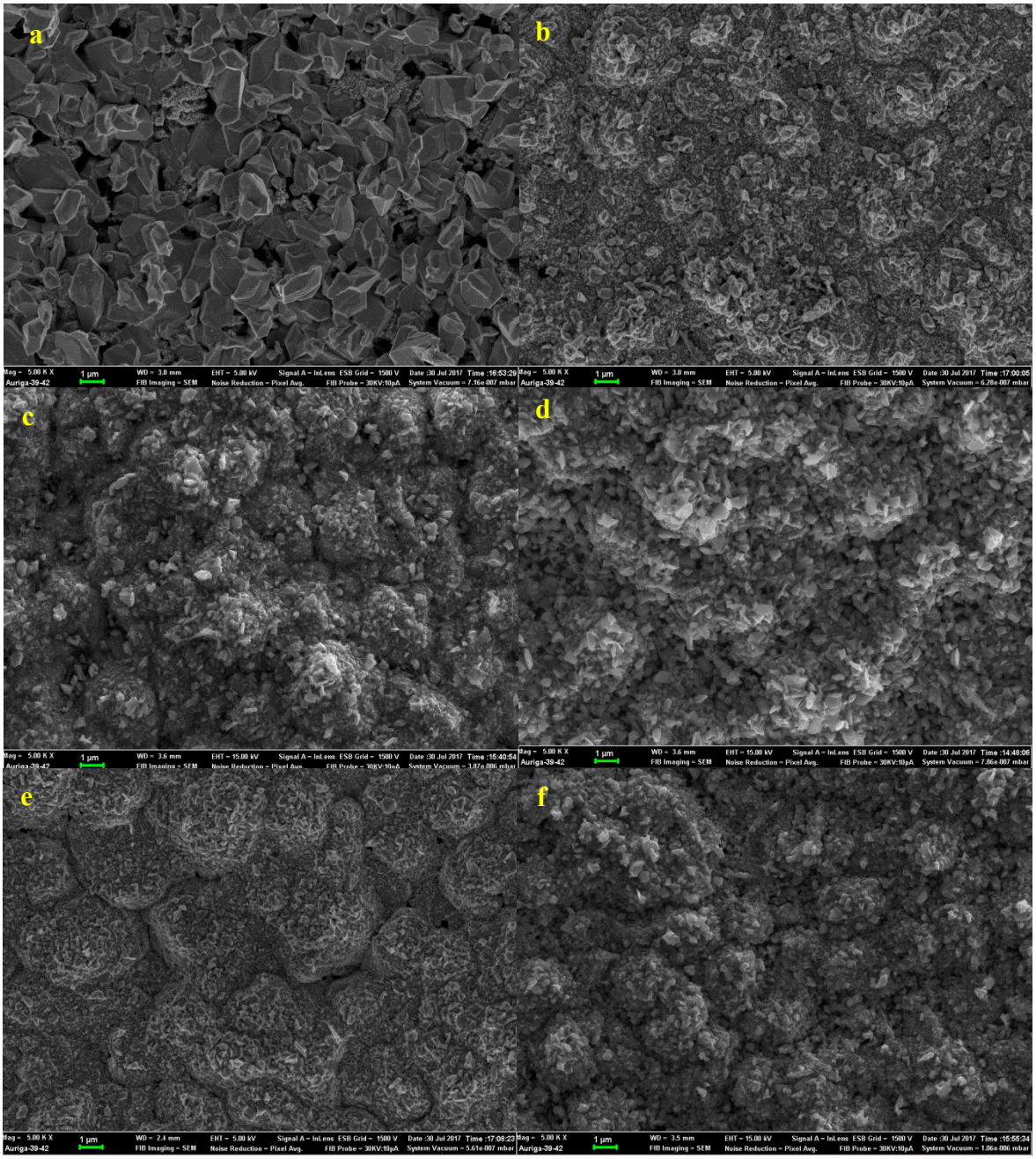

Figure 5.20: Electrodeposited SnBi films of ration 1:10 (a), 1:5 (b), 1:4 (c), 1:3 (d), 1:2 (e), 1:1 (f) for 100 cycles.

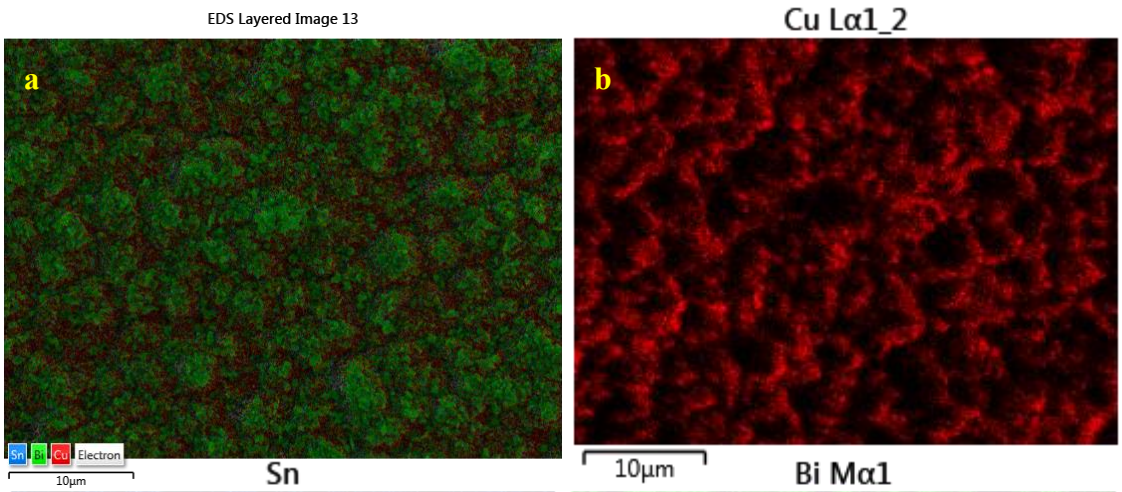

Figure 5.21: EDS map for electrodeposited SnBi films with a ratio of 1:3 for 100 cycles

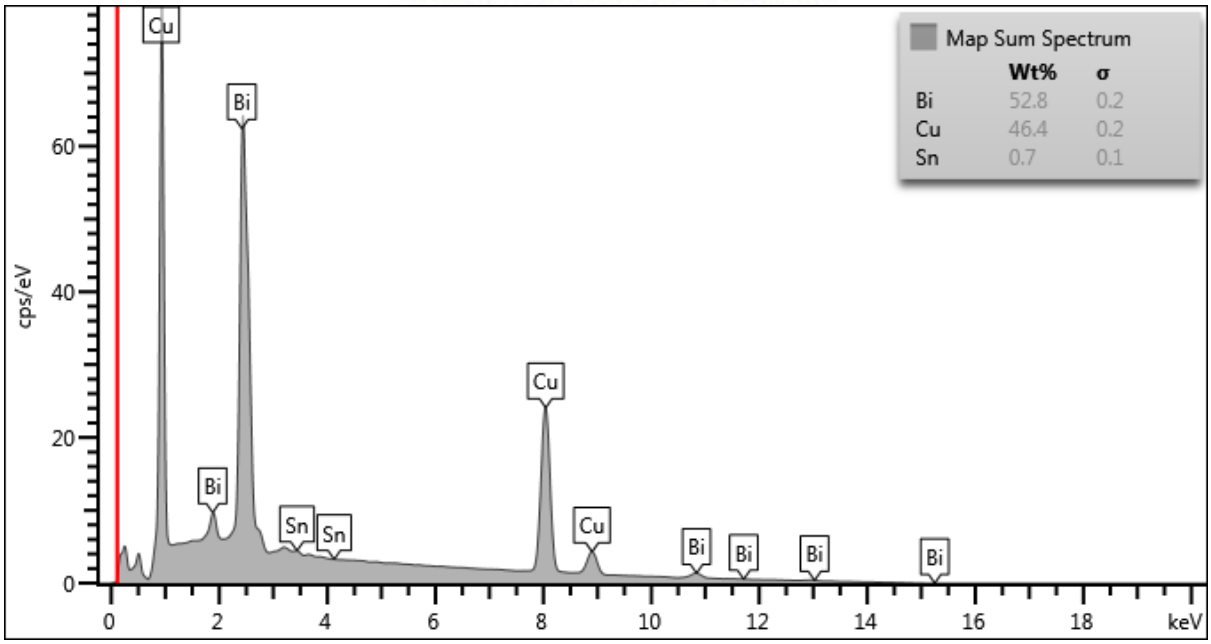

Figure 5.22: EDS spectra for electrodeposited SnBi films with a ratio of 1:3 for 100 cycles

Table 5.1: Summary of SnBi content from ICP MS analysis

BiSn ratio in solution	Sn on the deposit / mg	Bi on the deposit / mg	Sn:Bi ratio after deposition
1:1	0.004511±7.409E-04	0.3589±9.251E-03	1:80
1:2	0.004471±5.093E-05	0.1808±1.246E-03	1:40
1:5	0.003443±2.812E-04	0.1190±2.195E-03	1:34
1:10	0.005481±3.543E-04	0.1162±4.357E-03	1:21

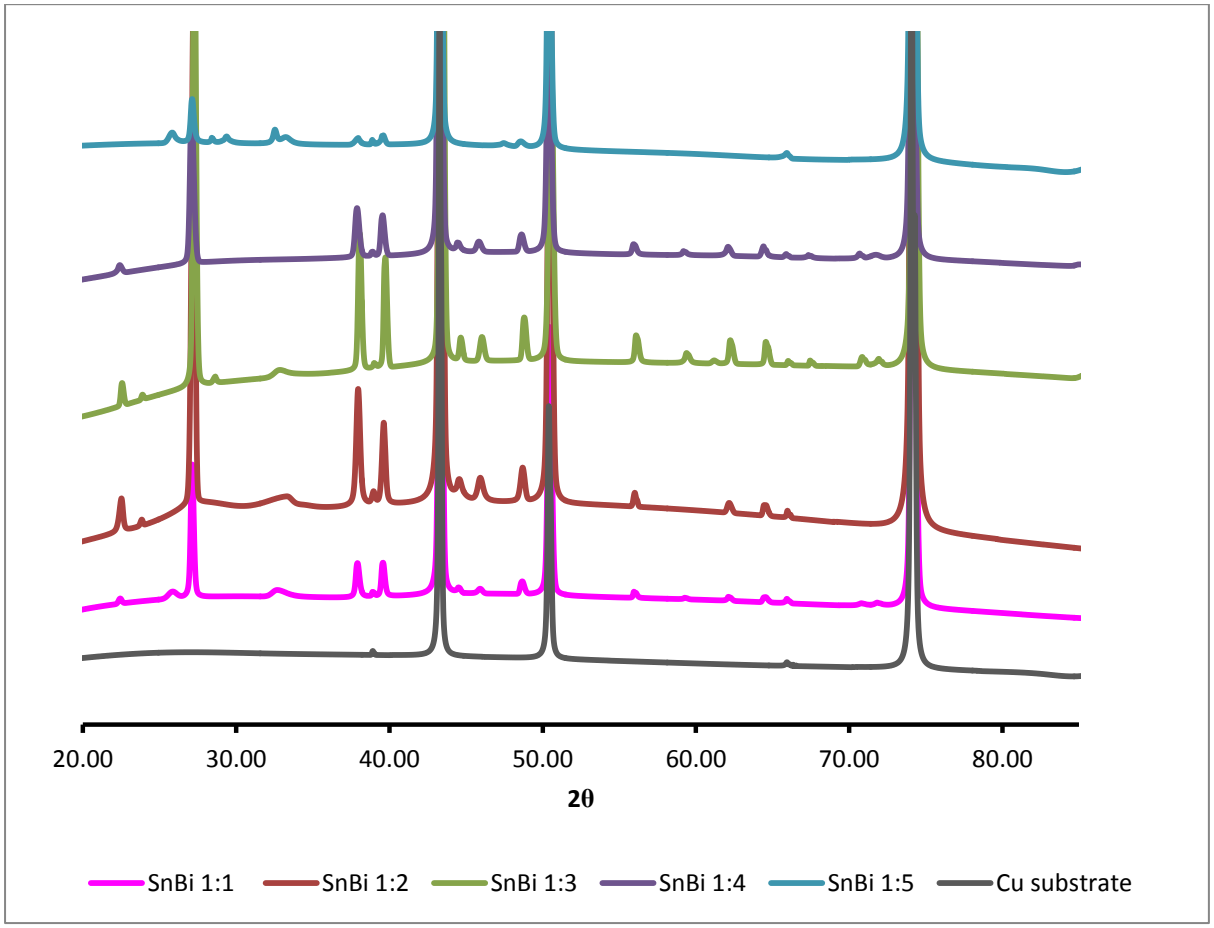

Figure 5.23: XRD pattern for electrodeposited SnBi films with a various Sn distribution in solution.

The thickness of the deposit was investigated and the cross sectional images for a 100 cycle deposit (Figure 5.24 c-d) and for a 300 cycle deposit (Figure 5.24 a-b) are shown. The 300 cycle material was found to be 2 µm thick while the 100 cycle was 0.5µm, the thickness slightly varies along the deposit. Based on these two measurements it can be observed that

the thickness increased with cycle number. The variation in thickness along the deposit is due to the material growing into a rough Cu substrate; using single crystal Cu substrate would result in better quality films. Laminar flow also needs to be established early in the flow channel during deposition, failure to do this result in uneven growth. It was also confirmed with the XRD results that, Sn is alloying with the substrate forming CuSn intermetallic phases by diffusion on Sn and Cu atoms (Fujiwara and Enomoto 2004; Lee *et al.* 2012). This makes the uniformity of each layer difficult to control and results in varied thickness of the film (Lee *et al.* 2012). The elemental analysis done on the cross sections in Figure 25 shows that both Sn and Bi are present, Sn is evenly distributed across the material while Bi is predominantly found on the surface.

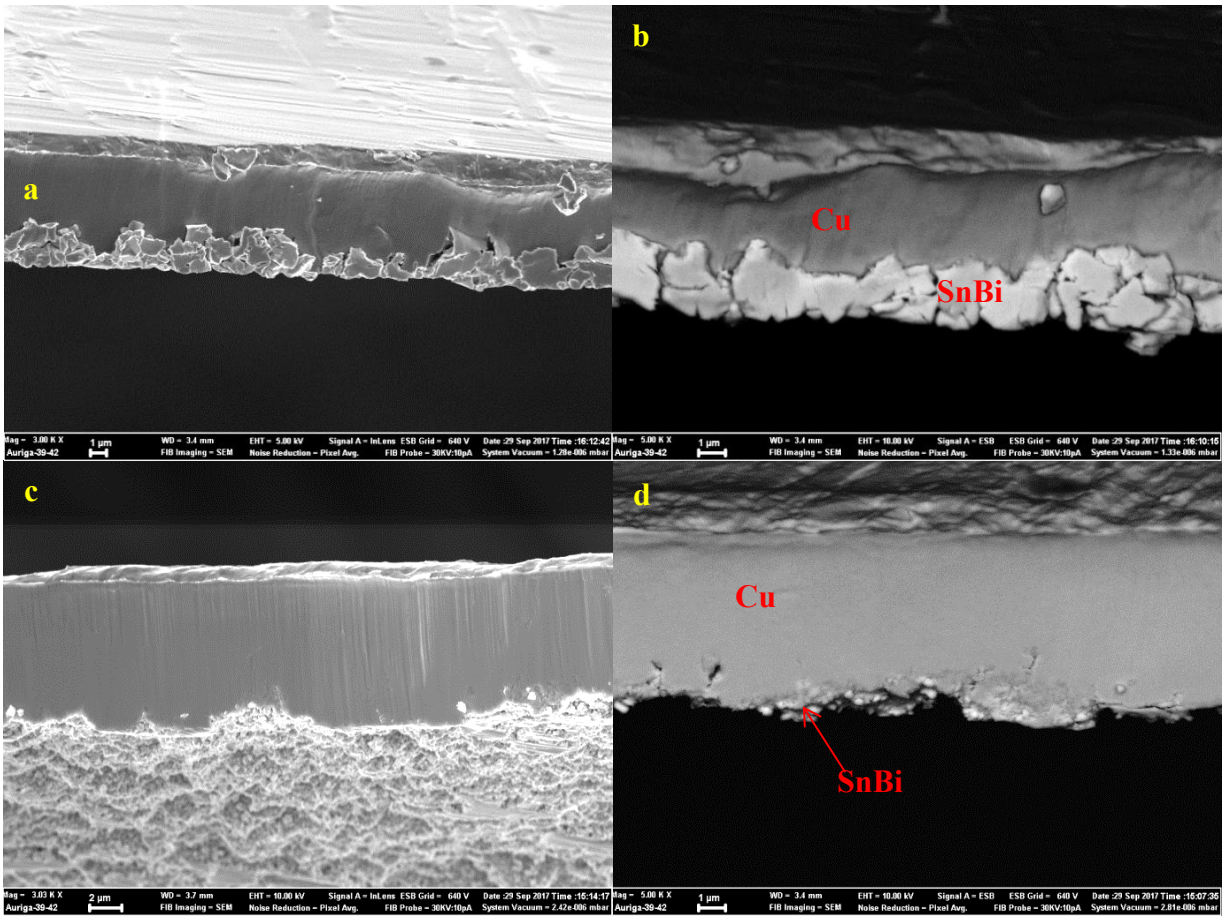

Figure 5.24: Thickness of SnBi Deposit. a-b SnBi 300 cycle deposit, c-d SnBi 100 cycle deposit.

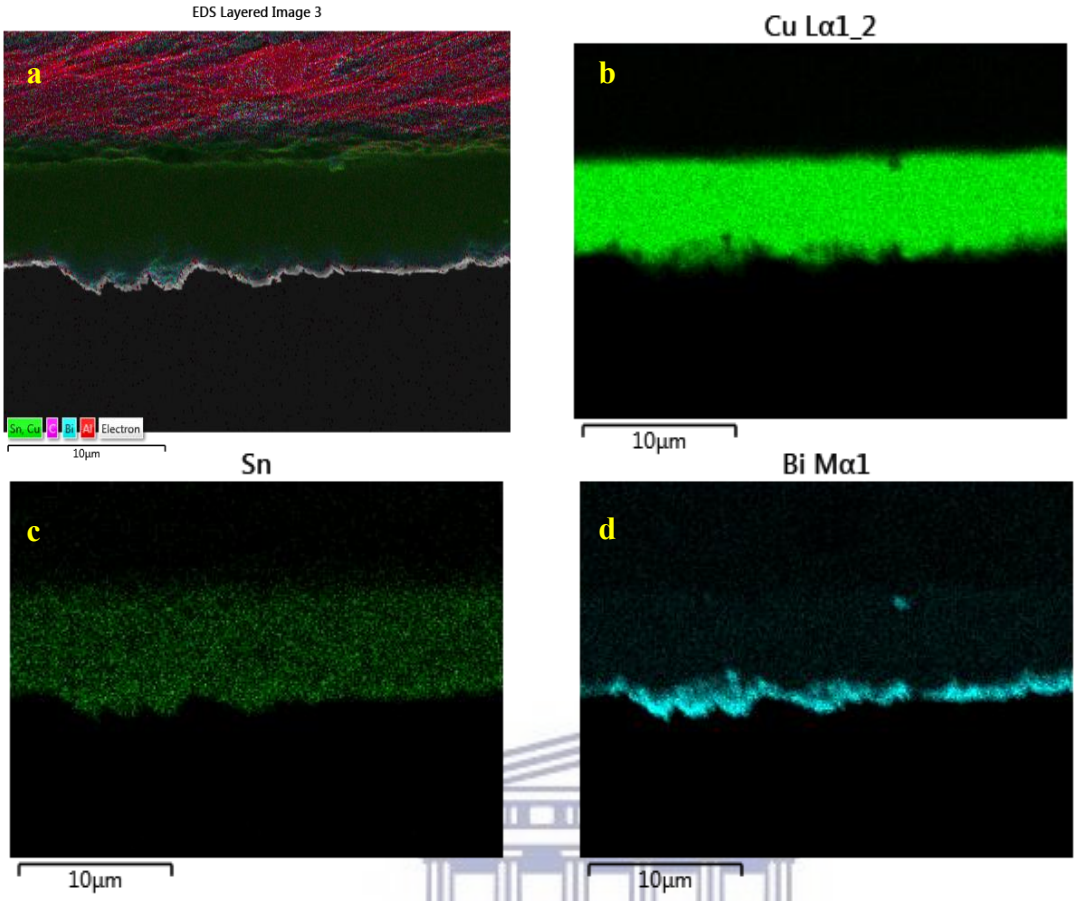

Figure 5.25: EDS map of SnBi Deposit 300 cycle deposit

5.3.3 Electrochemical tests for sodium ion batteries

The electrochemical behaviour of SnBi electrodes with two different ratios as anode material for sodium ion batteries was investigated using galvanostatic charge/discharge (GC), cyclic voltammetry (CV) and electrochemical impedance spectroscopy (EIS).

5.3.3.1 Electrochemical performance of SnBi electrodes

When the SnBi (1:1) and SnBi (3:1) electrode was galvanostatically tested within the voltage range of 0.05 V-1.5 V at 0.1 C. An initial discharge capacity of 1900 mAh/g for SnBi (1:1) and 338 mAh/g for SnBi (3:1) was obtained as shown in Figure 5.26 and Figure 5.27 respectively. The charge and discharge curves of both sample show two plateaus at 0.67 V and 0.5 V in the discharge curve and at 0.77 V and 0.6 V for the charge curve.

These plateaus occurred between 0.2 V – 1.0 V region, indicating that this is where the reaction occurs (Su *et al.* 2015). When comparing the two electrode materials, it was found that the materials SnBi (1:1) had a much higher initial discharge capacity than the SnBi (3:1). The former was also able to retain capacity for a longer period of 100 cycles (38 mAh/g) while the latter crashed much earlier at the 12th cycle (1.8 mAh/g) and zero beyond until the 20th cycle. Similar studies reported an initial discharge capacity of 1013 mAh/g at 40 mA/g for bismuth and graphene nano composite, and 310 mAh/g for a bare bismuth electrode.

$$Bi + xNa^+ + xe^- \leftrightarrow Na_xBi \quad (26)$$

$$Na_xBi + (3-x)Na^+ + (3-x)e^- \leftrightarrow Na_3Bi \quad (27)$$

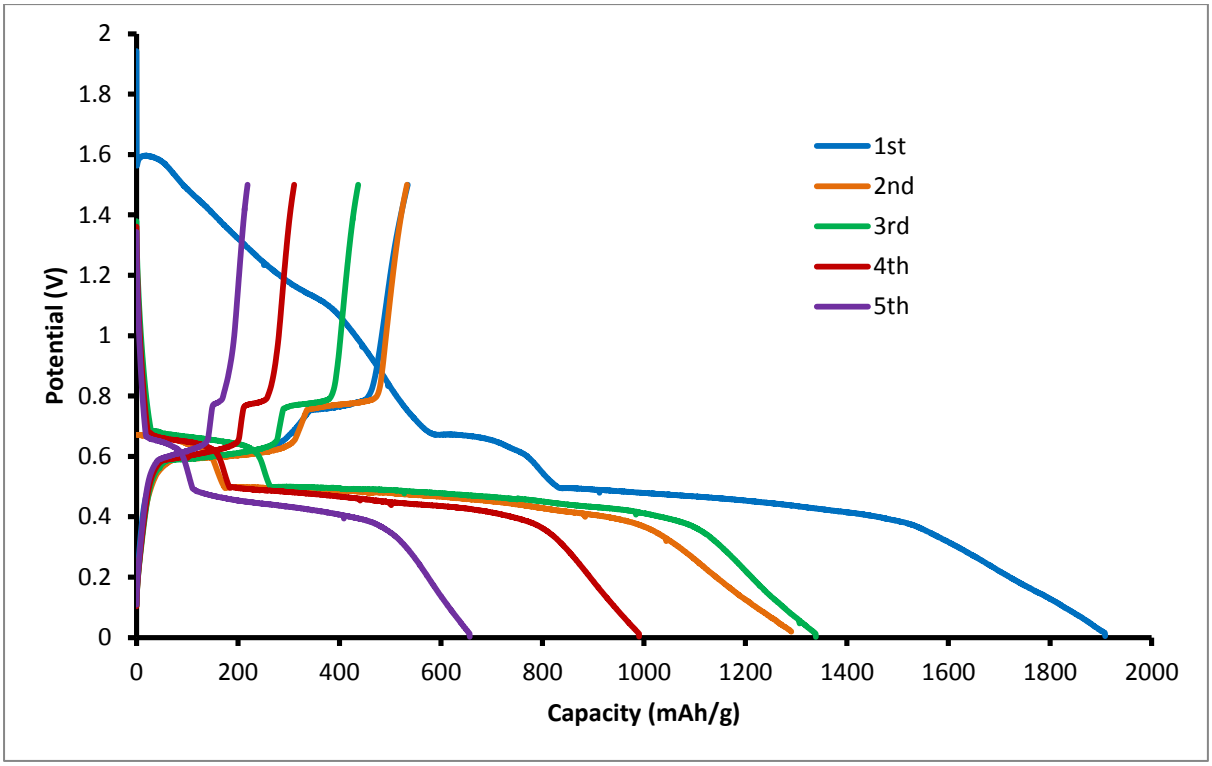

Figure 5.26: Discharge and charge profiles of SnBi (1:1) for the first 5 cycles at 0.1 C (38.5 mA g^{-1}) within 0.05-1.5 V range.

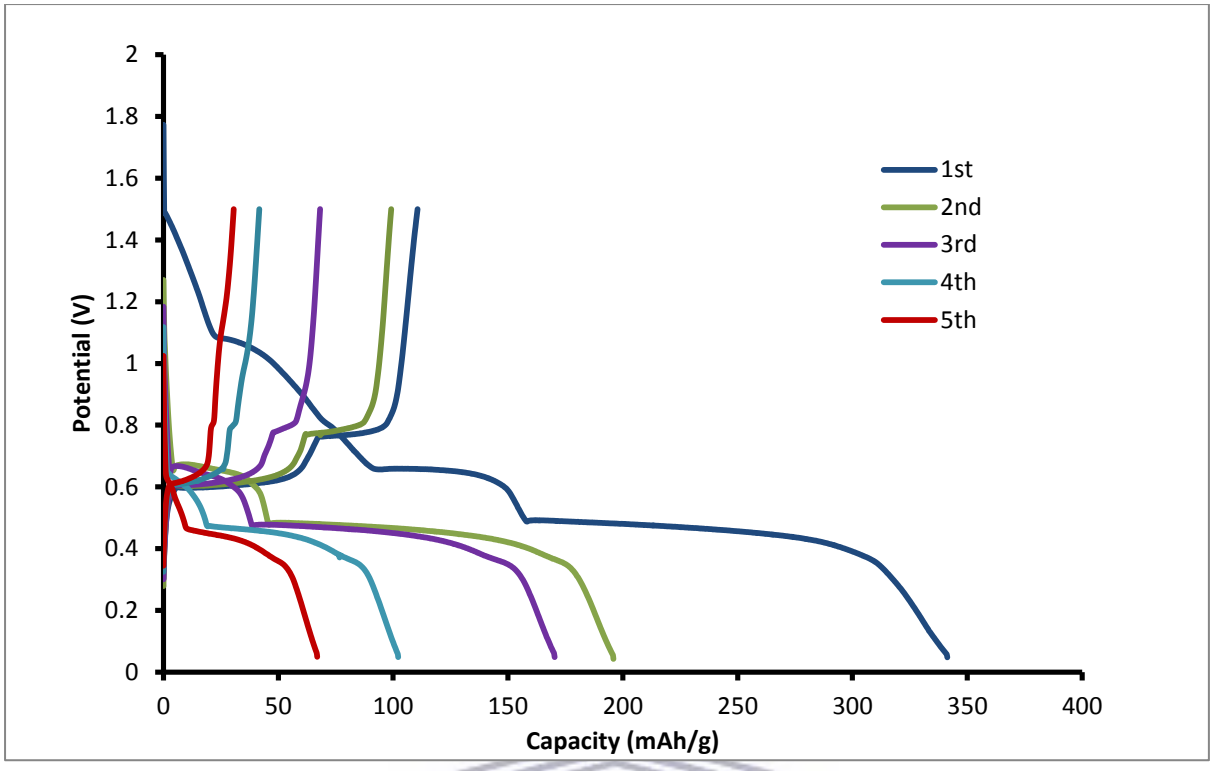

Figure 5.27: Discharge and charge profiles of SnBi (3:1) for the first 5 cycles at 0.1 C (38.5 mA g^{-1}) within 0.05-1.5 V range.

The cyclic voltammetry further confirmed the presence of two redox pairs as shown in Figure 5.28 and Figure 5.29. The CV for SnBi 1:1 and SnBi (1:3) (Figure 5.28 and Figure 5.29) show two oxidation peaks at 0.70 V and 0.81 V, and the corresponding reduction pairs at 0.60 V and 0.37 V for the sodiation and desodiation process respectively. This is consistent with that found in literature (Liu *et al.* 2016; Liu *et al.* 2017). The CV redox pairs are reversible and correspond to the formation of Na-Bi and Na_3Bi (Liu *et al.* 2016; Yin *et al.* 2017). The initial reduction cycles shows further peaks at 1.5 V and 1 V, these disappear on the subsequent cycles. These peaks are possibly due to formation of solid interphase (SEI) layer and irreversible reactions (Liu *et al.* 2016; Zhang *et al.* 2016). The CV curves for SnBi 3:1 corresponds with the charge and discharge curves. The peaks shifted to higher potential after the first cycle due to polarisation of the electrode. The reduction peak at 0.37 V has a characteristic small shoulder peak, and this peak is more pronounced at the CV for SnBi 3:1. This peak could be due to the presence of Sn, Sn suffers more volumetric changes during cycling, it segregates and fails to intercalate Na resulting in the capacity fade (Li *et al.* 2015).

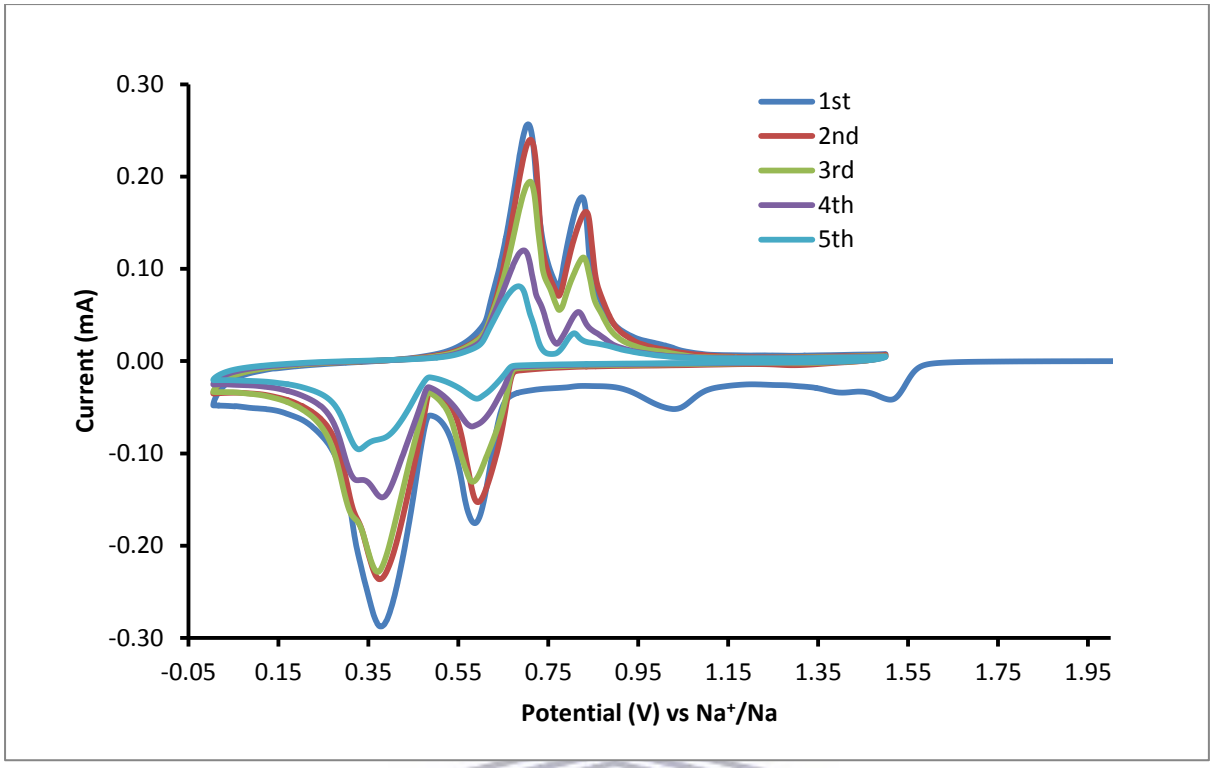

Figure 5.28: Cyclic voltammogram of SnBi (1:1) electrode at a scan rate of 0.1 mV/s within the potential range of 0.05-1.5 V *versus* Na^+/Na.

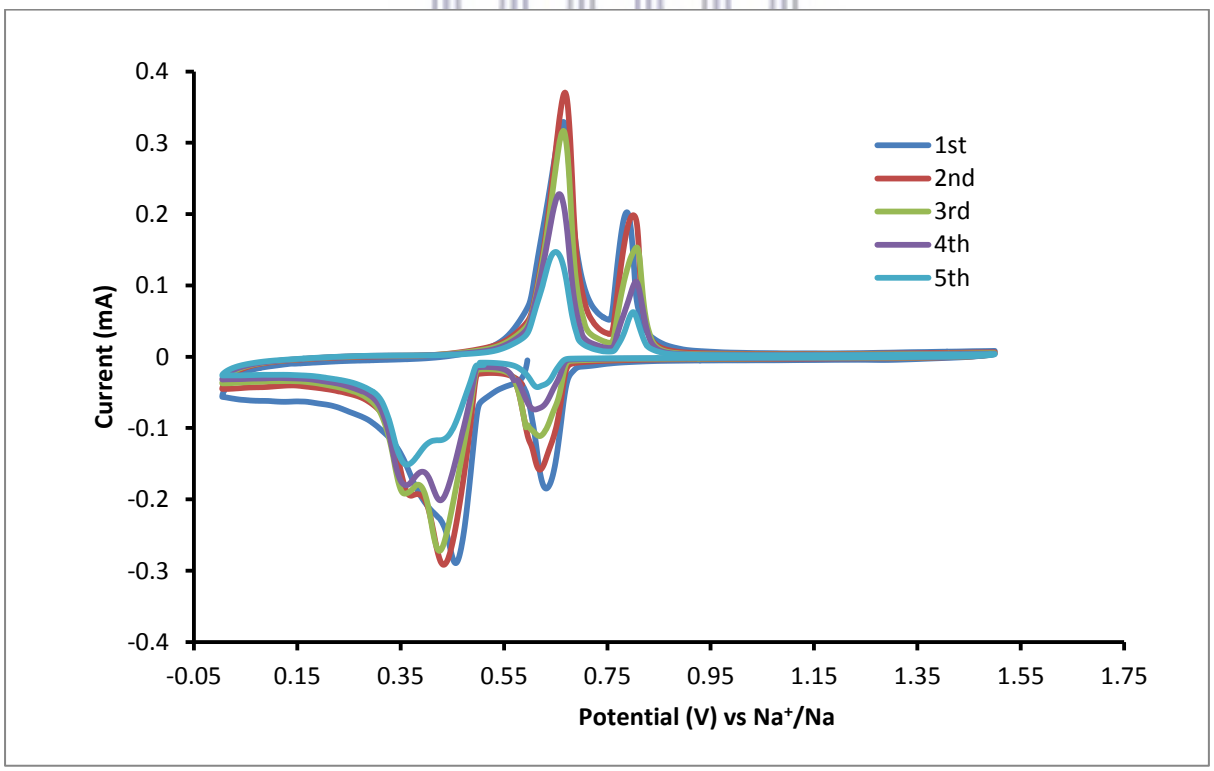

Figure 5.29: Cyclic voltammogram of SnBi (3:1) electrode at a scan rate of 0.1 mV/s within the potential range of 0.05-1.5 V *versus* Na^+/Na.

The cycling performance of the SnBi 1:1 electrode is shown in Figure 5.30. The graph shows that the initial capacity of 1900 mAh/g drops rapidly to 140 mAh/g within 10 cycles continues to drop until 60 mAh/g at 50 cycles until it reaches 35 mAh/g at 100 cycles. While the cycling performance of SnBi 3:1 (Figure 5.31) showed a rapid capacity loss within the first ten cycles to 20 mAh/g and then to zero on the cycle number 12. The capacity fade shows that the material is not stable. The electrochemical kinetics of the SnBi 3:1 electrode is faster than that of SnBi 1:1 electrode. The redox pairs were found to be slightly shifted on the two electrodes while the charge and discharge plateau remained the same as shown in Table 5.2. The CV curves for both electrodes resembles that of a pure Bi electrode material, and the charge and discharge plateaus were found to match those of the pure Bi electrode tested by Su and co-workers (Su *et al.* 2015). This indicates that Bi is the dominant material, which possible because the electrode material contains much higher content of Bi as opposed to Sn. Previous studies show that tin charge and discharge curves contain four plateaus that become less distinct with cycling, usually three are visible, which is not the case on this material (Li *et al.* 2015; Cui *et al.* 2017).

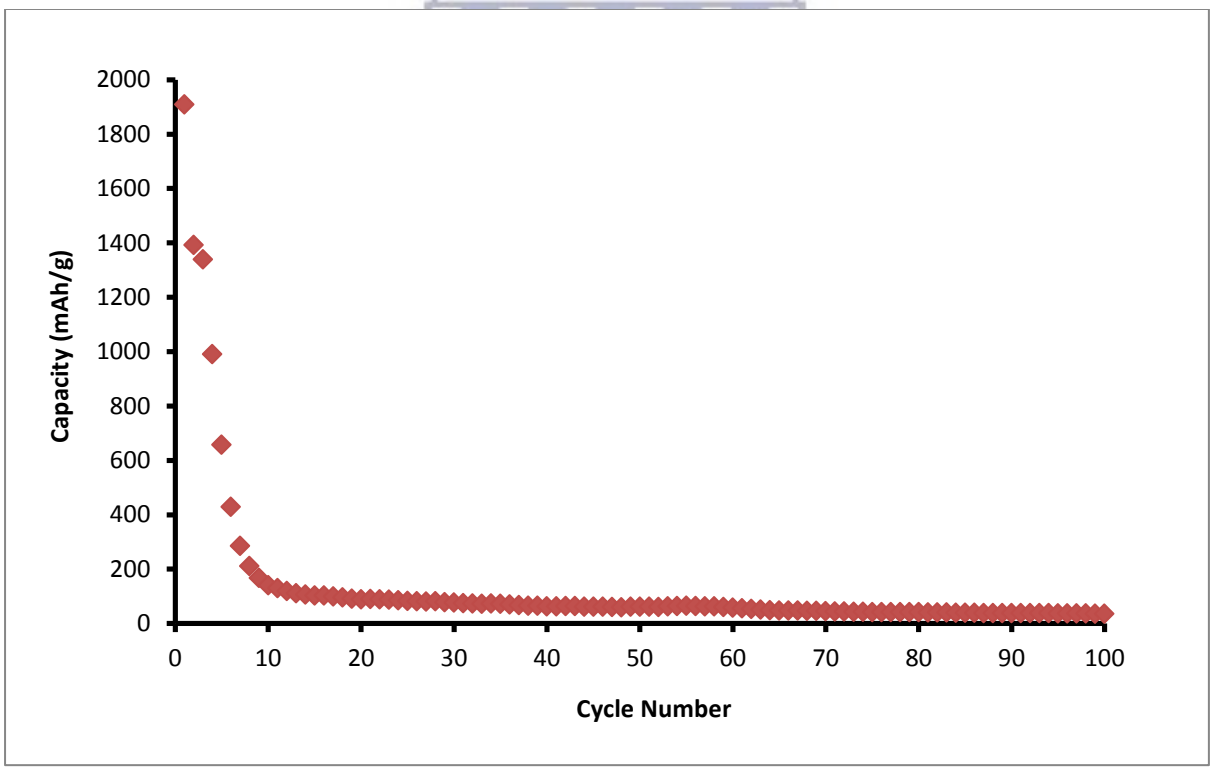

Figure 5.30: Cycling performance of SnBi electrode at 0.1 C (38.5 mA g^{-1}) within 0.05-1.5 V range.

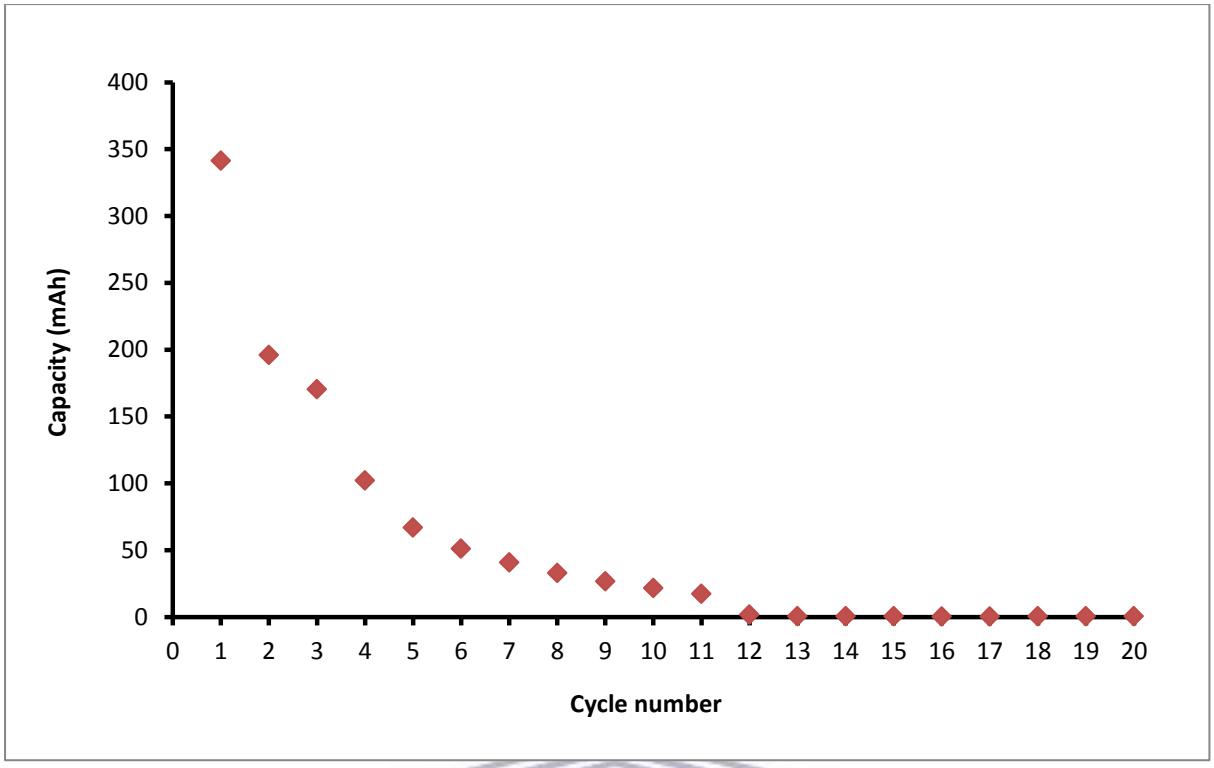

Figure 5.31: Cycling performance of SnBi (3:1) electrode at 0.1 C (38.5 mA g^{-1}) within 0.05-1.5 V range.

Table 5.2: Comparison of the electrode materials electrochemical from Figure 5.26 and Figure 5.27.

	SnBi (1:1)		SnBi (1:3)	
Initial discharge capacity (mAh/g)	1900		338	
Second cycle (mAh/g)	1297		195	
5th cycle (mAh/g)	633		67	
10th cycle (mAh/g)	140		22	
Discharge plateau (V)	0.5	0.67	0.6	0.76
Charge plateau (V)	0.5	0.67	0.6	0.76

The SnBi electrode material has a lot of potential as an anode for Na ion batteries and this is demonstrated by comparing it with similar materials from literature. The Nyquist plots of the SnBi (1:1) and (3:1) electrodes are shown in Figure 5.32 and Figure 5.33. The Nyquist plots were fitted using the electrical circuit (inset figure 5.32 and 5.33) and the fitted parameters of the samples and the comparison to other Bi electrode is shown in Table 5.3. The SnBi (1:1)

and SnBi (3:1) electrode were found to have a R_{ct} of 326 Ω and 55 Ω, and a R_f value of 12.69 Ω and 2.15 Ω respectively. These findings indicate that the film with lower film and charge transfer resistance should give a higher capacity, which is not what was found as the SnBi 3:1 gave a lower capacity. This can be attributed to the increased amount of Sn but further studies need to confirm this. Lui and co-workers (2017) synthesized bismuth nanosheets on carbon fiber cloth (Bi/CFC), which is a self-supported electrode material. This material was found to exhibit excellent properties with R_{ct} of 473 Ω; they also reported that of Bi powder found to be 986 Ω. These values are much higher than that obtained for a SnBi (1:1) and SnBi (3:1) electrode indicating that our material is good for Na storage but lacks capacity retention and stability. The Bi/CFC was found to be much more stable and was able to maintain a much higher capacity over a 100 cycles. Nevertheless, SnBi on Cu foil electrode lacks the support that CFC provides to enhance stability caused by volumetric expansion during cycling.

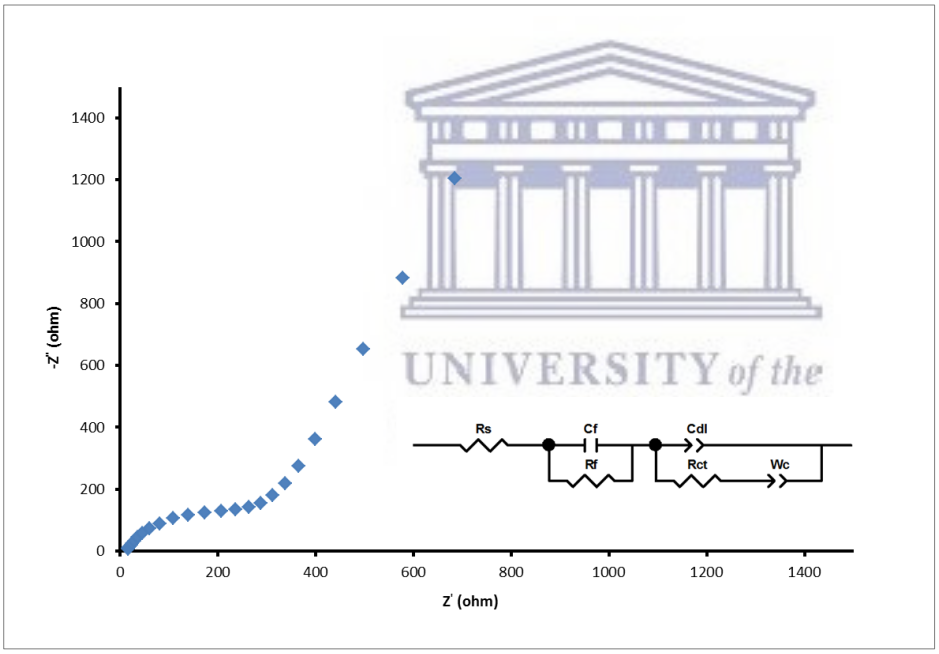

Figure 5.32: Nyquist plot of the electrochemical impedance spectroscopy of the SnBi 1:1 electrode with an insert of circuit of electrode and values of the circuit components (Rs: electrolyte resistance and ohmic resistance; R_f: resistance of the SEI; R_{ct}: charge transfer resistance; C_f: surface passivating layer capacitance; C_{dl}: double layer capacitance; W_c: Warburg impedance).

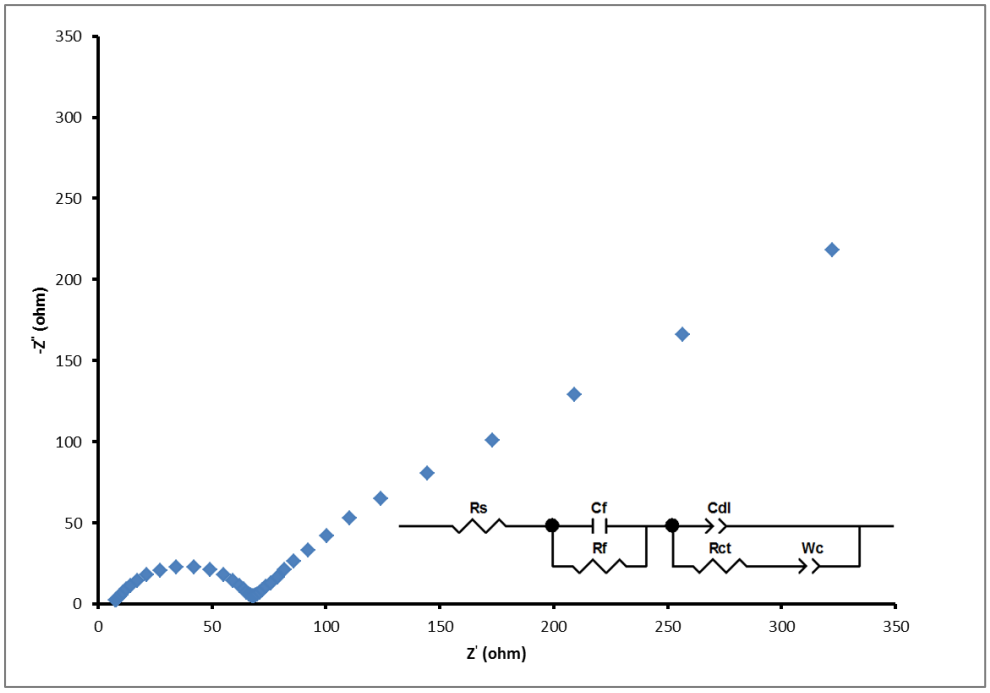

Figure 5.33: Nyquist plot of the electrochemical impedance spectroscopy of the SnBi 3:1 electrode.

Table 5.3: EIS measurement of Bi based electrodes.

Electrode	**R_s (Ω)**	**R_f (Ω)**	**R_{ct} (Ω)**
SnBi/Cu foil (1:1)	14.16	12.69	326
SnBi/Cu foil (3:1)	7.37	2.15	55
Bi/CFC	4.28	23.32	473
Pure Bi powder	17.42	10.2	986

5.4 Conclusion

Thin films of Bi and SnBi were fabricated using electrochemical atomic layer deposition on Cu foil substrates. Parameters including the deposition potential of Bi, and the concentration of Sn were investigated for their effect on the structure and morphology of the films. The UPD potential of Sn was found to be -0.48 V, and that of Bi was -0.2 V. These were used to develop a cycle for deposition of pure Bi films and for both SnBi films. The Bi thin films formed at varied potentials were structurally different. It was found that well defined

structures with larger particles were formed when Bi and Sn content were the same. The deposited material was found to be crystalline, Bi films were mainly bismuth and bismuth oxide, SnBi films contained bismuth tin oxide and other phases of Cu and Sn. A ration of 1:80 of SnBi films formed using equal amounts of Sn and Bi precursors. The thickness was found to increase with cycle number and varied along the film. Sn was distributed evenly across the film while some Bi was found more concentrated on the surface. The SnBi thin films grown on Cu foil using E-ALD technique were tested for Na ion batteries. The electrode exhibited an initial discharge capacity of 1900 mAh/g for SnBi 1:1 and 338 mAh/g for SnBi (3:1) at 38.5 mA/g. The electrode suffered major capacity loss within the first ten cycles, and it was able to retain low capacity until a 100 cycles. Further work needs to be done to improve stability during cycling. In summary, SnBi thin film alloy materials were formed on Cu foils using E-ALD, better quality films can be produced if single crystal Cu substrates were used.

5.5 References

Banga, D, Jarayaju, N, Sheridan, L, Kim, Y-G, Perdue, B, Zhang, X, Zhang, Q, Stickney, J (2012) Electrodeposition of $CuInSe_2$ (CIS) via electrochemical atomic layer deposition (E-ALD). *Langmuir* **28**, 3024-3031.

Banga, D, Kim, Y-G, Stickney, J (2011) PbSe⁄ PbTe Superlattice formation via E-ALD. *Journal of the Electrochemical Society* **158**, D99-D106.

Cui, J, Yao, S, Kim, J-K (2017) Recent progress in rational design of anode materials for high-performance Na-ion batteries. *Energy Storage Materials* **7**, 64-114.

Czerniawski, JM, Perdue, BR, Stickney, JL (2016) Potential pulse atomic layer deposition of Cu2Se. *Chemistry of Materials* **28**, 583-591.

Czerniawski, JM, Stickney, JL (2016) Electrodeposition of In2Se3 Using potential pulse atomic layer deposition. *Journal of Physical Chemistry C* **120**, 16162-16167.

Dahbi, M, Yabuuchi, N, Kubota, K, Tokiwa, K, Komaba, S (2014) Negative electrodes for Na-ion batteries. *Physical Chemistry Chemical Physics* **16**, 15007-15028.

Fonticelli, M, Tucceri, RI, Posadas, D (2004) Deposition and stripping processes of tin on gold film electrodes studied by surface conductance. *Electrochimica Acta* **49**, 5197-5202.

Fujiwara, Y, Enomoto, H (2004) Intermetallic phase formation in electrochemical alloy deposition. *Journal of Solid State Electrochemistry* **8**, 167-173.

Gao, Y, Hu, W, Gao, X, Duan, B (2014) Electrodeposition of SnBi coatings based on deep eutectic solvent. *Surface Engineering* **30**, 59-63.

Gichuhi, A, Boone, BE, Shannon, C (2002) Resonance Raman scattering and scanning tunneling spectroscopy of CdS thin films grown by electrochemical atomic layer epitaxy - thickness dependent phonon and electronic properties. *Journal of Electroanalytical Chemistry* **522**, 21-25.

Gregory, BW, Stickney, JL (1991) Electrochemical atomic layer epitaxy (ECALE). *Journal of Electroanalytical Chemistry* **300**, 543-561.

Hu, C-C, Tsai, Y-D, Lin, C-C, Lee, G-L, Chen, S-W, Lee, T-C, Wen, T-C (2009) Anomalous growth of whisker-like bismuth–tin extrusions from tin-enriched tin–Bi deposits. *Journal of Alloys and Compounds* **472**, 121-126.

Jayaraju, N, Banga, D, Thambidurai, C, Liang, XH, Kim, YG, Stickney, JL (2014) PtRu nanofilm formation by electrochemical atomic layer deposition (E-ALD). *Langmuir* **30**, 3254-3263.

Jayaraju, N, Vairavapandian, D, Kim, YG, Banga, D, Stickney, JL (2012) Electrochemical atomic layer deposition (E-ALD) of Pt nanofilms using SLRR cycles. *Journal of the Electrochemical Society* **159**, D616-D622.

Kubota, K, Komaba, S (2015) Practical issues and future perspective for Na-ion batteries. *Journal of The Electrochemical Society* **162**, A2538-A2550.

Lee, SF, Goh, YX, Haseeb, A, Ieee (2012) Effects of Stacking Sequence of Electrodeposited Sn and Bi Layers on reflowed Sn-Bi Solder Alloys. In '2012 35th IEEE/CPmt International Electronic Manufacturing Technology Symposium.'

Li, Z, Ding, J, Mitlin, D (2015) Tin and tin compounds for sodium ion battery anodes: phase transformations and performance. *Accounts of Chemical Research* **48**, 1657-1665.

Liang, XH, Zhang, QH, Lay, MD, Stickney, JL (2011) Growth of Ge nanofilms using electrochemical atomic layer deposition, with a "bait and switch" surface-limited reaction. *Journal of the American Chemical Society* **133**, 8199-8204.

Liu, S, Feng, J, Bian, X, Liu, J, Xu, H (2016) Advanced arrayed bismuth nanorod bundle anode for sodium-ion batteries. *Journal of Materials Chemistry A* **4**, 10098-10104.

Liu, S, Luo, Z, Guo, J, Pan, A, Cai, Z, Liang, S (2017) Bismuth nanosheets grown on carbon fiber cloth as advanced binder-free anode for sodium-ion batteries. *Electrochemistry Communications* **81**, 10-13.

Mkwizu, TS, Mathe, MK, Cukrowski, I (2010) Electrodeposition of multilayered bimetallic nanoclusters of ruthenium and platinum via surface-limited redox-replacement reactions for electrocatalytic applications. *Langmuir* **26**, 570-580.

Mortazavi, M, Ye, Q, Birbilis, N, Medhekar, NV (2015) High capacity group-15 alloy anodes for Na-ion batteries: Electrochemical and mechanical insights. *Journal of Power Sources* **285**, 29-36.

Okamoto, N, Fujii, Y, Kurihara, H, Kondo, K (2009) effects of microstructure of deposited sn films and orientation index of Cu foils on Sn whisker formation using substitutionally-deposited Sn films. *Materials Transactions* **50**, 2570-2577.

Pan, H, Hu, Y-S, Chen, L (2013) Room-temperature stationary sodium-ion batteries for large-scale electric energy storage. *Energy & Environmental Science* **6**, 2338-2360.

Sandnes, E, Williams, ME, Vaudin, MD, Stafford, GR (2008) Equi-axed grain formation in electrodeposited Sn-Bi. *Journal of Electronic Materials* **37**, 490-497.

Sheridan, LB, Czerwiniski, J, Jayaraju, N, Gebregziabiher, DK, Stickney, JL, Robinson, DB, Soriaga, MP (2012) Electrochemical atomic layer deposition (E-ALD) of palladium nanofilms by surface limited redox replacement (SLRR), with EDTA complexation. *Electrocatalysis* **3**, 96-107.

Sheridan, LB, Gebregziabiher, DK, Stickney, JL, Robinson, DB (2013) Formation of palladium nanofilms using electrochemical atomic layer deposition (E-ALD) with chloride complexation. *Langmuir* **29**, 1592-1600.

Stevens, D, Dahn, J (2000) High capacity anode materials for rechargeable sodium-ion batteries. *Journal of the Electrochemical Society* **147**, 1271-1273.

Stickney, JL, Ehlers, CB (1989) Surface chemistry of electrodes: Cu(111) in aqueous HCl. *Journal of Vacuum Science & Technology A: Vacuum, Surfaces, and Films* **7**, 1801-1805.

Su, D, Dou, S, Wang, G (2015) Bismuth: A new anode for the Na-ion battery. *Nano Energy* **12**, 88-95.

Suh, M-S, Park, C-J, Kwon, H-S (2006) Effects of plating parameters on alloy composition and microstructure of Sn–Bi electrodeposits from methane sulphonate bath. *Surface and Coatings Technology* **200**, 3527-3532.

Tsai, Y-D, Hu, C-C (2009a) Composition control of lead-free Sn–Bi deposits using experimental strategies. *Journal of the Electrochemical Society* **156**, D58-D63.

Tsai, YD, Hu, CC (2009b) Composition control of Sn-Bi deposits: interactive effects of citric acid, ethylenediaminetetraacetic acid, and poly(ethylene glycol). *Journal of the Electrochemical Society* **156**, D490-D496.

Tsai, YD, Hu, CC (2011) Composition and microstructure control of tin-bismuth alloys in the pulse plating process. *Journal of the Electrochemical Society* **158**, D482-D489.

Tsai, YD, Lien, CH, Hu, CC (2011) Effects of polyethylene glycol and gelatin on the crystal size, morphology, and Sn2+-sensing ability of bismuth deposits. *Electrochimica Acta* **56**, 7615-7621.

Venkatasamy, V, Mathe, MK, Cox, SM, Happek, U, Stickney, JL (2006) Optimization studies of HgSe thin film deposition by electrochemical atomic layer epitaxy (EC-ALE). *Electrochimica Acta* **51**, 4347-4351.

Ward, LC, Stickney, JL (2001) Electrodeposition of Sb onto the low-index planes of Cu in aqueous chloride solutions: studies by LEED, AES and electrochemistry. *Physical Chemistry Chemical Physics* **3**, 3364-3370.

Yin, H, Li, Q, Cao, M, Zhang, W, Zhao, H, Li, C, Huo, K, Zhu, M (2017) Nanosized-bismuth-embedded 1D carbon nanofibers as high-performance anodes for lithium-ion and sodium-ion batteries. *Nano Research* **10**, 2156-2167.

Zhang, JQ, Yang, JY, Liu, M, Li, G, Li, WX, Gao, S, Luo, YB (2014) Fabrication of CdTe quantum dots sensitized TiO2 nanorod-array-film photoanodes via the route of electrochemical atomic layer deposition. *Journal of the Electrochemical Society* **161**, D55-D58.

Zhang, Y, Lu, S, Wang, M-Q, Niu, Y, Liu, S, Li, Y, Wu, X, Bao, S-J, Xu, M (2016) Bismuth oxychloride ultrathin nanoplates as an anode material for sodium-ion batteries. *Materials Letters* **178**, 44-47.

Zhu, W, Yang, JY, Hou, J, Gao, XH, Bao, SQ, Fan, XA (2005) Optimization of the formation of bismuth telluride thin film by using ECALE. *Journal of Electroanalytical Chemistry* **585**, 83-88.

CHAPTER 6

6 Pd, PdSn, PdBi, and PdBiSn Catalysts for the Electro-Oxidation of Alcohols in Alkaline Direct Alcohol Fuel Cells

Pd, PdSn, PdBi, PdBiSn on Au substrate thin films were prepared using electrochemical atomic layer deposition for the electro-oxidation of ethanol and glycerol in alkaline media. Scanning electron microscopy results showed that the nanoparticles were evenly distributed on the surface, while the elemental analysis confirmed the presence of all elements on the prepared materials. Cyclic voltammetry studies were used to test the activity of the catalysts towards alcohol electro oxidation reaction (AOR). AOR revealed that the addition of Sn and Bi on Pd improved the activity and that all the catalysts were more active towards ethanol oxidation than glycerol.

6.1 Introduction

Direct alcohol fuel cells (DAFCs) are attractive alternative power sources over hydrogen fuel cells for electronics and hybrid electric vehicles (Zhang *et al.* 2016). DAFCs use alcohols (methanol, ethanol, glycerol, ethylene glycol, propanol, and butanol) as fuel, which is widely available as a by-product in the biofuels industry, providing clean energy (Yi *et al.* 2015). Other advantages of using alcohols are that they are easily stored and distributed, as well as high gravimetric and volumetric energy density.

Alkaline Fuel Cells (AFCs) can theoretically outperform Proton Exchange Membrane Fuel Cells (PEMFCs). AFCs also have several advantages over PEMFCs on both faster cathode kinetics and Ohmic polarization. Moreover, the alkaline environment, which is less corrosive, ensures a longer durability and the use of non-noble cheap oxygen reduction reaction electro-catalysts cuts down the costs of the fuel cell drastically. A major limitation of AFCs however, was the progressive carbonation of the alkaline electrolyte due to CO_2 formation from air or the oxidation product of the fuel. This problem was addressed mainly by the application of anion exchange membranes (AEMs) (Markovic *et al.* 1997; Cifrain and Kordesch 2003; Blizanac *et al.* 2007; Antolini and Gonzalez 2010; Friedl and Stimming 2013; Kamarudin *et al.* 2013). Over the past decade, alkaline direct alcohol fuel cells (ADAFCs) have attracted increasing interest due to the favourable reaction kinetics in alkaline media, easy handling of the liquid fuels and the higher energy densities achievable. ADAFCs using AAEMs have

several advantages over conventional alkaline fuel cells: 1) no electrolyte leaking, 2) since there is no mobile cation, there is no precipitated carbonate, 3) reduced alcohol crossover, 4) potential simplified water management due to the fact that water is produced at the anode and consumed at the cathode, and 5) potentially reduced corrosion (Antolini and Gonzalez 2010; Braunchweig *et al.* 2013).

The oxidation of alcohols is necessary for energy production and this requires breaking the C-C bonds which is difficult to do (Zalineeva *et al.* 2014; Zhang *et al.* 2016). The main catalysts used in the electro-oxidation of alcohols uses Pt catalysts, and this has been done in acidic media. The extensive use of Pt catalysts is not economically viable due to Pt cost, the slow kinetics of the reaction, and also the CO poisoning of the catalyst (Feng *et al.* 2013; Yi *et al.* 2015). Pd based catalysts in basic media are great alternatives. Pd and Pt have similar chemistries (same group elements). The electro-oxidation reaction of ethanol using Pd in alkaline media is limited by slow kinetics. The rate is limited by the removal of adsorbed acetyl species by reacting with hydroxyl species forming acetates (Yi *et al.* 2015; Zhang *et al.* 2016). A minor quantity of the acetyl species goes towards decomposition to form hydrocarbons and carbon monoxide further oxidised to carbon dioxide. This reaction mechanism is shown in Figure 6.1.

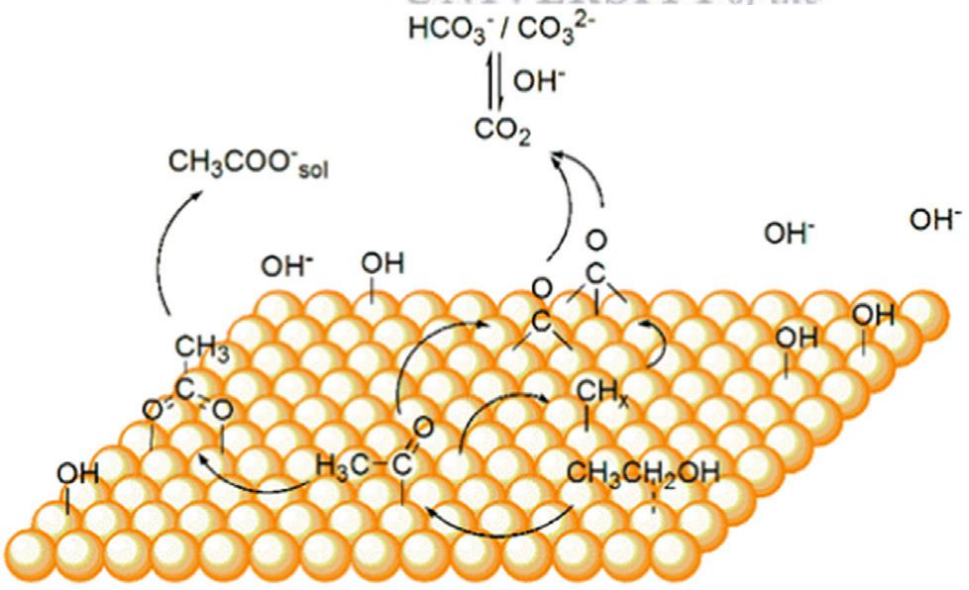

Figure 6.1: Mechanism for ethanol electro-oxidation on Pd surface (Zhang *et al.* 2016)

Pd based catalysts have been investigated for AOR in alkaline media, and further research still needs to be done to improve activity, selectivity and stability of the catalysts (Dutta *et al.* 2011; Modibedi *et al.* 2011; Cai *et al.* 2013; Feng *et al.* 2013; Friedl and Stimming 2013; Modibedi *et al.* 2013; Dutta *et al.* 2017). This can be done by formation of nano sized catalysts for high surface area, and the addition of other elements to Pd to improve catalytic activity. Electrochemical atomic layer deposition (E-ALD) allows the formation of well ordered, tailor made, and thin films material using monolayer formation on well-ordered surfaces using underpotential deposition and surface limited redox reactions (Gregory *et al.* 1991). The formation of Pd nanostructures on Au substrates is well covered in literature (Kibler *et al.* 1999; Kibler *et al.* 2000; El-Aziz and Kibler 2002; Hoyer *et al.* 2003; Kibler *et al.* 2003; Tang *et al.* 2005).

This study aims to fabricate PdSn, PdBi and PdBiSn thin films on Au electrodes using E-ALD technique. Pd was deposited via SLRR of Cu UPD on Au electrode; while Pd containing Sn and or Bi was deposited using SLRR of Cu UPD followed by direct UPD of Sn or Bi. The deposition cycle used was developed from the study of the reduction and oxidation of each element using cyclic voltammetry. The formed material was characterised using field emission scanning electron microscope (FESEM) for morphology equipped with energy dispersive detector (EDS) for the elemental analysis. The activity of each material towards AOR of ethanol and glycerol was investigated using cyclic voltammetry. Ethanol is attracting great attention as fuel since it is less toxic than methanol and can be massively produced from agricultural products or biomass, in addition to the advantage of high-specific energy (Hoogers 2002). Hence, tremendous efforts have been made in the development of alkaline direct ethanol fuel cells (ADEFCs). Ethanol has also been proven by research to have a lower crossover rate and affects the cathode performance less severely than methanol (Carmo *et al.* 2013). Another attractive fuel is glycerol. As a main product in biodiesel production, glycerol is supplied in large quantities at low price. Therefore glycerol is expected to be used in ADAFCs as an inexpensive, renewable, and environmental friendly fuel.

The challenge therefore remains to fully oxidize the ethanol which releases 12 electrons and not to end up with acetaldehyde or acetic acid, which leads to a low faradaic efficiency (17-33% of the theoretical energy) and to non-value-added compounds. For glycerol the challenge is the removal of poisonous intermediates at low overpotentials, as these intermediates decreases the total efficiency of the system.

6.2 Method

6.2.1 Materials and Reagents

High purity (≤ 1 μS/cm) deionised water and ACS Reagent grade chemicals (Sigma Aldrich) were used in the preparation of all solutions. The chemical solutions prepared were as follows: 0.1 mM $PdCl_2$ in 0.5 M HCl, 1 mM $CuSO_4$ in 0.1 M H_2SO_4, 0.2 mM SnO in 0.1 M H_2SO_4 , and 0.2 mM Bi_2O_3 in 0.1 M H_2SO_4.

6.2.2 Substrate treatment

Au-coated glass slides containing 100 nm Au film on 5 nm Ti on glass (evaporated metal films, Ithaca, NY) used. Prior use, they were cleaned by sonication in acetone for 5 minutes, deionised water rinse, dipped in concentrated HNO_3 for 2 minutes, deionised water rinse, and finally dried with nitrogen.

6.2.3 Electrodeposition of Pd based materials on Au substrate

The electrodeposition of Pd based materials was done using Cu UPD on Au substrate was adapted from the work done by Mkwizu and co-workers (Mkwizu *et al.* 2010) ,and Modibedi and co-workers (Modibedi *et al.* 2013), as well as other sources (Sheridan *et al.* 2012; Sheridan *et al.* 2013). It was carried out as follows. (i) Pump the Cu solution into the cell at an applied potential (E_{app}), (ii) Keep the Cu solution in the flow cell to deposit Cu at E_{app} ,(iii) Pump Pd solution into the cell at open circuit potential (E_{ocp}), (iv) Keep Pd solution in the cell for deposit Pd (SLRR) at E_{ocp}, (v) Rinse with electrolyte at E_{ocp}. This cycle was repeated as many times as required to form the deposit. Pd materials containing Sn and Bi were formed by introducing a second element in the following steps and depositing it at UPD as described in results section.

6.2.4 Characterisation

The electrochemical activity of the prepared Pd based catalysts was evaluated using an electrochemical flow cell with three electrode system as described in chapter 4 and 5, as well in literature (Sheridan *et al.* 2012; Modibedi *et al.* 2013; Czerniawski and Stickney 2016). Cyclic and linear sweep voltammetry in N_2 saturated 0.1 M KOH, 0.1 M EtOH, and 0.1 M glycerol on a potentiostat Metrohm PGSTAT101 controlled by NOVA 1.8 software was conducted. The morphology of the materials was evaluated using a scanning electron microscope performed on a LEO 1525 field emission scanning microscope (FE-SEM) with the acceleration voltage of 2.00 kV, and equipped with dispersive detector (EDS) for elemental mapping.

6.3 Results and discussion

6.3.1 Electrodeposition of various Pd on Au catalysts

The characteristic cyclic voltammogram (CV) of 1 mM $CuSO_4$ in 0.1 M H_2SO_4 on Au electrode is shown in Figure 6.2. The scan began at 0.35 V negatively until a lower limit of -0.35 V and reversed. The negative scan shows a bulk deposition peak onset at -0.025 V and the corresponding bulk stripping peak at 0.05 V. The insert graph A shows the UPD region where it was found to occur between 0.2 V to 0 V. This is consistent to the values reported in literature (Sheridan *et al.* 2012; Sheridan *et al.* 2013; Aldana-Gonzalez *et al.* 2015). The obtained Cu UPD was used to form a Pd deposition cycle, where Pd was deposited at a set potential, followed by replacement with Pd at open circuit potential. The deposition cycle was made up of the following steps: (i) Pump Cu^{2+} solution for 15 s at OCP; (ii) Deposit Cu at 50 mV for 10 s at 150 mV; (iii) Pump Pd^{2+} solution for 15 s at OCP; (v) Hold the solution at OCP for 10 s; (iv) rinse in blank for 15 s at OCP. The cycle was repeated 25 and 50 times for films growth. The formation of Pd based catalysts containing Sn and Bi will be done by building from the above deposition cycle.

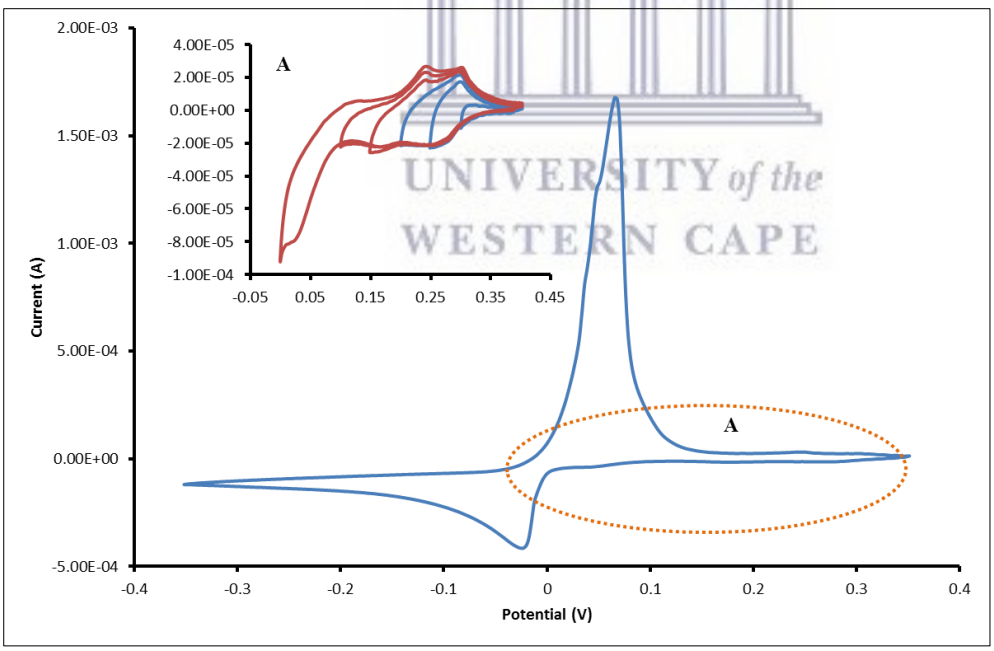

Figure 6.2: Cyclic voltammogram of 1 mM $CuSO_4$ in 0.1 M H_2SO_4 on Au at a scan rate of 10 mV/s, and an insert of the window opening.

The cyclic voltammograms of a Au electrode, Bi^{3+} and Sn^{2+} are discussed in detail in chapter 4 figures 4.1, 4.2 and 4.3, where the UPD of Bi^{3+} and Sn^{2+} was found to be at 50 mV and -325 mV respectively. The obtained information from the CV studies was used to deduce a

deposition cycle for catalysts materials containing Pd, Sn and Bi. Materials made up of PdSn, PdBi and PdBiSn were made using the above deposition cycle followed by Sn or Bi UPD or both. The binary catalyst PdSn deposition cycle steps were as follows: (i) Pump Cu^{2+} solution for 15 s at OCP; (ii) Deposit Cu at for 10 s at 50 mV; (iii) Pump Pd^{2+} solution for 15 s at OCP; (v) Hold the solution at OCP for 10 s; (iv) rinse in blank for 15 s at OCP; vi) Pump Sn^{2+} solution for 15 s at OCP; (vii) Deposit Sn at for 10 s at -325 mV; (viii) rinse in blank for 15 s at OCP. A similar deposition cycle was used for PdBi by replacing Sn UPD with Bi UPD of 50 mV. The formation of a material by alternating Pd SLRR followed by Bi and Sn at UPD was unable to form a deposit, due to Sn and Bi UPD being too far apart as explained in detail in chapter 4. This resulted in the ternary material deposition cycles being designed to avoid this by depositing Pd and Bi first, followed by depositing Pd and Sn, simply as deposition using the PdBi cycle and then the PdSn cycle. Two materials were made namely PdBiSn 25 and PdBiSn 30. The ternary PdBiSn 30 was deposited using a sequence made up of the PdBi cycle repeated 15 times followed by the PdSn cycle repeated 15 times. The PdBiSn 25 was made by depositing PdBi 13 time and PdSn 12 times. The CV is shown in figure 6.3.

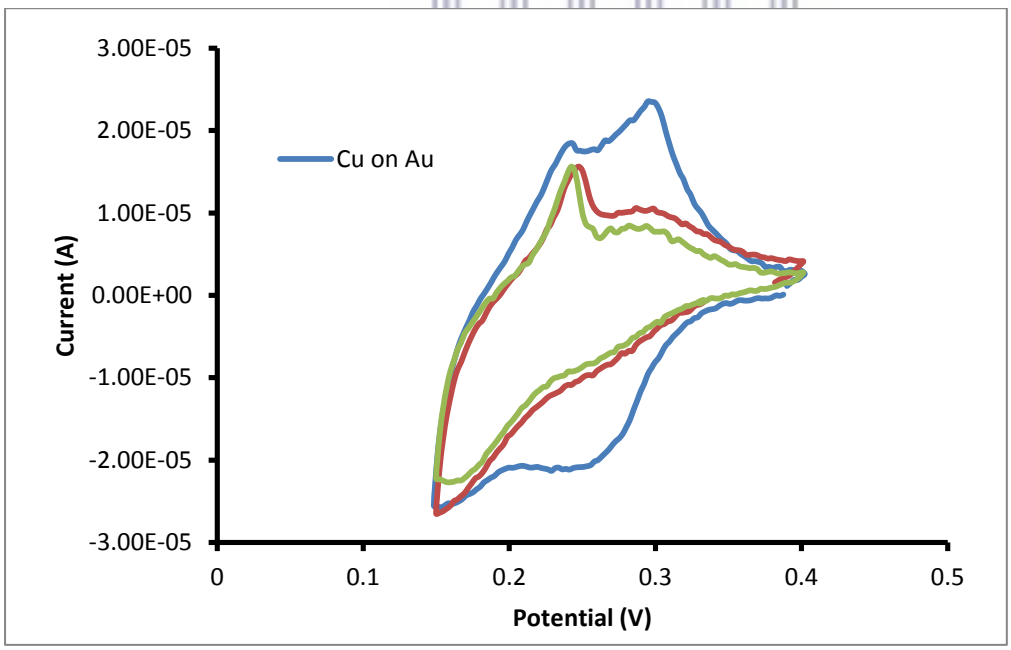

Figure 6.3: Cyclic voltamogram of 1 mM $CuSO_4$ in 0.1 M H_2SO_4 on Bi covered Au, and Sn covered Au, at a scan rate of 10 mV/s.

The possibility of depositing Sn or Bi on top of the Pd layer to form PdSn or PdBi was explored. A CV of Cu^{2+} UPD on Bi and Sn deposited on Au monolayer (Figure 6.3) showed

that the Cu^{2+} UPD has not changed. This resulted in the deposition cycle for SnPd and BiPd being the reverse of PdSn and PdBi. A visible deposit for BiPd was not able to form. The summary of the deposition sequence for each material is given in Table 6.1.

Table 6.1: List of possible Pd based materials catalyst deposition description

Material	Sequence	Number of cycles
Pd	Cu UPD; Pd SLRR at OCP; x25 cycles	25
PdSn	Cu UPD; Pd SLRR, Sn UPD; x25 cyles	25
PdBi	Cu UPD; Pd SLRR; Bi UPD; x25 cycles	25
PdBiSn 30	(i) Cu UPD; Pd SLRR; Bi UPD; x15 cycles; (ii) Cu UPD; Pd SLRR; Sn UPD; x15 cycles	30
PdBiSn	Cu UPD; Pd SLRR; Bi UPD; Sn UPD; x25 cycles	25
SnPd	Sn UPD; Cu UPD; Pd SLRR; x25 cycles	25
BiPd	Bi UPD; Cu UPD; Pd SLRR; x25 cycles	25
PdBiSn 25	(i) Cu UPD; Pd SLRR; Bi UPD; x13 cycles; (ii) Cu UPD; Pd SLRR; Sn UPD; x12 cycles	25

6.3.2 Structural characterisation

The morphology of the formed deposits was investigated using SEM. The Pd deposits were found to have rounded particles clustered all over the surface, in some areas they were found to agglomerate as illustrated in Figure 6.4 and the deposit was found to contain Pd distributed all over the surface as shown on the map and spectra in Figure 6.4. Pd deposits form larger structures on the surface and this is prominent when the number of cycles was increased or for thicker deposits as shown in Figure 6.5 a-b .The PdBi deposits (Figure 6.5 d) were found to contain well rounded larger particles on the surface distributed evenly as well were smaller particles. The elemental map indicated that the surface was evenly covered with Pd and Bi. PdSn and SnPd deposits (Figure 6.5 c and e) were found to have similar characteristics to

each other, where smaller particles are dominant on the surface and few larger randomly distributed particles. Elemental map did not reveal any differences in particles composition. PdBiSn 25 was also similar structurally to the other catalysts (Figure 6.5 f), and the elemental map of PdBiSn 25 in Figure 6.6 shows the presence of Pd, Sn and Bi on the surface directly on top of each other all over the surface. When comparing all the materials, only the PdBi materials exhibited a different morphology to the rest of the prepared materials.

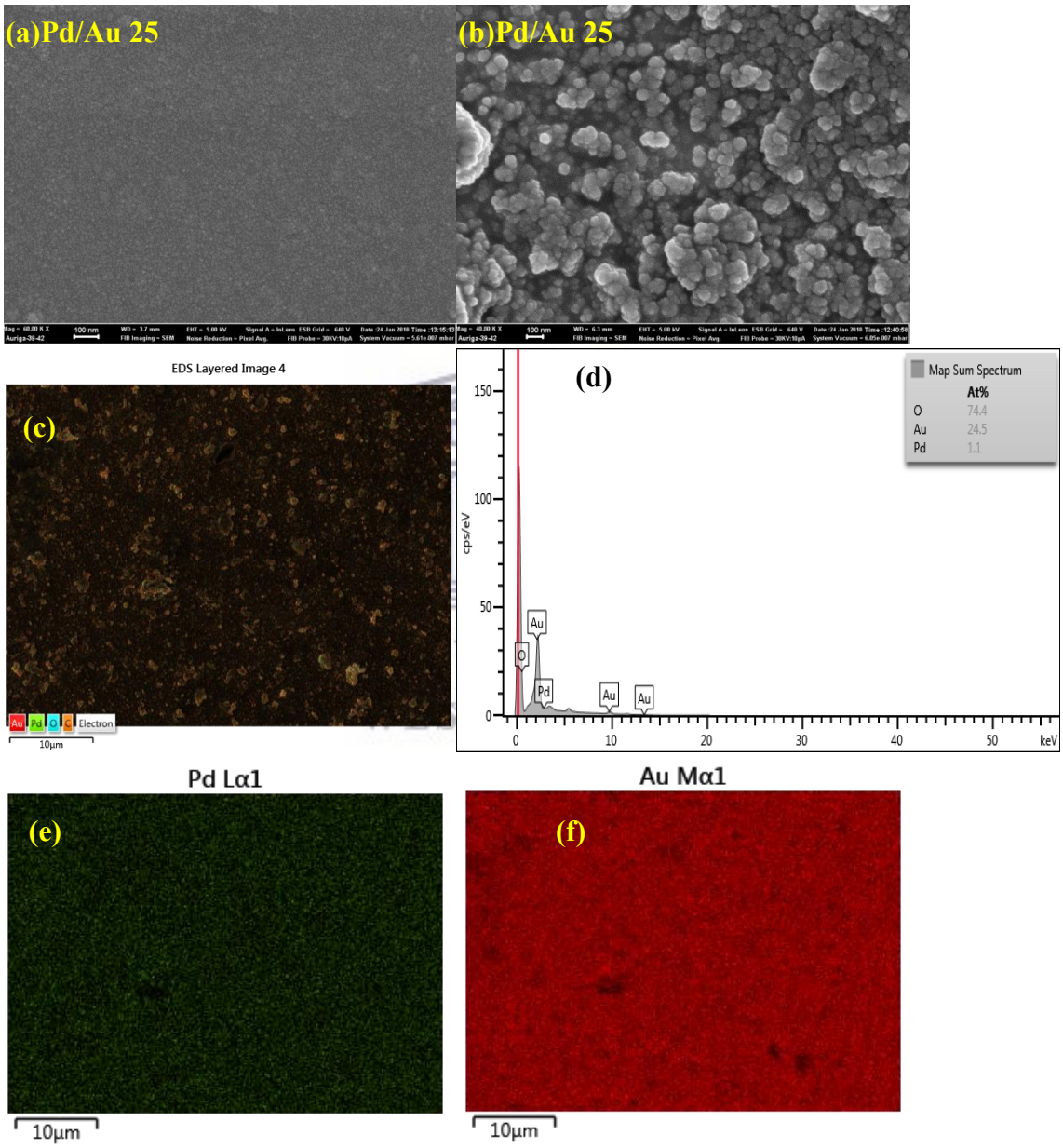

Figure 6.4: SEM images of Pd/Au 25 at different magnification (a and b), and Pd catalysts elemental map (c, e, and f) and spectrum (d).

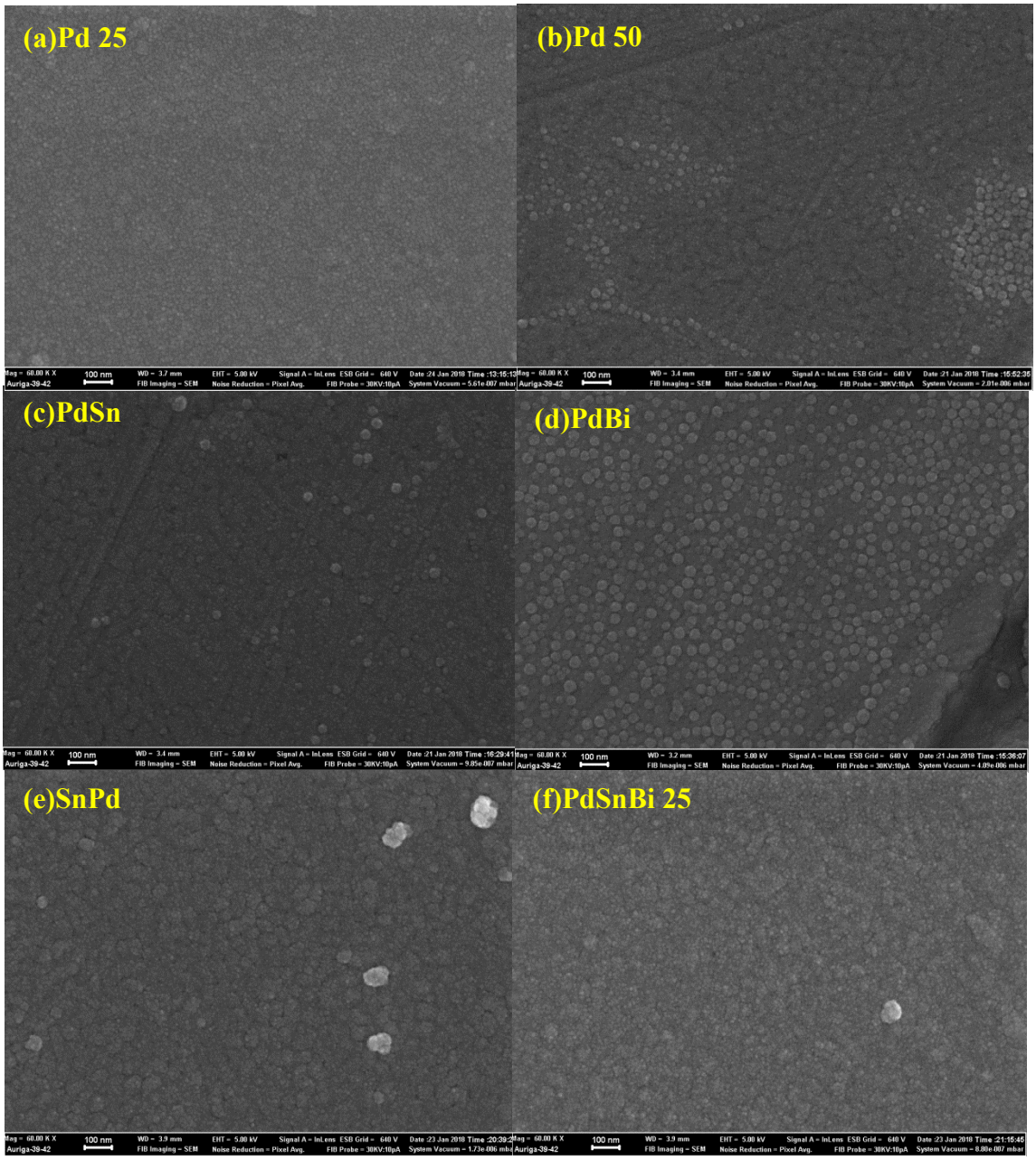

Figure 6.5: SEM images of Pd, Bi and Sn catalysts (a-f).

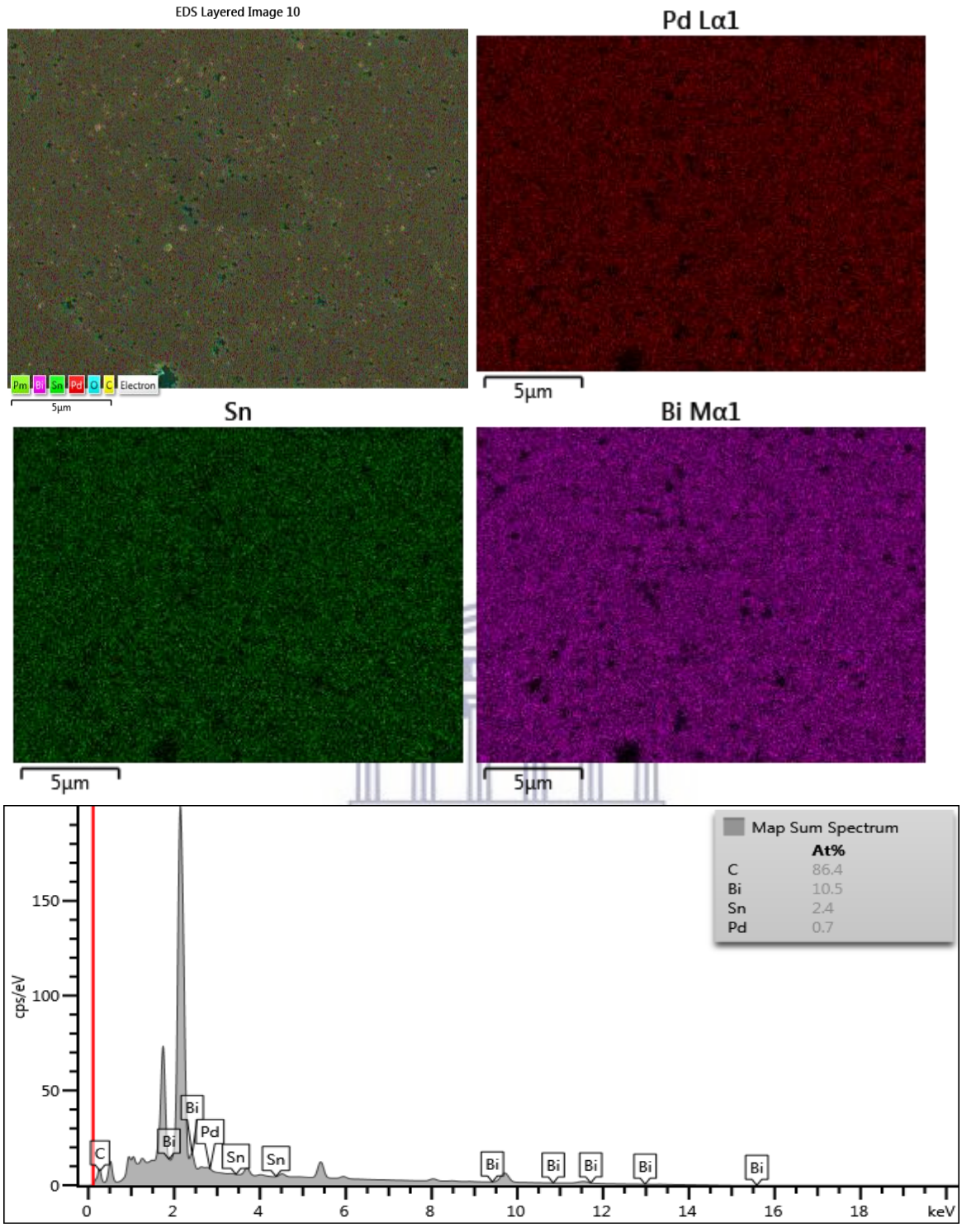

Figure 6.6: Elemntal map and EDS spectra of PdBiSn 25 catalyst.

6.3.3 Electrochemical Characterisation

The cyclic voltammograms of the Pd and Pd modified catalysts in 0.1 M KOH solution are presented in Figure 6.7 and Figure 6.8. The peaks found below -0.8 V onwards are due hydrogen absorption and adsorption on Pd surface. Au is not prone to hydrogen evolution reactions (Feng *et al.* 2013) hence no peaks were observed for Au. The oxidation peaks found at 0V and above is due to the oxidation of Au oxides. The reduction peak observed in the region of 0V towards -0.3V is caused by the reduction of the Pd oxides. This peak is different for all the catalysts, indicating that the modified catalysts have different electrochemical activity. The Pd on Au catalyst exhibited the most pronounced peaks in the hydrogen evolution region (-0.8 V and below), and a higher charging current. The CV shows the signature of Pd in alkaline electrolyte, The SnPd and PdBiSn 25 catalyst had the exact same interaction with KOH, as indicated by their cyclic voltammograms matching. The reduction peaks for all the catalysts occurred at different potentials indicating all the material has a different Pd dispersion on the surface. The current associated with this reduction peak is directly proportional to the charge required to reduce Pd oxides as shown in equation 28 used to calculate the electrochemical active surface (EAS) of the catalyst (Feng et al., 2013). The charge obtained by integrating the area under the Pd reduction peak is shown in Table 6.2. The results shows that BiPd has the highest charge, followed by PdBi, the other catalysts had charge values lower than that of the Pd catalyst. Therefore, the BiPd and PdBi catalysts will have a higher EAS compared to the other catalysts, the presence of Bi improved the exposed surface area of the Pd catalysts.

$$\mathrm{EAS}(\mathrm{m}^2\mathrm{g}_{\mathrm{Pd}}^{-1}) = \frac{\mathrm{Q_r}}{(4.24\ \mathrm{C\ m^{-2}} \times \mathrm{W_{Pd}})Ag(cm2)} \quad (28)$$

Q_R = reduction charge

W_{Pd} = Pd loading mass in grams

A_g = geometry of the surface area

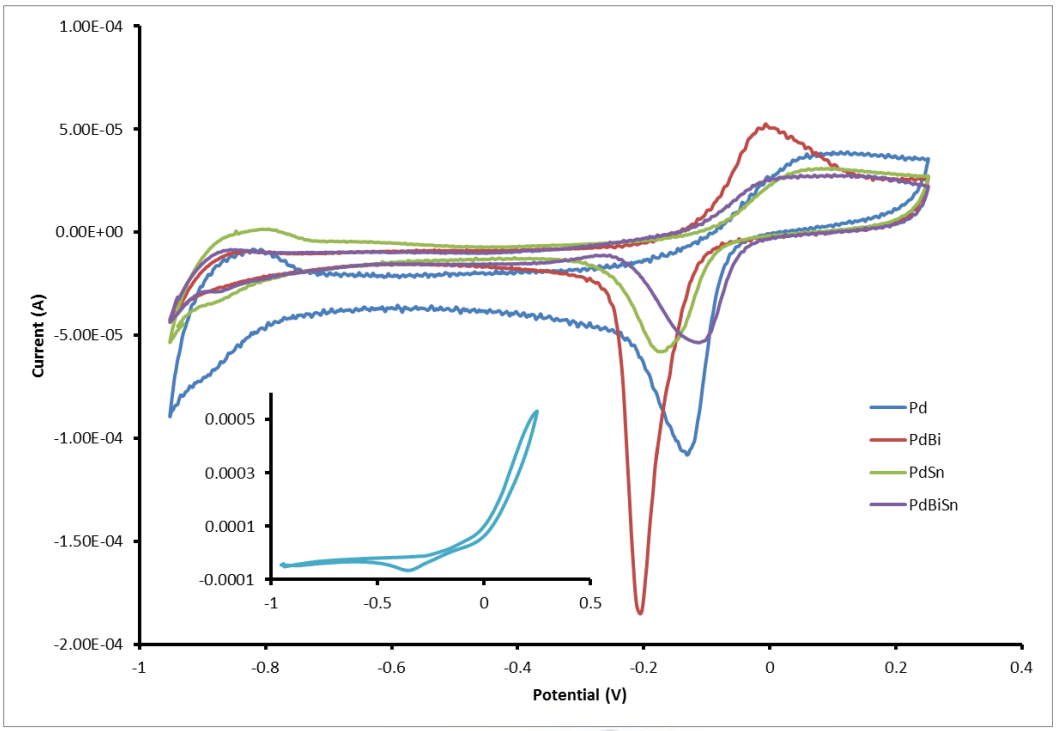

Figure 6.7: Cyclic voltammogram of Pd, PdBi, PdSn and PdBiSn catalysts in 0.5 M KOH at a scan rate of 10 mV/s.

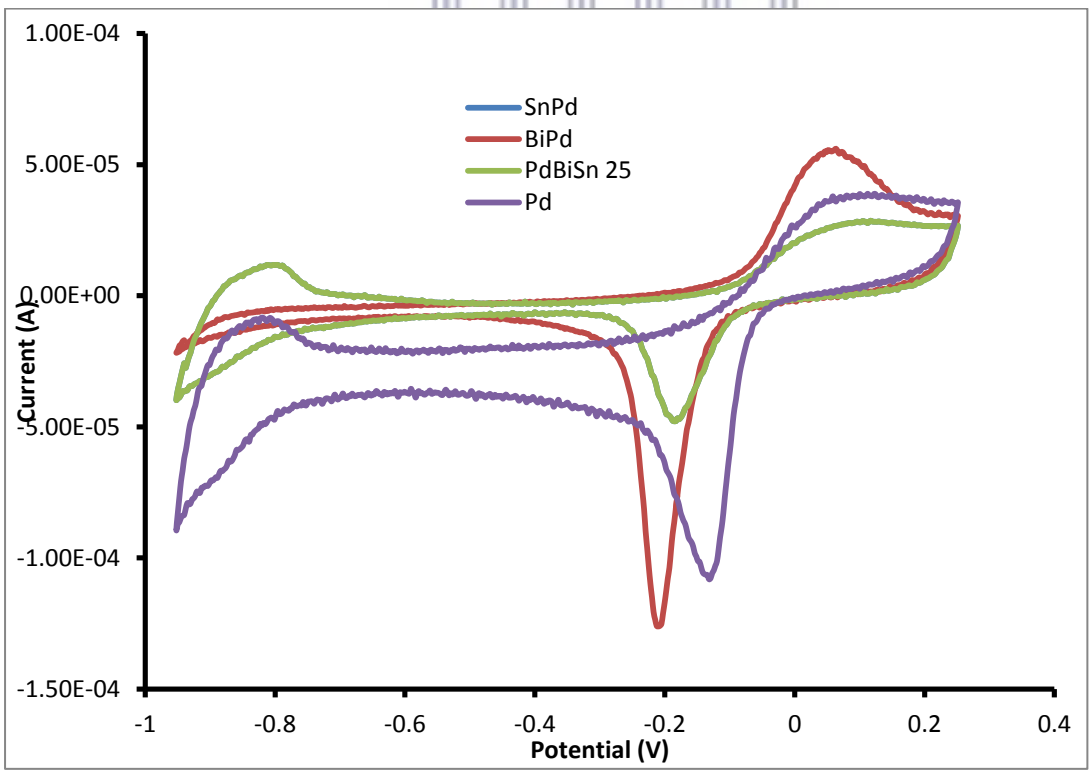

Figure 6.8: Cyclic voltammogram of Pd, BiPd, SnPd and PdBiSn 25 catalysts in 0.5 M KOH at a scan rate of 10 mV/s.

Table 6.2: Summary of the charge for the prepared catalysts

Catalyst	Charge / C
Pd	1.50E-05
PdSn	7.57E-06
SnPd	5.12E-06
PdBi	1.32E-05
BiPd	1.07E-05
PdBiSn 25	5.10E-06
PdBiSn 30	6.88E-06

6.3.3.1 Ethanol electro-oxidation

The activity of the prepared catalysts toward ethanol electro oxidation reaction (EOR) was investigated using cyclic voltammetry in 0.1 M KOH solution and 0.1 M EtOH and this is shown in Figure 6.9-10 and the summary of the results shown in Table 6.2. The forward scan of the CV curves for all the catalysts had lower peak currents than the reverse scans except for the PdBi catalysts. The BiPd catalysts showed no activity towards ethanol oxidation and therefore excluded for further studies. The Pd catalyst exhibited the lowest peak current and broader peaks compared to all the other catalysts for the forward reaction (Figure 6.9), indicating a slow consumption of EtOH on the catalyst (Feng *et al.* 2013). The highest peak currents were observed from the SnPd and SnBiPd 25 catalysts for the reverse CV scan (Figure 6.10), these two materials showed the same activity for EOR, and also had the same interaction with KOH. The sharpness and rapid increase in peak currents is due to the fast removal of the adsorbed acetate intermediate species that were partially oxidised during the forward reaction. This is the rate limiting step for EOR as shown in equation 29-32 where equation 31 shows the rate limiting step (Feng *et al.* 2013; Zhang *et al.* 2016).

$$\text{Pd} + OH^- \rightarrow Pd - OH_{ads} + e^- \quad (29)$$

$$\text{Pd} + CH_3CH_2OH \rightarrow Pd - (CH_3CH_2OH)_{ads} \quad (30)$$

$$Pd - (CH_3CH_2OH)_{ads} + 3OH^- \rightarrow Pd - (CH_3CO)_{ads} + 3H_2O + 3e^- \quad (31)$$

$$Pd - (CH_3CO)_{ads} + Pd - OH_{ads} + OH^- \rightarrow CH_3COO^- + 2Pd + H_2O \quad (32)$$

The CVs in figure 6.10 and, 6.11 show the onset potential for the EOR reaction for the different catalysts. Pd catalyst had an onset potential of -0.37 V, PdBi and PdSn had -0.46 V, SnPd and PdBiSn 25 had -0.50 V, and lastly PdBiSn 30 had -0.53 V. These results show that modifying Pd with either Sn or Bi improves catalytic activity due to earlier onset of EOR on the modified catalysts compared to Pd catalyst. The similarities between PdBi and PdSn activities could be due to the similar chemical properties of Sn and Bi. While the PdBiSn 25 catalyst showed higher activity due to the presence of both Sn and Bi. The more negative onset potential was found on PbBiSn 30 material as expected because this material contains more Pd (30x deposition cycles) than the others (25x deposition cycles).

The PdSn and SnPd catalysts in comparison showed that SnPd catalysts had the highest $I_{forward}$ and $I_{reverse}$ compared to PdSn, as well as the sharper $I_{reverse}$ peak, indicating that it removes the adsorbed carbonate species much faster than PdSn does. PdBiSn 30 catalyst had a slower ethanol oxidation due to broader peak for forward scan. The rapid drop of current observed for PdBiSn 25 indicates a faster EOR, accompanied by a sharp increase for the reverse scan indicating faster by product removal. The ratio of the forward and reverse current ($I_{forward}$ / $I_{reverse}$) is summarized in Table 6.3,with the highest obtained for PdBi catalyst compared to all the prepared catalysts. The highest value of 1.25 was obtained for PdBi catalyst followed by PdBiSn 30 with 0.74, showing that PdBi is the least susceptible to poisoning.

The chronoamperometry scans illustrating the stability of the catalysts in ethanol at -0.2V is shown in Figure 6.13. The initial high current decreased rapidly within the first 60 s, followed by a gradual decrease over time as the catalysts get poisoned. The highest current was obtained for PdBiSn 30 catalyst over 60 min. The order of the catalysts stability based on current was found to be PdBiSn 30>PdSn>PdBiSn 25>SnPd>PdBi>Pd.. The charge results also confirm the catalyst stability trend shown above. Pd catalyst was found to be the most susceptible towards poisoning, and the addition of both Sn and Bi improved the stability of the catalyst, which supports the bifunctional mechanism stated in literature (Modibedi *et al*. 2013).

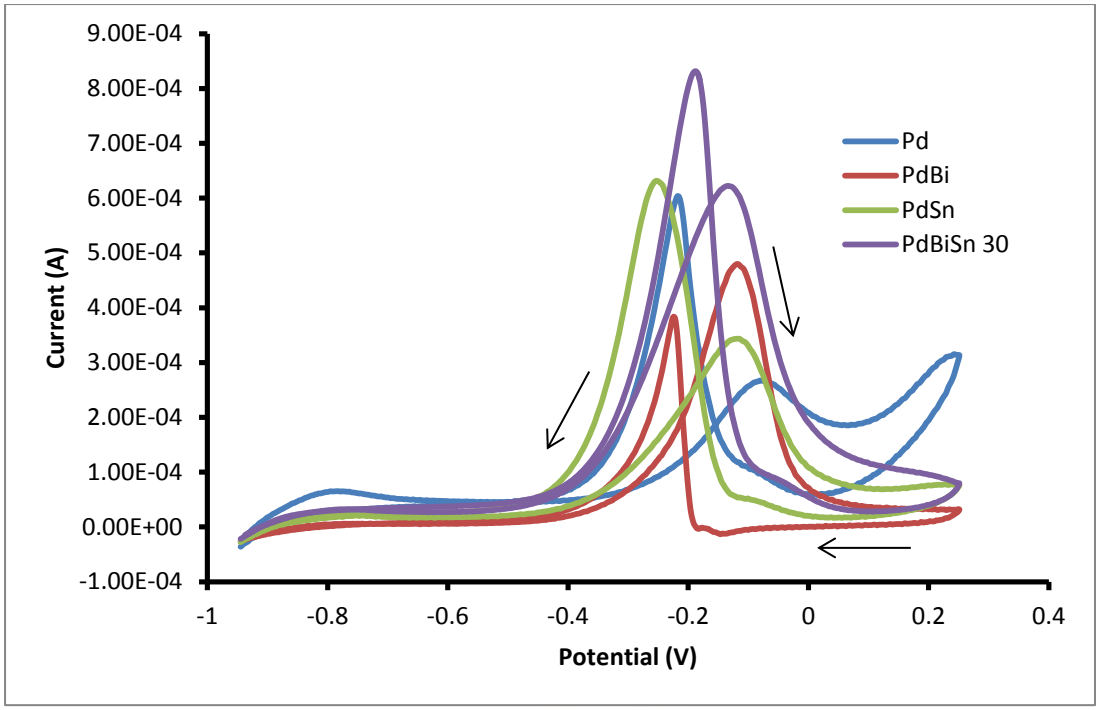

Figure 6.9: Cyclic voltammogram of Pd, PdBi, PdSn and PdBiSn catalysts in 0.1 M KOH + 0.1 M EtOH at a scan rate of 10 mV/s.

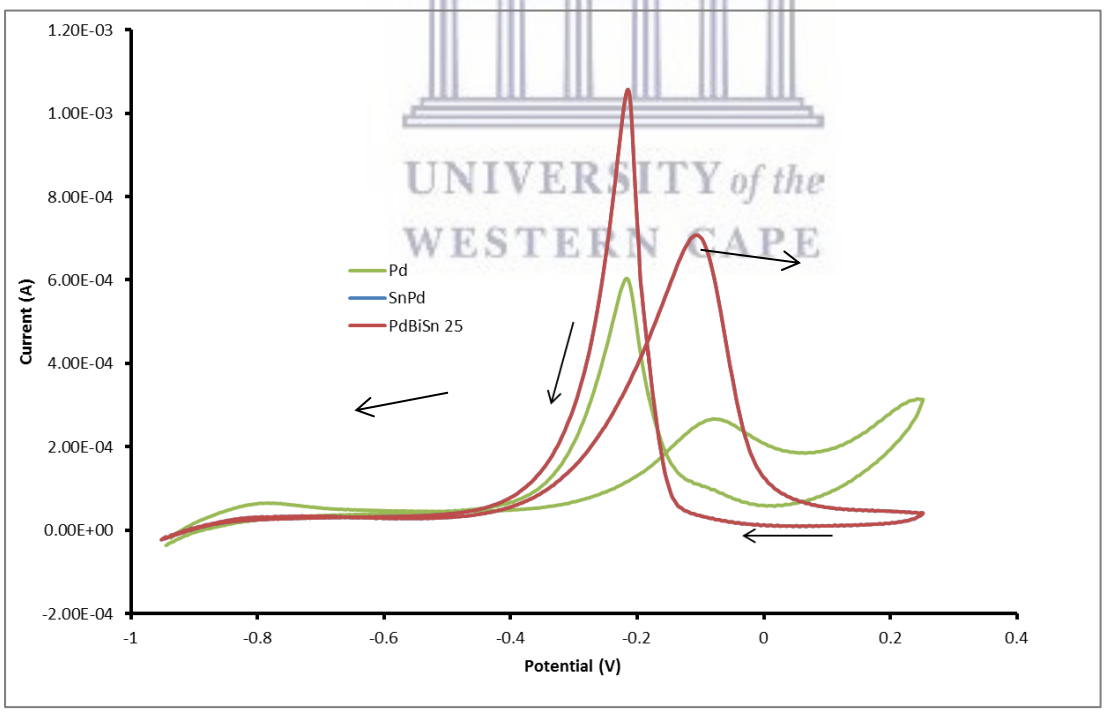

Figure 6.10: Cyclic voltammogram of Pd, SnPd and PdBiSn 25 catalysts in 0.1 M KOH + 0.1 M EtOH at a scan rate of 10 mV/s.

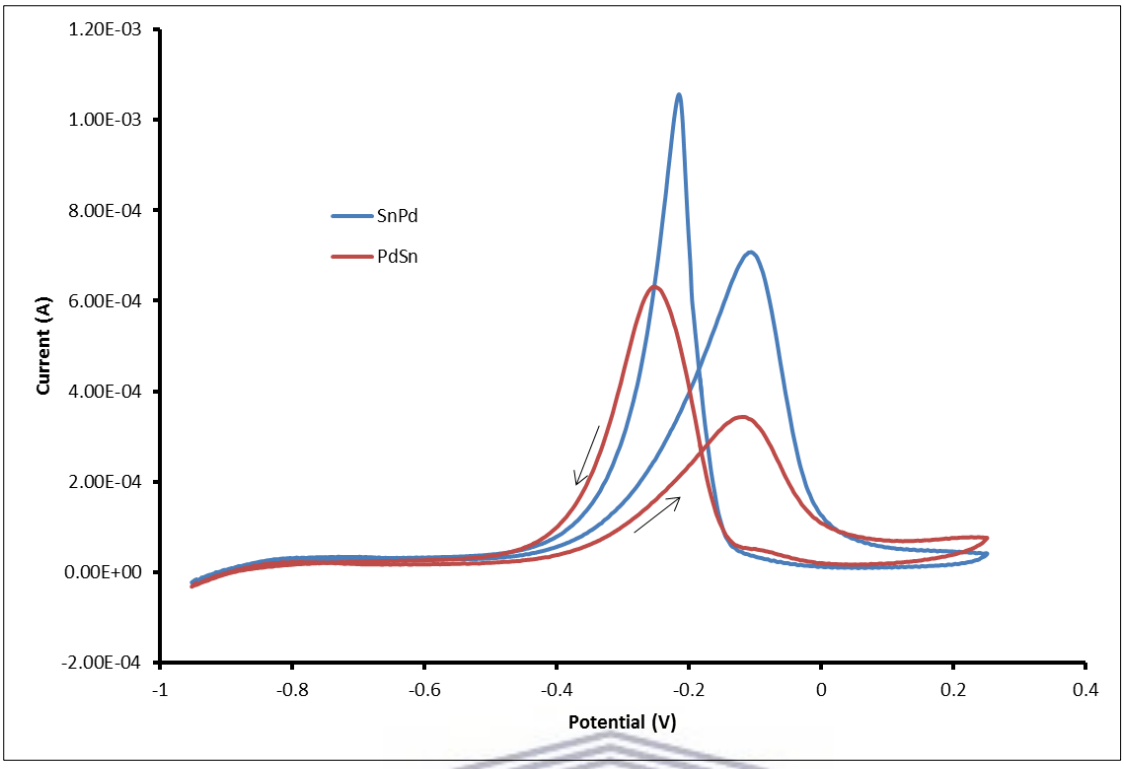

Figure 6.11: Cyclic voltammograms for the ethanol comparison of PdSn and SnPd catalysts at a scan rate of 10 mV/s.

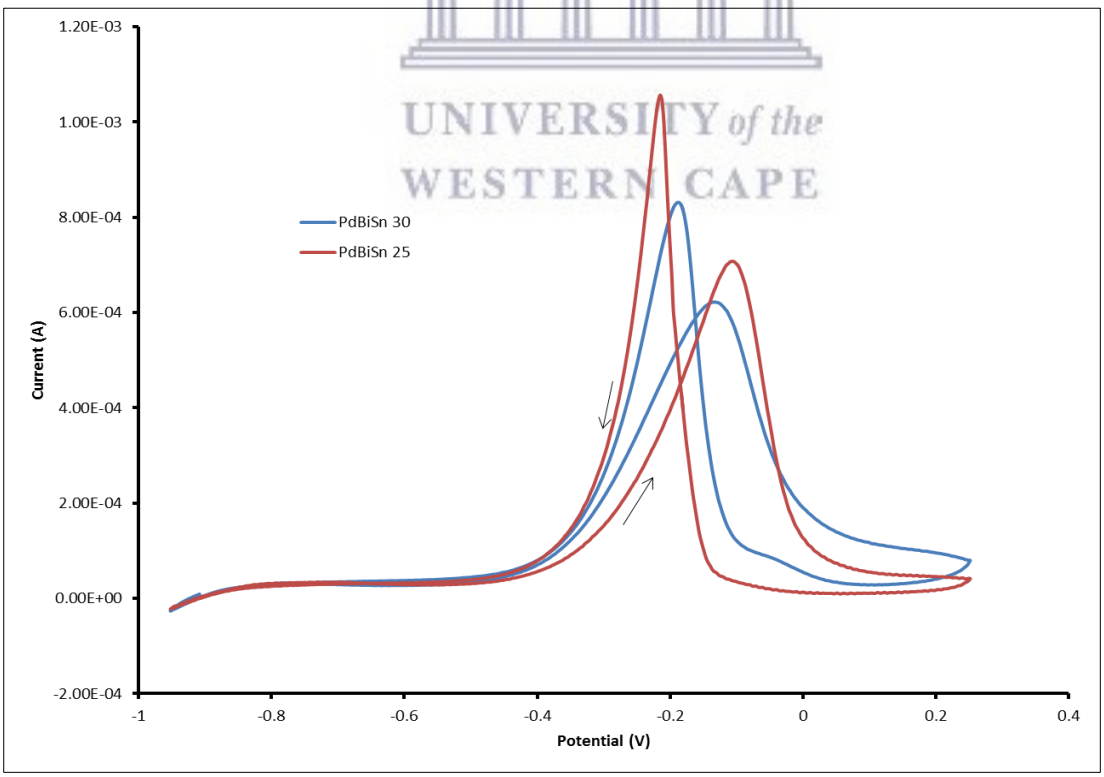

Figure 6.12: Cyclic voltammogram for the ethanol comparison of PdBiSn 25 and PdBiSn 30 catalysts at a scan rate of 10 mV/s

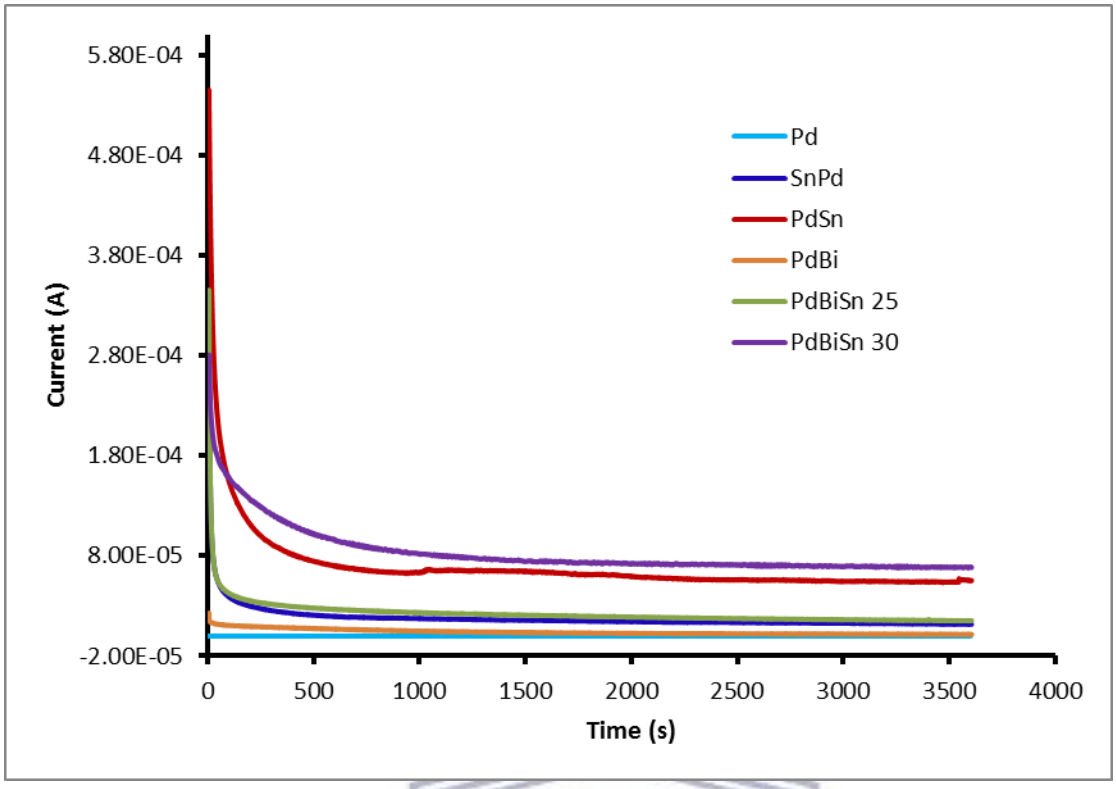

Figure 6.13: Chronoamperometric curves at -0.2 V of ethanol electro-oxidation in 0.1 M KOH+0.1 M ethanol.

Table 6.3: Summary of ethanol electro oxidation parameters for the different catalysts

Catalyst	**Onset potential (V)**	$I_{forwards}/I_{reverse}$	**Forward scan**	
			Current (A)	**Potential (V)**
Pd	-0.37	0.44	2.78E-04	-0.075
PdSn	-0.46	0.55	3.43E-04	-0.12
PdBi	-0.46	1.25	4.79E-04	-0.12
PdBiSn 30	-0.53	0.74	6.22E-04	-0.14
SnPd	-0.5	0.67	7.07E-04	-0.11
PdBiSn 25	-0.5	0.67	7.07E-04	-0.11

6.3.3.2 Glycerol electro oxidation

The electrocatalytic activity of the prepared catalysts towards glycerol oxidation in alkaline media was evaluated using cyclic voltammetry in 0.1 M KOH and 0.1 M glycerol. The results are shown in Figure 6.14-15 and summarised in Table 6.4. The Pd catalyst was found to have a high $I_{forward}$ and low $I_{reverse}$ as shown in figure 6.9. Similar observations were found to occur with the PdBi catalyst, as well as the SnPd, PdBiSn 25 catalysts in Figure 6.15. The reverse was found to occur for PdSn and PdBiSn 30 catalyst, where $I_{forward}$ was low and high $I_{reverse}$. The PdBiSn 30 catalyst had the highest I_{foward} and $I_{reverse}$; the forward scan had a very broad oxidation peak indicating the slow consumption of glycerol, whereas the reverse reduction scan showed rapid reduction of adsorbed carbonate species. $I_{forwards}/I_{reverse}$ ratios in Table 6.4, suggests that SnPd is the least susceptible to poisoning than Pd due to the highest value of 1.81. The other catalysts are not good for glycerol oxidation, glycerol is a polyol and has a lot of intermediates formed during its oxidation, these catalysts still need to be improved for glycerol oxidation reaction.

The modified Pd catalysts were found to have early onset potentials for glycerol oxidation with the exception of the SnPd catalyst. The more negative onset potential of -0.35 V was obtained using PdBi, followed by PdBiSn 25 with -0.34 V, PdSn and PdBiSn 30 with 0.33 V, and lastly SnPd with 0.27 V similar to Pd catalyst (Figure 6.14 and 6.15). These onset potentials Bi modified Pd catalysts have been found to favour electro oxidation of glycerol (Zalineeva *et al*. 2014). While the presence of Sn does not improve the onset potential of Pd, it does improve the reduction of carbonate species; the presence of Bi only improved the onset potential for glycerol oxidation. The presence of both Bi and Sn on the ternary PdBiSn catalyst was able to shift the oxidation of glycerol from -0.27 V for Pd to -0.33 V for the PdBiSn catalyst accompanied also by high peak current.

The PdBiSn 30 catalyst and PdBiSn 25 catalyst exhibited completely different interactions with glycerol (Figure 6.16). The PdBiSn 30 was found to have low I_{foward} accompanied by a rapid high $I_{reverse}$. It should be noted that even though the reduction current peak height for PdBiSn 25 was lower than for the oxidation, it was as rapid as the PdBiSn 30. These differences are due to PdBiSn 30 having higher catalyst loading. Similar observations were made for the comparison of PdSn and SnPd catalysts (Figure 6.17), where the PdSn catalysts had better activity towards glycerol oxidation based on the early onset potential, whereas SnPd was less prone to poisoning based on $I_{forwards}/I_{reverse}$.

The stability of the catalysts in glycerol at -0.15 V is shown in Figure 6.18. The initial current start high and rapidly decreases within the first 30 s, followed by a gradual decrease over time due to catalysts poisoning. The highest current was obtained for PdBiSn 30 and PdBi catalysts over 60 min. The order of the catalysts stability based on current was found to be PdBi≈PdBiSn 30>PdSn≈PdBiSn 25>SnPd>Pd. Pd catalysts was found to be the most susceptible towards poisoning, and the order of stability indicates that the addition of Bi improved catalysts stability while addition of Sn alone does not.

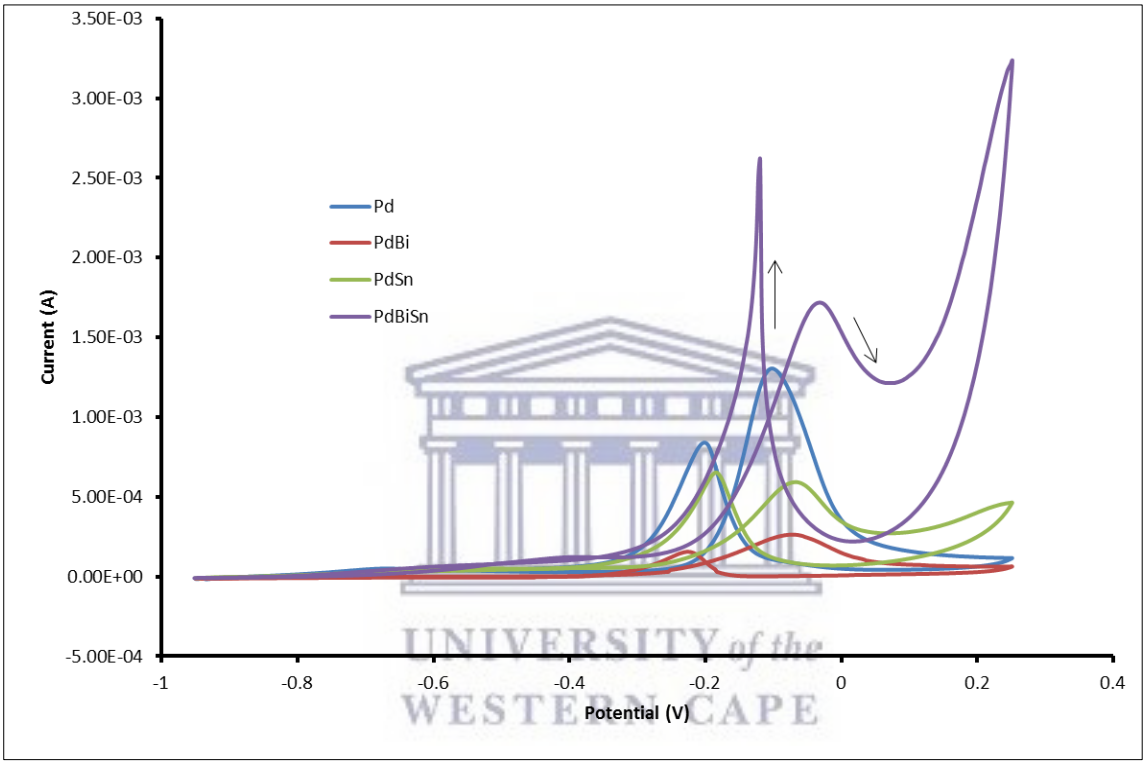

Figure 6.14: Cyclic voltammogram of Pd, PdBi, PdSn and PdBiSn catalysts in 0.1 M KOH + 0.1 M glycerol at a scan rate of 10 mV/s.

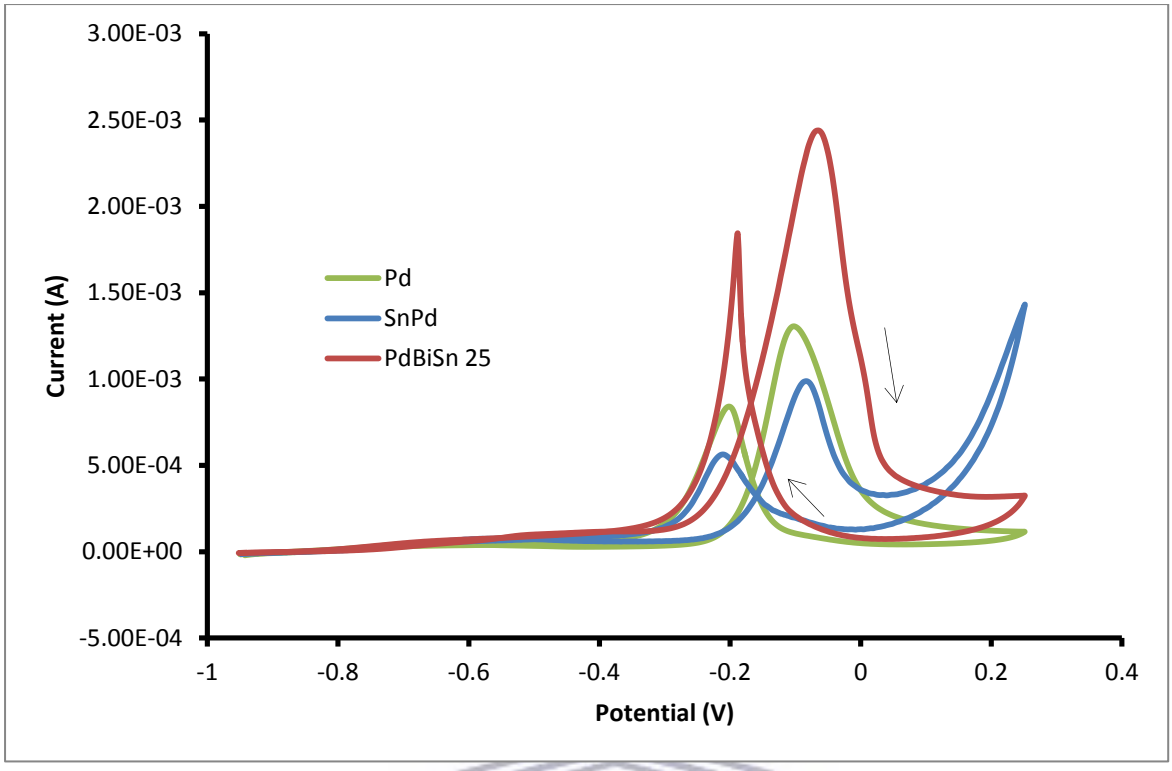

Figure 6.15: Cyclic voltammogram of Pd, SnPd and PdBiSn 25 catalysts in 0.1 M KOH + 0.1 M glycerol at a scan rate of 10 mV/s.

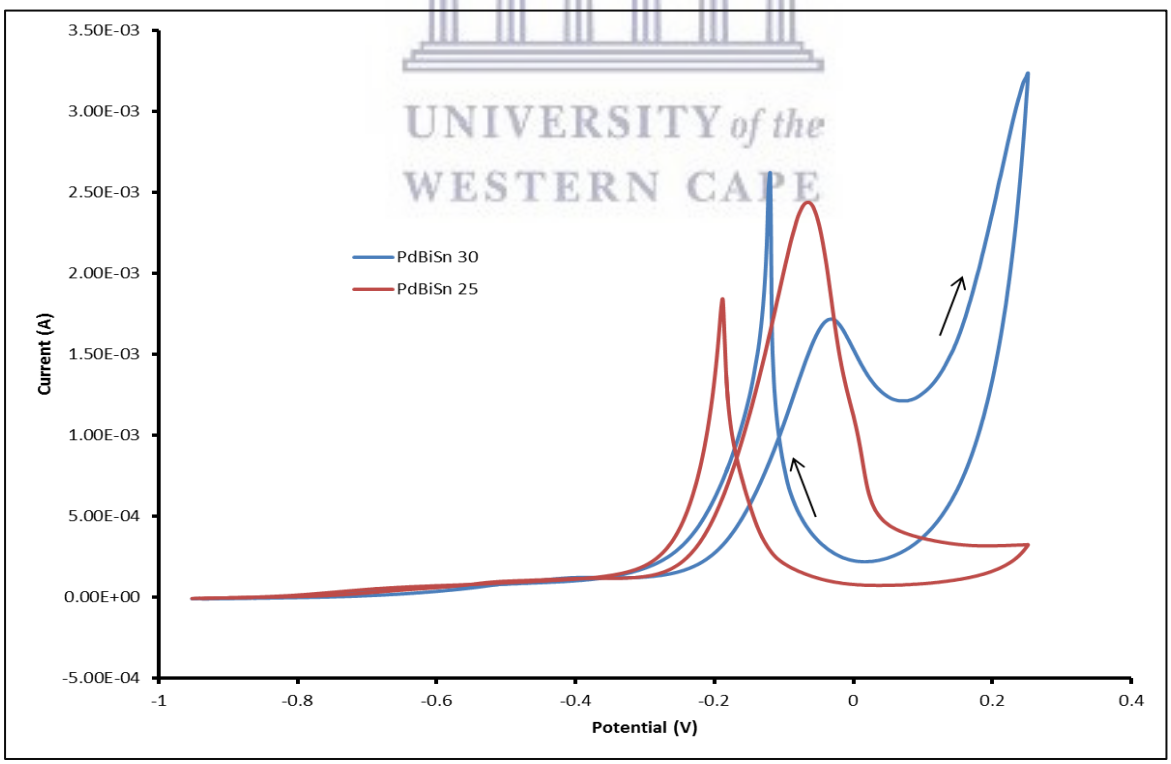

Figure 6.16: Cyclic voltammogram for the glycerol comparison of PdBiSn 25 and PdBiSn 30 catalysts at a scan rate of 10 mV/s.

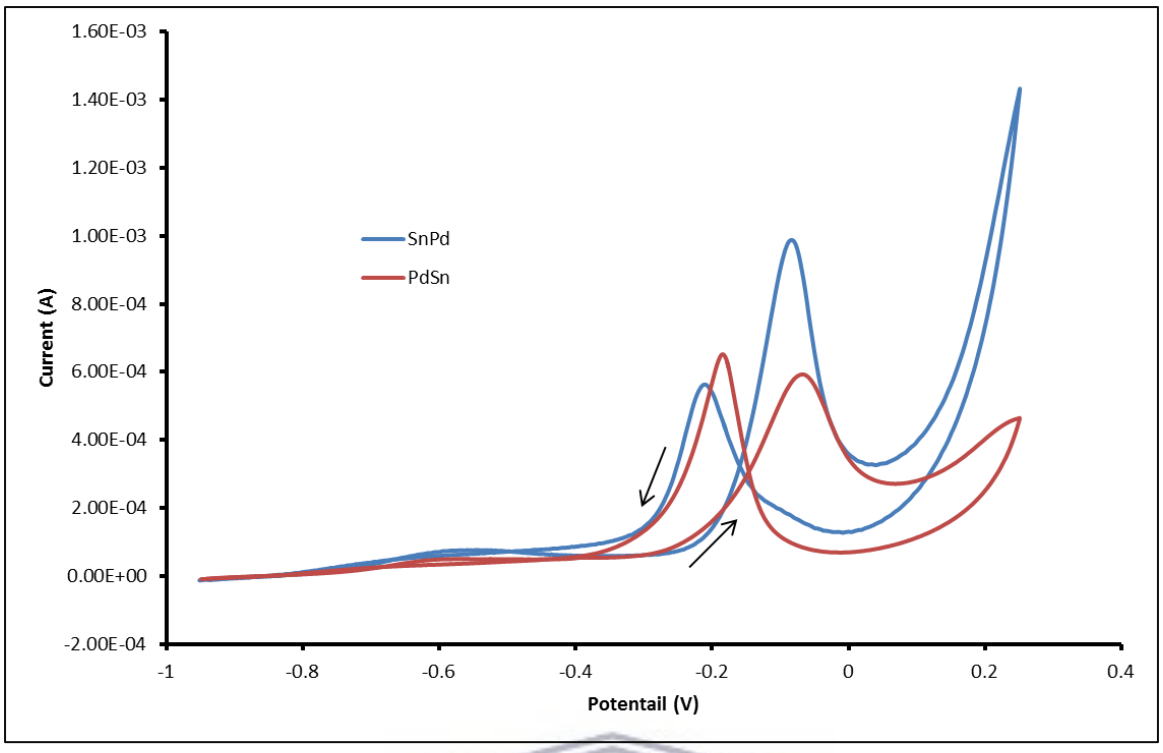

Figure 6.17: Cyclic voltammogram for the glycerol comparison of PdSn and SnPd catalysts at a scan rate of 10 mV/s.

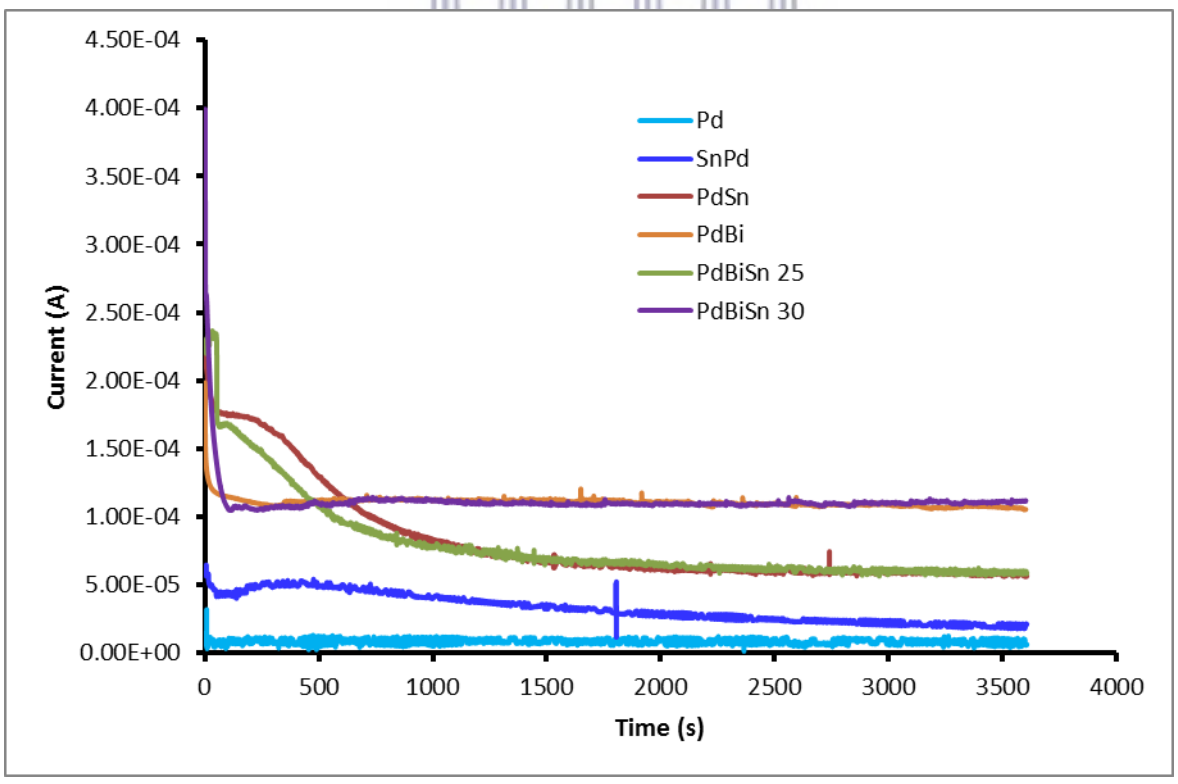

Figure 6.18: Chronoamperometric curves at -0.15 V of glycerol electro-oxidation in 0.1 M KOH+0.1 M glycerol.

Table 6.4: Summary of glycerol electro -oxidation parameters for the different catalysts

Catalyst	Onset potential (V)	$I_{forward}$ /$I_{reverse}$	Forward scan	
			Current (A)	Potential (V)
Pd	-0.27	1.51	1.31E-03	-0.10
PdSn	-0.33	0.83	5.60E-04	-0.083
PdBi	-0.35	1.44	2.63E-04	-0.076
PdBiSn 30	-0.33	0.65	1.72E-03	-0.034
SnPd	-0.27	1.81	9.82E-04	-0.088
PdBiSn 25	-0.34	1.33	2.44E-03	-0.068

6.3.3.3 Comparison of alcohol electro oxidation for the various catalysts

The electrochemical activity of each catalyst towards either ethanol or glycerol oxidation was evaluated by comparing the cyclic voltammetry scan for each catalyst in each alcohol in alkaline media. PdBiSn 30 catalyst showed better activity towards ethanol oxidation based on the earlier onset potential for ethanol oxidation (Figure 6.19), and less prone to poisoning based on high $I_{forwards}/I_{reverse}$. All the prepared catalysts were found to exhibit higher ethanol oxidation activity over glycerol electro oxidation as shown in Figure 6.19-6.23. PdBi catalyst was found to be the least prone to poisoning in glycerol and ethanol. However, they were all found to be less susceptible to poisoning in glycerol oxidation than in ethanol.

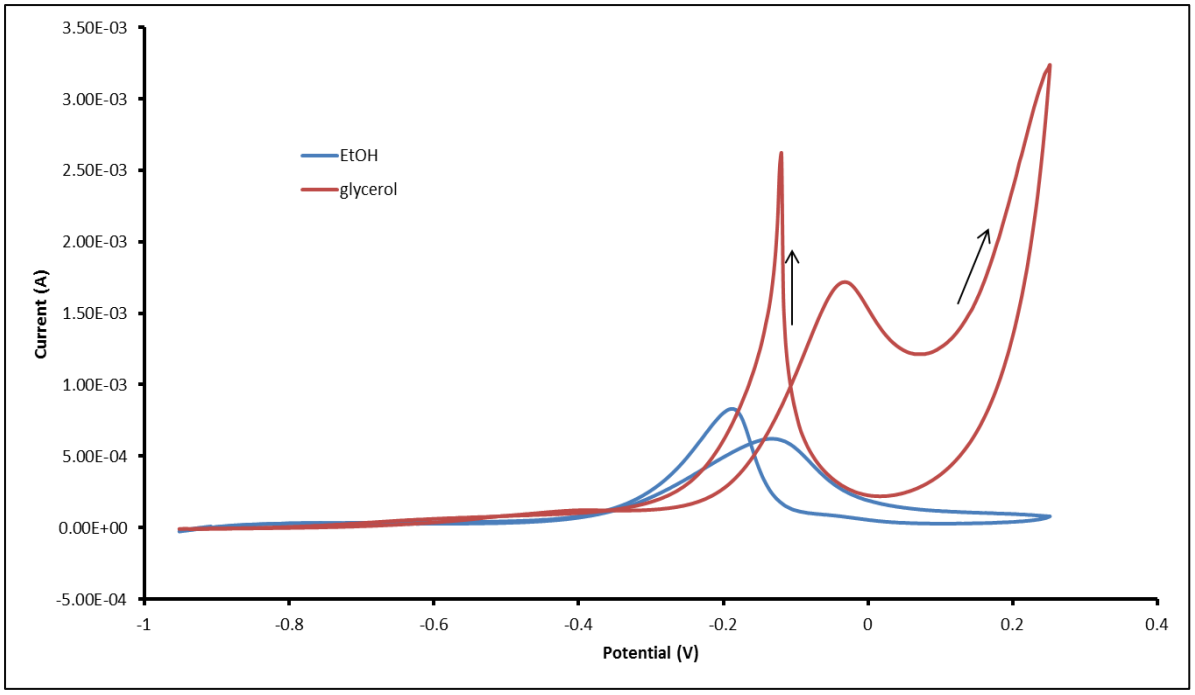

Figure 6.19: Cyclic voltammogram for the alcohol comparison of PdBiSn 30 catalyst at a scan rate of 10 mV/s.

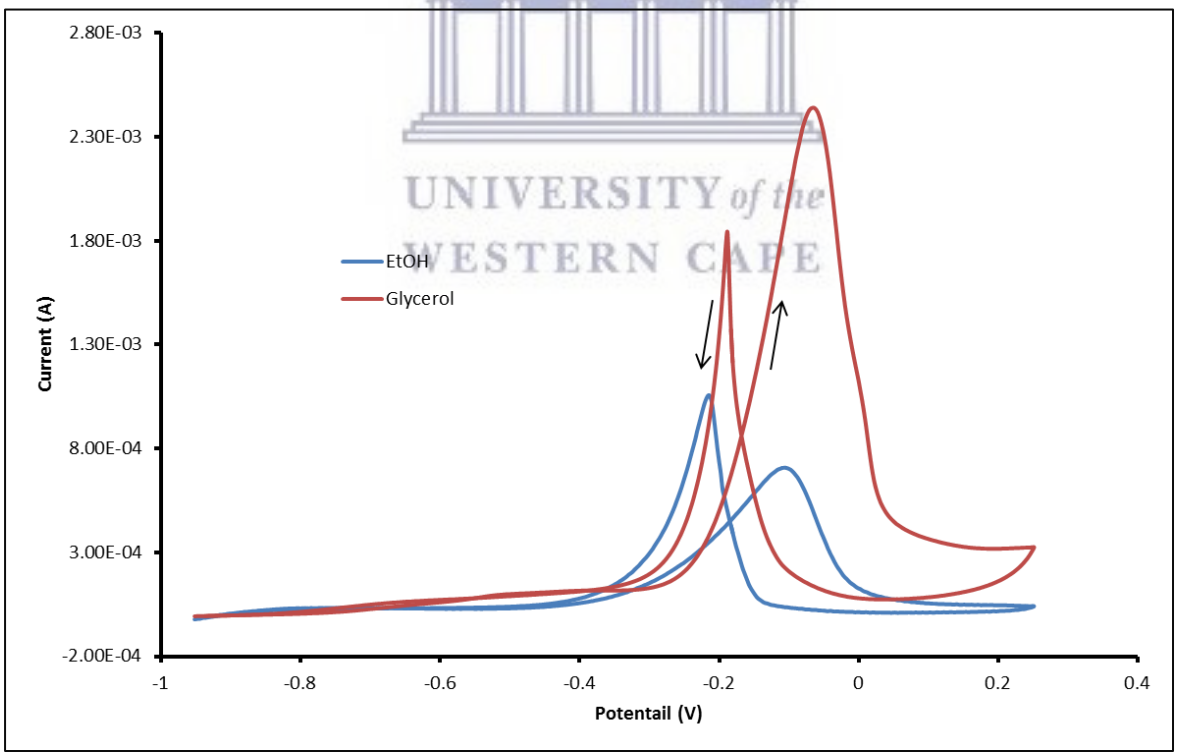

Figure 6.20: Cyclic voltammogram for the alcohol comparison of PdBiSn 25 catalyst at a scan rate of 10 mV/s.

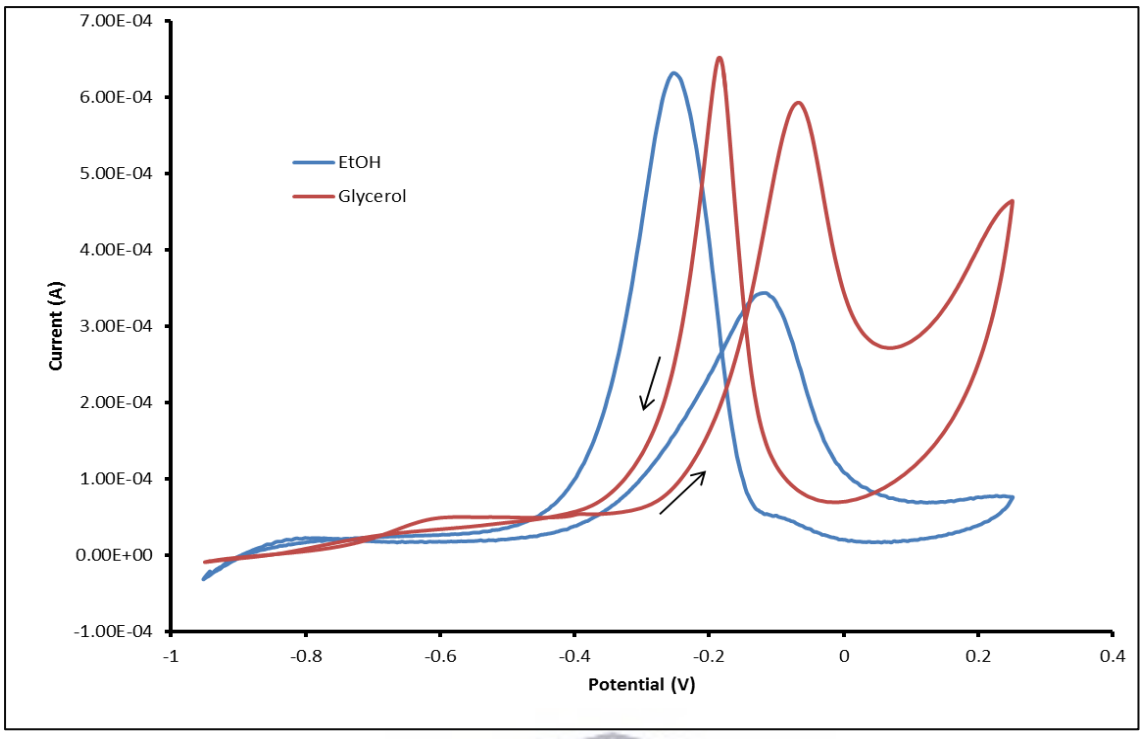

Figure 6.21: Cyclic voltammogram for the alcohol comparison of PdSn catalyst at a scan rate of 10 mV/s.

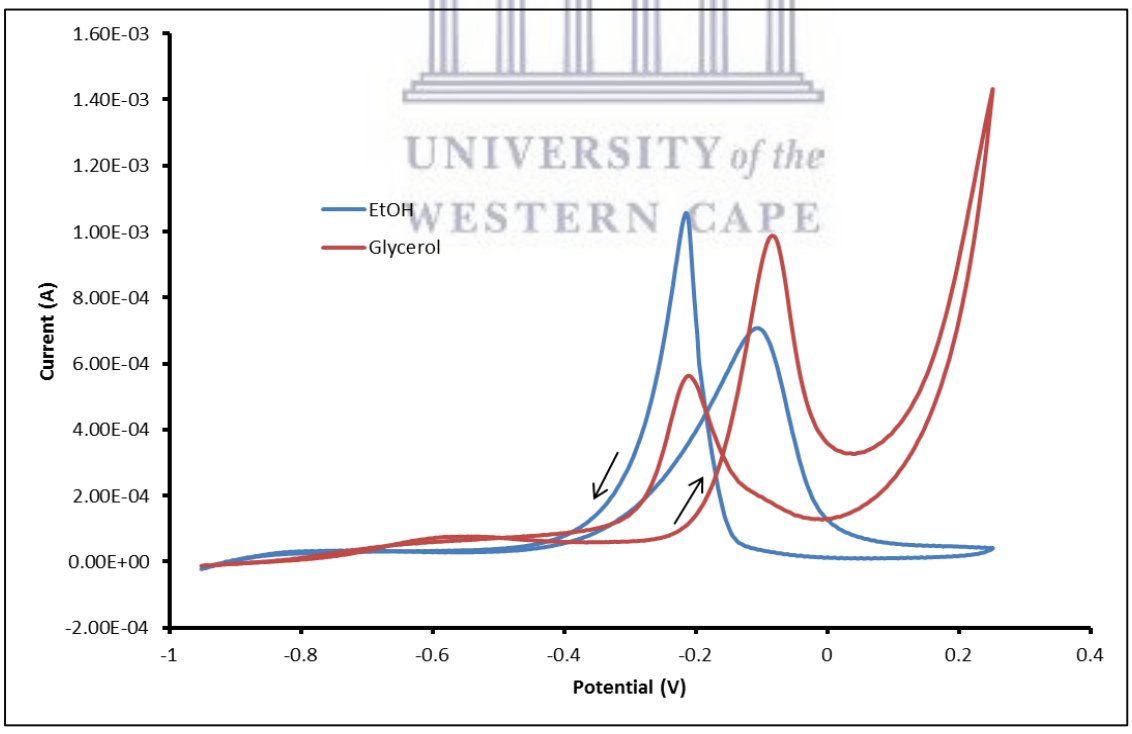

Figure 6.22: Cyclic voltammogram for the alcohol comparison of SnPd catalyst at a scan rate of 10 mV/s.

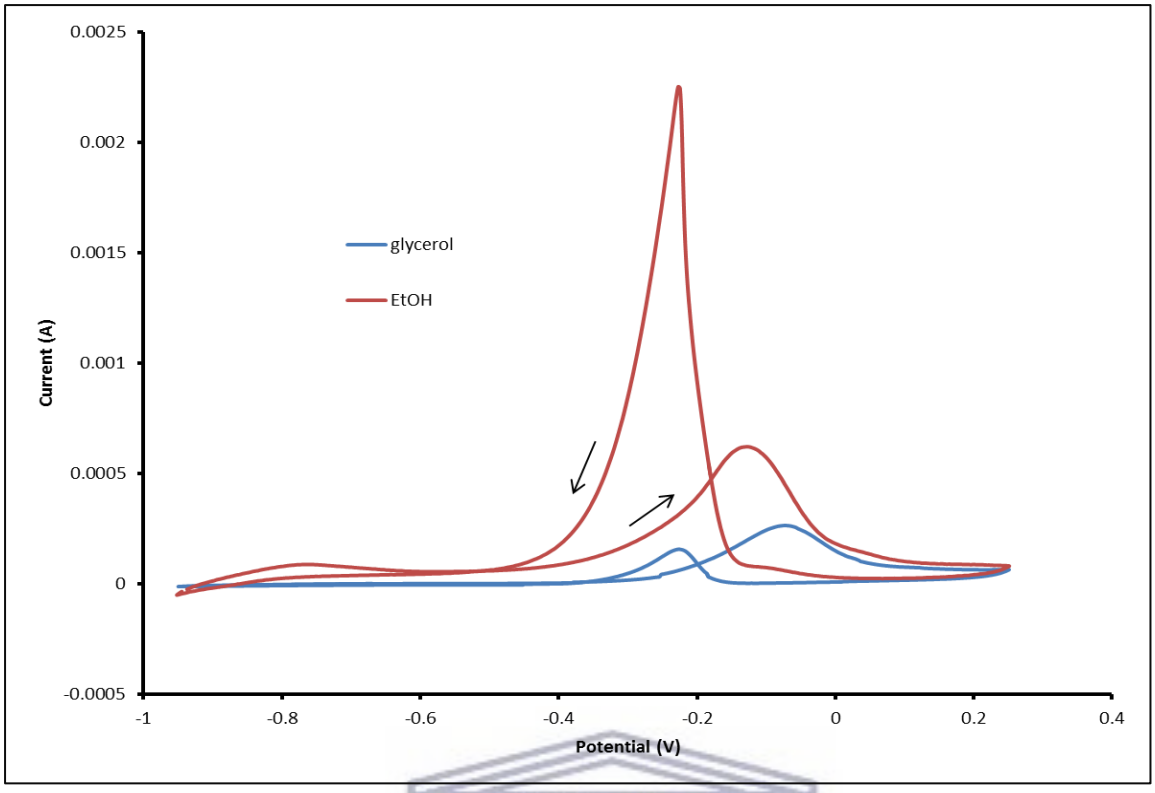

Figure 6.23: Cyclic voltamogram for the alcohol comparison of PdBi catalyst at a scan rate of 10 mV/s.

The charge associated with the current at two time intervals was calculated using time and corresponding current for both ethanol and glycerol as shown in Table 6.5. The results showed that ethanol electro oxidation is favoured over glycerol due to higher charge value obtained for glycerol compared to ethanol. This is a result of glycerol being a polyol therefore it will be difficult to oxidise and produce many intermediates as compared to ethanol, hence lower activity on PdBi, PdSn, PdSnBi than ethanol.

Table 6.5: Summary of Charge for ethanol and glycerol oxidation for the different catalysts obtained from chronoamperometry.

Material	**EtOH Charge (*Q*)**		**Glycerol Charge (*Q*)**	
	t_1 **= 1000 s**	t_2 **= 3000 s**	t_1 **= 1000 s**	t_2 **= 3000 s**
Pd	0.00	0.00	0.00574	0.0217
SnPd	0.0174	0.0381	0.0403	0.0612
PdSn	0.0638	0.163	0.0833	0.180
PdBi	0.0049	0.00595	0.112	0.327
PdBiSn 25	0.0233	0.0488	0.0780	0.182
PdBiSn 30	0.0819	0.208	0.112	0.330

6.4 Conclusion

Pd, Sn and Bi based binary and ternary catalysts were prepared using underpotential deposition method and tested for the electro-oxidation of ethanol and glycerol in alkaline media. Pd catalysts were deposited using Cu SLRR method while Sn and Bi were directly deposited at UPD. These materials were found to exhibit similar morphology with the exception of PdBi material. The activity towards oxidation was evaluated for each catalyst. All the prepared catalysts showed better activity towards ethanol oxidation compared to glycerol oxidation. The addition of Sn and Bi to Pd was found to improve activity of the catalysts for ethanol and glycerol oxidation, and also makes these catalysts least susceptible to poisoning. The addition of Bi improved catalyst stability in glycerol while both Sn and Bi improved the catalysts stability in ethanol. Ethanol is easily oxidised on all prepared catalysts than glycerol.

6.5 References

Aldana-Gonzalez, J, Olvera-Garcia, J, De Oca, MM, Romero-Romo, M, Ramirez-Silva, M, Palomar-Pardave, M (2015) Electrochemical quantification of the electro-active surface area of Au nanoparticles supported onto an ITO electrode by means of Cu upd. *Electrochemistry Communications* **56**, 70-74.

Antolini, E, Gonzalez, E (2010) Alkaline direct alcohol fuel cells. *Journal of Power Sources* **195**, 3431-3450.

Blizanac, B, Ross, P, Markovic, N (2007) Oxygen electroreduction on Ag (1 1 1): The pH effect. *Electrochimica Acta* **52**, 2264-2271.

Braunchweig, B, Hibbitts, D, Neurock, M, Wieckowski, A (2013) Electrocatalysis: A direct alcohol fuel cell and surface science perspective. *Catalysis Today* **202**, 197-209.

Cai, J, Huang, Y, Guo, Y (2013) Bi-modified Pd/C catalyst via irreversible adsorption and its catalytic activity for ethanol oxidation in alkaline medium. *Electrochimica Acta* **99**, 22-29.

Carmo, M, Doubek, G, Sekol, RC, Linardi, M, Taylor, AD (2013) Development and electrochemical studies of membrane electrode assemblies for polymer electrolyte alkaline fuel cells using FAA membrane and ionomer. *Journal of Power Sources* **230**, 169-175.

Cifrain, M, Kordesch, K (2003) Hydrogen/oxygen (air) fuel cells with alkaline electrolytes. *Handbook of Fuel Cells*

Czerniawski, JM, Stickney, JL (2016) Electrodeposition of In2Se3 using potential pulse atomic layer deposition. *Journal of Physical Chemistry C* **120**, 16162-16167.

Dutta, A, Mahapatra, SS, Datta, J (2011) High performance PtPdAu nano-catalyst for ethanol oxidation in alkaline media for fuel cell applications. *International Journal of Hydrogen Energy* **36**, 14898-14906.

Dutta, A, Mondal, A, Broekmann, P, Datta, J (2017) Optimal level of Au nanoparticles on Pd nanostructures providing remarkable electro-catalysis in direct ethanol fuel cell. *Journal of Power Sources* **361**, 276-284.

El-Aziz, A, Kibler, L (2002) Influence of steps on the electrochemical oxidation of CO adlayers on Pd (111) and on Pd films electrodeposited onto Au (111). *Journal of Electroanalytical Chemistry* **534**, 107-114.

Feng, Y-Y, Liu, Z-H, Xu, Y, Wang, P, Wang, W-H, Kong, D-S (2013) Highly active PdAu alloy catalysts for ethanol electro-oxidation. *Journal of Power Sources* **232**, 99-105.

Friedl, J, Stimming, U (2013) Model catalyst studies on hydrogen and ethanol oxidation for fuel cells. *Electrochimica Acta* **101**, 41-58.

Gregory, BW, Suggs, DW, Stickney, JL (1991) Conditions for the deposition of CdTe by electrochemical atomic layer epitaxy. *Journal of the Electrochemical Society* **138**, 1279-1284.

Hoogers, G (2002) 'Fuel cell technology handbook.' CRC press.

Hoyer, R, Kibler, L, Kolb, D (2003) The initial stages of palladium deposition onto Pt (1 1 1). *Electrochimica Acta* **49**, 63-72.

Kamarudin, M, Kamarudin, SK, Masdar, M, Daud, WRW (2013) Direct ethanol fuel cells. *International Journal of Hydrogen Energy* **38**, 9438-9453.

Kibler, L, El-Aziz, A, Kolb, D (2003) Electrochemical behaviour of pseudomorphic overlayers: Pd on Au (1 1 1). *Journal of Molecular Catalysis A: Chemical* **199**, 57-63.

Kibler, L, Kleinert, M, Kolb, D (2000) Initial stages of Pd deposition on Au (hkl): Part II: Pd on Au (100). *Surface Science* **461**, 155-167.

Kibler, L, Kleinert, M, Randler, R, Kolb, D (1999) Initial stages of Pd deposition on Au (hkl) Part I: Pd on Au (111). *Surface Science* **443**, 19-30.

Markovic, N, Gasteiger, H, Ross, PN (1997) Kinetics of oxygen reduction on Pt (hkl) electrodes: implications for the crystallite size effect with supported Pt electrocatalysts. *Journal of the Electrochemical Society* **144**, 1591-1597.

Mkwizu, TS, Mathe, MK, Cukrowski, I (2010) Electrodeposition of multilayered bimetallic nanoclusters of ruthenium and platinum via surface-limited redox-replacement reactions for electrocatalytic applications. *Langmuir* **26**, 570-580.

Modibedi, RM, Louw, EK, Ozoemena, KI, Mathe, MK, 2013. The electrochemical atomic layer deposition of Pt and Pd nanoparticles on Ni foam for the electro-oxidation of alcohols. *Electrochemical Society Transactions* 50, 9-18.

Modibedi, RM, Masombuka, T, Mathe, MK (2011) Carbon supported Pd–Sn and Pd–Ru–Sn nanocatalysts for ethanol electro-oxidation in alkaline medium. *International Journal of Hydrogen Energy* **36**, 4664-4672.

Sheridan, LB, Czerwiniski, J, Jayaraju, N, Gebregziabiher, DK, Stickney, JL, Robinson, DB, Soriaga, MP (2012) Electrochemical atomic layer deposition (E-ALD) of palladium nanofilms by surface limited redox replacement (SLRR), with EDTA Complexation. *Electrocatalysis* **3**, 96-107.

Sheridan, LB, Gebregziabiher, DK, Stickney, JL, Robinson, DB (2013) Formation of palladium nanofilms using electrochemical atomic layer deposition (E-ALD) with chloride complexation. *Langmuir* **29**, 1592-1600.

Tang, J, Petri, M, Kibler, L, Kolb, D (2005) Pd deposition onto Au (111) electrodes from sulphuric acid solution. *Electrochimica Acta* **51**, 125-132.

Yi, Q, Chu, H, Chen, Q, Yang, Z, Liu, X (2015) High performance Pd, PdNi, PdSn and PdSnNi nanocatalysts supported on carbon nanotubes for electrooxidation of C2-C4 alcohols. *Electroanalysis* **27**, 388-397.

Zalineeva, A, Serov, A, Padilla, M, Martinez, U, Artyushkova, K, Baranton, Sv, Coutanceau, C, Atanassov, PB (2014) Self-supported Pd x Bi catalysts for the electrooxidation of glycerol in alkaline media. *Journal of the American Chemical Society* **136**, 3937-3945.

Zhang, L, Chang, Q, Chen, H, Shao, M (2016) Recent advances in palladium-based electrocatalysts for fuel cell reactions and hydrogen evolution reaction. *Nano Energy* **29**, 198-219.

CHAPTER 7

7 Conversion of CO_2 to Synfuels Using Bi/Au Catalyst

Electrodeposited Bi/Au electrodes will be tested as catalysts for CO_2 conversion to synfuels. These electrodes were prepared and characterised fully in chapter 4. Cyclic voltammetry was used to test the electrochemical activity in CO_2 saturated solution and for testing possible by-products. The eminent product was identified as urea.

7.1 Introduction

Carbon dioxide is one of the greenhouse gases and studies have shown it to be the cause of the current global warming crisis (Gattrell and Gupta 2006; Hu *et al.* 2013; Lim *et al.* 2014; Zhang *et al.* 2017). The high content of carbon dioxide in the atmosphere is a result of fossil fuel consumption. Efforts are being made to sequester and capture CO_2 at the large power plants to reduce atmospheric CO_2. Conversion of CO_2 to useful chemicals and fuels is a much more viable strategy. Electrochemical conversion methods provide an opportunity to reduce CO_2 while also being environmentally friendly compared to the current petrochemical process (Fischer-Tropsch process) (Jones *et al.* 2014; Lim *et al.* 2014). CO_2 can be converted to chemicals including methanol, ethanol, formic acid, salicylic acid, urea and other hydrocarbons (Whipple and Kenis 2010). Metal electrodes have been studied for their ability to convert CO_2 to chemical fuels (Lim *et al.* 2014). Carbon supported bismuth oxide (BiO_X/C) nanoparticles have been used in the production of formate (Lee *et al.* 2017), bismuth films and nanoparticles were used to convert CO_2 to CO (Zhang *et al.* 2016; Lv *et al.* 2017), tin lead alloys reduced CO_2 to formate (Choi *et al.* 2016), Cu electrodes formed methane (Kaneco *et al.* 2002), group 11-14 electrodes including Cr, Fe, Sn, Pb, Ni, Rh, Rh, Mn, Cr, In amongst many formed urea, formic acid, nitrite ions and ammonia (Shibata *et al.* 1998). Research efforts in this area are focusing on discovering materials that are selective towards formation of a single product and also that are efficient. This study aims to use electrodeposited Bi/Au catalyst and test these catalysts for CO_2 conversion. Bi was electrodeposited on Au coated glass substrate using E-ALD. The electrochemical reduction studies were done using cyclic voltammetry, and the possible products tested electrochemically.

7.2 Experimental

7.2.1 E-ALD deposition

The preparation method of Bi/Au thin films is given in section 4.2 including chemicals, solutions, and substrate treatment.

7.2.2 CO_2 reduction studies

Electrochemical activity of the Bi/Au electrode was investigated using cyclic voltammetry (CV). A potentiostat (Metrohm, PGSTAT302) equipped with NOVA 2.0 software was used. A standard three electrode system was used where, Pt rod (Metrohm), Ag/AgCl/ 3 M KCl and Bi/Au connected using Cu tape served as counter, reference, and working electrodes respectively. CV scans were done in 0.5 M $NaHCO_3$ solution (pH 8.62) between 1.3 V and -1.3 V at a scan rate of 50 mV/s. Each sample was scanned in air, N_2, and CO_2 saturated $NaHCO_3$ solution. The by-products were identified by CV scans in methanol, ethanol, formic acid and ethylene glycol N_2 saturated solutions.

7.3 Results and Discussion

Electrodeposited thin films of Bi on Au substrates were evaluated for their ability to electrochemically reduce carbon dioxide into useful fuels. This was done by exposing the prepared Bi on Au (Bi/Au) electrode to CO_2 saturated solution (0.5 M $NaHCO_3$, pH 8.62). Firstly, the activity of the Au electrode in the aqueous electrolyte was investigated using cyclic voltammetry (CV). All CV scans were conducted at 50 mV/s ramped between 1.3 V to -1.3 V negatively under air and N_2. The scan started from positive potential to negative potential, a sharp peak labelled A in figure 7.1 is the reduction of Au, followed by sharp tail at the end of the negative scan representing hydrogen evolution, the scan continues positively where a broad oxidation of Au peak labelled B was found. The observed reduction peak shifted slightly to more negative potential of 0.35 V due to the presence of N_2.

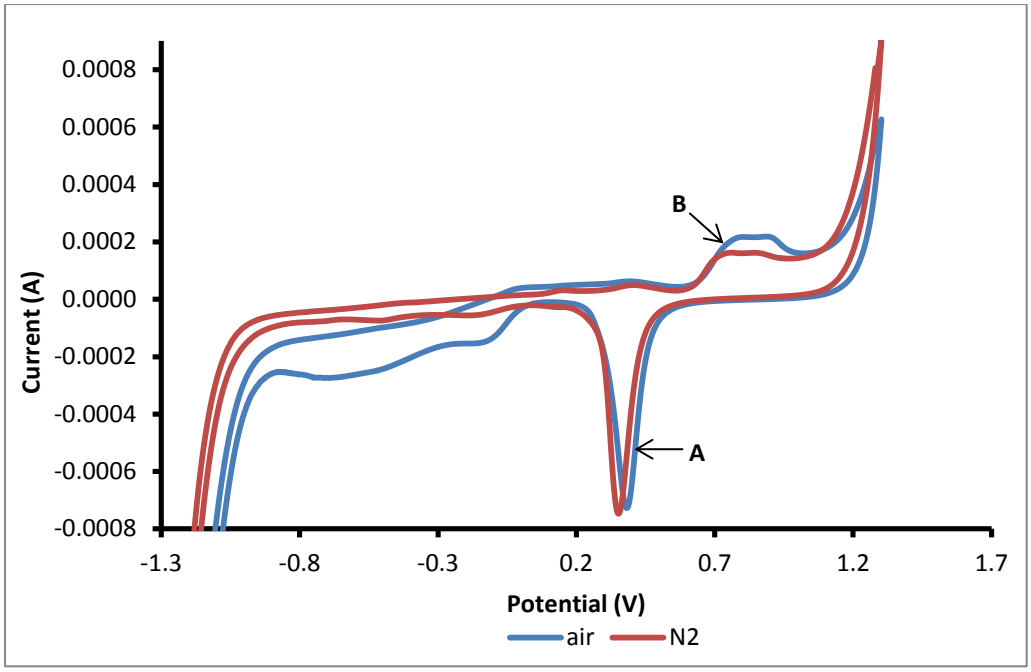

Figure 7.1: CV of Au electrode in 0.5 M $NaHCO_3$ at 50 mV/s vs. Ag/AgCl.

The electrochemical activity of the Bi/Au electrode was studied by cyclic voltammetry in the presence of CO_2 saturated $NaHCO_3$ solution as shown in Figure 7.2. The redox peaks attributed to Au substrate are visible as explained earlier; two distinctive peaks emerged at -0.2 V and -0.53 V denoted as C and D respectively due to presence of Bi catalyst. The effect of catalyst loading was investigated using deposited Bi/Au samples by depositing Bi on Au electrode using different cycles 300x and 50x as shown in Figure 7.2. All the peaks were more visible (higher current) in the 300 cycle (thicker) deposit compared to 50 cycle deposited sample. The peaks were also found to shift to slightly more negative potential with the increase in catalyst loading.

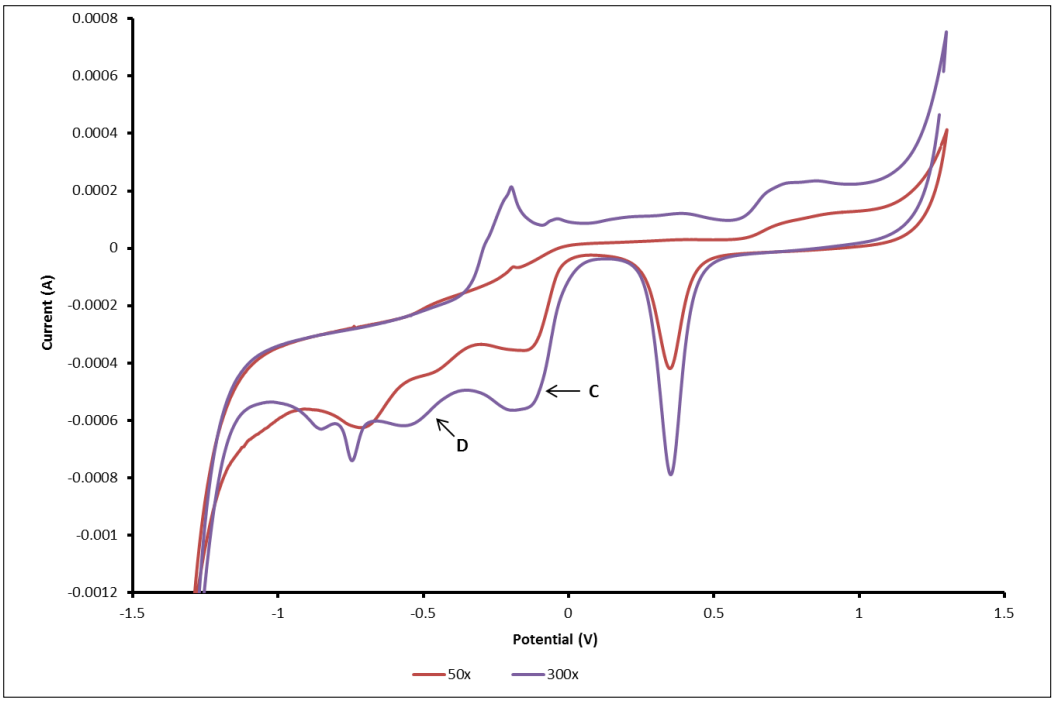

Figure 7.2: CV of a 300 and 50 cycles Bi on Au electrode in 0.1 M $NaHCO_3$ CO_2 saturated solution at 50 mV/s vs Ag/AgCl.

The Bi/Au electrode was further studied by scanning the electrode in the presence of N_2 and CO_2 saturated $NaHCO_3$ solution as shown in Figure 7.3, including an insert of the CV for Au electrode. The redox peaks attributed to Au substrate are denoted by A and B and the Bi/Au catalyst peaks denoted as C and D as explained earlier were found. Further, as we move from high to low potentials, oxidation reduction peaks E and F at -0.76 V and -0.90 V respectively for oxygen reduction were observed. These peaks were significantly reduced due to the presence of N_2, CO_2 and the formation of by-products. The Hydrogen evolution began at -1.1 V. All peaks were found to slightly shift to more negative potentials when the solution is purged with N_2 and but remained in the same peak positions in the presence of CO_2 saturated solutions.

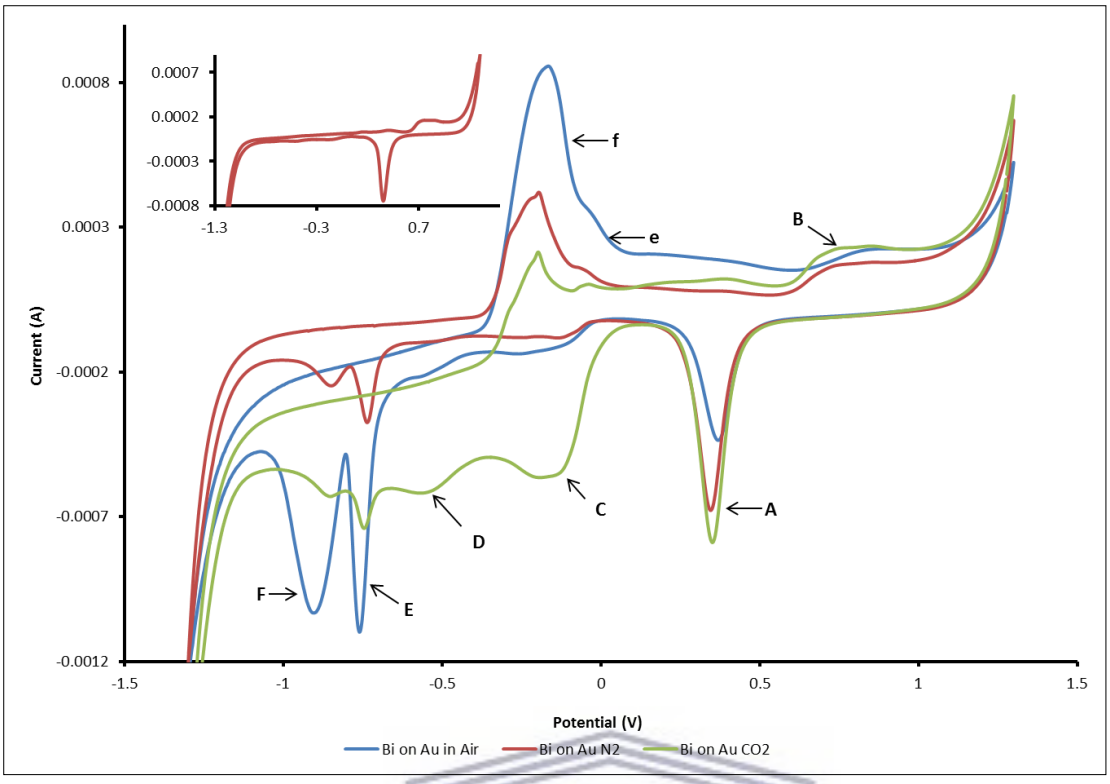

Figure 7.3: CV of Bi on Au electrode in 0.5 M $NaHCO_3$ at 50 mV/s vs Ag/AgCl and an insert of the CV of Au electrode.

The comparison of the CV scan between CO_2 saturated electrolyte solution and that obtained in urea solution is revealed by Figure 7.4. The formed products were identified by cyclic voltammetry scan of Bi/Au electrode in solutions containing different possible products (respectively), and were compared to the CV scan of CO_2 saturated $NaHCO_3$ solution. The products were methanol, ethanol, formic acid, ethylene glycol, and urea. From the many possible products, urea was more eminent, Figure 7.4 C. The CV scan of Bi on Au electrode in urea was found to have a reduction peak at -0.1 V, which resembled the shape of peak C, but found at more positive potential than peak C, Figure 7.4. Therefore, urea was identified as the main products formed.

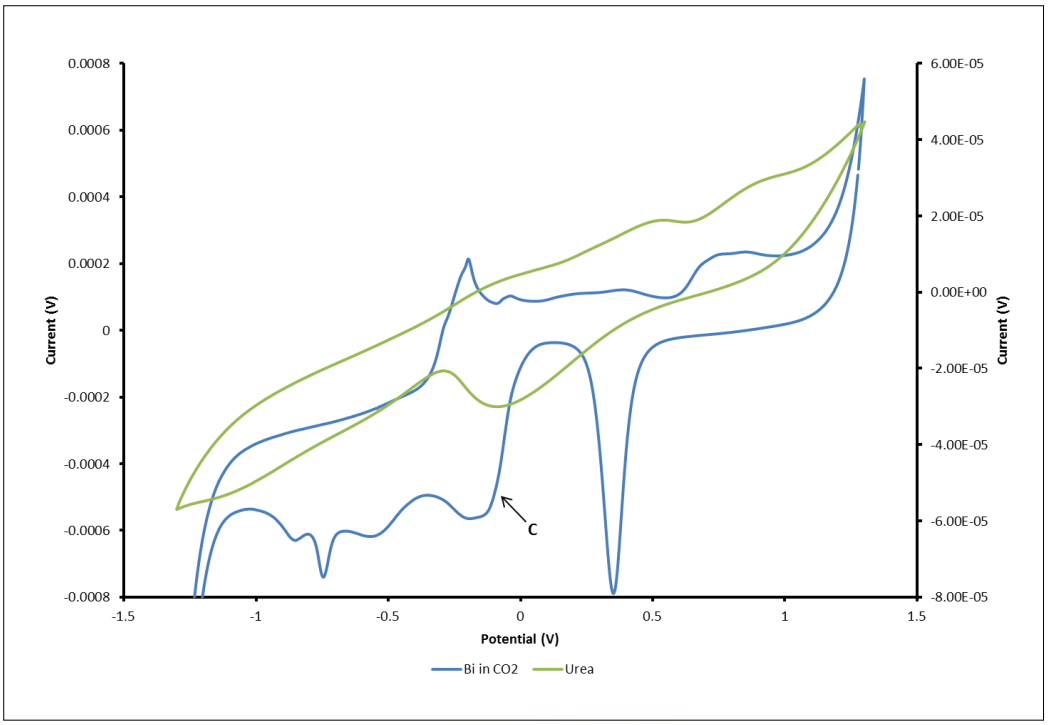

Figure 7.4: CV of a Bi on Au electrode in 0.5 M $NaHCO_3$ and in 0.1 M Urea at 50 mV/s vs Ag/AgCl and an insert of the CV of Au electrode.

The mechanism for the reduction of CO_2 at metal electrodes is illustrated in Figure 7.5 (Jones *et al.* 2014). The generation of CO_2^{*-} intermediate occurs in the first step; it is the rate determining step and dictates which product is formed. The electrodes are grouped based on their ability to bind to the intermediate species generated and the ability to reduce CO_2. The mechanism illustrates that Au electrodes has the ability to bind the CO_2^{*-} intermediate and forms CO as a major product, while Bi has a low ability to bind CO_2^{*-} intermediate forming formate as major product. Studies of CO_2 reduction on Au electrodes and Bi electrodes have confirmed the formation of CO and formate respectively. This mechanism is also described and is in agreement with the reviews done on the reduction of CO_2 by other authors (DiMeglio and Rosenthal 2013; Medina-Ramos *et al.* 2014; Walker *et al.* 2015; Lee *et al.* 2017; Lv *et al.* 2017; Vickers *et al.* 2017).

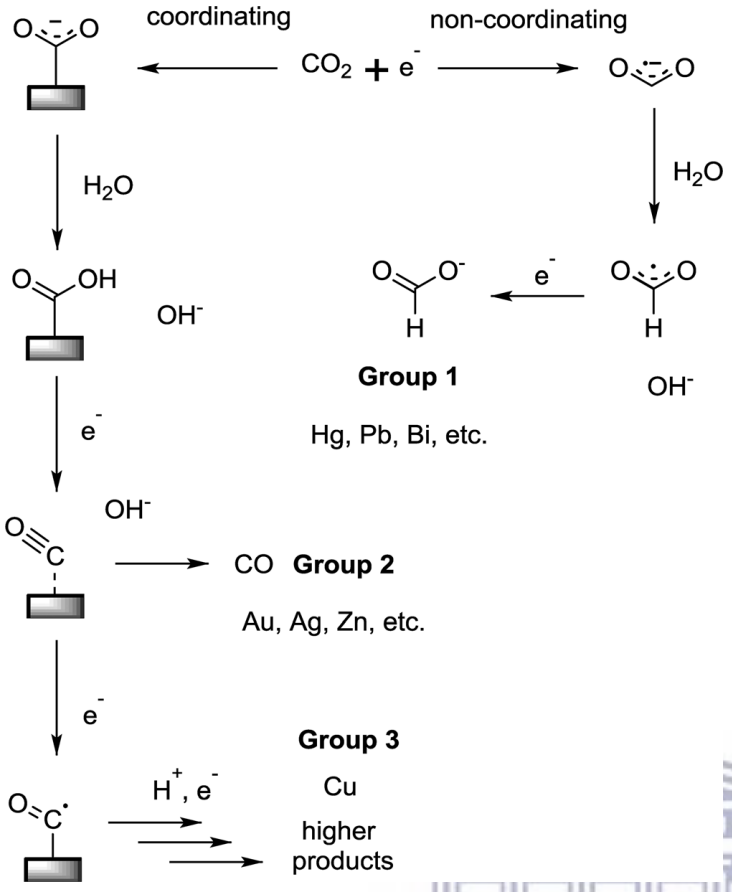

Figure 7.5: Scheme for the mechanism for the electrochemical reduction of CO_2 (Jones *et al.* 2014).

Urea is one of the many possible products formed during reduction of CO_2, others include methanol, methane, polymers and other higher hydrocarbons (Agarwal *et al.* 2014). The formation of urea occurs during the simultaneous reduction of CO_2 and nitrite ions as shown in reaction 29-31 (Shibata *et al.* 1998). This study was based on the formation of urea, CO, formic acid and ammonia at gas diffusion electrodes with Au, Cu and Ag catalysts. They were unable to detect the formation of ammonia precursor (equation 33), and concluded that the reaction mechanism of urea formation (33-35) still applied as the possibility.

$$CO_{2\,(g)} + 2H^+ + 2e^- \rightarrow CO + H_2O \quad (33)$$

$$N_2^- + 6H^+ + 5e^- \rightarrow NH_2 + H_2O \quad (34)$$

$$CO + NH_2 \rightarrow (NH_2)_2CO \quad (35)$$

7.4 Conclusion

The development of highly selective, robust and efficient catalyst is important to successfully reduce CO_2 to valuable products. The electrochemical reduction of CO_2 at Bi/Au electrode was demonstrated. The catalyst used showed excellent selectivity towards the formation of a single product, which was qualitatively identified as urea. Further work needs to be done to confirm the products using other methods (gas chromatography) and quantification of the products to determine selectivity that were hindered from being completed due to unavailability of resources.

7.5 References

Agarwal, AS, Rode, E, Sridhar, N, Hill, D (2014) Conversion of CO_2 to value-added chemicals: Opportunities and challenges. *Handbook of Climate Change Mitigation and Adaptation* 1-40.

Choi, SY, Jeong, SK, Kim, HJ, Baek, I-H, Park, KT (2016) Electrochemical reduction of carbon dioxide to formate on tin–lead alloys. *ACS Sustainable Chemistry & Engineering* **4**, 1311-1318.

DiMeglio, JL, Rosenthal, J (2013) Selective conversion of CO_2 to CO with high efficiency using an inexpensive bismuth-based electrocatalyst. *Journal of the American Chemical Society* **135**, 8798-8801.

Gattrell, M, Gupta, N (2006) A review of the aqueous electrochemical reduction of CO_2 to hydrocarbons at copper. *Journal of Electroanalytical Chemistry* **594**, 1-19.

Hu, B, Guild, C, Suib, SL (2013) Thermal, electrochemical, and photochemical conversion of CO2 to fuels and value-added products. *Journal of CO_2 Utilization* **1**, 18-27.

Jones, JP, Prakash, G, Olah, GA (2014) Electrochemical CO_2 reduction: recent advances and current trends. *Israel Journal of Chemistry* **54**, 1451-1466.

Kaneco, S, Hiei, N-h, Xing, Y, Katsumata, H, Ohnishi, H, Suzuki, T, Ohta, K (2002) Electrochemical conversion of carbon dioxide to methane in aqueous $NaHCO_3$ solution at less than 273 K. *Electrochimica Acta* **48**, 51-55.

Lee, CW, Hong, JS, Yang, KD, Jin, K, Lee, JH, Ahn, H-Y, Seo, H, Sung, N-E, Nam, KT (2017) Selective electrochemical production of formate from carbon dioxide with bismuth-based catalysts in an aqueous electrolyte. *ACS Catalysi* **2**, 931-937.

Lim, RJ, Xie, M, Sk, MA, Lee, J-M, Fisher, A, Wang, X, Lim, KH (2014) A review on the electrochemical reduction of CO_2 in fuel cells, metal electrodes and molecular catalysts. *Catalysis Today* **233**, 169-180.

Lv, W, Zhou, J, Bei, J, Zhang, R, Wang, L, Xu, Q, Wang, W (2017) Electrodeposition of nano-sized bismuth on copper foil as electrocatalyst for reduction of CO_2 to formate. *Applied Surface Science* **393**, 191-196.

Medina-Ramos, J, DiMeglio, JL, Rosenthal, J (2014) Efficient reduction of CO_2 to CO with high current density using in situ or ex situ prepared Bi-based materials. *Journal of the American Chemical Society* **136**, 8361-8367.

Shibata, M, Yoshida, K, Furuya, N (1998) Electrochemical synthesis of urea at gas-diffusion electrodes: Part II. Simultaneous reduction of carbon dioxide and nitrite ions at Cu, Ag and Au catalysts. *Journal of Electroanalytical Chemistry* **442**, 67-72.

Vickers, JW, Alfonso, D, Kauffman, DR (2017) Electrochemical carbon dioxide reduction at nanostructured gold, copper, and alloy materials. *Energy Technology*

Walker, RJ, Pougin, A, Oropeza, FE, Villar-Garcia, IJ, Ryan, MP, Strunk, J, Payne, DJ (2015) Surface termination and CO_2 adsorption onto bismuth pyrochlore oxides. *Chemistry of Materials* **28**, 90-96.

Whipple, DT, Kenis, PJ (2010) Prospects of CO_2 utilization via direct heterogeneous electrochemical reduction. *The Journal of Physical Chemistry Letters* **1**, 3451-3458.

Zhang, W, Hu, Y, Ma, L, Zhu, G, Wang, Y, Xue, X, Chen, R, Yang, S, Jin, Z (2017) Progress and Perspective of Electrocatalytic CO_2 Reduction for Renewable Carbonaceous Fuels and Chemicals. *Advanced Science*

Zhang, Z, Chi, M, Veith, GM, Zhang, P, Lutterman, DA, Rosenthal, J, Overbury, SH, Dai, S, Zhu, H (2016) Rational design of Bi nanoparticles for efficient electrochemical CO_2 reduction: the elucidation of size and surface condition effects. *ACS Catalysis* **6**, 6255-6264.

CHAPTER 8

8 Conclusion and Recommendations

Electrochemical atomic layer deposition was used to prepare thin films of Sn and Bi materials on Au coated glass and Cu foil substrates for applications in sodium ion batteries and electro oxidation of alcohols for the alkaline direct alcohol fuel cells. Different types of deposition procedures were used and parameters that affect film formation, growth and structure were also evaluated using suitable techniques. These materials were tested for their activity for each application.

8.1 Summary

Thin films of SnBi and Bi on Au coated glass were prepared using an indirect underpotential deposition method and surface limited replacement reaction respectively. The thin films of SnBi were found to contain both Sn and Bi while the Bi thin films contained Bi only. Well-defined structures both Sn and Bi were evenly distributed on the surface. Crystalline thin films were formed, contained Bi, AuSn, SnBi intermetallic phases. The absence of Sn phases on the XRD was due to low Sn content.

SnBi and Bi on Cu foil substrate were fabricated using electrochemical atomic layer deposition. The effect of the deposition potential (current density) of Bi and the concentration of Sn on the structure and morphology of the films were investigated. The Bi thin films formed at varied potentials, within the UPD region, were structurally different. It was found that well defined structures with larger particles were formed when Bi and Sn content were the same. The deposited film materials were crystalline. Bi films consisted mainly of bismuth and bismuth oxide while SnBi films contained bismuth tin oxide and other phases of Cu and Sn. The thickness of the films increased with cycle number and varied along the. Sn was distributed evenly across the film while some Bi was found more concentrated on the surface. SnBi on Cu foil were tested as anode material for Na ion batteries. The electrode exhibited high initial discharge capacity of, but suffered 65% capacity loss within the first five cycles.

Pd, Sn and Bi based catalysts were prepared via the surface limited redox replacement reaction (SLRR) and direct UPD methods. The activity of these films towards the electro oxidation of ethanol and glycerol in alkaline media was tested. The following catalysts were prepared: Pd, PdSn, PdBi, PdBiSn, BiPd, and SnPd on Au substrate. The morphology of the

materials was found to be similar with the exception of PdBi material. The addition of Sn and Bi to Pd was found to improve activity and stability of the catalysts for ethanol and glycerol oxidation. All the prepared catalysts showed better activity towards ethanol oxidation compared to glycerol oxidation. Ethanol is easily oxidised on all prepared catalysts than glycerol.

The electrodeposited Bi/Au was tested for CO_2 conversion. The by-products formed were indicated by the presence of foreign peaks. These peaks were matched with possible products resulting in urea being the eminent product. This catalyst showed excellent selectivity forwards formation of a single product.

8.2 Recommendation

The method used was able to feasibly demonstrate that Sn and Bi can be deposited on Au substrates without the use of additives; higher Sn content containing thin films can thus far be obtained by using additives. This technique needs to be used in applications where low Sn content is not a problem. Further work needs to be done to improve the Sn content.

The application of the EALD method to make self-supported anode electrodes for Na ion batteries was explored for the first time in this study and excellent initial discharge capacities were obtained. However, the stability of the SnBi electrodes during cycling, and capacity failure needs further investigations as well as the effect Sn has on the electrode performance. Explore ways of introducing carbon support material into the electrodes during cell assembly to increase the electrode loading and packing, which might improve the capacity or reduce capacity fading.

The Pd catalysts for electro oxidation of alcohols showed great potential. Based on the obtained results, these catalysts need to be used for ethanol oxidation compared to glycerol. The catalysts need further work to improve glycerol oxidation and can be tested for oxidation of other alcohols.

The use of Bi/Au catalyst for CO_2 reduction is promising and has demonstrated good selectivity. Further work need to be done to quantitatively identify and analyse the by-product using other techniques.